



UNIVERSITYTRANSPORTATIONCENTER
FOR UNDERGROUND TRANSPORTATION INFRASTRUCTURE

**APPLYING PROBABILISTIC APPROACHES FOR RELIABLE
SEQUENTIAL EXCAVATION METHOD TUNNEL DESIGN AND
CONSTRUCTION**

FINAL PROJECT REPORT

by

Haotian Zheng¹

Michael Mooney¹

Marte Gutierrez¹

¹ Colorado School of Mines

Sponsorship

UTC-UTI and cost matching external sponsors

For

University Transportation Center for
Underground Transportation Infrastructure
(UTC-UTI)

April 4, 2022



COLORADOSCHOOLOFMINES
EARTH • ENERGY • ENVIRONMENT

Disclaimer

The contents of this report reflect the views of the authors, who are responsible for the facts and the accuracy of the information presented herein. This document is disseminated in the interest of information exchange. The report is funded, partially or entirely, by a grant from the U.S. Department of Transportation's University Transportation Centers Program. However, the U.S. Government assumes no liability for the contents or use thereof.

1. Report No.	2. Government Accession No.	3. Recipient's Catalog No.	
4. APPLYING PROBABILISTIC APPROACHES FOR RELIABLE SEQUENTIAL EXCAVATION METHOD TUNNEL DESIGN AND CONSTRUCTION		5. April 4 th , 2022	
		6. Performing Organization Code	
7. Haotian Zheng Michael Mooney Marte Gutierrez		8. Performing Organization Report No.	
9. Performing Organization Name and Address University Transportation Center for Underground Transportation Infrastructure (UTC-UTI) Tier 1 University Transportation Center Colorado School of Mines Coolbaugh 308, 1012 14th St., Golden, CO 80401		10. Work Unit No. (TRAIS)	
		11. Contract or Grant No.	
12. Sponsoring Agency Name and Address United States of America Department of Transportation Research and Innovative Technology Administration		13. Type of Report and Period Covered	
		14. Sponsoring Agency Code	
15. Supplementary Notes Report also available at: https://zenodo.org/communities/utc-uti			
16. The sequential excavation method (SEM) is commonly employed in soft ground urban tunnel construction. Large-scale SEM in the midst of urban infrastructure is complex because allowable ground deformations are relatively small. Considerable uncertainties exist during SEM design and construction due to limited knowledge of ground conditions and flexible construction measures as allowed by contractual guidelines. The conventional practice using deterministic analysis to evaluate SEM-induced ground and structural responses does not account for the uncertainties, and therefore is less adaptive and robust, leaving the SEM design and construction blindly risk-taking. Given the considerable technical and financial risks taken by SEM projects, it is imperative to develop efficient and accurate probabilistic approaches to help designers and contractors make well-grounded decisions based on updated knowledge of risk along the SEM construction process.			
17. Sequential excavation method tunneling; probabilistic analysis; back-analysis; surrogate modeling; reliability analysis		18. Distribution Statement No restrictions.	
19. Security Classification (of this report) Unclassified	20. Security Classification (of this page) Unclassified	21. No of Pages 205	22. Price NA

ABSTRACT

The sequential excavation method (SEM) is commonly employed in soft ground urban tunnel construction. Large-scale SEM in the midst of urban infrastructure is complex because allowable ground deformations are relatively small. Considerable uncertainties exist during SEM design and construction due to limited knowledge of ground conditions and flexible construction measures as allowed by contractual guidelines. The conventional practice using deterministic analysis to evaluate SEM-induced ground and structural responses does not account for the uncertainties, and therefore is less adaptive and robust, leaving the SEM design and construction blindly risk-taking. Given the considerable technical and financial risks taken by SEM projects, it is imperative to develop efficient and accurate probabilistic approaches to help designers and contractors make well-grounded decisions based on updated knowledge of risk along the SEM construction process.

As the first contribution of the thesis, a comprehensive case study of the Regional Connector Transit Corridor (RCTC) cavern construction is conducted. The performance of the three-drift seven-stage urban SEM was assessed, and complex ground and structural behaviors were evaluated every excavation step by analyzing the field observations. The average total ground surface settlement is about 20 mm. The total volume loss of 0.45% is considered an excellent-quality practice considering the large scale and shallow overburden of the cavern. An automated program was developed to analyze four-dimensional deformation measurements in real time, providing prompt ground and structural behavior assessment to facilitate the decision-making process.

Second, a three-dimensional (3D) finite-difference method (FDM) model is developed to simulate the SEM construction process and surrogate models are developed to accurately and efficiently capture the complex 3D FDM deformation responses induced by SEM tunneling. The efficacies of four surrogate methods were examined. A sensitivity analysis was performed to determine the most influential geotechnical parameters as the surrogate model inputs. A design of experiments was performed based on Sobol sequence sampling. The results indicate two Polynomial-Chaos-Kriging (PCK) models exhibit the best performance with the model-average normalized root mean square errors (NRMSE) less than 3%.

Third, a surrogate-based Bayesian approach is developed to update uncertain ground parameters and deformation predictions during the RCTC SEM construction. The PCK surrogate model developed in the previous part was used to evaluate SEM-induced ground and structure deformations to be compared with the field observations. Time-series observations of multiple measurements are used to form the likelihood function. The posterior distributions derived from the affine invariant ensemble sampling method reveal higher elastic modulus and cohesion of the fresh Fernando formation than what was assumed before the construction. The uncertainties of the geotechnical parameters are substantially reduced, which translates into reduced risk simply because prediction uncertainty is far less. The updated parameters for all considered monitoring sections show similar results, indicating similar ground conditions along the cavern alignment.

Lastly, a reliability approach is developed to evaluate ground and structural stabilities induced by SEM construction under the uncertainty of ground conditions and the variability of design measures. The variations of two geotechnical parameters, two shotcrete parameters, and three types of SEM toolbox items were considered in the reliability analysis. The influence of each parameter on the two reliability indices was quantified and discussed.

TABLE OF CONTENTS

ABSTRACT.....	iii
TABLE OF CONTENTS.....	v
LIST OF FIGURES	xi
LIST OF TABLES	xvi
ACKNOWLEDGMENTS	Error! Bookmark not defined.
CHAPTER 1	1
1.1 Motivation	1
1.2 Research Objectives	3
1.3 Thesis organization	3
CHAPTER 2	5
2.1 SEM background.....	5
2.2 Analysis tools for evaluating SEM-induced ground and structural deformations	7
2.2.1 Empirical methods	8
2.2.2 Analytical methods	8
2.2.3 Computational modeling.....	9
2.3 Back-analysis in tunnel construction.....	13
2.4 Reliability analysis of tunnel construction	14

2.5	Surrogate modeling	17
2.5.1	Polynomial response surface.....	19
2.5.2	Radial basis functions	19
2.5.3	Polynomial chaos expansion.....	20
2.5.4	Kriging	21
2.5.5	Support vector regression	22
2.5.6	Artificial neural networks	23
2.5.7	Polynomial chaos Kriging.....	23
CHAPTER 3	26
3.1	Abstract	26
3.2	Introduction	26
3.3	Project Overview	29
3.3.1	Project background	29
3.3.2	Geological and Geotechnical Conditions.....	31
3.3.3	Construction Sequence.....	32
3.3.4	Instrumentation	35
3.4	Analysis of field measurements	36
3.4.1	Observed Ground Surface Settlement.....	36
3.4.2	Subsurface Settlement.....	43
3.4.3	Tunnel Convergence	45

3.4.4	Multi-level Deformation Interpretation	51
3.5	Real-Time Analysis in SEM Construction.....	53
3.6	Conclusions and Recommendations.....	55
3.7	Acknowledgments	60
CHAPTER 4	61
4.1	Abstract	61
4.2	Introduction	61
4.3	Project background	64
4.4	3D finite-difference modeling.....	66
4.5	Surrogate modeling methodology	70
4.5.1	Polynomial Chaos Expansion	71
4.5.2	Kriging	71
4.5.3	Polynomial Chaos-Kriging	72
4.5.4	Procedure of SEM surrogate modeling.....	74
4.6	Sensitivity analysis to determine surrogate model input parameters	75
4.7	Construction and validation of the surrogate model	78
4.8	Conclusions and discussion.....	88
4.9	Acknowledgments	90
CHAPTER 5	91
5.1	Abstract	91

5.2	Introduction	91
5.3	A progressive Bayesian updating framework for SEM tunneling	94
5.3.1	Bayesian inference for model updating	94
5.3.2	MCMC simulation using AIES.....	95
5.3.3	Procedure of the proposed progressive Bayesian updating	96
5.4	Application to RCTC SEM cavern project.....	97
5.4.1	Project background.....	97
5.4.2	3D Numerical modeling.....	100
5.4.3	Construction and validation of the surrogate model	103
5.4.4	Bayesian updating ground parameters and model predictions using field measurements	106
5.5	Conclusions	113
5.6	Acknowledgments	114
CHAPTER 6	115
6.1	Abstract	115
6.2	Introduction	115
6.3	Deterministic model and probabilistic analysis for SEM construction.....	117
6.3.1	3D finite-difference model of SEM tunnel construction	117
6.3.2	Key performance indicators for SEM construction	122
6.3.3	Probabilistic analysis using surrogate modeling.....	124

6.4	Initial support design concerns using LRFD.....	126
6.5	Reliability analysis of SEM-induced ground deformation and lining forces.....	129
6.6	Conclusions	134
6.7	Acknowledgments.....	135
CHAPTER 7		136
7.1	Conclusions	136
7.2	Recommendations for future research.....	137
REFERENCES		139
APPENDIX A.....		154
A.1	Ground surface measurements.....	Error! Bookmark not defined.
A.2	Subsurface measurements.....	Error! Bookmark not defined.
A.3	Tunnel convergence.....	Error! Bookmark not defined.
A.3.1	Left lining convergence.....	Error! Bookmark not defined.
A.3.2	Right lining convergence	Error! Bookmark not defined.
A.3.3	Center lining convergence.....	Error! Bookmark not defined.
A.4	Pore water pressure measurements.....	Error! Bookmark not defined.
APPENDIX B		154
APPENDIX C		158
APPENDIX D.....		163

LIST OF FIGURES

Figure 2.1 Typical SEM construction sequence: (a) longitudinal view, and (b) cross-section view (after Thomas, 2019).	6
Figure 2.2 The relationship between LDP, GRC, and SRC for using the CCM (after Vlachopoulos and Diederichs, 2009).	9
Figure 2.3 Distribution of Q , R , G and illustration of the probability of failure.....	15
Figure 2.4 3D illustration of the probability of failure with two random variables.....	16
Figure 2.5 Illustration of surrogate modeling.	18
Figure 2.6 Flow chart for the optimal PCK model construction.....	25
Figure 3.1 (a) Cross-section of the SEM cavern and subsurface conditions. (b) Interpretation of field and laboratory tests (cohesion c' , friction angle ϕ' , unconfined compression strength UCS , water content ω , dry unit weight γ_{dry} , and elastic modulus E).	29
Figure 3.2 Alignment and monitoring layout of the LA RCTC SEM cavern.....	29
Figure 3.3 SEM construction progress: (a) Left drift (I: left top heading, II: left invert); (b) Right drift (III: right top heading, IV: right invert); (c) Center drift (V: center top heading, VI: center bench, VII: center invert); and (d) Temporary wall demolition.....	31
Figure 3.4 Excavation sequence for the SEM cavern: (a) cross-section view; (b) plan view; (c) side drift sequence; and (d) center drift sequence.	33
Figure 3.5 Initial support system: (a) shotcrete support LTH; (b) cast-in-place concrete support CINV; (c) TBM ring removal; (d) strength development. [Images (a–c) by Christophe Bragrad.]	34
Figure 3.6 Main types of instrumentation. (Images by authors.).....	36
Figure 3.7 Surface settlement at Sta. 0 + 15 (daily measurements). SL = left side GSSP; and SR = right side GSSP.	37
Figure 3.8 Surface settlement for all monitoring sections.	38
Figure 3.9 Surface settlement contours at different stages: (a) left and right drifts started; (b) left and right drifts finished, center top heading excavated; (c) center bench and invert excavated; and (d) all excavation finished.	39
Figure 3.10 Curves fitted to settlement data at transverse sections: (a) Sta. 0+15; (b) Sta. 0+30; (c) Sta. 0+45; (d) Sta. 0+60; (e) Sta. 0+76; and (f) expected settlement from design	

analysis (L: left drift passed; R: right drift passed; CTH: center top heading passed; and CINV: center bench and invert passed.)	42
Figure 3.11 Subsurface deformation at Sta 0+20.	44
Figure 3.12 Subsurface deformation at Sta. 0+45.	45
Figure 3.13 In-tunnel convergence at left drift Sta. 0+15: (a) measured displacements M2 and M3 where subscript H and V represent horizontal and vertical displacement components; (b) measured displacements M4 and M5 where subscript H and V represent horizontal and vertical displacement components; and (c) relative movements.....	47
Figure 3.14 In-tunnel convergence at left drift Sta. 0+45: (a) measured displacements M2 and M3 where subscript H and V represent horizontal and vertical displacement components; (b) measured displacements M4 and M5 where subscript H and V represent horizontal and vertical displacement components; and (c) relative movements.....	49
Figure 3.15 Measurements of center crown convergence beginning after CTH excavation.....	50
Figure 3.16 Measurements of center invert convergence (uplift) beginning after CINV installation.	51
Figure 3.17 Field displacement at Sta. 0+15, including surface, subsurface, and in-tunnel deformation.....	52
Figure 3.18 Field displacement at Sta. 0+45, including surface, subsurface, and in-tunnel deformation.....	53
Figure 3.19 Architecture of real-time deformation analysis in the SEM construction.	55
Figure 4.1 LA RCTC SEM cavern layout: (a) plan view and (b) vertical profile at Sta. 0+15 (adapted from (Zheng et al., 2021a)).....	65
Figure 4.2 Construction sequence for the SEM cavern (adapted from (Zheng et al., 2021a)).	66
Figure 4.3 3D Finite-difference model simulation.	67
Figure 4.4 Shotcrete lining model: (a) Shotcrete age at i^{th} round behind the excavation face; (b) Time-dependent elastic modulus of liner elements realized in finite-difference model.	70
Figure 4.5 Flow chart for constructing PCK model.....	74
Figure 4.6 3D FDM model outputs of interest (monitoring section at Sta. 0+15).....	77
Figure 4.7 Sensitivity indices of the six model outputs w.r.t. the model input parameters.	78

Figure 4.8 Pair plots of 500 samples DoE (The diagonal plots show univariate histograms of the data in each column; the upper diagonal plots show detailed bivariate sample scatters; the lower diagonal plots show the contours of the bivariate distribution density).	80
Figure 4.9 Influence of sample size (total number of samples used for 80% training and 20% testing) on the surrogate model testing performance: (a) NRMSE; (b) validation error.	82
Figure 4.10 Prediction time costs of the surrogate models (time to compute a single prediction).	83
Figure 4.11 Training and testing performance comparison for the surrogate models (200-sample dataset).....	84
Figure 4.12 NRMSE distributions for test data throughout the surrogate input space with respect to the output: (a) S_L , (b) S_R , (c) MP, (d) C_{M2M3} , (e) C_{CTH} , and (f) C_{CINV} (tested on an independent 100-sample dataset)	88
Figure 5.1 LA RCTC SEM cavern layout: (a) plan view and (b) vertical profile (adapted from (Zheng et al., 2021a)).	98
Figure 5.2 Cross-section view of the SEM construction sequence of stages: I: left top heading (LTH), II: left invert (LINV), III: right top heading (RTH), IV: right invert (RINV), V: center top heading (CTH), VI: center bench (CBEN), VII: center invert (CINV).	99
Figure 5.3 Construction sequence for each drift: (a) side drift sequence; (b) center drift sequence.	99
Figure 5.4 3D FDM model simulation of SEM construction.	100
Figure 5.5 Longitudinal visualization of the most probable geology from geostatistical modeling (geology also varies into the page).....	101
Figure 5.6 3D FDM model outputs used for back-analysis (monitoring section at Sta. 0+15)..	103
Figure 5.7 NRMSE distributions for test data throughout the input parameter space.....	106
Figure 5.8 Histograms of posterior distributions for (a) $Tf1-E50ref$, (b) $Tf2-E50ref$, (c) $Tf2-E0ref$, (d) $Tf2-c'$, and (e) GWT updated at different phases (using measurements at Sta. 0+15).....	108
Figure 5.9 Predictions of final displacements versus the field observations at Sta. 0+15 from different update phases.	110
Figure 5.10 Goodness factors of the updated displacement predictions for each Phase	110

Figure 5.11 Comparison of prior and posterior predictions of time-series measurements for Sta. 0+15: (a) S_L , (b) MP , (c) C_{M2M3} , (d) C_{CTH} , and (e) C_{CINV}	112
Figure 6.1 3D Finite-difference (FD) modeling.	119
Figure 6.2. SEM design toolbox options: (a) Face support (FC), (b) Temporary invert (TI), and (c) Lattice girder (LG).	121
Figure 6.3. 3D FDM model results of M and N obtained from the deterministic analysis for stages at (a) RTH arrives the monitoring plane; (b) RTH is 20 m beyond the monitoring plane; (c) LTH is one round behind the monitoring plane; (d) LTH is 20 m beyond the monitoring plane (using mean values of ground parameters, $RL=2$ m, and no toolbox items).	124
Figure 6.4 NRMSE distributions for test data throughout the surrogate input space with respect to the output M^A , N^A , and S_{max}	125
Figure 6.5. Factored MNID for various sets of characteristic ground properties and probabilistic QuA from 300 MCS (for the design using $t=300$ mm, $f_c=35$ MPa, without any toolbox item applied).....	128
Figure 6.6. Factored MNIDs for various designs of shotcrete thickness (for the design using mean soil properties, $f_c=35$ MPa, without any toolbox item applied).	128
Figure 6.7. Illustration of the limit state function g_1 using 500 MCS by varying ground parameters with constant $t=300$ mm and $f_c=35$ MPa.....	130
Figure 6.8. Convergence of MCS for (a) limit state g_1 and (b) limit state g_2 for the base design.	131
Figure 6.9. Influence of (a) $E50ref$ mean, (b) c' mean, (c) $E50ref$ COV, and (d) c' COV on the reliability indices (other parameters are the same as the base design).	132
Figure 6.10. Influence of (a) f_c and (b) t on the reliability indices (using Design 2 and ground parameter variabilities defined in Table 1).....	134
Figure A.1 Measured building settlement.....	155
Figure A.2 Comparison of building settlement and greenfield settlement (fitted).	155
Figure A.3 Evaluation of angular distortion and lateral strain.....	156
Figure A.4 Damage category assessment of Building I.....	156
Figure A.5 Damage category assessment of Building II.	157
Figure B.1 Cross-section view of the RCTC cavern and the cohesion c' , friction angle ϕ' interpreted from direct shear tests and consolidated isotropic undrained compression (CIUC) triaxial tests.	159
Figure B.2 Determination of $E50ref$ and stress-level dependencies of (a) Tf1 and (b) Tf2.....	159

Figure B.3 Determination of E_{urref} from pressuremeter tests.	160
Figure B.4 Determination of E_{0ref} for Tf1 and Tf2 from geophysical shear wave tests.	162
Figure C.1 Convergence of the MPSRF for the first updating.	163
Figure C.2 Trace plots of MCMC simulations for all chains during the first updating.....	164

LIST OF TABLES

Table 3.1 Building information.....	30
Table 3.2 Average values of settlement trough parameters.....	42
Table 4.1 Geotechnical properties adopted in 3D FDM model.....	67
Table 4.2 Main properties of structural elements.	70
Table 4.3 Probabilistic information of uncertain parameters.....	77
Table 4.4 Surrogate model accuracy metrics for each model output (500-sample dataset with cross-validation performed).....	84
Table 5.1 Geotechnical properties adopted in the model.....	101
Table 5.2 Main properties of structural elements.	102
Table 5.3 Probabilistic information of uncertain parameters.....	105
Table 5.4 Normalized root mean square error (NRMSE) of the PCK surrogate model on testing set.....	105
Table 5.5 Major update phases and corresponding observations	106
Table 5.6 Posterior parameters after Phase V updating for all monitoring sections.....	112
Table 6.1 Model parameters of HSS soil and shotcrete lining.	119
Table 6.2 Statistics of variables used in the deterministic model and probabilistic analysis.	121
Table 6.3 Reliability results of six design examples using $t=300$ mm and $f_c=35$ MPa.....	Error!
Bookmark not defined.	

INTRODUCTION

1.1 Motivation

The sequential excavation method (SEM), also known as the New Austrian Tunneling Method (NATM) or sprayed concrete lining (SCL) method, has been increasingly used for tunnel construction in urban soft ground environments. Compared with the mechanized tunneling approach using a tunnel boring machine (TBM) to excavate and support ground, SEM is more flexible in design and construction and is favorably applied to tunnel schemes with complex geometries, short tunnels, and large span tunnels (Hung et al., 2009a).

The basic concept of the SEM is to favorably utilize the self-supporting capability of the ground as an integrated part of the tunnel support system thus achieving economy and efficiency in ground support without compromising safety. In contrast to the SEM applications in rock tunnels, the development of the SEM in soft ground tunnel construction is relatively new (less than 50-year history). Although generally, they share similar principles, there are still several differences. Minimizing ground deformation and its influence on surface and subsurface structures becomes the major concern when using SEM in urban soft ground settings. Mobilizing a high degree of ground self-support is not often possible as is commonly applied in rock tunneling or in rural areas. Generally, an early and stiff initial support is employed to reduce ground deformation. Meanwhile, the lining structure is expected to sustain higher loads.

Even though the SEM has been successfully applied in numerous soft ground tunnel projects around the world in recent three decades, comprehensive analyses and characterizations of the responses induced by large shallow SEM construction in urban soft ground conditions are quite limited (Berg et al., 2003; Fang et al., 2012; Irshad and Heflin, 1988; Lunardi, 2008a; New and Bowers, 1984; Su, 2013; Thomas, 2019). Most urban SEM projects now utilize advanced instrumentation systems enabling monitoring various types of responses in real time. However, the instrumentation data were usually under-analyzed during the construction stage, leading to a delayed understanding of ground behavior and inefficient communications between contractors and designers. The instrumentation data not only needs to be processed properly but also timely, especially for soft ground SEM tunneling, where the system can evolve rapidly and the control of ground and structure deformations are of high priority.

Physics-based computational modeling using the finite difference method (FDM) or finite element method (FEM) that can predict SEM-induced ground and structural deformations is an important tool. The three-dimensional (3D) nature of the multi-face excavation and complex ground-structural interactions of SEM demand the use of 3D computational modeling (Janin et al., 2015; Möller and Vermeer, 2008; Neuner et al., 2020; Svoboda et al., 2010; Vlachopoulos and Diederichs, 2014). However, considering considerable uncertainty in computational model parameters and numerous SEM design strategies needed to be evaluated, probabilistic studies to assess the effect of changing variables on the model responses are crucial. Depending on the number of variables considered, probabilistic analyses usually require hundred to thousands of model runs. A single 3D computational simulation modeling SEM construction usually takes hours to days to finish. Directly employing a 3D computational model to conduct such analyses is not affordable and arguably impossible. Therefore, an intelligent surrogate model needs to be

developed to accurately capture 3D computational responses induced by SEM tunneling, yet with affordable computational costs.

Due to limited knowledge of ground conditions before construction, the SEM usually adopts a flexible and progressive design that continues into the construction phase as allowed by contractual guidelines. Engineers rely on the observational method (OM) (Peck, 1969) by utilizing the instrumentation data collected during construction to update the knowledge and adapt the SEM design as appropriate. However, the current practices of the OM in SEM construction are less rigorous and robust, mainly relying on experience and engineering judgment. It is highly valuable to utilize the power of computational model and incorporate a back-analysis procedure to update computational model parameters and predictions during SEM construction. Most previous back analysis studies applied in tunnel construction used deterministic methods (Gioda and Maier, 1980; Karakus and Fowell, 2005; Khamesi et al., 2015; Miranda et al., 2011; Ninić and Meschke, 2015; Qi and Fourie, 2018; Vardakos et al., 2016, 2012; Y. Zhang et al., 2020; Zhao et al., 2015). However, fixed values back-analyzed from a deterministic approach can capture neither the uncertainty in the parameters nor the uncertainty in the model predictions (Qi and Zhou, 2017). A single set of parameters will yield a single prediction, based on which of the decisions made to modify SEM construction are risk-taking. Very limited attempts adopted probabilistic back analysis methods such as Bayesian updating for SEM construction, all of which used empirical equations or simplified 2D convergence and confinement method as the stress-deformation prediction model (Janda et al., 2018a). However, the updated geotechnical parameters with models inadequately considering complex SEM behavior may not reflect the real physical characteristics of the ground material and are therefore less valuable. This motivates the development of an efficient Bayesian updating approach to update ground parameters and model predictions based on 3D computational modeling of SEM construction. The aim is to provide quantitative assessments incorporating the observations during SEM construction to help designers and contractors make informed and well-grounded decisions accordingly.

Furthermore, minimizing ground deformation while maintaining structural stability is the key concern when utilizing SEM for shallow urban tunnel construction. Generally, an early and stiff initial support is employed to reduce ground deformation. Meanwhile, the lining structure is expected to sustain higher loads. It is more complex and challenging for designers to come up with a reliable yet economical SEM design. In current industrial practices, the assessments of ground settlement and lining stability for SEM tunnels are separated and the uncertainty of ground conditions are not explicitly considered. For initial support design, current practice adopts the load and resistance factor design (LRFD) approach to handle uncertainty by applying factors at the sides of the load and resistance terms. However, applying rigid factors at each side simply ignores the correlation between loads, support resistance, and deformation. Besides, a design by LRFD provides no explicit information on the probability of failure, nor explicit guidance on how LRFD factors are to be modified given various types and levels of safety requirements (Kong and Phoon, 2015). On the other hand, reliability analysis provides means of evaluating the combined effects of uncertainties and a more consistent and complete measure of risk, which becomes a beneficial tool for SEM design. However, only limited studies utilized reliability approaches for tunnel design. Most of them adopted closed-forms solutions or 2D numerical models that are inadequate to capture complex SEM 3D behavior. Also, the influence of various design variables commonly applied in SEM construction has not been considered.

Therefore, developing a reliability approach to evaluate ground and structural stabilities induced by SEM construction under the uncertainty of ground conditions and the variability of design measures is of great interest.

1.2 Research Objectives

Given the aforementioned motivations, the following objectives were pursued and are reported in this thesis:

- (1) Analyze the observed performance of the Regional Connector SEM cavern construction in urban soft ground by characterizing the ground and structural responses at spatial and temporal scales; develop a real-time analysis tool assisting tunnel engineers to promptly understand ground and structure behavior during the SEM construction, facilitating the decision-making process and enabling an adaptive design.
- (2) Develop a surrogate model to accurately and efficiently capture the ground and structural deformations induced by SEM tunneling based on full 3D computational analysis. Examine the global surrogate accuracy and the accuracy for each individual output. Examine the surrogate model performance throughout the given input parameter space.
- (3) Develop a Bayesian-based approach for updating ground parameters and model predictions within an application of the OM in SEM construction; Evaluate the reduction in uncertainty in ground parameters and the consequent ground and structural deformations by progressively incorporating the field measurements harvested during the construction of the Regional Connector SEM cavern.
- (4) Develop a reliability-based approach to quantify the impacts of geotechnical parameter uncertainty and design variability on two major concerns of urban soft ground SEM projects—ground deformation and structural stability.

1.3 Thesis organization

The thesis is divided into six chapters. Besides the current chapter for introduction, the remaining five are organized as follows:

Chapter 2 provides the necessary background and a literature review of the prior research relevant to this thesis objectives. A brief introduction and history of the SEM are presented. Various analysis tools used in evaluating SEM-induced ground and structural deformations and their advantages and limitations are discussed. Then the purpose and main types of back-analysis

applied in tunneling are reviewed. Finally, the idea of surrogate modeling and commonly used surrogate approaches are presented.

Chapter 3 presents a comprehensive analysis of the Regional Connector Transit Corridor (RCTC) SEM cavern construction in downtown Los Angeles. The assessment of the SEM performance in constructing an urban large-span cavern is presented. The characterization of complex ground and structural behavior is presented. A framework of real-time analysis during SEM construction is highlighted and the benefits for adaptive design and rigorous decision making are illustrated through examples. Several recommendations for shallow soft ground SEM construction in urban areas are summarized based on the lessons learned from the practice.

Chapter 4 examines the capability of four surrogate methods, Polynomial Chaos Expansion (PCE), Kriging, sequential Polynomial-Chaos-Kriging (PCK-SEQ) and optimal Polynomial-Chaos-Kriging (PCK-OPT), for accurately and efficiently capturing the ground and structural deformations induced by SEM tunneling. A procedure for developing a surrogate model for SEM construction is presented, including a step-by-step 3D computational modeling of SEM construction process, a sensitivity analysis to determine surrogate input parameters, and a model training-testing process using the aforementioned surrogate methods. The accuracy of each surrogate model is evaluated and compared.

Chapter 5 introduces a surrogate-based Bayesian approach to update uncertain geotechnical parameters during SEM construction. The proposed approach is applied to the RCTC project to progressively reduce the uncertainty of key geotechnical parameters by incorporating observations of ground and structural deformations. The deviations of the updated parameters from the initial estimations are discussed. The progressive improvement of ground and structural deformation predictions compared to the field measurements is presented.

Chapter 6 presents a reliability-based approach to assist SEM tunnel design, considering both the uncertainty of ground parameters and the design variability in shotcrete parameters and toolbox item selection.

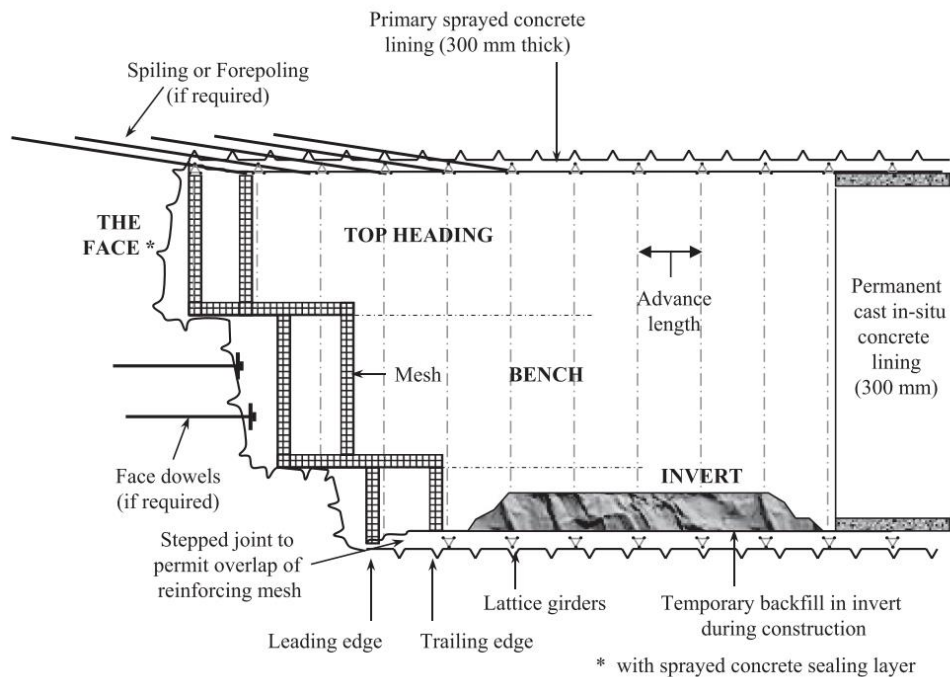
Chapter 7 provides a summary of key findings and contributions of this research. The limitations and suggestions for future research are also discussed.

CHAPTER 2

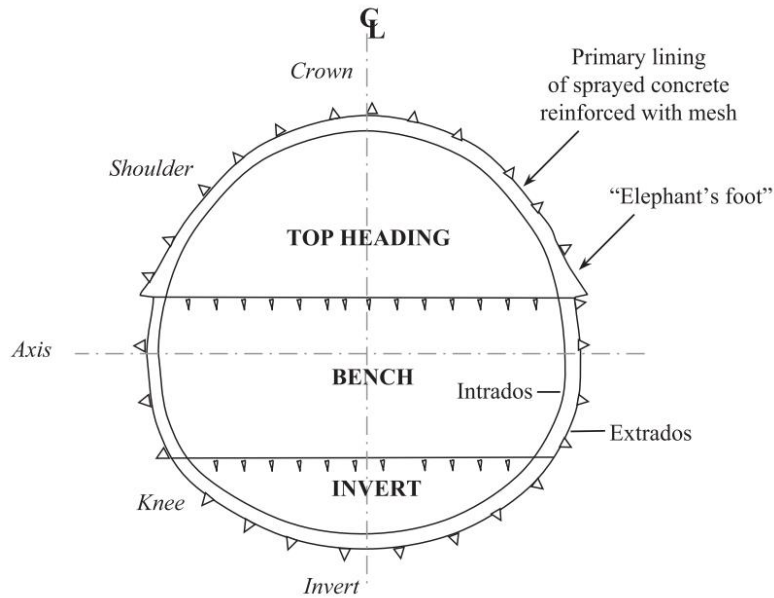
BACKGROUND AND LITERATURE REVIEW

2.1 SEM background

During SEM construction, when a tunnel cross-section is large and full-face excavation is not feasible due to stability or deformation concerns, the tunnel profile is divided into multiple working drifts or headings. The ground exposed from the excavation is rapidly and consistently supported with sprayed concrete in combination with fiber reinforcement, lattice girders, and local ground reinforcement (Thomas, 2019; Tonon, 2010). Figure 2.1 depicts a typical SEM construction sequence and related terminologies. The excavation sequence and support measures are designed based on tunnel geometry, geological condition, and available equipment. The main principle of SEM is to favorably utilize ground strength as part of the support component. SEM was originally formalized by Rabcewicz (1964) and its earliest implementation dates back to 200 years ago according to Sandstrom (1963). Although a variety of terms have been used around the world, such as the New Austrian Tunneling Method used in Europe, sprayed concrete lining (SCL) method used in the United Kingdom, etc., they share the same construction concept. In North America, NATM was first applied in the late 1970s and was adopted as the term in the beginning. With growing utilization for underground construction, however, SEM has become a commonly used term in North America (Munfah et al., 2016; Romero, 2002).



(a)



(b)

Figure 2.1 Typical SEM construction sequence: (a) longitudinal view, and (b) cross-section view (after Thomas, 2019).

The first application of SEM in soft ground was the Frankfurt metro in Germany in 1969 (Karakus and Fowell, 2004). After several early attempts, some doubts had been raised at the time about the use of SEM in soft ground at shallow depth (Kovari 1994). The collapse of three parallel tunnels in the Heathrow Express Rail Link project in 1994 further put this method under examination (Karakus and Fowell, 2004). However, as experience with the method gradually grew, proper guidance was developed to conduct SEM safely in soft ground (HSE 1996; ICE 1996). Two main concerns of SEM in soft ground are difficulty in minimizing deformations with complex excavation sequences and control of construction to avoid collapse.

SEM was first introduced to China at the end of the 1960s. The first soft ground SEM practice in China is the Jundushan railway tunnel project constructed in 1985. In 1986, SEM was applied in the Fuxingmen U-turn subway project with shallow overburden in soft ground. Since then, with the burgeoning growth of China's metro system, SEM has been utilized in hundreds of urban tunnel projects. Through the early attempts employing SEM in shallow soft ground conditions, a new term called 'shallow tunneling method (STM)' was invented by Chinese engineers to distinguish it from general SEM. The major difference between general SEM and STM was concluded as the degree of ground strength mobilization to allow controllable deformation (Fang et al., 2012). Guidelines and key principles to apply STM was summarized by Wang (2006), including (a) proper auxiliary methods, (b) sequential excavation with short advance length, (c) rigid support with quick installation, (d) short ring closure time, and (e) systematic deformation monitoring.

In recent decades, SEM has been increasingly utilized in urban settings. Moritz and Brandtner (2008) reported a 3-kilometer-long urban Lainzer Tunnel excavated by a three-drift SEM in silt and clay with an overburden ranging from 6m to 26 m. The measured cumulative surface settlement was 40 to 52 mm and the overall final convergence of the sidewall in the galleries was up to 40 mm. Fang et al. (2012) presented the performances of nine subway station construction projects in downtown Beijing using five different SEM approaches. Cumulative surface settlements ranging from 17 mm to 100 mm were recorded. Ağbay and Topal (2020) evaluated a twin tunnel-induced surface deformation constructed by two and three-drift SEM in Tehran Alluvium. A maximum 90 mm and an average 50 mm surface settlement were reported within the cover depth from 4.5 m to 40 m. More recent experience on the London Crossrail project includes several km of SEM tunnels, among which the Stepney Green caverns represent the largest span and were excavated with two-side-drift sequences. A maximum 60 mm surface settlement and an average 1.6 % volume loss were observed after the excavation (Ssenyonga, 2018). Over the past 20 years, urban SEM tunneling became more popular as well as versatile in North America, with several major projects completed such as Toronto's Eglinton Crosstown, Ottawa Light Rail Transit, Chinatown station in San Francisco, the Beacon Hill station, and the Bellevue tunnel in Seattle (Brodback et al. 2018; Munfah, Gall, and Matthei 2016; Phelps et al. 2005; Spyridis et al. 2018). However, case histories documenting deformation behavior from those projects are rarely reported.

Executing SEM tunnel construction in urban areas with relatively shallow overburden, soft ground, and the presence of sensitive structures requires rigorous ground deformation control and construction management. In such cases, mobilizing a high degree of ground self-support while maintaining tolerable tunnel-induced deformation, as is possible in rock tunneling, is not often possible. Usually, early support is adopted to reduce convergence, and the initial lining is expected to sustain higher loads. As the loads increase, heavier support might be needed to ensure the structural capacity is not exceeded. While a thicker/stiffer lining will attract higher loads in turn. A valid design may need a great number of iterations. Adopting design principles commonly used in structural engineering may make SEM tunnels more expensive. This issue however has not been well studied and discussed in previous research. Round length and subdivision of the cross-section are carefully designed to aid the excavation and minimize deformations. With ample uncertainty in ground parameters, continuous monitoring and adjustment are critical for success.

2.2 Analysis tools for evaluating SEM-induced ground and structural deformations

The goal of SEM design is to determine an economic excavation method and support measures fulfilling the safety, serviceability and environmental protection requirements for the given ground conditions. A wide range of design tools is available assisting SEM tunnel design, such as empirical methods, analytical methods, numerical modeling, etc. Each tool provides an estimation of SEM-induced responses with its specific assumptions and simplifications, which is nothing more than an approximation of reality.

2.2.1 Empirical methods

Empirical methods are those methods based on experience, engineering judgments, and rules of thumb. These methods are quick and easy to use, thus are widely adopted in practice as a preliminary design or primary design method. The most commonly used empirical equation to estimate the tunneling-induced ground deformation is using the Gaussian settlement profile introduced by Peck (1969). Following his work, multiple empirical equations for the prediction of tunneling-induced ground settlement have been developed based on the field measurements obtained from different projects (Chakeri and Ünver, 2014; Ercelebi et al., 2011; Mair et al., 1993; New and Bowers, 1984; O'Reilly and New, 1982).

However, limitations are obvious for these methods. These empirical equations are fitted from field observations in specific ground conditions, and the selection of parameters are highly based on experience and engineering judgements. The ground stress-deformation behavior and failure mechanism are not considered. Therefore, empirical methods are less useful for predicting complex SEM-induced ground deformation.

2.2.2 Analytical methods

Closed-form solutions for tunnel excavation problems provide another way to evaluate the stress and deformation induced by tunnel excavation in rock or soil. Most methods are developed based on elastic theory and two-dimensional idealization. To estimate liner forces and deformation, Einstein and Schwarz method (Einstein and Schwartz, 1979) amongst others is the most popular one and is still widely used today. This method accounts for the mechanical interaction of ground and support. Other similar analytical approaches are also available—e.g., Muir-Wood (1975), Bobet (2001), Carranza-Torres et al. (2013). For non-circular SEM tunnels, an equivalent radius calculated from the tunnel cross-section area is usually used to apply the analytical methods. Another well-known 2D plane strain analysis considering the ground-structure interaction is the convergence confinement method (CCM). The CCM provides a 2D solution to simulate the 3D tunneling problem by utilizing the relationship between three curves—the ground reaction curve (GRC), the longitudinal displacement profile (LDP), and the support reaction curve (SRC). The principle and applications of CCM have been well-documented in the literature (Carranza-Torres and Fairhurst, 2000; Panet and Guenot, 1982; Vlachopoulos and Diederichs, 2009).

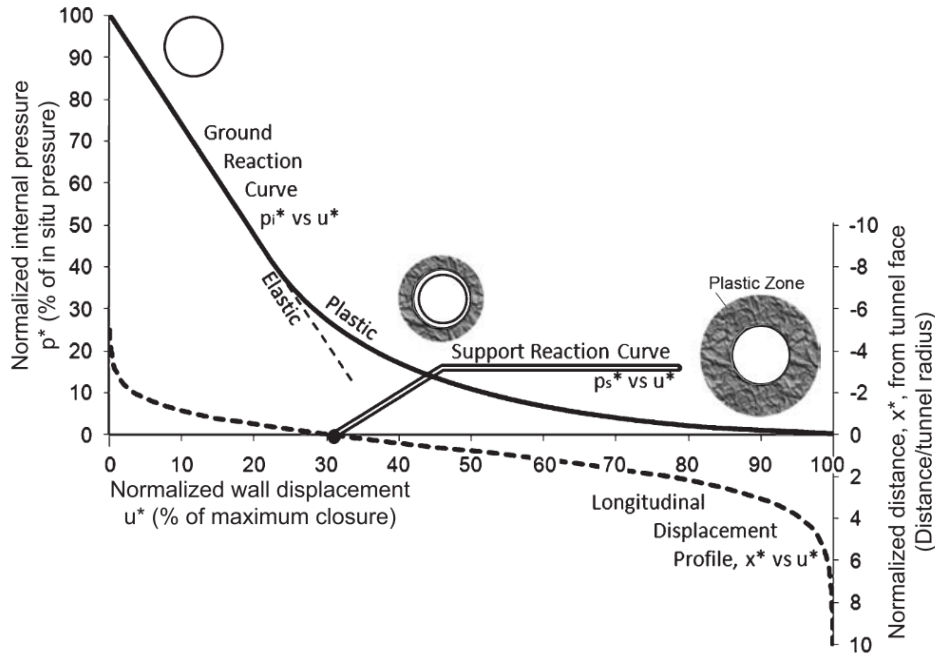


Figure 2.2 The relationship between LDP, GRC, and SRC for using the CCM (after Vlachopoulos and Diederichs, 2009).

There are also various closed-form solutions for estimating tunneling-induced ground deformation. The deformation patterns are assumed by a uniform or oval-shaped radial ground movement around the opening. Verruijt and Booker (1996) introduced an approximate solution for estimating ground deformation in a homogeneous elastic halfspace by extending the virtual image method proposed by Sagaseta (1987). The method was further improved by Loganathan (2011) and is recommended by AASHTO LRFD Tunnel Design guidelines (AASHTO, 2017). Other categories of analytical solutions include the complex variable solution (Verruijt, 2021; Verruijt and Strack, 2008; Wang et al., 2009; Z. Zhang et al., 2020), the stress function elastic theory (Bobet, 2001; Chou and Bobet, 2002; Park, 2005), and stochastic medium theory (Yang et al., 2004; Yang and Wang, 2011; Zeng and Huang, 2016).

Although analytical solutions are helpful and user-friendly, especially for preliminary design and validation check of numerical methods, their limitations are obvious and they serve as a complementary role in current tunnel design. Most of these analytical methods are developed for deep circular tunnels, constructed in full-face in homogeneous elastic ground. This becomes one of the major drawbacks when designing SEM tunnels, considering irregular excavation shape and complex excavation sequences usually involved.

2.2.3 Computational modeling

The limitations using empirical and analytical methods are overcome by using numerical methods, such as the finite element method (FEM) and the finite difference method (FDM) based on continuum modeling, discrete element method (DEM), and boundary element method (BEM).

Muniz de Farias (de Farias et al., 2004) and Negro and Queiroz (Negro and Queiroz, 1999) presented a summary of numerical approaches used for tunneling analysis. They collected more than 65 literature before the early 2000s, in which the finite element method (FEM) accounts for 96%, becoming the most popular approach, and the remaining cases used the finite differences method (FDM) or others. They noted that 92% of the cases were still conducted in 2D under the hypothesis of plane strain conditions. 3D modeling becomes more common nowadays and is usually required in most SEM project designs. Commonly used software to implement numerical analysis for SEM tunneling include FLAC^{3D} (Itasca Consulting Group Inc., 2019), ABAQUS (Abaqus, 2011), PLAXIS^{3D} (Brinkgreve et al., 2013), Phase2 (Rocscience, 2008), UDEC or 3DEC (Itasca Consulting Group, 2016, 2014). The model of SEM construction should ideally consider the following (Thomas, 2019):

- (1) The construction sequence and the three-dimensional stress redistribution around the tunnel face
- (2) The time-dependent behavior of the sprayed concrete
- (3) Nonlinear material behavior of the ground material and sprayed concrete

Tunnel construction disturbs the initial state of the ground stress around the opening and continuously forms new equilibrium states along the excavation process. Close to the excavation face of each heading, the arching effect is in three dimensions. This 3D disturbance begins up to two excavation diameters ahead of the tunnel face and ends around one excavation diameter behind the face (Hung et al., 2009a). Only at a distance where the tunnel is no longer affected by the 3D disturbance or at far-field ahead of excavation, a two-dimensional stress state can be considered. To accurately simulate SEM construction, it is important to capture this effect in numerical analysis. However, despite the great enhancement of current computing capabilities, 3D models are still too time-consuming and complex for simulation-intensive use. In current SEM research or industrial practices, 2D analyses are still dominant in probabilistic analysis for design trials or uncertainty assessment. In 2D modeling, CCM is widely utilized to mimic the 3D tunneling effects. One approach is applying gradually reduced internal pressure at tunnel circumferential boundary to simulate the pre-convergence happened before lining installation. Another popular technique is the use of ground modulus reduction within the excavation perimeter. In these cases, an appropriate selection of the stress release coefficient λ or property reduction ratio is the key. Möller and Vermeer (Möller and Vermeer, 2008) conducted a numerical study concluding that whether the purpose is to estimate ground deformations or support stresses leads to a different selection of stress release coefficient. De Farias et al. (2004) performed a series of 3D FEM models to simulate NATM excavation. They found that a substantial percentage of the final stabilized settlement is induced before the face arrival, which can only be accurately captured via 3D analyses modeling the longitudinal arching effect. Vlachopoulos & Diederichs (2014) examined the validity of the assumptions and the error inherent in the 2D tunnel analysis. The results indicated that SEM modeling with top heading and bench poses a problem for the LDP approach and a correct installation step is critical for staged 2D modeling to prevent overloading or excess deformations. Similar conclusions were found in other literature showing that 2D SEM model using CCM always needs careful calibration to predict reliable displacement or stress results (Janin et al., 2015; Neuner et al.,

2020; Svoboda et al., 2010). Although 2D model can be calibrated by 3D analysis, with varied ground properties and multiple non-circular excavations, the calibration process is cumbersome.

Suitable constitutive laws should be assigned to represent the ground behavior given the knowledge of ground conditions from geotechnical investigations. Tunnel excavation disturbs ground initial stress and initiates the development of deformations. For SEM tunnel construction, a typical strain level of 10^{-4} to 10^{-1} is expected. Depending on medium properties, higher amplitudes of strain usually develop close to the opening while lower strains are constrained in the far field.

SEM construction involves complex sequences and geometries and the ground material undergoes sophisticated stress paths such as sequentially loading/unloading. There is a growing appreciation that more advanced constitutive models are needed to capture the ground behavior. The most common model representing general soft ground or intact rock is the Mohr-Coulomb (MC) elastic-perfectly plastic model. Several drawbacks have long been noticed when applying the MC model to simulate tunnel construction, such as constant elastic modulus without considering the strain level and non-differentiating of load and unload modules, which usually causes underestimation of the surface ground movements and overestimation of the invert convergence (Obrzud and Truty, 2018). The MC model is still widely used at least in preliminary analyses and for cases where the number of lab/field tests is limited. Many researchers have employed the elastic-perfectly plastic model to predict SEM-induced responses and found satisfactory results (Janda et al., 2018b; Kitchah and Benmebarek, 2016; Li et al., 2016; Ng et al., 2004; Zheng et al., 2021b).

Other advanced constitutive models commonly used in soft ground tunneling include Cam Clay, modified Cam Clay, hardening soil (HS) and hardening soil small strain (HSS) model. For instance, Janin et al. (2015) used a non-linear elastoplastic hardening soil constitutive model (HSM) to represent the Phyllitic bedrock behavior and compared 2D and 3D analyses of conventional tunnel construction. Sharifzadeh et al. (2013) used hardening soil model to simulate an SEM tunneling process in Tehran Alluviums formations, which mainly consist of high to medium cemented gravelly sand. Mašin (2009) presented a numerical analysis of an NATM tunnel in stiff clays, comparing with two different constitutive models to represent London Clay, namely a hypoplastic model and modified Cam Clay model. They concluded that the hypoplastic model provided a satisfactory estimate of the settlement magnitude with a slight overestimation of the settlement trough width. They also emphasized the significance of parameter calibration for the small and large strain stiffness and the rate of stiffness degradation.

Generally, if the serviceability analysis is of interest, advanced constitutive models that can predict the stress-strain relation more accurately are preferred. In many cases, most intact ground material can be modeled by the family of hardening soil models (HS or HSS). The HS model was developed by Schanz et al. (1999) on the basis of the Double Hardening model by Vermeer (1978). Two hardening mechanisms—the deviatoric hardening mechanism and the volumetric hardening mechanism—are considered in the HS model. Ten material parameters are required for the HS model, which can be determined through conventional laboratory tests and engineering judgment. The HSS model is an enhanced version of the HS model and was developed by Benz (2007a) to account for high stiffness developed in the domain of small strains. The HSS model requires two additional parameters, namely the maximum small strain

shear modulus G_0 and the shear strain $\gamma_{0.7}$ at which $G_s=0.7G_0$. Many examples have demonstrated that the HS and HSS models can generate realistic deformations and stresses for underground excavation problems, e.g., (ÇELİK, 2017; Epel et al., 2021; GRAGNANO et al., 2015; Janin et al., 2015; R. F. Obrzud, 2010; Paternesi et al., 2017b; G. Zheng et al., 2018).

Shotcrete is the main component of SEM initial support. It immediately absorbs stresses and deforms during the hydration process. Therefore, the material properties, especially the strength development, are of essential importance (Macht, 2002). The time-dependent shotcrete properties can be implemented based on linear elasticity with gradually increased Young's modulus, which is commonly used in practice (Karakus & Fowell, 2005; C. W. W. Ng, Fong, & Liu, 2018; Paternesi, Schweiger, & Scarpelli, 2017; Li et al., 2016; Kitchah & Benmebarek, 2016). Other advanced shotcrete models are also available including the viscoplastic shotcrete model proposed by Meschke et al. (1996), the elastoplastic shotcrete model proposed by Schädlich and Schweiger (2014), the SCDP model presented by (Neuner et al., 2017b), and the thermo-chemo-mechanical material model developed by Lackner and Mang (2003). A detailed overview of different shotcrete models can be found in (Hammer et al., 2020; Neuner et al., 2017a; Thomas, 2019). It is demonstrated by many researchers that using a non-linear constitutive model for shotcrete could reduce the internal lining forces predicted by the numerical model (Paternesi et al., 2017a; Schweiger et al., 2017). A linear model usually yields excessive high lining forces, leading to an uneconomic design. However, it is not fair to say advanced constitutive models are always superior to a linear model. From a practical point of view, there is insufficient data for most projects to determine many parameters required by those advanced models.

Supplemental toolbox items deployed during construction to pre-support or improve the ground or within the tunnel should also be modeled properly. These include but are not limited to: bolting (Kitchah and Benmebarek, 2016), compensation grouting (Soga et al., 1999), pipe umbrella pre-support system to stabilize the tunnel crown, and cutting face (Kitchah and Benmebarek, 2016) (Janin et al., 2015) (Yeo et al., 2009) (Peila et al., 2017). Elements of the initial support system other than shotcrete are usually modeled implicitly to avoid too many contact regions between different types of elements thus saving computational cost. In the cases of using steel sets in combination with shotcrete as initial support, the contribution from steel sets can be considered in numerical model using the 'equivalent section' approach (Carranza-Torres and Diederichs, 2009).

No matter what constitutive model is selected, a proper estimation of ground properties is critical for a reliable SEM analysis. However, great uncertainty exists to interpret the constitutive model parameters, which stems from many disparate sources such as inherent variability of soil material, measurement error, and transformation uncertainty as concluded by (Phoon and Kulhawy, 1999). In addition, some parameters in advanced constitutive models cannot be directly derived from the lab test data. The behavior derived from the laboratory scale may not represent the behavior on the macro engineering scale (Tang et al., 1999). A back-analysis procedure performed during construction in the framework of the OM is valuable to reduce the parameter uncertainty and associated risk of the SEM project. In this context, physics-based computational modeling that can predict SEM-induced responses to be compared with field measurements is an important tool needed to carry out the OM.

2.3 Back-analysis in tunnel construction

There are generally two common categories of back-analysis methodologies for identifying or updating geotechnical/constitutive parameters in tunneling practice: one is deterministic back-analysis and the other is probabilistic back-analysis.

In deterministic back analysis, with observations available, a set of fixed values are identified for uncertain constitutive parameters through an optimization process. Based on the optimization algorithm used to minimize the difference between predicted and measured responses, the deterministic back analysis can be further classified to gradient-based methods and heuristic methods. In gradient-based methods, the infinitesimal change of the solution path and the corresponding gradients are used to control the solution-solving process (Vardakos et al., 2012). They usually require the calculation of the first or second-order derivatives and thus are more computationally expensive. Heuristic methods refer to experience-based techniques for problem-solving, learning, and discovery that find a globally optimal solution, including artificial neural networks, genetic algorithms, annealing methods, swarm intelligence algorithms, etc. Heuristic methods have been demonstrated to be more robust and efficient for highly non-linear problems or highly irregular objective functions with multiple local optima (Cao et al., 2021; Mottahedi et al., 2018; Vardakos et al., 2016; Zhao et al., 2015). Deterministic back-analysis was first introduced in tunnel engineering by (Gioda and Maier, 1980) and then successfully applied in multiple underground projects (Qi and Fourie, 2018; Vardakos et al., 2012; Zhao et al., 2015). However, fixed values back-analysis from a deterministic approach can capture neither the uncertainty in the parameters nor the uncertainty in the model predictions (Qi and Zhou, 2017). As a result, the deterministic back-analyzed results from one state provide little prior knowledge to the analysis in the next state. Also, a single set of parameter values will yield a single prediction, based on which of the decisions made to modify SEM construction are risk-taking. Another issue faced by inverse analysis of most geotechnical problems is the non-uniqueness of the solution. The difficulty of non-uniqueness cannot be solved by deterministic back-analysis approaches but can be overcome by probabilistic back-analysis approaches such as Bayesian inference (Agostinetti and Malinverno, 2010; Honjo et al., 1994; Malinverno, 2002). These limitations notwithstanding, the deterministic back-analysis approaches are still prevailing in most current underground practices.

Probabilistic approaches such as Bayesian updating provide a framework to combine uncertainties from objective and subjective sources, and to calibrate the model with new observations through Bayesian inference (Oden et al., 2010). The advantage and efficacy of Bayesian updating have been demonstrated in many geotechnical applications including slope and embankment stability, braced excavations, and tunnel construction (de Queiroz et al., 2005; Janda et al., 2018a; Jiang et al., 2018; Juang et al., 2013; Li et al., 2021; Miro et al., 2015; Qi and Zhou, 2017; Sousa and Einstein, 2012; Špačková and Straub, 2013; Wu et al., 2020; D. Zheng et al., 2018). Given the features of SEM and the associated uncertainties, the Bayesian framework is well-suited for SEM projects. Janda et al. (Janda et al., 2018a) applied Bayesian approach to update three Mohr-Coulomb parameters and the stress release factor used in the convergence-confinement method to predict SEM-induced settlements. Improved agreement and confidence level of the predictions were reported Li et al. (Li et al., 2021) adopted a Bayesian method to a full-face excavated rock tunnel, using an empirical approach to predict tunnel convergence.

Based on the measured tunnel convergence, four empirical parameters were updated and the performance of the prediction was improved. Previous Bayesian analyses on SEM construction all adopt empirical equations or simplified 2D convergence and confinement method as the stress-deformation prediction model. Such simplified methods are relatively abstract and imprecise, and cannot adequately model complex multi-face excavation sequences and ground interactions properly (Janin et al., 2015; Neuner et al., 2020; Vlachopoulos and Diederichs, 2014). As a result, the updated geotechnical parameters may not reflect the real physical characteristics of the ground material and are therefore less valuable for future projects. However, there has not been any attempt to incorporate more accurate 3D SEM computational analysis into Bayesian updating framework.

2.4 Reliability analysis of tunnel construction

The purpose of reliability analysis is to quantify uncertainty, which is consistent with the philosophy of the OM and can be considered as its logical extension (Duncan, 2000). Reliability approaches provide a means of evaluating the combined effects of uncertainties, and a means of distinguishing between conditions where uncertainties are particularly high or low. Such analyses proved a more consistent and complete measure of risk as the probability of failure is invariant to all mechanically equivalent definitions of safety (Sayed et al., 2010).

Reliability analysis deals with a quantitative assessment of the probability of occurrence of defined failures. Such failures can be defined as either ultimate limit state (ULS) or serviceability limit state (SLS). A limit state function $G(\mathbf{X})$ is defined as a state beyond which a system no longer satisfies certain performance criteria (Phoon and Ching, 2018). For the simplest case with two independent random variables, load Q and resistance R , the limit state equation can be formulated as:

$$G(\mathbf{X}) = R - Q \quad (2.1)$$

where \mathbf{X} represents the vector of random input variables. When $G(\mathbf{X}) > 0$, the system (e.g., structural element or deformed ground) is operating safely and when $G(\mathbf{X}) < 0$, the performance is unsatisfactory and the system is unsafe. The boundary that separates the safe and unsafe domain is known as the limit state surface. The illustration of this relationship is shown in Figure 2.4. The probability of failure (P_f) is defined as the probability that unsatisfactory performance occurs:

$$P_f = P(G(\mathbf{X}) \leq 0) \quad (2.2)$$

If the random vector of variables \mathbf{X} can be described by a joint probability density function $\mathbf{X} \sim f_{\mathbf{X}}(\mathbf{X})$, the failure probability is calculated as follows:

$$P_f = \int_{\{\mathbf{X}: G(\mathbf{X}) \leq 0\}} f_{\mathbf{X}}(\mathbf{X}) d\mathbf{X} \quad (2.3)$$

Another measure characterizing reliability is the reliability index β , which is defined as the distance in the unit of standard deviation σ between the mean value of the limit state function and the limit state surface as shown in Figure 2.3:

$$\beta = \frac{\mu_G}{\sigma} \quad (2.4)$$

In the case where the load $Q(\mathbf{X})$ and resistance $R(\mathbf{X})$ can be approximated using normal distributions, thus $G(\mathbf{X})$ is also a normal distribution, the reliability index can be directly calculated from the probability of failure:

$$\beta = \Phi^{-1}(1 - P_f) \quad (2.5)$$

where Φ^{-1} is the inverse of the standard normal cumulative distribution function. Figure 2.4 presents a 3D illustration of a limit state function with two random variables.

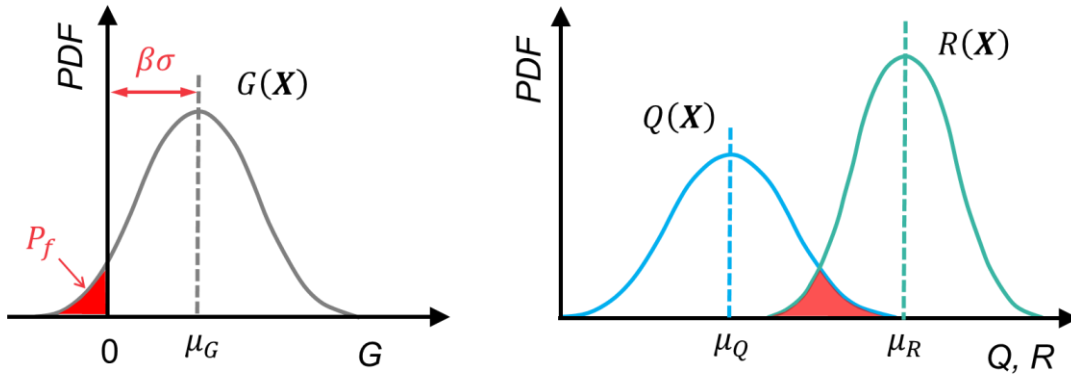


Figure 2.3 Distribution of Q , R , G and illustration of the probability of failure.

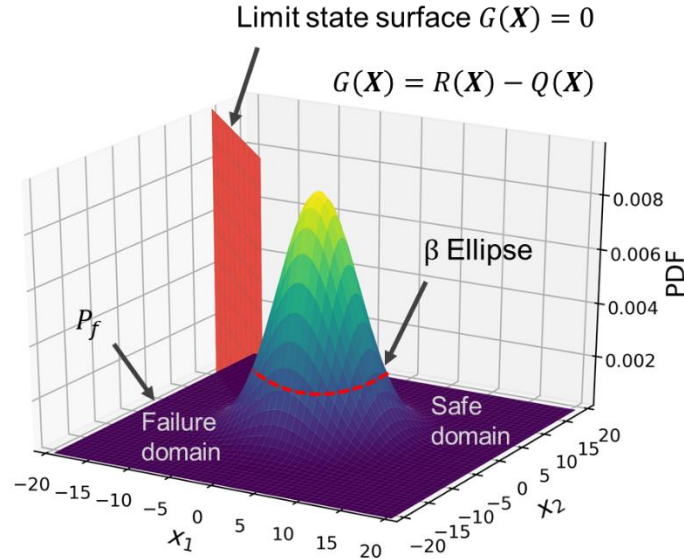


Figure 2.4 3D illustration of the probability of failure with two random variables.

In order to evaluate the probability of failure, two categories of approaches are usually employed, namely approximation-based method and simulation-based method. Approximation methods are based on approximating the limit state function locally at a reference point (e.g., first-order or second-order Taylor expansions). The most famous and widely used methods are the first-order reliability method (FORM) and the second-order reliability method (SORM). A detailed formulation and applications of these two methods can be found in (Cai and Elishakoff, 1994; Ditlevsen, 1981; Fiessler et al., 1979; Hasofer and Lind, 1974; Hohenbichler and Rackwitz, 1988; Low and Tang, 2007, 2004; Lü and Low, 2011; Phoon and Ching, 2018; Tvedt, 1983, 1990; Zhao and Ono, 1999). Simulation methods estimate the probability of failure by sampling the joint distribution of random variables \mathbf{X} and using sample-based experiments to estimate the integral in Eq. 2.3. Monte Carlo simulation (MCS) is a direct sample-based estimation method, which estimates the failure probability by calculating the fraction of samples that cause failure over the total number of samples. Because of its statistically sound formulation, it is usually used as a benchmark solution to compare the results calculated by other approximate approaches. Depending on the complexity of the limit-state function, however, the convergence of MCS sometimes is slow. Importance sampling is a variance reduction method that improves the efficiency of MSC by modifying the sampling density to shift towards the failure region (Glynn and Iglehart, 1989). When the number of random variables is large and the complexity of the failure region increases, adaptive simulation methods such as Subset simulation can be employed. Subset simulation replaces the original probability space with a sequence of simulations of more frequent events in the conditional probability spaces. The conditional probabilities are then evaluated by a Markov chain MCS method (Au and Beck, 2001).

In recent two decades, reliability-based approaches have found wide application in geotechnical engineering (Baecher and Christian, 2005) (Phoon et al., 2003) (Scott et al., 2003) (Griffiths and Fenton, 2008) (Allen, 2012) (Fenton et al., 2015). However, applications of reliability analysis in underground construction are very limited. In general, both ULS and SLS

failure modes are considered in reliability analysis of underground construction, mainly including local or global instability of tunnel face in soft ground or rock mass, the deformation and structural stability of lining system, ground deformations, the capacity of support elements (e.g., rock bolts), etc. Hoek (1998) introduced a brief exposition of reliability approaches suitable for underground openings. Lü & Low (2011) conducted a reliability analysis of a horseshoe-shaped tunnel with respect to the permissible tunnel convergence criterion and compared the results calculated by FORM and SORM. Zhang and Goh (2012) proposed a quantitative probabilistic assessment by using RMR system to determine the global factor of safety required under different ground conditions and an application in underground rock cavern design. Wang et al. (2016) utilized a radial basis function metamodel to approximate the performance function defined based on the plastic zone limit. The proposed procedure was demonstrated by an analytical example and a 2D finite element analysis case. Mollon et al. (2009a, 2009b) presented a reliability analysis of a deep circular tunnel in a homogeneous soil by integrating numerical modeling, the first-order reliability method and the response surface methodology (RSM). The performance functions were defined based on the limit face pressure and the maximum ground settlement.

Most of the previous reliability analyses for tunnels use closed-forms solutions or 2D numerical models, which was demonstrated to be inadequate to accurately capture complex SEM behavior as mentioned in section 2.2.3. Furthermore, the limit state of initial lining capacity was considered as a single limit value or an elastic limit curve in previous studies instead of a more realistic non-linear capacity curve for fiber reinforced concrete (FRC) material. For shallow SEM construction in soft ground, ground surface deformation is one of the major concerns and should be integrated into the limit state functions. Previous RBD analyses only focus on one or two design variables (e.g., rockbolt length, unsupported length), a wider range of design options is available for SEM construction and should be investigated thoroughly.

2.5 Surrogate modeling

Given the complexity of SEM responses and the reliance of construction design on computational predictions, back-analysis is needed to update uncertain computational model parameters. Furthermore, multiple SEM construction strategies (e.g., round length, shotcrete thickness, excavation sequence, support toolbox, etc.) are available to handle expected or unexpected ground conditions. Design optimization is essential and usually conducted throughout the entire SEM design and construction stages. Therefore, various types of probabilistic analyses are needed for quantifying uncertainties and optimizing SEM design.

A 3D computational model is preferred to accurately simulate the physical process of SEM construction. However, 3D simulations are computationally expensive as more detailed knowledge of the real system is included (e.g., explicit construction sequence, 3D realization of ground material). A single 3D FDM simulation modeling SEM construction usually takes hours to days to finish. The aforementioned probabilistic analyses of SEM tunneling usually require a large number of model runs. Employing 3D SEM FDM modeling to conduct such analyses is not

affordable and arguably impossible as some of the probabilistic analyses require thousands to millions of runs.

This limitation motivates the development surrogate model to approximate the computational expensive 3D numerical model. Surrogate modeling, also called metamodeling, has evolved and been extensively used in many engineering fields over the past decades. A wide variety of methods and tools have been introduced for surrogate modeling aiming to develop and utilize computationally efficient surrogates of high-fidelity models mostly in optimization frameworks (Razavi et al., 2012). To train a surrogate model, a dataset needs to be obtained via the original numerical simulations given the design parameter space. By assembling the pairs of inputs and outputs in the dataset, a surrogate model can be constructed through different methods. An illustration of using the surrogate model to replace the 3D numerical model is shown in Figure 2.5.

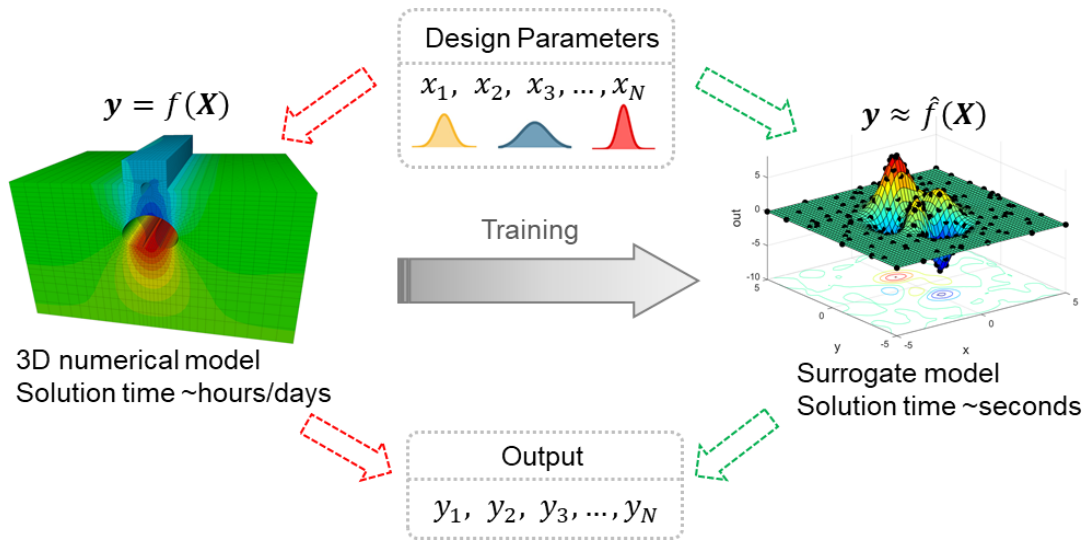


Figure 2.5 Illustration of surrogate modeling.

In order to select the input parameters spreading out uniformly across the design space, a design of experiments (DoE) strategy is needed. The main purpose of DoE is to understand which set of variables in a process affects the performance most and then determine the best levels for these variables to obtain satisfactory output functional performance in products (Antony, 2014). Various DoE techniques are available and can be generally classified into two major categories, namely static and adaptive. An adaptive or sequential DoE is incorporating system knowledge to generate samples incrementally or progressively to obtain the best design with the smallest sample set. Commonly used DoE approaches include Latin Hypercube sampling (LHS), orthogonal array sampling (OAS), Sobol sampling, Hammersley sampling (HAM), Halton sampling, etc (Garud et al., 2017). Readers can refer to Garud et al. (2017) for a more detailed review of DoE strategies.

Once the training samples are determined by DoE, their corresponding outputs are evaluated by the computational model. Based on the dataset obtained, surrogate algorithms are

then utilized to train and test a surrogate model. Surrogate modeling can be seen as a special case of supervised machine learning applied in the field of engineering design. Thus many popular machine learning techniques are also utilized in developing surrogate models. Several most widely adopted surrogate modeling techniques are summarized below.

2.5.1 Polynomial response surface

The classic polynomial response surface method is the most widely used form of surrogate model in engineering design. The method was first introduced by Box (1951) and has been evolved to various versions. The uncertain 3D FDM model input parameters (geotechnical and design parameters) can be represented by independent random variables $\mathbf{X} = \{X_1, \dots, X_m\}$, and the 3D FDM model output (ground and structural deformations) can also be represented by a random variable \mathbf{F} , which can be approximated by polynomials with a maximum order of m :

$$\mathbf{F} \approx f_{PRS}(\mathbf{X}) = \sum_{i=0}^m a_i \mathbf{X} \quad (2.6)$$

where the coefficient $\mathbf{a} = \{a_0, a_1, \dots, a_m\}$ can be estimated through a least-squares solution. An increase of m will usually yield a more accurate approximation. However, the possibility of overfitting or poor generalization also increases. Polynomial surrogates are less suitable for highly non-linear, multi-model, and multi-dimensional design problems as it may not be possible to estimate all polynomials accurately (Forrester and Keane, 2009). A wide application of response surface methods in underground construction has been reported (Hamrouni et al., 2017; Langford and Diederichs, 2014; Lü et al., 2017a; Lü and Low, 2011; Mollon et al., 2011, 2009a; Youn and Choi, 2004).

2.5.2 Radial basis functions

Radial basis functions (RBF) employ a weighted sum of simple functions in an attempt to emulate complicated engineering problems (Broomhead and Lowe, 1988). An RBF approximation of \mathbf{F} can be written as:

$$\mathbf{F} \approx f_{RBF}(\mathbf{X}) = \sum_{i=1}^k \omega_i \phi(||\mathbf{X} - \mathbf{c}_i||) \quad (2.7)$$

where \mathbf{c}_i denotes the center of the i^{th} radial basis function. ϕ is the basis function. Several options are available to select the basis function, such as linear, cubic, thin plate spline, multi-quadratic, and Gaussian function. ω_i is the weight coefficient that can be estimated using the matrix methods of linear least squares given the interpolation condition:

$$f_{RBF}(\mathbf{X}_j) = \sum_{i=1}^k \omega_i \phi(\|\mathbf{X}_j - \mathbf{c}_i\|) = \mathbf{Y}_j, \quad j = 1, \dots, n \quad (2.8)$$

where a sampling strategy $\mathcal{X} = \{\mathbf{X}_1, \dots, \mathbf{X}_n\}$ yields the model outputs $\mathbf{Y} = \{\mathbf{Y}_1, \dots, \mathbf{Y}_n\}$. There are two main groups of RBF, namely global RBF and compactly support RBF (Wendland, 2006). RBF applications can be found in the field of neural networks, pattern recognition, fuzzy systems, etc.

2.5.3 Polynomial chaos expansion

Polynomial chaos expansion (PCE) approximates the computational model by a basis of orthogonal stochastic polynomials. The model output \mathbf{F} can be approximated by a sum of orthonormal polynomials:

$$\mathbf{F} \approx f_{pce}(\mathbf{X}) = \sum_{\alpha \in A} y_{\alpha} \Psi_{\alpha}(\mathbf{X}) \quad (2.9)$$

where $\Psi_{\alpha}(\mathbf{X})$ are multivariate polynomials orthonormal with respect to the input distributions, $\alpha \in A$ are multi-indices, and y_{α} are corresponding coefficients. The classical families of multivariate polynomials are given in (Xiu and Karniadakis, 2002). Hermite polynomials are widely used if input variables follow normal distributions. A truncation scheme is usually adopted to calculate a finite number of terms in Eq. (2.9). Considering all multivariate polynomials of the degree less than or equal to p , the number of PCE terms or the number of unknown coefficients is

$$P = \frac{(M + p)!}{M! p!} \quad (2.10)$$

Several methods are available to calculate the coefficients y_{α} . The most commonly used method is the least-square minimization method. Equation (2.9) can be approximated by its truncated version:

$$f_{pce}(\mathbf{X}) = \mathbf{y}^T \mathbf{\Psi}(\mathbf{X}) \quad (2.11)$$

where $\mathbf{y} = \{y_1, \dots, y_P\}$ is a vector containing the coefficient and $\mathbf{\Psi}(\mathbf{X}) = \{\Psi_0(\mathbf{X}), \dots, \Psi_{P-1}(\mathbf{X})\}$ is the matrix containing all the orthonormal polynomials. Given a set of n samples of the experimental design $\mathcal{X} = \{\mathbf{X}_1, \dots, \mathbf{X}_n\}$ and the corresponding outputs $\mathbf{Y} = \{\mathbf{Y}_1, \dots, \mathbf{Y}_n\}$, the least-square solution calculates the coefficients as:

$$\mathbf{y} = (\Psi(\mathcal{X})^T \Psi(\mathcal{X}))^{-1} \Psi(\mathcal{X})^T \mathbf{Y} \quad (2.12)$$

2.5.4 Kriging

Kriging theory is a statistical interpolation method that employs a Gaussian process to represent a sophisticated input and output mapping system. This method was first proposed in the field of geostatistics by Krige (1951) and Matheron (1963). It then has been widely applied in the design and analysis of computer experiments (Sacks et al., 1989). A Kriging model in its most general form can be described as:

$$\mathbf{F} \approx f_{KRIG}(\mathbf{x}) = \boldsymbol{\beta}^T \mathbf{f}(\mathbf{X}) + \sigma^2 Z(\mathbf{X}) \quad 2.13$$

where the first term $\boldsymbol{\beta}^T \mathbf{f}(\mathbf{X})$ describes the trend, which is the mean value of the Gaussian process, which consists of m arbitrary functions $\{f_1, f_2, \dots, f_m\}$ and the corresponding coefficients $\{\beta_1, \beta_2, \dots, \beta_m\}$. The second term contains the variance of the Gaussian process σ^2 and a zero mean, unit variance, stationary Gaussian process $Z(\mathbf{X})$. The local deviation at two sample points \mathbf{X} and \mathbf{X}' is described in terms of a correlation function $R = R(|\mathbf{X} - \mathbf{X}'|; \boldsymbol{\theta})$ and its hyperparameters $\boldsymbol{\theta}$.

Given a set of n samples of the experimental design $\mathcal{X} = \{\mathbf{x}_1, \dots, \mathbf{x}_n\}$ and the corresponding outputs $\mathbf{Y} = \{\mathbf{Y}_1, \dots, \mathbf{Y}_n\}$, The estimation of the response value $\hat{Y}(\mathbf{X})$ of an arbitrary input sample point \mathbf{X} is a Gaussian random variable characterized by

$$\mu_{\hat{Y}}(\mathbf{X}) = \mathbf{f}(\mathbf{X})^T \boldsymbol{\beta} + \mathbf{r}(\mathbf{X})^T \mathbf{R}^{-1} (\mathbf{Y} - \mathbf{F} \boldsymbol{\beta}) \quad (2.14)$$

$$\sigma_{\hat{Y}}^2(\mathbf{X}) = \sigma^2 (1 - \mathbf{r}^T(\mathbf{X}) \mathbf{R}^{-1} \mathbf{r}(\mathbf{X}) + \mu^T(\mathbf{X}) (\mathbf{F}^T \mathbf{R}^{-1} \mathbf{F})^{-1} \mu(\mathbf{X})) \quad (2.15)$$

where $\mathbf{F}_{ij} = f_j(\mathbf{x}_i)$ is the observational matrix; and $\mathbf{R}_{ij} = R(|\mathbf{x}_i - \mathbf{x}_j|; \boldsymbol{\theta})$ is the correlation matrix of the experimental design points. $\mathbf{r}(\mathbf{X}) = R(|\mathbf{X} - \mathbf{x}_i|; \boldsymbol{\theta})$ is the cross-correlations between the prediction point \mathbf{X} and the experimental design point \mathbf{x}_i ; and $\mu(\mathbf{X}) = \mathbf{F}^T \mathbf{R}^{-1} \mathbf{r}(\mathbf{X}) - \mathbf{f}(\mathbf{X})$. The hyperparameters $\boldsymbol{\theta}$ can be estimated via maximum likelihood estimation. The kriging parameters $\{\boldsymbol{\beta}, \sigma^2\}$ can be calculated by generalized least-squares solution (Santner et al., 2003)

$$\boldsymbol{\beta} = (\mathbf{F}^T \mathbf{R}^{-1} \mathbf{F})^{-1} \mathbf{F}^T \mathbf{R}^{-1} \mathbf{Y} \quad (2.16)$$

$$\sigma^2 = \frac{1}{n}(\mathbf{Y} - \mathbf{F}\boldsymbol{\beta})^T \mathbf{R}^{-1}(\mathbf{Y} - \mathbf{F}\boldsymbol{\beta}) \quad (2.17)$$

A more detailed description of Kriging and its application in optimization analysis can be found in (Bhosekar and Ierapetritou, 2018; Oliver and Webster, 1990).

2.5.5 Support vector regression

Support vector regression (SVR) was developed based on the theory of support vector machine, which was mainly developed at AT&T Bell Laboratories (Smola and Schölkopf, 2004). A nonlinear SVR is equivalent to finding a functional relationship between inputs \mathbf{X} and outputs \mathbf{F} that can be cast as the following form:

$$\mathbf{F} \approx f_{SVR}(\mathbf{X}) = \sum_{i=1}^N (\alpha_i - \alpha_i^*) k(\mathbf{X}_i, \mathbf{X}) + b \quad (2.18)$$

where $\alpha_i \geq 0$ and $\alpha_i^* \geq 0$ are Lagrange multipliers. $k(\mathbf{X}_i, \mathbf{X})$ is a positive definite kernel function, and b is an offset parameter to be estimated. The parameters in Equation (2.18) are set by maximizing an objective function:

$$\begin{aligned} L(\alpha, \alpha^*) = & -\frac{1}{2} \sum_{i=1}^N \sum_{j=1}^N (\alpha_i - \alpha_i^*)(\alpha_j - \alpha_j^*) k(\mathbf{x}_i, \mathbf{x}_j) - \sum_{i=1}^N (\alpha_i + \alpha_i^*) \varepsilon \\ & + \sum_{i=1}^N (\alpha_i - \alpha_i^*) y_i \end{aligned} \quad (2.19)$$

which is subjected to the following constraints:

$$\sum_{i=1}^N (\alpha_i - \alpha_i^*) = 0 \quad \text{and} \quad \alpha_i, \alpha_i^* \in [0, C] \quad (2.20)$$

where C is a regularization parameter. Once the Lagrange multipliers are found, the prediction at any unknown point can be obtained by Eq. (2.18). The kernel function can have various forms (Vapnik, 2013). The most widely used ones are Gaussian, polynomial, sigmoid, and exponential kernels. Once the kernel is chosen, the optimal hyperparameters of the SVR model were found using an optimization algorithm.

2.5.6 Artificial neural networks

Artificial neural networks (ANN) are computer architectures to simulate the biological central nervous system. A collection of connected artificial neurons is aggregated into layers. The connection can transmit signals between neurons and the neuron receives a signal then processes it to the next layer. A weight is assigned to each connection and is adjusted as learning proceeds. For a general introduction and overview of ANN, readers are referred to (Prieto et al., 2016; Schmidhuber, 2015). The most commonly used ANN model is the back-propagation neural network (BPNN). The architecture of BPNN consists of an input layer, one or multiple hidden layers, and one output layer, which can generally approximate any nonlinear system. The feature of the back-propagation learning algorithm enables it to adjust weights and bias according to the error through optimization processes (Hecht-Nielsen, 1992). For a network with n input neurons, m hidden neurons, and one output neuron, a training process can be formularized as:

$$y_j = f_h \left(\sum_{i=1}^n \omega_{j,i} x_i + b_j \right), \quad j = 1, 2, \dots, m \quad (2.21)$$

$$f(x) = \frac{1}{1 + e^{-x}} \quad (2.22)$$

where y_j is the output of the hidden layer, and f_h is the activation function, usually a sigmoid function. The output in the output layer is given as follows:

$$Z = f_o \left(\sum_{j=1}^m \omega_{z,j} y_j + b_z \right) \quad (2.23)$$

where f_o is the activation function for the output layer, usually linear. $\omega_{j,i}$ and $\omega_{z,j}$ are weights connecting the input-hidden layers and hidden-output layers, b_j and b_z are bias in hidden and output layers, respectively.

2.5.7 Polynomial chaos Kriging

Polynomial chaos Kriging (PCK) is a surrogate algorithm developed by Schobi et al. (2015) combining two well-established techniques—PCE and Kriging. By linking Equation (2.9) and Equation (2.13) together, the global behavior of the computational model can be captured by PCE and local approximation can be well represented by Kriging interpolation:

$$\mathbf{F} \approx f_{pck}(\mathbf{X}) = \sum_{\alpha \in A} y_{\alpha} \Psi_{\alpha}(\mathbf{X}) + \sigma^2 Z(\mathbf{X}) \quad (2.24)$$

where the parameters have the same definition in Equation (2.9) and Equation (2.13). The promising performance of PCK model in many engineering fields has been demonstrated in recent literature (Schöbi et al., 2017). Also, the general lack of extrapolation using Kriging only is compensated by the PCE process.

The accuracy of the PCK model can be assessed by two error functions, leave-one-out error and validation error (Schöbi et al., 2015). Besides, the standard regression accuracy measure—Normalized Root Mean Squared Error (NRMSE) (Khaledi et al., 2014) is also adopted here. Those accuracy metrics are defined by

$$\epsilon_{LOO} = \frac{\sum_{i=1}^n [f(\mathbf{X}_i) - f_{pck}^{D/i}(\mathbf{X}_i)]^2}{\sum_{i=1}^n [f(\mathbf{X}_i) - \mu_Y]^2} \quad (2.25)$$

$$\epsilon_{Val} = \frac{n_{Val} - 1}{n_{Val}} \left[\frac{\sum_{i=1}^{n_{Val}} (f(\mathbf{X}_i^{Val}) - f_{pck}(\mathbf{X}_i^{Val}))^2}{\sum_{i=1}^{n_{Val}} (f(\mathbf{X}_i^{Val}) - \mu_{Y_{Val}})^2} \right] \quad (2.26)$$

$$NRMSE = \sqrt{\frac{\sum_{i=1}^n (f(\mathbf{X}_i) - f_{pck}(\mathbf{X}_i))^2}{\sum_{i=1}^n (f(\mathbf{X}_i))^2}} \quad (2.27)$$

where n is the number of experiment samples, $f(\mathbf{X}_i)$ is the real response at the point \mathbf{X}_i , $f_{pck}^{D/i}(\mathbf{X}_i)$ denotes the response predicted by the PCK model constructed with all the sample points except \mathbf{X}_i . μ_Y is the sample mean of the experimental design response. The validation error is calculated on an independent validation dataset $[\mathbf{X}^{Val}, \mathbf{Y}^{Val} = f(\mathbf{X}^{Val})]$ with n_{Val} samples. $\mu_{Y_{Val}}$ is the sample mean of the experimental response for the validation set.

Given the same dataset obtained by designed computational simulations, there are several ways to construct a PCK model. In this study, two PCK approaches, namely the sequential PCK (PCK-SEQ) and the optimal PCK (PCK-OPT) (Schöbi et al., 2015) are examined and compared. Figure 2.6 illustrates the procedure of constructing a PCK surrogate model using the two approaches. A dataset containing pairs of inputs and outputs is first generated by a series of numerical simulations. A sparse set of orthonormal multivariate polynomials is determined by the least-angle regression (LAR) algorithm for the optimal PCE model. In PCK-SEQ approach, the PCE model is used directly as the trend for the Kriging model. The PCK-SEQ model is then obtained by calibrating Kriging hyperparameters. In PCK-OPT approach, the sparse set of P polynomials is ranked in decreasing order. The next step is to build P universal Kriging models by adding each polynomial one by one to the trend part. For each model, the coefficients of the trend, Kriging parameters, and hyperparameters are calibrated. The PCK-OPT model is then selected as the one with minimal ϵ_{LOO} value.

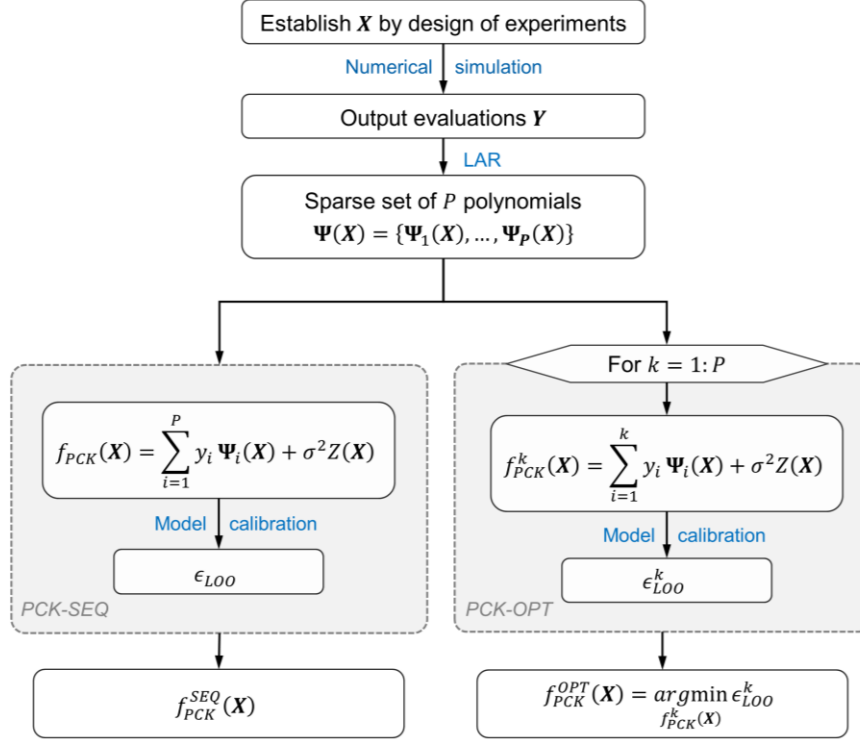


Figure 2.6 Flow chart for the optimal PCK model construction.

Besides the methods mentioned above, other surrogate methods are also available. Several surrogate approaches that have been reported to exhibit good performance in underground construction problems include the multivariate adaptive regression splines (MARS) method (Zhang, 2019), proper orthogonal decomposition (Buljak and Maier, 2011), and combinations and variants of surrogate techniques. It should be noted that no single type of surrogate model outperforms all other models for all types of problems. Selecting a proper surrogate model depends on the computational resources and the output to be estimated but also depends on engineering expertise. The best type of surrogate model for the problem at hand should be investigated and validated case by case.

CHAPTER 3

OBSERVED PERFORMANCE AND ANALYSIS OF SEM CAVERN CONSTRUCTION IN DOWNTOWN LOS ANGELES

Reproduced from a paper published in the Journal of Geotechnical and Geoenvironmental Engineering (Zheng et al., 2021) and presented with minor variations.

3.1 Abstract

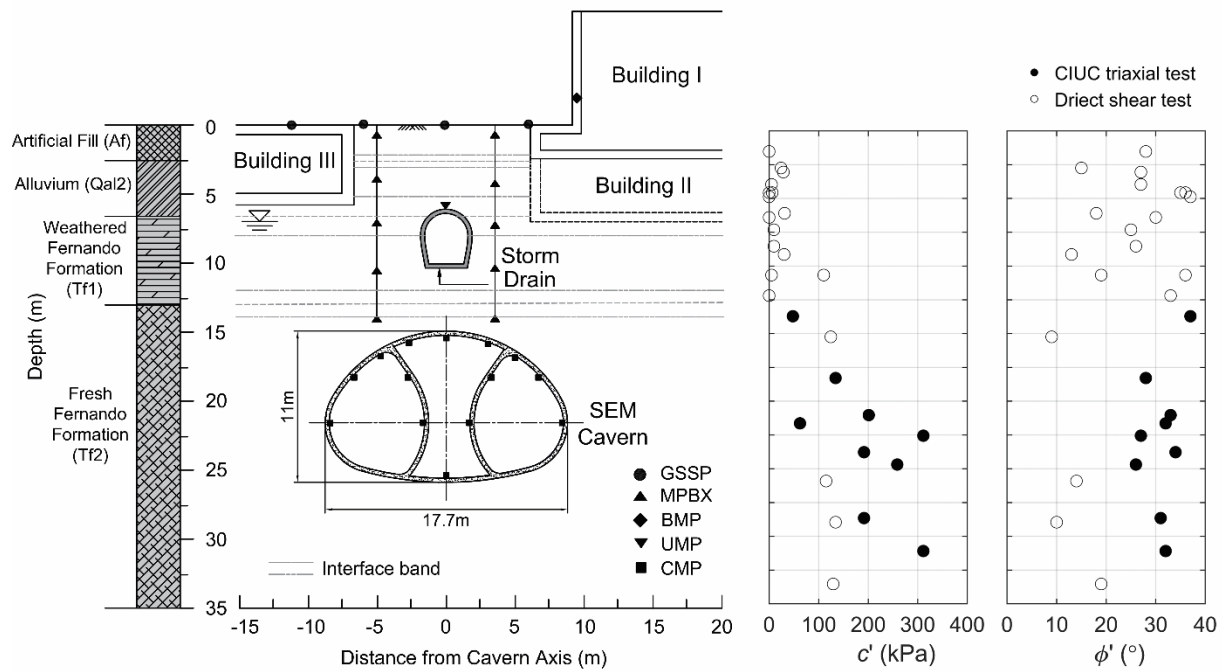
The Regional Connector Transit Corridor (RCTC) project consists of an 89-meter-long, 17.7-meter-wide, and 11-meter-high large span crossover cavern constructed beneath critical infrastructure using the sequential excavation method (SEM) at relatively shallow depth (15 m below ground surface) in downtown Los Angeles. The cavern construction involved a complex three-drift, two-sidewall configuration and was excavated in the Fernando formation, a weak clayey siltstone. This paper presents a comprehensive case study of the cavern excavation and initial support construction. The performance of the urban SEM was assessed and complex ground behavior was examined once per excavation step during the construction process. The overall average surface settlement was 20 mm and the largest single-stage incremental movements occurred in the center bench and invert excavation, accounting for 30–40 % of the total deformation. The subsurface experienced less differential settlement during the side drift excavations due to the ovate excavation profile and the restriction from surrounding infrastructure. The measured center crown vertical displacement varied between 5 and 10 mm and the center invert initial support was recorded to heave 8 to 12 mm. A systematic procedure was developed to apply a deliberate observational method. The lessons learned support that appropriate real-time analysis improves the quality of regular data review, continuously updating the knowledge of risk and enabling prompt adaptations and optimizations of the design and construction along the SEM tunneling process.

3.2 Introduction

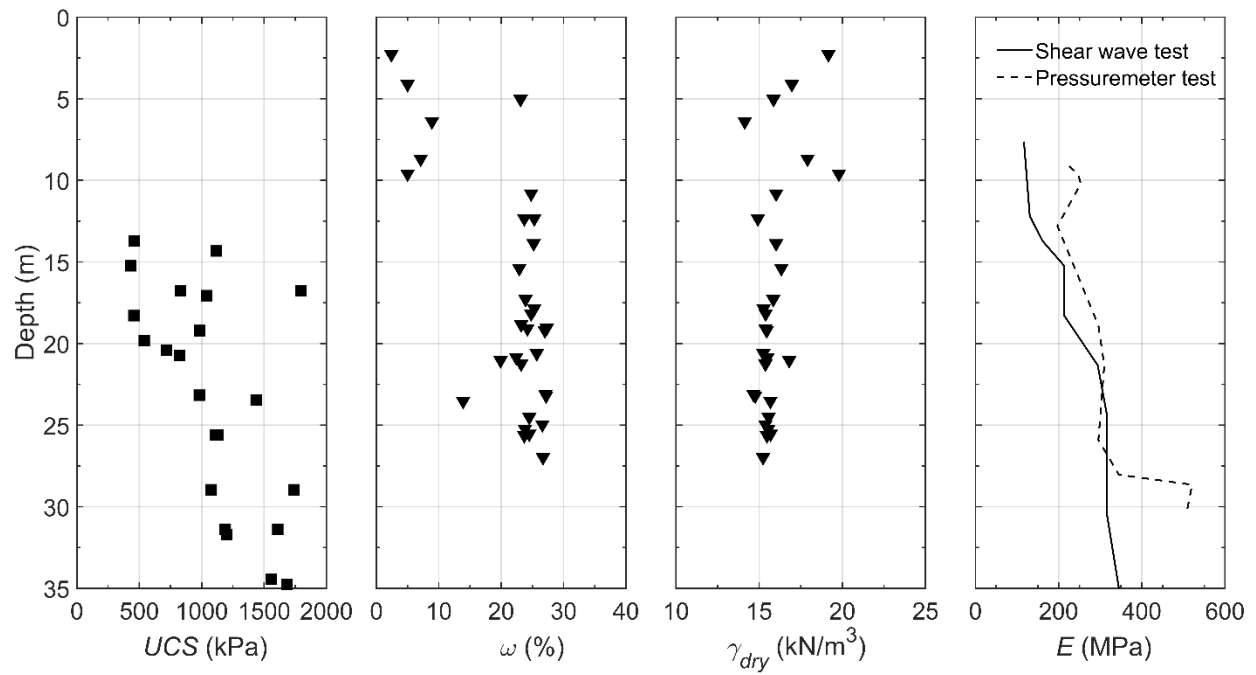
The construction of the Regional Connector Transit Corridor (RCTC) project in downtown Los Angeles included a crossover cavern to allow trains to switch tracks. The large span cavern, measuring 17.7 m wide by 11 m tall and 89 m in length, was designed by Mott MacDonald and constructed by Skanska and Traylor Brothers. Once completed, the cavern will be the largest tunneled cross-section in Los Angeles. As shown in Figure 3.1 the entire cavern was excavated in the Fernando formation. To reduce construction impacts on the sensitive downtown area, a three-drift seven-stage excavation configuration was designed and implemented (Herranz et al., 2016; Herranz and Penrice, 2018). One of the main design concerns was to limit ground movements to prevent damage to adjacent structures. The allowable settlement of building foundations was 13 mm and the allowable angular distortion between adjacent columns was 1/600, according to the Metro Rail Design Criteria (MRDC. 2013).

Cavern excavation in the midst of urban infrastructure is very complicated, and allowable deformations are relatively small. Thus a critical element of successful sequential excavation method (SEM) implementation is instrumentation and monitoring, which also forms an integral part of the observational method (Peck, 1969). The main objectives of using instrumentation during SEM construction are to quantify ground response, to verify preliminary design, and to optimize the project's tunneling process and evolving design. With the development of instrumentation devices and technologies, most of today's tunnel projects use advanced monitoring systems with recorded measurements made available in real time. However, there are very few case studies that fully utilize the extensive instrumentation data to evaluate the performance of SEM construction in soft ground conditions with shallow overburden (Berg et al. 2003; Sharifzadeh et al. 2013). Furthermore, a complex and sensitive urban environment requires SEM to be more flexible and adaptive, which should be realized through prompt analysis of instrumentation data on construction time scales. For most SEM projects, however, the instrumentation data were under-analyzed during the construction stage, leading to a delayed understanding of ground behavior and inefficient communications between contractors and designers.

This paper presents a comprehensive case study of the cavern excavation and initial support construction. The performance of the urban SEM was assessed and complex ground behavior was examined in real time. Three levels of deformation response—surface, subsurface, and in-tunnel—were collected, interpreted, and analyzed continuously during the course of the project. The ground behavior was characterized at both spatial and temporal scales, and developed deformations were correlated to each sequential excavation process. Prior to using SEM, tunnel boring machine (TBM) construction was used to construct the running tunnels. The combination of these methods creates irregular excavation profiles requiring extra accommodation for side drift excavation and precast tunnel liner demolition. Also, the proximity of the existing infrastructure influences the displacement propagation corresponding to different excavation stages. As far as the authors' knowledge, well-established case histories on ground movements and structural deformations for such a large SEM cavern constructed in dense metropolitan areas are very limited. An automated processing program was developed to utilize the real-time analysis of the deformation progress induced by the multi-drift tunneling processes. The information derived from such analysis improved contractors' and designers' knowledge of risk on a continual basis. This case study provides a valuable database to validate any analytical or numerical approach proposed in research and design analysis under similar conditions, and promotes adaptive data-driven decision-making procedure applied in future urban SEM practices.



(a)



(b)

Figure 3.1 (a) Cross-section of the SEM cavern and subsurface conditions. (b) Interpretation of field and laboratory tests (cohesion c' , friction angle ϕ' , unconfined compression strength UCS , water content ω , dry unit weight γ_{dry} , and elastic modulus E).

3.3 Project Overview

3.3.1 Project background

The RCTC crossover cavern is located adjacent to the east end of the 2nd/Broadway Station. It is constructed below 2nd Street and various utility structures, and is adjacent to three buildings, as shown in Figure 3.2. The entire RCTC light-rail project includes 1.6 km of twin-bored tunnels, 1.1 km of cut and cover tunnels, and three underground stations. The twin-bored tunnels were constructed prior to the cavern excavation by an earth pressure balance tunnel boring machine (EPB-TBM) with an excavated diameter of approximately 6.7 m. The tunnels were lined with a 267-millimeter-thick precast concrete tunnel lining (PCTL) with double gaskets and an inner diameter of 5.74 m. Considering the excavation span and environmental limitations, the cavern was excavated by SEM with a three-drift two-sidewall configuration. The adopted construction configuration was chosen to balance productivity, equipment and workforce capabilities, project schedule, and deformation requirements.

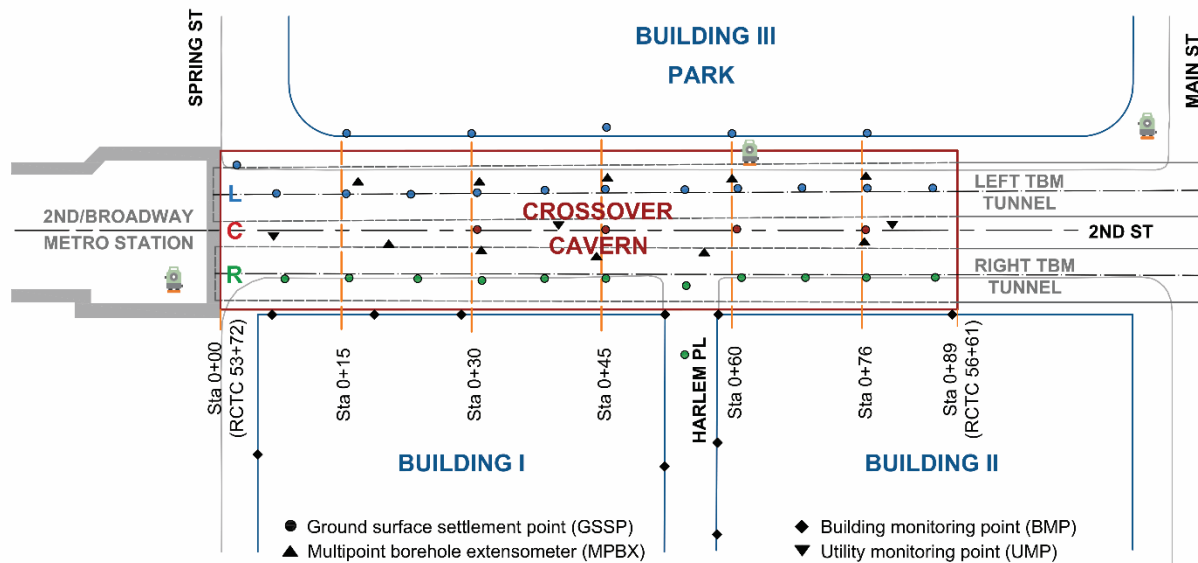


Figure 3.2 Alignment and monitoring layout of the LA RCTC SEM cavern.

Three existing buildings are located in the proximity of the crossover cavern. In addition, the cavern is beneath an LA County storm drain, a mined horseshoe-shaped tunnel structure with an interior height of 3.1 m and a clearance of 6 m above the cavern crown. The locations of the three buildings are shown in Figure 3.2 and a summary of these structures is listed in Table 3.1. It should be noted that the 10 story Building III is further apart from the cavern and what is closer to the SEM cavern is its parking structure under a park.

Table 3.1 Building information

Building	Type	Number of stories	Height (m)	Foundation depth (m)	Foundation type	Equivalent building surcharge (kPa)
Building III	Multistory building	10	48.8	6.7	Spread footing	52.6
Building I	Single story retail building	1	6.1	6.1	Spread footing	35.1
Building II	Multistory historic building	10	38.4	8.2 5.5	Continuous and spread footing	112.8

SEM construction commenced in May 2018 with the installation of an 18 m umbrella canopy from the 2nd/Broadway Station. Cavern excavation began with the left drift in a top heading and invert sequence, followed by a similar sequence for the right drift excavation. The side drift excavation included the demolition of the bored tunnels PCTL. The center drift was excavated in a top heading-bench-invert sequence and was followed by the demolition of the temporary sidewalls. The entire excavation and initial support installation process was finished in February 2019. Figure 3.3 presents on-site views of different construction stages.



(a)



(b)



Figure 3.3 SEM construction progress: (a) Left drift (I: left top heading, II: left invert); (b) Right drift (III: right top heading, IV: right invert); (c) Center drift (V: center top heading, VI: center bench, VII: center invert); and (d) Temporary wall demolition.

3.3.2 Geological and Geotechnical Conditions

The crossover cavern is situated within the Fernando formation, which ranges from slightly weathered to fresh clayey siltstone, as shown in Figure 3.1. Near the ground surface, the artificial fill soil (Af) is 2 to 3 m thick, underlain by 3 to 5 m of coarse-grained alluvial deposits (Qal2). The interface between the weathered and fresh Fernando formation varies within 2 m along the cavern alignment. The Fernando formation is comprised predominantly of massive siltstone, with some interbeds of sandstone and conglomerate (Lamar, 1970). Available historical and new exploratory borehole data indicate that this formation is generally poorly cemented and extremely weak to very weak with unconfined compressive strength (UCS) values of 0.2 to 2.5 MPa (Ulusay, 2014).

The geotechnical properties presented in Figure 3.1 were obtained through all available field investigations and laboratory tests on boreholes within the cavern area and similar stratigraphy along the tunnel alignment. The moisture content and dry density are relatively constant within the Fernando formation. Field observations show that the Fernando formation exhibits slacking behavior due to a decrease in moisture content. The cohesion and UCS results indicate a trend of increasing strength with depth in the Fernando formation, which can be partially attributed to the decreasing of weathering effects and increasing of confining stress with depth. The elastic modulus was determined based on both field shear wave tests and pressuremeter tests. The elastic modulus from the shear wave test (E_s) was calculated through the unit weight and Poisson's ratio according to equations (4.1) and (4.2):

$$G_0 = \rho \cdot V_s^2 \quad (4.1)$$

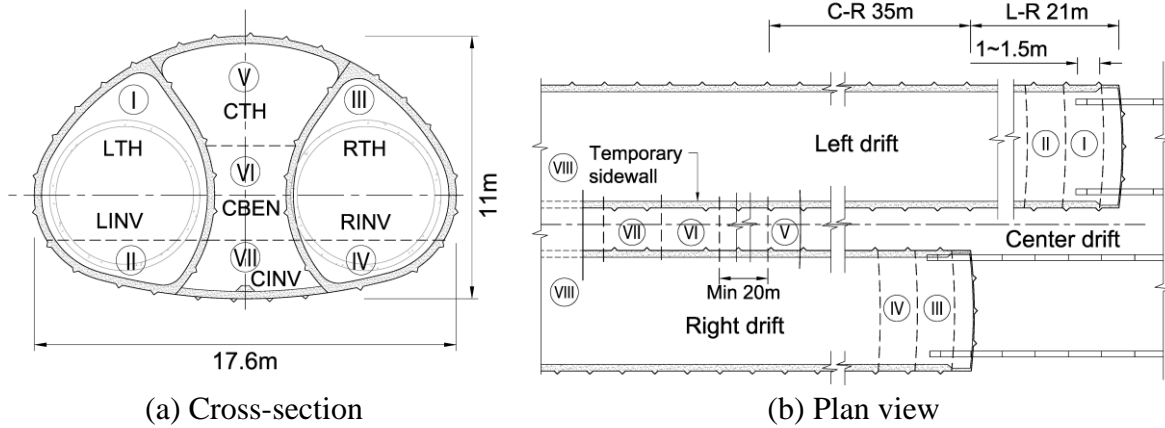
$$E_s = \alpha \cdot E_0 = \alpha \cdot 2G_0(1 + \nu), \quad (4.2)$$

where G_0 is the initial shear modulus, ρ is the mass density of the soil, V_s is shear wave velocity, ν is Poisson's ratio, and α is the modulus degradation factor. Here a modulus reduction factor of 0.3 was considered assuming a strain level of 0.1 % (Sabatini et al., 2002). The determination of the elastic modulus from the pressuremeter data was made using the unload–reload portion of the testing curve since the initial portion of the curve reflects more effects from borehole disturbance than the undisturbed material behavior (Clarke and Menard, 1997; Mair and Wood, 2013).

Based on drilling and piezometric measurements, a regional groundwater table was identified approximately 7 m below the ground surface and is expected to fluctuate seasonally by about ± 1.5 m. Due to its fine-grained texture and relatively intact condition, the Fernando formation has a relatively low permeability, with hydraulic conductivity ranging from 10^{-6} to 10^{-8} cm/s. Groundwater inflow into the cavern was neither anticipated nor experienced during excavation.

3.3.3 Construction Sequence

The cavern was sequentially excavated and supported with a three-drift seven-stage scheme (Figure 3.4). The side drifts were divided into left and right top heading (I/LTH and III/RTH) and invert (II/LINV and IV/RINV) sequences, and the center drift consisted of top heading (V/CTH), bench (VI/CBEN), and invert (VII/CINV) sequences. The two temporary walls were demolished in a staggered pattern following the center invert placement once the strength of the invert concrete reached 2 MPa. In order to increase the local stability around the cavern crown, the initial 18 m of the cavern was excavated under the protection of a 53 pipe umbrella canopy installed from the 2nd/Broadway Station shaft.



interrupting hoop stress flow around the ring. The segments were then removed one at a time by shearing the circumferential joint plastic dowels. The ring dismantling process required less than one hour per ring, thereby limiting the time that the ground was unsupported. By contrast, the traditional demolition method is expected to have taken 3 to 4 hours on average from previous experiences (e.g., San Francisco Chinatown project and early-stage trials on this project). The average duration for each excavation advance stage is about 24 h, 6 h, and 17 h for each side drift, center top heading, and center invert respectively, which guaranteed the average 5 hr curing time for the shotcrete lining would be reached before executing the next round.



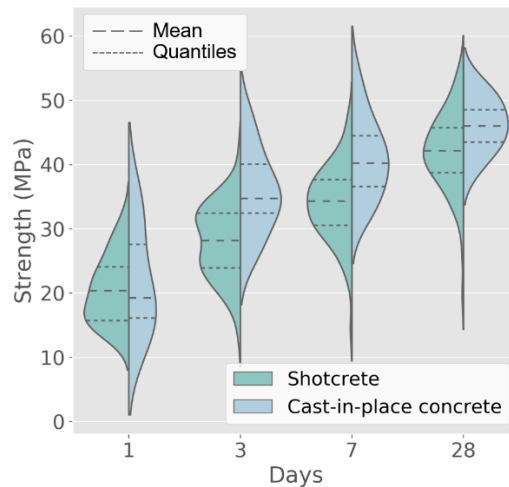
(a)



(b)



(c)



(d)

Figure 3.5 Initial support system: (a) shotcrete support LTH; (b) cast-in-place concrete support CINV; (c) TBM ring removal; (d) strength development. [Images (a–c) by Christophe Bragrad.]

3.3.4 Instrumentation

During the construction of the SEM cavern, extensive instrumentation was utilized to monitor the performance of the ground and initial lining. The instrumentation included ground surface settlement points (GSSP), multipoint borehole extensometers (MPBX), utility monitoring points (UMP), building monitoring points (BMP), and in-tunnel convergence monitoring points (CMP). The layout of the field instrumentations is shown in Figure 3.1a and Figure 3.2 and the main types of instrumentations installed on-site are presented in Figure 3.6. Ground surface and building monitoring were carried out using automated motorized total stations (AMTS) to monitor the spatial position of the prisms installed on the road pavement (GSSP) and buildings (BMP). Ten MPBXs were installed in boreholes within the cavern region, each of which contained five anchors monitoring the relative displacement between each sensor location and the top of the MPBX. Four UMPs were installed to contact the crown of the storm drain tunnel to keep track of the utility movement. The movements of the BMPs were also monitored by AMTSs, and the target prisms were fixed to buildings above tree level. There were 13 monitoring sections for tunnel convergence; the cross-section configuration of CMPs is shown in Figure 3.1a.

The recorded data were transferred in real time via a web portal–based instrumentation data management system created by Geocomp. The online monitoring system recorded data continuously and was available remotely to the project team (contractor, designer, project owner). When a measurement exceeded the pre-defined trigger limit, engineers and supervisors received alert messages, allowing for immediate discussion and implementation of corresponding countermeasures. Daily SEM meetings were held by the contractors, designers and the owner to review monitoring data, construction progress, geologic observations, and required actions according to up-to-date information. An automated processing procedure was developed to perform real-time analysis and provide pattern visualizations for daily review meetings. The interpretations were continuously updated, which improved the knowledge of risk and endorsed the design verifications or modifications.

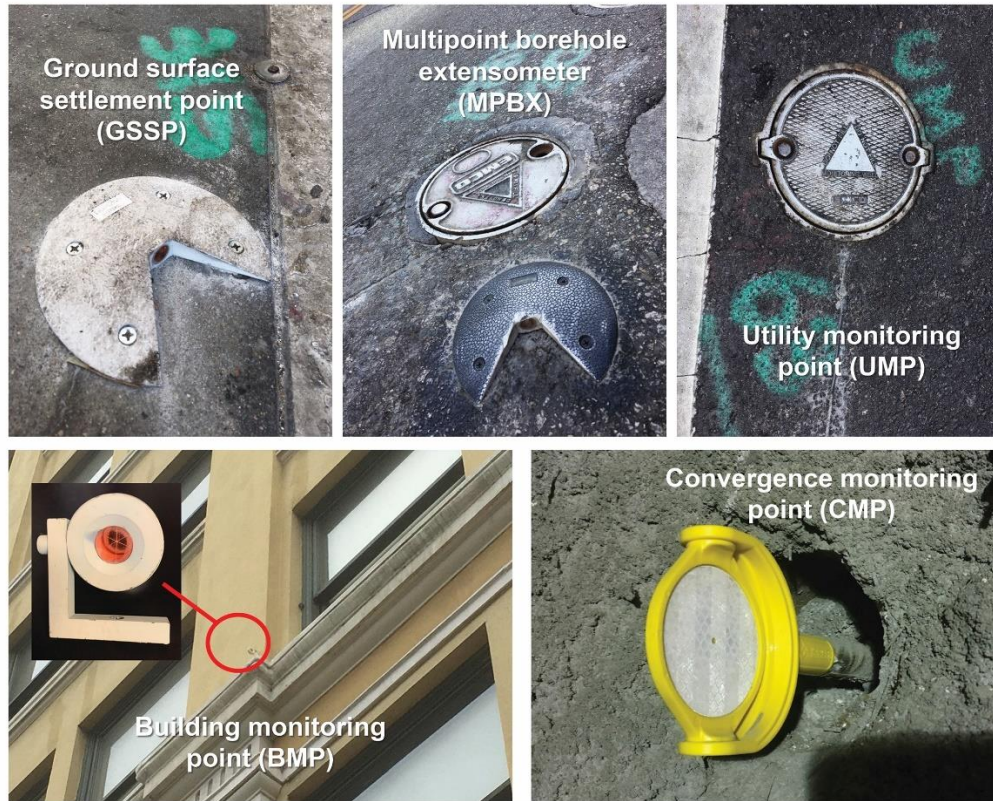


Figure 3.6 Main types of instrumentation. (Images by authors.)

3.4 Analysis of field measurements

3.4.1 Observed Ground Surface Settlement

GSSPs on the road surface and sidewalks were continuously monitored during the entire construction process. Three AMTSs recorded the x, y, and z positions of each GSSP every 15 min and delivered an average z position in an 8-hour interval to minimize errors from road traffic and obstacles. Figure 3.7 shows a plot of the ground surface settlements at Sta. 0+15 versus time as construction progressed. The deformation presented here is the relative value induced by SEM construction only. The surface settlements caused by TBM excavation were less than 2 mm and almost negligible in most sections. The accuracy of a AMTS reading is ± 0.7 mm. Surface settlement began to develop as left drift excavation started. Upon arrival of the LTH at the monitoring section, the surface settlement reached 10 % of its final amount (20 mm). As the left drift excavation passed the monitoring plane, the surface settlements at the left and right sides continuously increased with a slight increase of gradient with the arrival of the RTH. The settlement then leveled off after the RTH was 15 m past the monitoring plane, and approximately 45 % of the total surface settlement was developed. Surface settlement began to grow slightly when the CTH excavation was within 10 m of the monitoring plane. The surface settlement

plateaued after the CTH advanced approximately 18 m beyond the monitoring plane, equivalent to the overall width of the excavation. The CBEN excavation lagged behind the CTH face by more than 30 m, and the CINV face was kept two round lengths (2 m) behind the CBEN. A noticeable settlement increase was observed as the CBEN and CINV face approach and pass the monitoring plane. 40% of the total excavation surface settlement was developed after CBEN and CINV excavation. Surface settlement continued for 4 months despite full ring closure and CBEN/CINV faces more than 30 m ahead of the monitoring plane. The maximum surface settlement predicted from the design analysis is 19 mm at the GSSP location, which is close to the observed value.

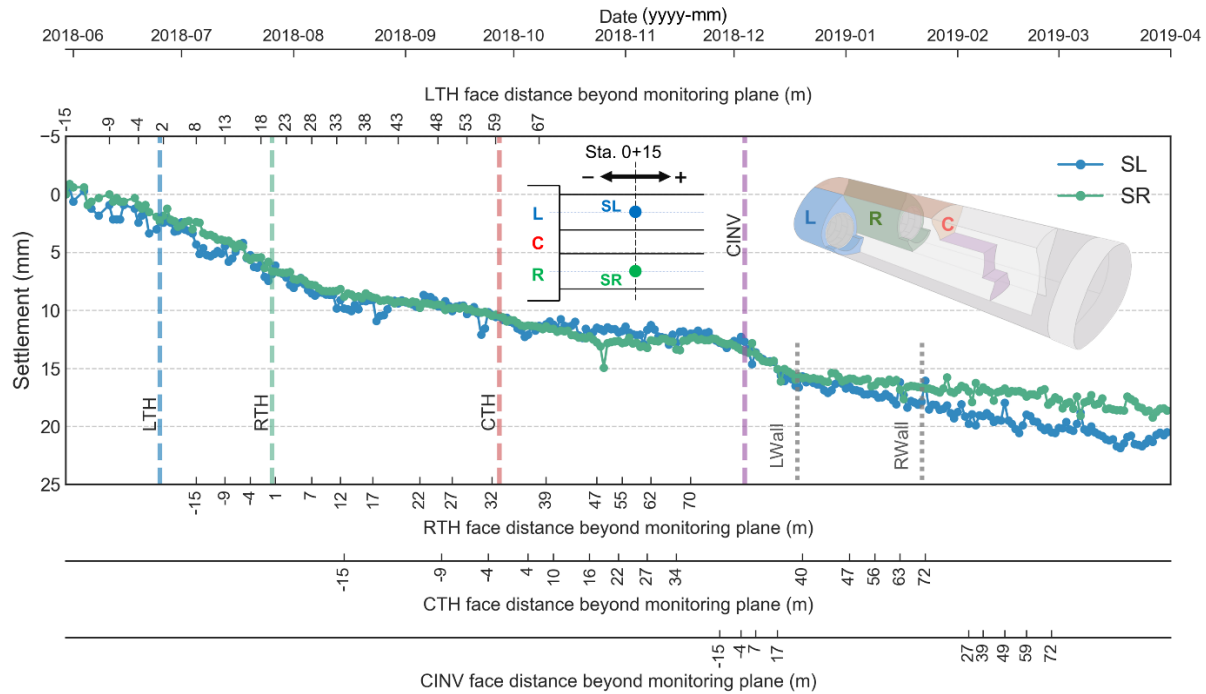


Figure 3.7 Surface settlement at Sta. 0 + 15 (daily measurements). SL = left side GSSP; and SR = right side GSSP.

Figure 3.8 presents a plot of the measured surface settlement for all monitoring sections versus the distances to the excavation faces. The surface deformation patterns are generally similar, regardless of position along the 90 m long cavern alignment, including achievement final surface settlement of approximately 20 mm. As observed in the mean and max/min trends, the pre-settlement and post-settlement for each drift excavation indicate an obvious three-dimensional (3D) effect of tunneling. When the lagged distance between drifts is close (left and right drifts), a superposed effect from both drifts influences the deformation behavior. The left and right drift excavation caused a greater increase in settlement in the corresponding side due to the distance from the influencing zone.

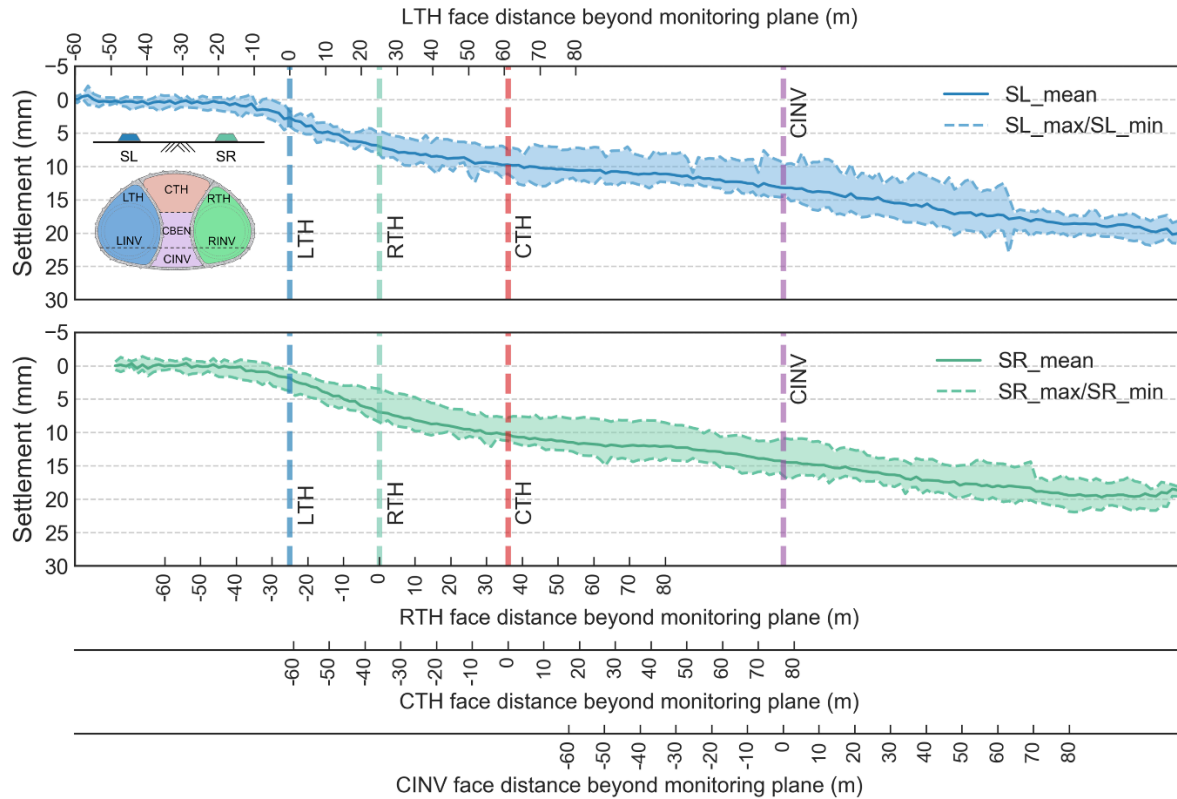


Figure 3.8 Surface settlement for all monitoring sections.

Surface settlement contour plots at different construction stages are shown in Figure 3.9. This figure indicates how the surface settlement developed in both longitudinal and transverse directions with the progress of the excavation faces. Some localized hot zones began to form after CTH excavation, and further developed with growing subsidence caused by the CBEN and CINV construction stages. The localized settlement that appeared in the first 10 m is attributed to the boundary effect from the station excavation. There is less restriction of lateral ground movement towards the opened trench compared with the greenfield condition. In contrast, there was less settlement at the far end of the cavern (Sta. 0+89). Several factors may have contributed to the increased settlements on the right side. For example, there is a utility trench located at approximately Sta. 0+30 to Sta. 0+38 that had been excavated and backfilled a long time before the cavern construction began. Also, the underground construction did not fully interrupt the road traffic above, and GSSPs sited on sidewalls were observed to often be blocked by parked vehicles within that area, which increased the average settlement readings.

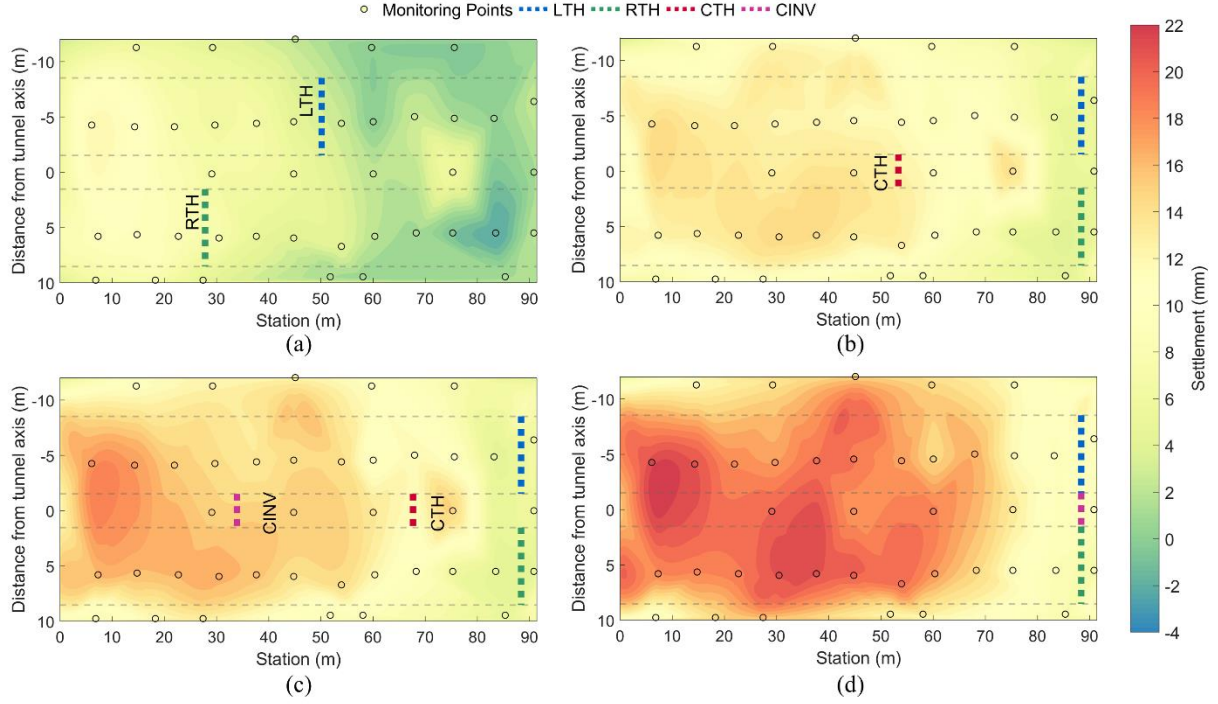


Figure 3.9 Surface settlement contours at different stages: (a) left and right drifts started; (b) left and right drifts finished, center top heading excavated; (c) center bench and invert excavated; and (d) all excavation finished.

Transverse surface settlement data were further processed by a modified Gaussian (MG) curve fitting, which uses the following form with three degrees of freedom (Vorster et al., 2005):

$$S_v = \frac{n}{(n-1) + \exp\left[\alpha\left(\frac{x}{i}\right)^2\right]} \cdot S_{vmax} \quad (4.3)$$

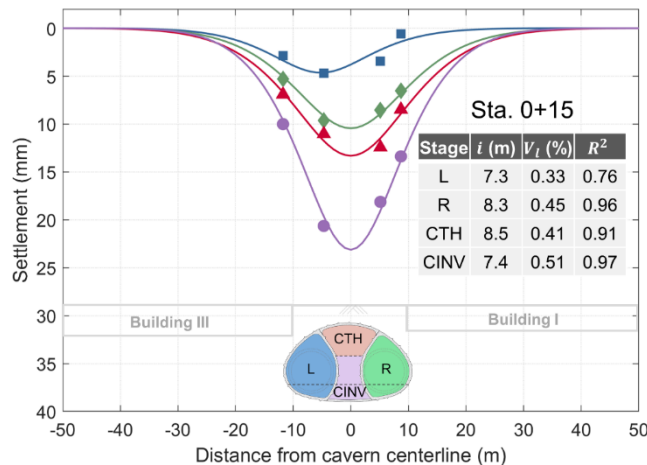
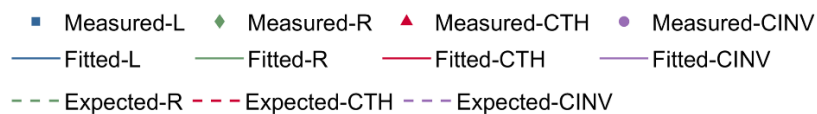
$$n = e^{\alpha} \frac{2\alpha - 1}{2\alpha + 1} + 1 \quad (4.4)$$

where S_{vmax} is the maximum surface settlement, x is the distance from the excavation centerline, i is the distance from the excavation centerline to the inflection point, and n , α are the shape function parameters controlling the width of the profile. The volume loss parameter V_l is calculated based on $V_l = A_s/A_{exc}$, where A_s is the area of the transverse settlement profile associated with the tunneling and A_{exc} is the excavated area at the corresponding stage.

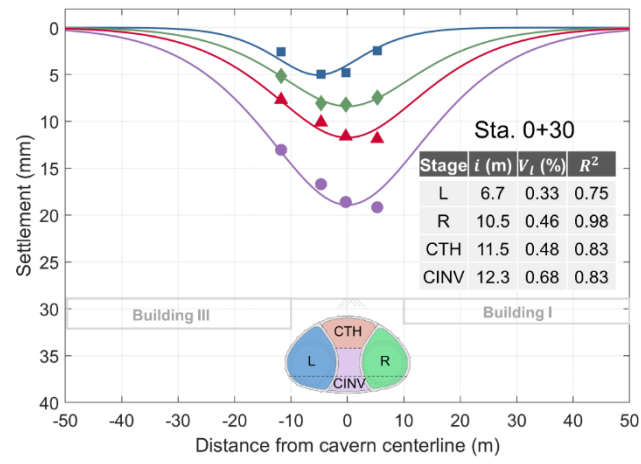
Figure 3.10 shows the development of the transverse settlement profile at each monitoring section. In each plot, the profiles reflect settlement when the excavated face is 15 m beyond the monitoring section. As expected, the fitted profile is shifted to the left when the LTH

passed, and generally centers over the cavern centroid after the RTH passes. In general, the modified Gaussian curves provide a good fit with limited measurements. The irregular and unsymmetrical excavation led to an unsymmetrical distribution of the settlement. In most sections, after the right drift was excavated, the settlement trough became symmetrical with respect to the cavern centerline. Cross-section Sta. 0+15 and Sta. 0+76 showed slightly different characteristics compared with other sections due to the boundary effects explained earlier. The characteristic parameters of settlement troughs are also listed in the figures for each construction stage. Figure 3.10f presents the anticipated settlement profiles according to the design analysis, which is generated by Gaussian curve-fitting on the numerical modeling results. In general, this was a good prediction in terms of the maximum settlement with slightly narrower trough widths compared with the observations.

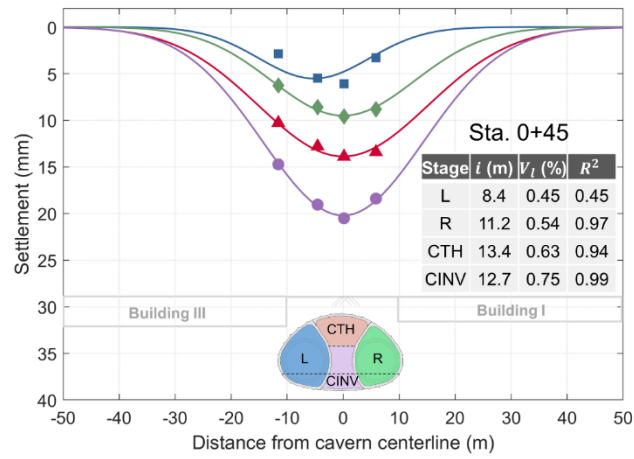
Table 3.2 summarizes the average values of the surface settlement trough parameters. The average volume loss was 0.39 % when the left drift passed, and increased to 0.65 % when the construction of the center bench and invert was finished. The total volume loss considering both TBM and SEM construction was also calculated. Since the pressurized TBM construction caused almost zero surface settlement, the average total volume loss decreased about 0.2 % when taking into account the excavated area of the bored tunnels. The results revealed that the highest increment of volume loss happened during the excavation of the center bench and invert, which accounts for about 20 % of the final volume loss. A typical value of volume loss using SEM in soft ground varies between 0.5 % to 2.0 % (Berg et al., 2003; Deane and Bassett, 2007; New and Bowers, 1984). While usually, the EPB-TBM can achieve a lower degree of volume loss with appropriate operation. Lower than 0.5 % volume losses have been reported for many recent EPB-TBM projects (Dindarloo and Siami-irdemoosa, 2015; Fargnoli et al., 2013; Ieronymaki et al., 2017; Jin et al., 2018; Mair, 2008; Pinto et al., 2014). In this case, considering the dimension of the excavation and such shallow overburden, a combined application of both TBM and SEM with a total volume loss of 0.45 % can be considered as an excellent-quality practice. After the SEM construction, no building damage was observed.



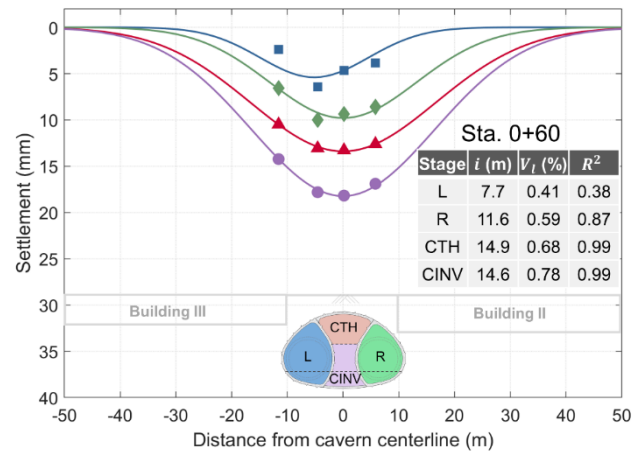
(a)



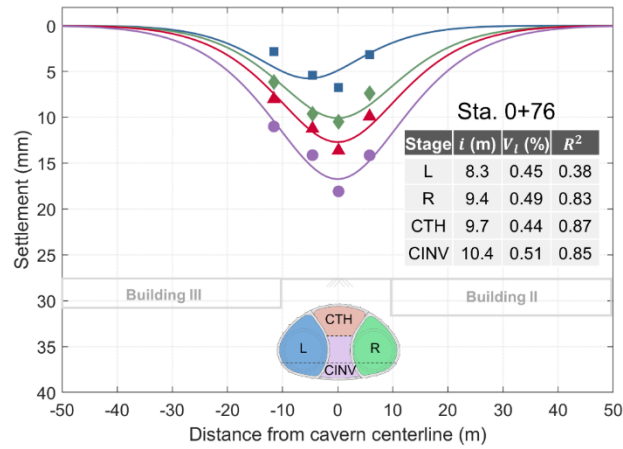
(b)



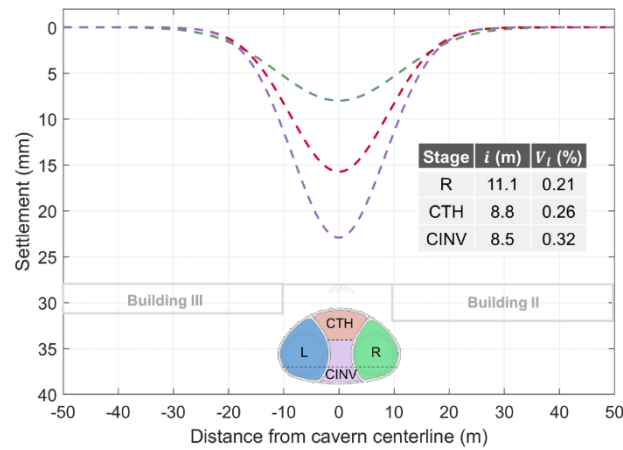
(c)



(d)



(e)



(f)

Figure 3.10 Curves fitted to settlement data at transverse sections: (a) Sta. 0+15; (b) Sta. 0+30; (c) Sta. 0+45; (d) Sta. 0+60; (e) Sta. 0+76; and (f) expected settlement from design analysis (L: left drift passed; R: right drift passed; CTH: center top heading passed; and CINV: center bench and invert passed.)

Table 3.2 Average values of settlement trough parameters.

Construction stage	Inflection point i (m)	SEM caused volume loss V_L (%)	Increment of SEM V_L (%)	Total volume loss V_L (%) ^{*a}	Increment of total V_L (%) ^{*a}
Left drift passed	7.7	0.39	-	0.23	-
Right drift passed	10.2	0.49	0.10	0.29	0.06

CTH passed	11.6	0.53	0.04	0.35	0.06
CINV passed	11.5	0.65	0.12	0.45	0.10

*^aCalculation of total volume loss considers both TBM and SEM construction.

3.4.2 Subsurface Settlement

Figure 3.11 shows the measured vertical subsurface settlement at Sta. 0+20. The depths of the five MPBX anchor points are shown in Figure 3.1, including A5 situated 1-m above the excavation crown. The surface settlement is similar to the 1-m deep A1 settlement and therefore not shown. The measured data indicate that during the excavation of the side drifts, the strata above the cavern subsided as a whole block. Several factors may have caused this response. First, the construction of side drifts enlarged the previously bored tunnel to an ovate profile, which gained more horizontal convergence than vertical deformation. Furthermore, the cover depth is relatively shallow, and part of the ground is braced by the surrounding building and utility structures.

During the CTH stage, noticeable differential displacement appeared between the A2 and A4 extensometers, coincident with the location of the weathered Fernando formation. The subsurface settlement increased with depth inducing relative vertical extension in the ground overlying the crown. The ground extension grows gradually and over the full height from A1 to A5 after excavation of the CINV, removal of the temporary walls and full cavern ring closure.

Figure 3.12 presents the observed deformation of the MPBX towards the right side at STA150. Here, A5 was situated 0.5 m above the excavation crown. The readings prior to LTH arrival contained errors due to a data logging issue. The differential vertical settlement grew when the CTH face approached the monitoring section. The considerable A5 settlement is attributed to its location just 0.5 m above the crown. The relative displacements between individual anchors are slightly different for Sta. 0+20 and Sta. 0+45; however, the average vertical strain induced by the excavation (between A1-A4) are similar. All other available MPBX data show similar behavior in general. The design analysis predicted an average 22 mm of total subsurface settlement at 14 m below ground surface.

Several factors may have influenced the measured MPBX results, such as the quality of installation and boundary conditions. Usually, the accuracy and repeatability of the extensometers are largely determined by the precise leveling of the extensometer heads (Berg et al., 2003). In this case, the extensometer heads were monitored by AMTS, which increases the accuracy and measured frequency compared with traditional manual reading. The data logger issue was the most frequently encountered problem for the MPBX measurements, and was mainly due to the lack of waterproofing and significant rainfall during construction. The quality of the grout that backfilled the MPBX boreholes influences the contact between the borehole

wall and grout, which determines the transmission of ground movements to the anchor points. Several MPBXs in this project were observed to lose their functions or fail to record data.

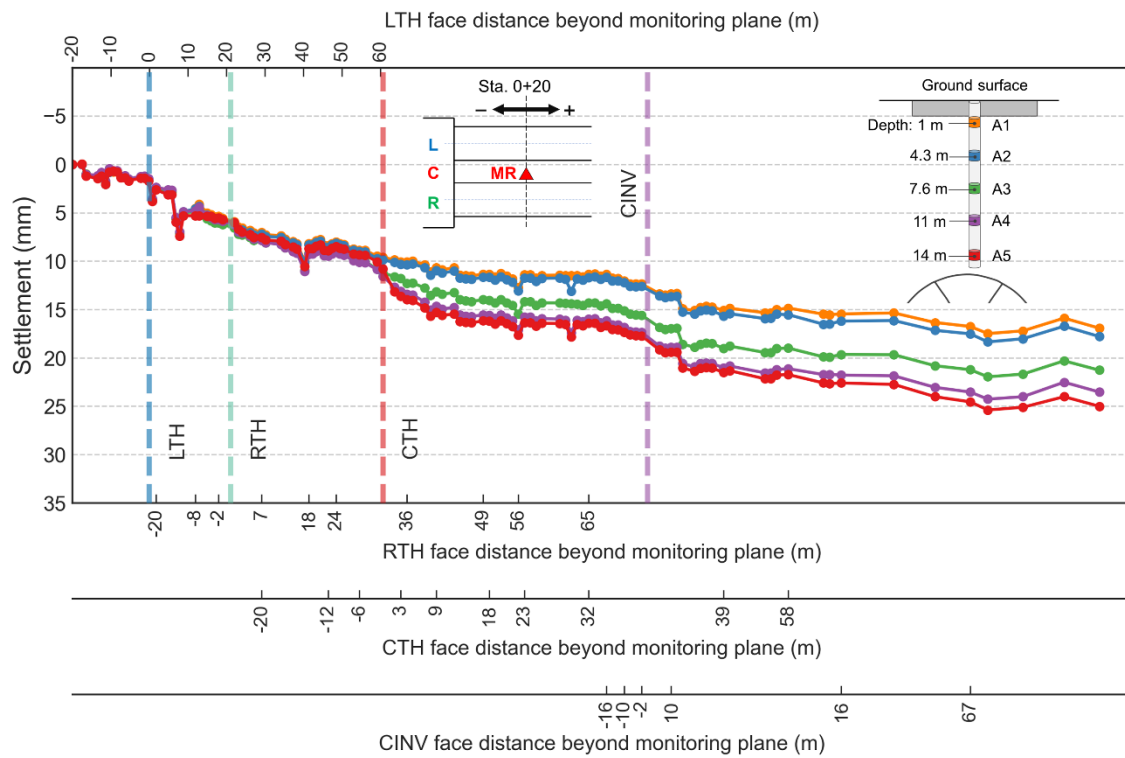


Figure 3.11 Subsurface deformation at Sta 0+20.

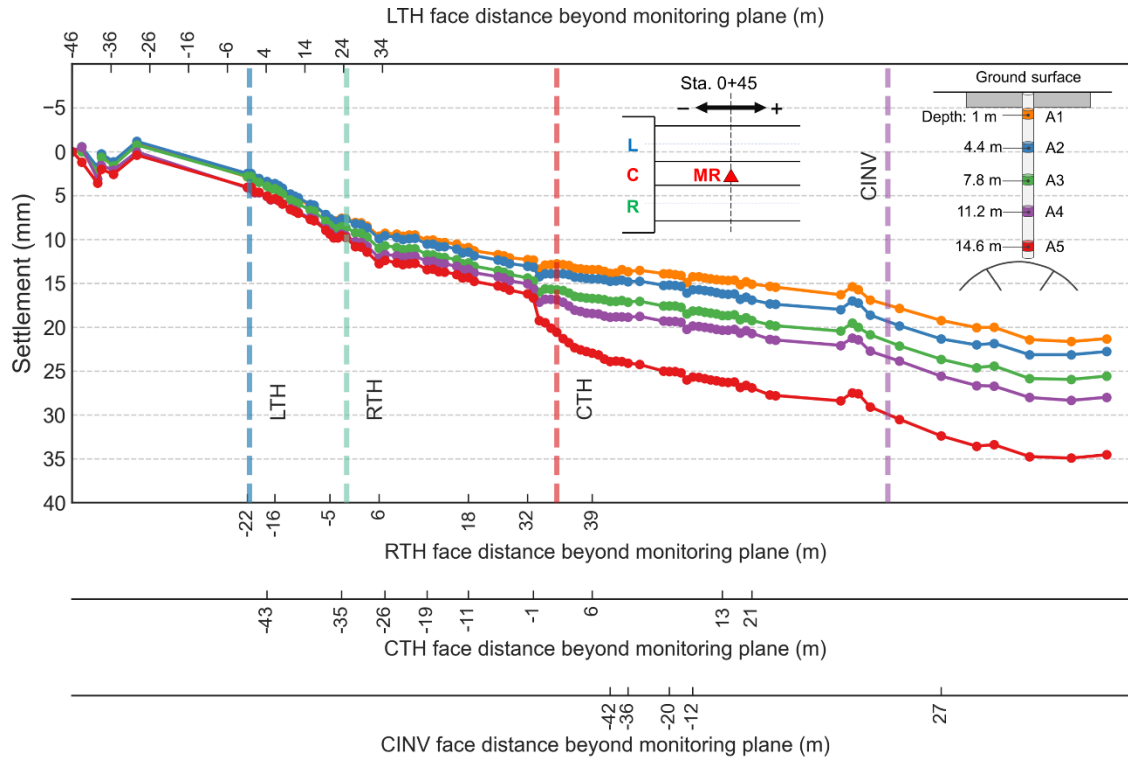


Figure 3.12 Subsurface deformation at Sta. 0+45.

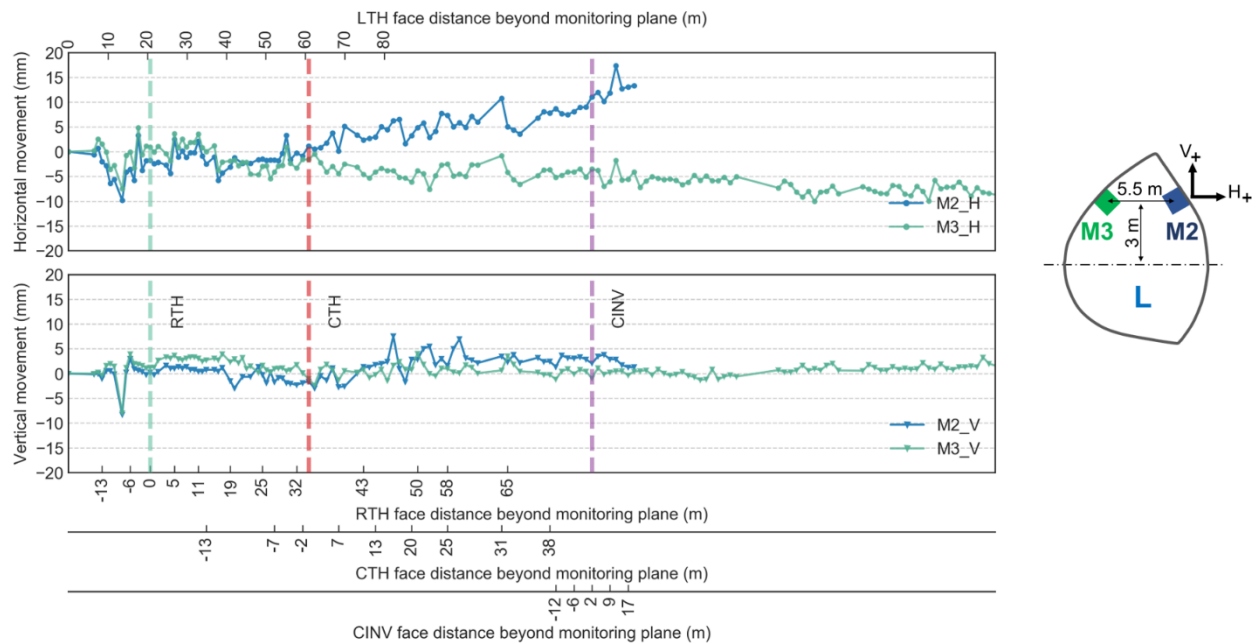
3.4.3 Tunnel Convergence

The monitored convergence of the shotcrete lining in the left drift is shown in Figure 3.13 and Figure 3.14, with the relative distance between the convergence monitoring plane and excavation faces on the horizontal axes. The target prisms were placed 0.6 m behind the face after the invert excavation was finished and the first 178 mm of shotcrete was placed. To this end, pre-convergence that occurred prior to shotcrete installation is not captured. The zero reading (0 mm) was taken approximately 2 to 4 h after the LINV excavation. Measurements were made manually with a total station every 12 h. The accuracy of the individual measurements is ± 5 mm and the variation is largely attributed to having to reset the tripod and perform backsighting for each measurement. The movement of reference points also can introduce observational error.

The individual displacements of M2, M3, M4, and M5 are shown in Figure 3.13a, Figure 3.13b, Figure 3.14a, and Figure 3.14b. The general trend indicates that M2 and M4 at the temporary wall were more sensitive to multi-drift excavation. In the beginning, after excavating and supporting the LINV, a limited amount of convergence was captured. When the RTH arrived, the excavation on the right side gradually induced ground stress relaxation, further causing the left liner to rebound and move to the right. Compared with Sta. 0+15, monitoring points at Sta. 0+45 show more vertical movement induced by the RTH excavation. The most

likely reason for this is that the rate of advance slowed when work was stopped on weekends as well as when the schedule was reorganized during the construction of the right drift around Sta. 0+45, which delayed ring closure time and induced more surrounding deformation. The movements were thereafter minimal until the CTH stage arrived. As can be seen in both sections, there was obvious movement as a result of the CTH construction. Removal of ground material led to M2 and M4 movement towards the center and upwards. The left and right initial supports were linked by the CTH lining, forming an integrated loading structure. Thus, slight squatting behavior was observed in M3 and M5. The CBEN and CINV excavation stages further relieved the temporary wall and caused a dramatic displacement of M2 and M4. Monitoring points M2 and M4 were then removed during the temporary wall demolition.

Besides individual displacement, Figure 3.13c and Figure 3.14c also show the relative movements between points at two levels, which can eliminate the error induced by the reference point to some extent and better capture the deformed shape of the left liner. The lower monitoring points, M4 and M5, experienced more divergence than M2 and M3 when the right drift passed. The influence on the left liner from the right drift is similar to a close twin-tunnel excavation with a pillar width of the center drift, which mainly causes a global rebound effect on the left liner. In contrast, the CTH, CBEN, and CINV excavations were closer to a relatively large amount of ground material removal. Coupled with a leaf shape structure of the support system, during the center drift excavation, the local relaxation at the left temporary wall led to a non-uniform distortion of the left drift lining. The deformation pattern of the right liner was similar to the left liner without a rebound phase caused by the side drift excavation.



(a)

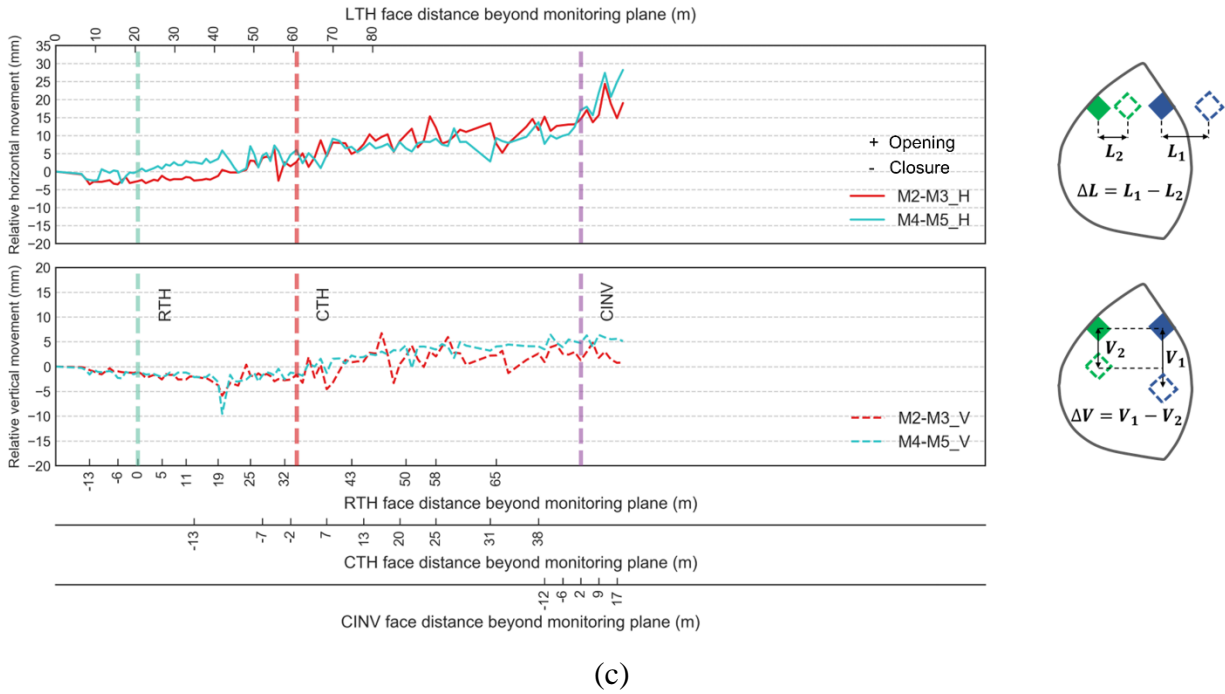
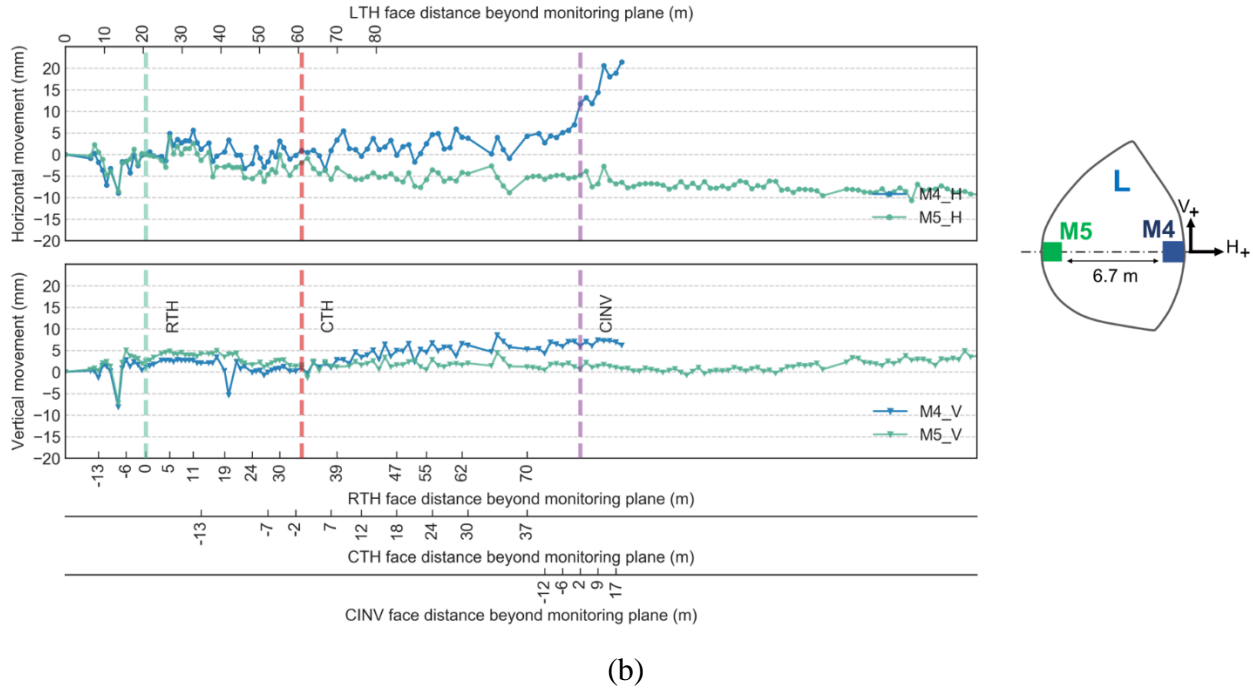
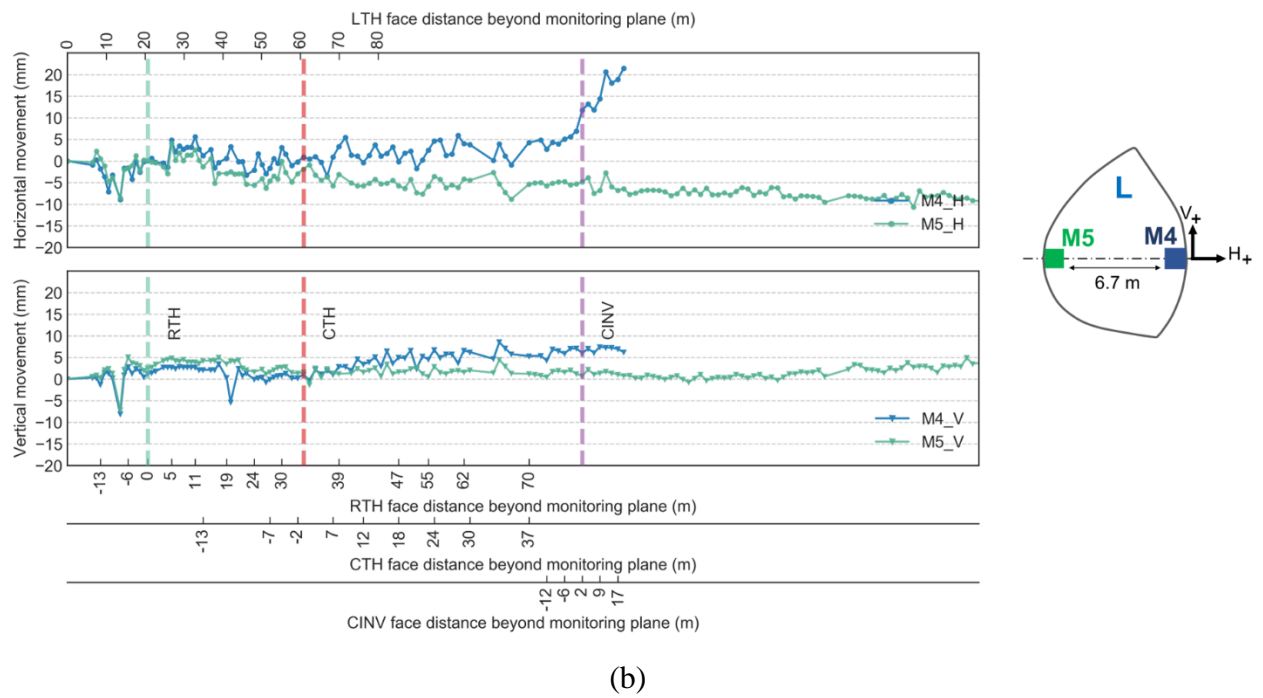
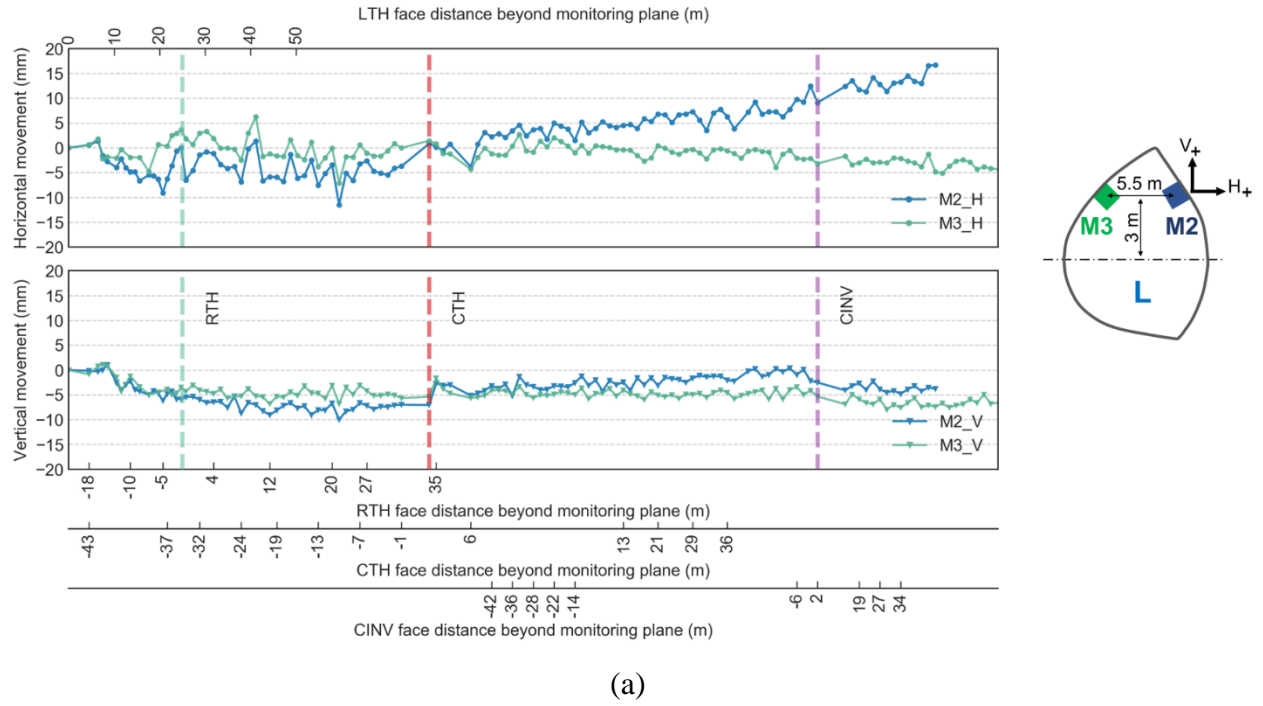


Figure 3.13 In-tunnel convergence at left drift Sta. 0+15: (a) measured displacements M2 and M3 where subscript H and V represent horizontal and vertical displacement components; (b) measured displacements M4 and M5 where subscript H and V represent horizontal and vertical displacement components; and (c) relative movements.



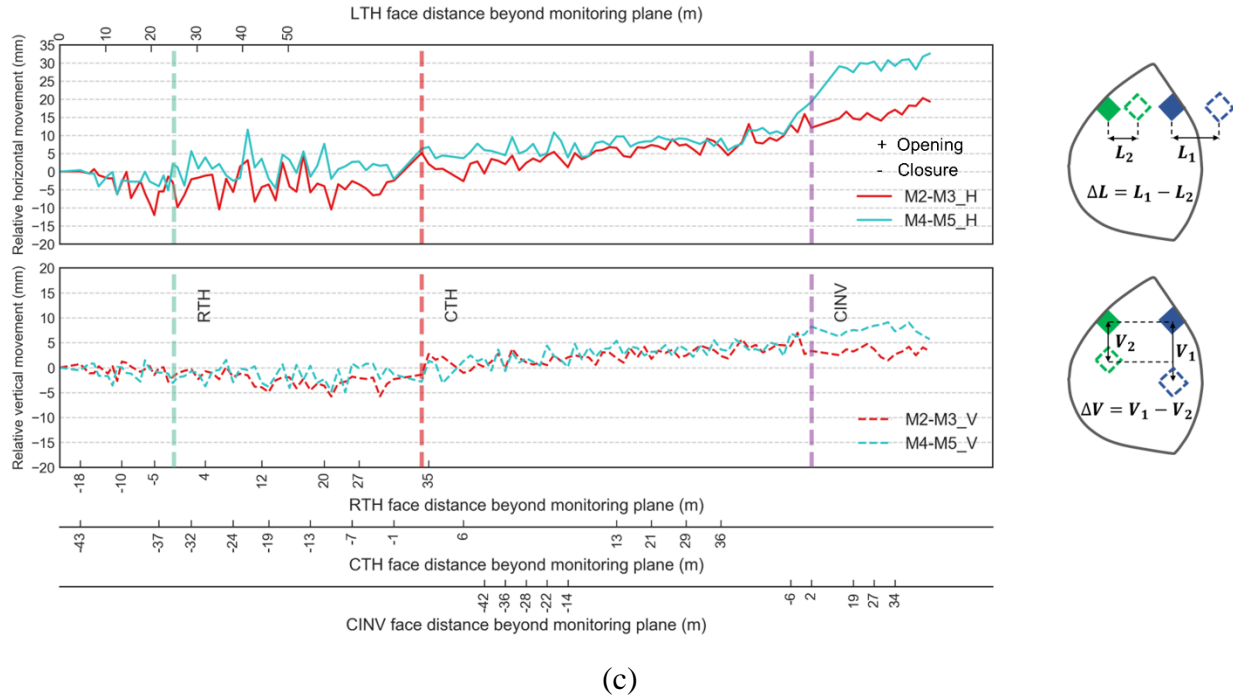


Figure 3.14 In-tunnel convergence at left drift Sta. 0+45: (a) measured displacements M2 and M3 where subscript H and V represent horizontal and vertical displacement components; (b) measured displacements M4 and M5 where subscript H and V represent horizontal and vertical displacement components; and (c) relative movements.

Figure 3.15 shows the measured vertical movements at the cavern crown. The zero readings were taken approximately 1 to 3 d after the CTH excavation because of the lack of access in the crowded operational space when the excavator was continually advancing. Therefore, only a limited part of center crown convergence was captured in the beginning. Some monitoring targets were accidentally disturbed and lost during the construction. The CBEN and CINV excavation caused a substantial amount of unloading effect, leading to both extrusion of ground material and convergence of temporary sidewalls, thus an obvious increase of settlement was observed as shown in the figure. Compared with the open area at the station side, the far-field medium exerts more restriction on the deformation of the core and surrounding ground material. Thus, the cross-sections away from the station trench showed less convergence at the center crown compared with those close to the station trench. After connecting the CINV liner to side liners through joints and pouring cast-in-place concrete, a closed structural ring was formed for the entire cavern. The center crown movements then leveled off and became stable. Before the excavation, a maximum 12 mm CTH liner convergence and 15 mm CINV liner convergence were anticipated based on the design analysis.

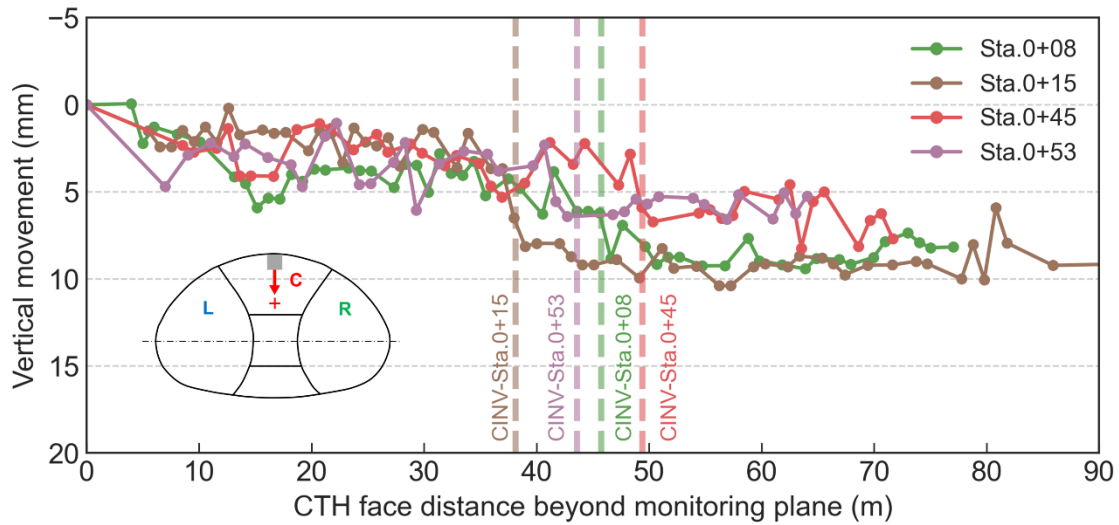


Figure 3.15 Measurements of center crown convergence beginning after CTH excavation.

Figure 3.16 presents the deformations of the tunnel invert monitoring points. After the installation of the CINV support and an average curing time of 5 h, the CINV was covered by temporary backfill to enable equipment and personnel movement for the next round of excavation. Considering more efforts were needed to access a CINV reading in a relatively crowded space, a lower monitoring frequency was adopted to minimize the interruption to routine construction. The invert lining gradually rose due to the unloading relief of the ground below the invert. The maximum heave reached about 12.7 mm and took a relatively long distance to stabilize. Initial sections Sta. 0+08 and Sta. 0+15 show some movement jumps, since the operation of munching walls and bottom connections was not smooth enough at the beginning of the temporary wall demolition. The CINV monitoring points were mounted on the embedded lattice girders, which were connected to adjacent parts located at the side drifts through joint panels. After excavating the CINV, the temporary walls tended to converge at the center, and invert liners at two sides also had a tendency to close the bottom gap. Consequently, the structural behavior induced by the frame deformation could partially contribute to the center invert rebounding effect.

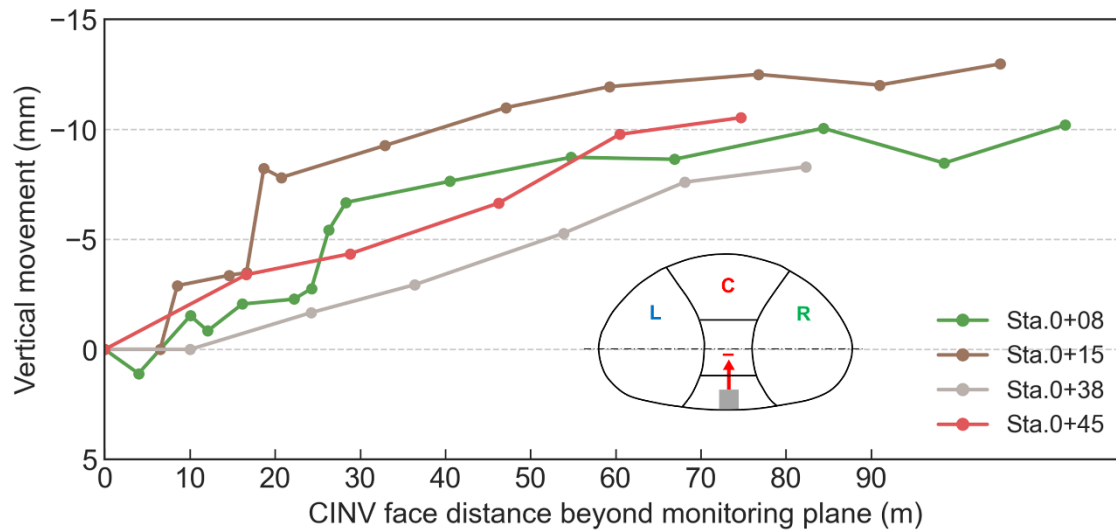
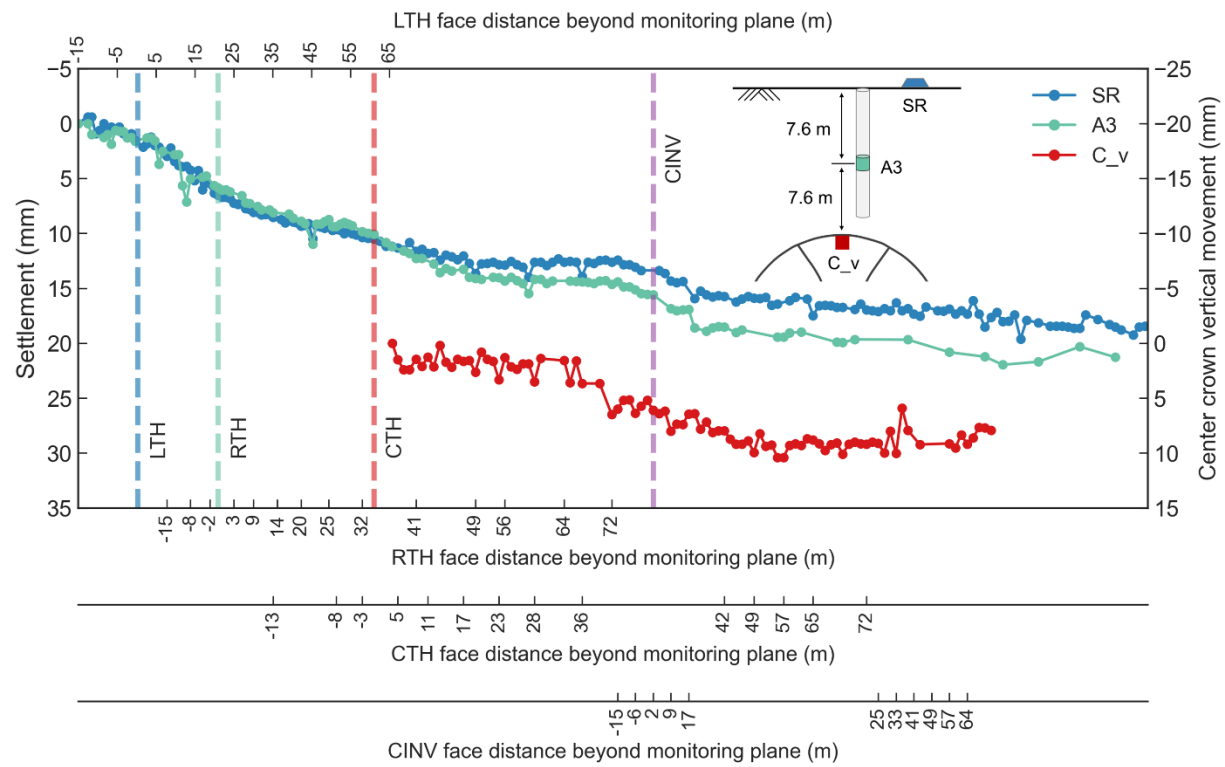


Figure 3.16 Measurements of center invert convergence (uplift) beginning after CINV installation.

3.4.4 Multi-level Deformation Interpretation

Ground deformation initiates around the opening and then propagates to the surface. To better explain the entire 3D deformation field at different levels, Figure 3.17 and Figure 3.18 present the surface, subsurface, and in-tunnel deformations together at two monitoring sections. The SR/SC is the surface monitoring point, A3 is the third anchor of the MPBX, and C_v is the center crown convergence point. The center crown convergence was plotted on a different y-axis in the same limit range as the settlement data. The initial settlement trends induced by the left and right drift excavation indicate almost no differential deformation from the surface to subsurface level, which is also the case in the MPBX observation described in the above section. The limited amount of material excavated for side drifts, shallow cover depth, and restriction from subsurface building structures are contributing factors for this behavior. At Sta. 0+15, the differential vertical settlement between surface and subsurface initiated after the CTH stage passed, while Sta. 0+45 shows an early initiation of the differential settlement. This is because various stratifications at Sta. 0+45 and Sta. 0+15 influenced the propagation of vertical displacement and the as-built location of A3 is closer to the right drift at Sta. 0+45, attracting more deformation when the right drift excavated. As shown in Figure 3.17 and Figure 3.18, compared with surface and subsurface trends, the CBEN and CINV excavation caused more deformation to be developed at the cavern crown.



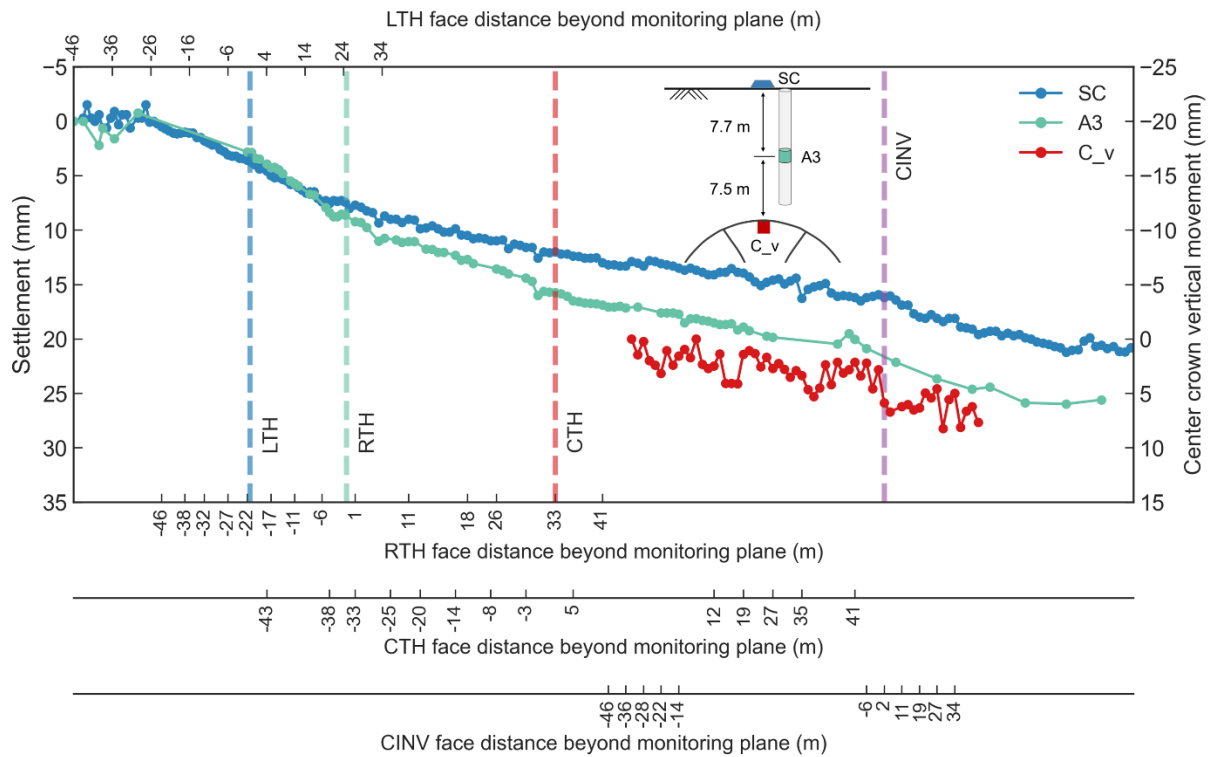


Figure 3.18 Field displacement at Sta. 0+45, including surface, subsurface, and in-tunnel deformation.

The tunnel convergence should be a good indicator of the deformation trend, but care should be taken when considering different purposes and construction stages. Lunardi (2008) concluded that the tunnel convergence is only the last manifestation of ground deformation and indicates the effect of the deformation of the ground ahead of the face. Considering the required installation after excavation, and the reliability of the instruments (as fluctuations shown in the figures), the order of the instrumentation ranking should lower the convergence weight when interpreting observations and setting rational trigger values for the project. For multi-stage excavation, however, tunnel convergence is still a valuable indicator since, once recorded, the instrumentation is able to capture a full range of deformation progress for the subsequent stages.

3.5 Real-Time Analysis in SEM Construction

Monitoring alone serves no useful purpose and is not the same as an observational method. Eurocode 7 summarizes the steps to implement the OM, where it states: “the response time of the instruments and the procedures for analyzing the results shall be sufficiently rapid in relation to the possible evolution of the system.” The data not only need to be processed properly but also timely, especially for soft ground SEM tunneling, where the system can evolve rapidly and the control of ground and structure deformations are of high priority. Instead of a traditional batch-style analysis or post-project evaluation, all the deformation analysis and interpretations

introduced above were performed every excavation step, which enabled continuous updating of risk assessment along the SEM tunneling process. Tailored data processing for SEM projects can tease out underlying features and patterns that best assist tunnel engineers. The visualization in Figure 3.7 and Figure 3.8, for example, not only present settlement vs. excavation face but also include multiple x-axes representing the multiple headings, providing deeper information for the SEM evaluation besides simplistic time vs. settlement graphs. The processing procedure was automated through a MATLAB-based program that was connected to the web portal-based data system allowing real-time data query and transfer.

Figure 3.19 illustrates a framework of the real-time data analysis applied during the SEM construction. The first step was to collect the instrumentation data needed. With all available data sources, in this case, the multi-level deformation measurements, a real-time analysis was conducted by the author. The raw data were first filtered and cleaned based on the quality of the measurements to eliminate errors and noises (e.g., effect of temperature, optical cover by moving subjects, etc.). Then the time-series data was further translated to pattern language that can speak to the tunneler, the designer, and the other team members. After processing, a real-time dashboard was created by the author including a series of high-quality graphic interpretations, which augmented the RESS reports on a daily basis. The documented materials were fed into daily review meetings (DRM) to communicate to all involved parties. The daily digestion yielded instructions for the following tunneling and additional actions needed for amending anomalous behavior.

Furthermore, a real-time back analysis was performed based on measured data available in the database. Through an iterative procedure, the back analysis aimed to identify geotechnical parameters used in the numerical model and validated the model at each step. The deformation predictions were updated according to any construction changes. This generated a sense of comfort of where the risk is heading in the final step and created a systematic feedback which can be classified into three types: a) Confirming the design and increase the confidence level of the risk; b) Demonstrating less favorable behavior than expected: a recalibration allows to define what additional measures (e.g., adjust the round length, concrete thickness, additional spiles, etc.) that would need to be implemented; c) Demonstrating better reaction than expected and that after quantifying consequences, some requirements can be relaxed.

Based on the actual behavior of the ground-structure system, design modifications were assessed through real-time analysis to improve performance and safety. For instance, Due to the uncertainty of ground condition, the initial design considers the variability of excavation advance length. A 1-m round length for side drift excavation was initially prescribed by the contractors and the designer based on available knowledge of most probable ground condition and similar projects experiences to limit ground deformation. To accommodate the existing 1.5-meters long PCTL demolition, the radial joints of the PCTL were able to align with the excavation face every three side drift rounds, or 3 m intervals, and the segments were removed in the first two steps. However, after 60 m of left drift excavation, it was observed that the local over-excavation to reach the end of the segment diminished productivity and resulted in construction quality issues. At the same time, with available monitored data, a numerical back analysis was performed to close the gaps in knowledge of ground properties and the updated design model showed that changing the side drift round from 1.0 m to 1.5 m causes minimal change of ground and lining deformation. Therefore, the team proposed to relax the side drift round length to 1.5 m to better

accommodate PCTL removal as long as certain performance requirements were met (Herranz et al., 2019). Trends and patterns of ground settlement then were carefully examined through the real-time analysis. It was justified that no significant impact of settlement trends and patterns compared with previously observed in terms of both magnitude and range of influence zone. Other design modifications such as center drift lag distance and the temporary wall demolition sequence were made by the contractors and the designer during the construction, following the same evaluation procedure and reviewing process.

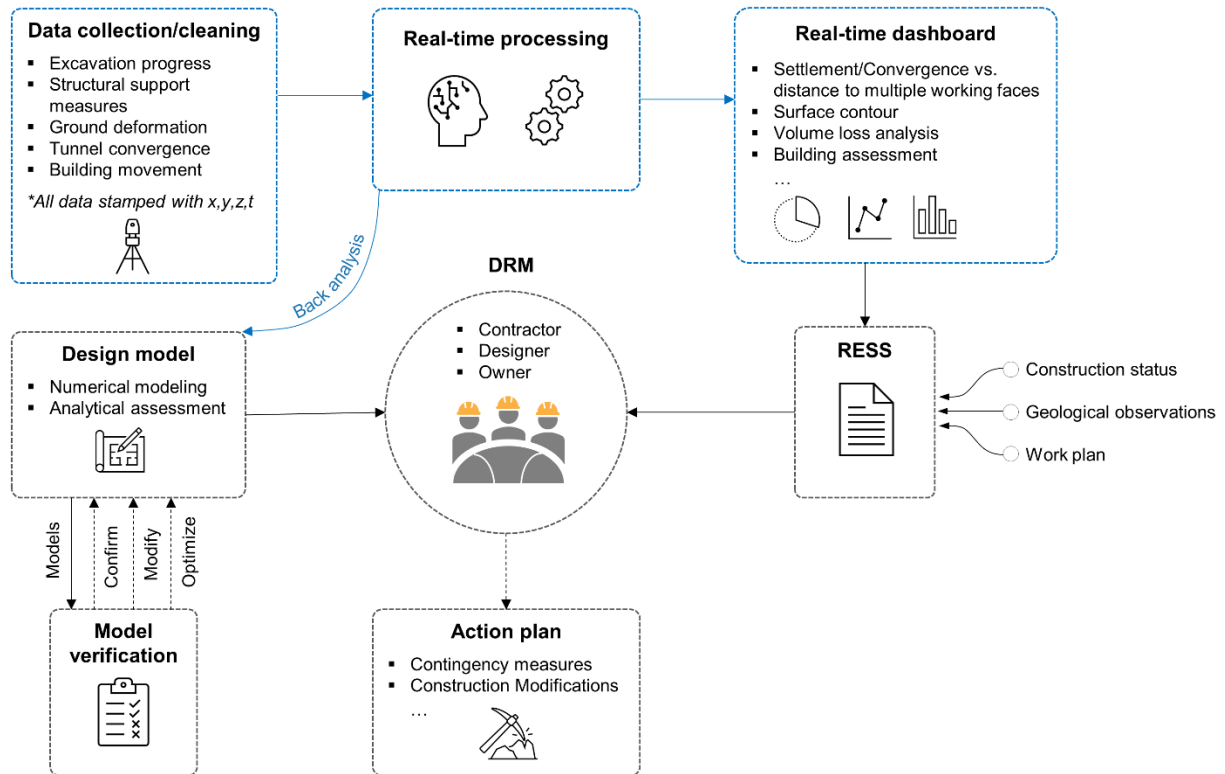


Figure 3.19 Architecture of real-time deformation analysis in the SEM construction.

3.6 Conclusions and Recommendations

This paper presented a case study of a three-drift seven-stage SEM cavern construction project in urban soft ground settings. The tunneling response was monitored by measuring surface, subsurface, and in-tunnel deformations. The performance of the SEM excavation and initial support construction was evaluated every excavation step by analyzing the field observations, and the deformation responses were characterized and related to the multi-stage SEM tunneling process, from which the following conclusions were obtained:

- A relatively homogeneous behavior of the Fernando formation was observed during the

SEM construction. The observed ground and structural deformations are generally close to the design expectations. Ground surface settlement accumulated with the progression of drift excavation. The average total surface settlement reached about 20 mm. Upon the arrival of the LTH at the monitoring section, the surface settlement reached 10 % of its final amount. The surface settlement caused by the side drift construction varied between 30 % and 45 % of the total settlement. The largest single-stage incremental movements occurred during the CBEN and CINV excavation and account for 30–40 % of the total deformation. The total volume loss of 0.45% is considered as excellent-quality practice.

- When adopting SEM in urban tunneling, it should be recognized that the settlement pattern and process are influenced by surrounding infrastructure. A total of 25 mm to 35 mm of subsurface settlement occurred 14 m below the ground surface and 1 m above the excavation crown. The side drift excavation induced a rigid-body ground movement and an obvious differential settlement between each anchor was only observed after the CTH excavation. The relatively uniform vertical deformations at different ground depths can be mainly attributed to the shallow cover depth, the unique ovate excavation shape of the side drifts, and the bracing effect caused by subsurface structures.
- The observed convergence measurements indicate that the initial liner at the left drift experienced four deformation stages and the deformation pattern is a combined result of the sequential excavation and the leaf shape of the structure. The initial convergence of the left liner was 5 mm to 10 mm. The subsequent right drift excavation mainly caused a global rebound of the left liner with horizontal movements of 5 mm to 15 mm. The CTH, CBEN, and CINV excavation mainly induced local relaxation with temporary wall CMPs moving 10 mm to 25 mm towards the center. Temporary walls experienced more

deformation since the demolition did not happen immediately after the CINV excavated.

The measured CTH convergence varied between 5 mm to 10 mm, and the CINV was measured to rebound 8 mm to 12 mm after excavation.

- The MPBX monitoring close to the cavern crown can approximately reflect the pre-convergence, which usually cannot be captured by the tunnel convergence monitoring. The delay of the zero reading and the vulnerability of optical surveying diminished the reliability of the in-tunnel convergence measurements. When setting trigger values to assess the performance of an SEM tunnel, the order of instrumentation ranking should not only consider the time sequence and spatial location, but also the reliability of the instruments. A certain degree of fluctuations can be expected, thus sometimes trends are more meaningful than individual readings in evaluating and analyzing tunneling responses.
- A deliberate OM approach was implemented through the design and construction stages. The deformation interpretation and analysis were performed every excavation step automatically through a MATLAB-based program. A back analysis procedure was conducted to validate and update the design model. The results were regularly discussed in DRM among the contractor, designer and owner, yielding instructions and modifications for the following SEM steps. This systematic procedure enabled adaptive design and construction and facilitated the timely decision-making process, which benefited several design changes during the construction, such as modifying the side drift round length from 1 m to 1.5 m.

The following recommendations are made based on lessons learned during this case study:

- When SEM tunneling involves an enlargement of the bored tunnel section where a routine removal of TBM rings is needed, a different SEM round length with PCTL width is a potential source of conflict. This variability should be considered during the design stage and the round length should be optimized by monitoring ground response and proving the performance. To remove a PCTL ring, it is recommended to start with dislodging the key segment, followed by removing the remainder of the segments one at a time in a reverse ring building sequence by shearing the circumferential joint plastic dowels. The technique introduced during construction was demonstrated to highly improve productivity and constructability, reducing the excavation sequence time as well as the ground exposure time.
- The design of instrumentation should have an appropriate amount of built-in redundancy in case of damage, which is often encountered in convergence targets installed on the lining. CTH targets were found more vulnerable to be damaged mainly due to limited operating space. In this case, two or more CMPs should be installed at critical locations such as the cavern crown. The convergence monitoring design should consider the influence of temporary facilities that might be installed (e.g. ventilation systems) during the construction. The installation of optical targets and zero-reading measurement should follow the initial support installation immediately. In that case, smooth coordination and communication between the excavation and survey team are the keys, considering limited operating space and access restrictions are frequently expected.
- The reliability of MPBX measurements highly depends on the quality of installation and the leveling of the MPBX heads. In order to maintain a good transmission of ground movements to the subsurface anchor points, the types and proportions of grout mix

backfilled into the MPBX borehole should be tailored according to the surrounding ground material.

- The application of real-time analysis with high-quality and functional interpretations during SEM construction is recommended, especially for urban projects. The translation from time-series deformation data to pattern language that directly speaks to construction personnel would make a worthwhile contribution to timely understanding the ground behavior and extracting deeper insights from the instrumentation. This frames a data-driven decision-making process that adapts the knowledge of risk along with the entire project. This automated processing procedure can be further evolved and integrated into platforms and tools that enable data streaming and event processing algorithms.
- The back analysis procedure in real time serves as a useful project function to validate the design by either confirming the initial design, demonstrating less favorable behavior than expected, or showing better performance than predicted. Based on the back analysis results and real-time analysis of observed data, the corresponding measures and modifications can be implemented accordingly. There is great value to add a back analysis designer on site as part of the tools applied in the SEM project.
- Engagement of the contractor during the design stage providing input with respect to means and methods, and participation of the designer on the daily meetings during construction to help analyze monitoring data and streamline decision making in a collaborative environment are key for SEM construction success. This highly depends on the project delivery method. On a Design-Build project contractor and designer are part of the same team, so they work together from the beginning. On a Design-Bid-Build the

designer might have finalized the design when the contractor gets involved. In this case there should be agile processes in place to facilitate decision making.

3.7 Acknowledgments

Funding from the Center of Underground at the Colorado School of Mines and by the University Transportation Center for Underground Transportation Infrastructure (UTC-UTI) at the Colorado School of Mines under Grant No. 69A3551747118 from the U.S. Department of Transportation (DOT) is gratefully acknowledged. Partial funding for this study was also provided by Skanska and Traylor Bros. We would also like to express our gratitude to Traylor Bros., Skanska, Mott Macdonald, Geocomp, Sixense Soldata, and LA Metro for sharing the project data and providing the opportunity to join in this project.

CHAPTER 4

SURROGATE MODEL FOR 3D GROUND DEFORMATION IN TUNNELING BY THE SEQUENTIAL EXCAVATION METHOD

*Reproduced from a draft to be submitted to the Journal of Computers and Geotechnics and is
presented here with minor variations.*

4.1 Abstract

Ground deformation control to avoid damage to above-ground structures is one of the key challenges faced during urban tunneling when using the sequential excavation method (SEM). Three-dimensional (3D) numerical analysis is a powerful and essential tool to assess SEM-induced ground and structural deformations. The main challenge in numerical modeling is the uncertainties in data needed to build a model. Various analyses are needed, such as parametric and back-analysis, to update ground parameters during the SEM construction and quantify uncertainties and their impacts on SEM model predictions. However, such analyses require thousands to millions of repeated model evaluations making 3D numerical simulations expensive. One technique to make the modeling more manageable is reducing the model size by using model reduction techniques or by using a smaller surrogate model that captures the main elements of a full 3D model. This paper examines the capability of four surrogate modeling methods, namely the Polynomial Chaos Expansion (PCE), Kriging, sequential Polynomial-Chaos-Kriging (PCK-SEQ), and optimal Polynomial-Chaos-Kriging (PCK-OPT), to reduce the model size that will accurately and efficiently capture the ground and structural deformations induced by SEM tunneling. A 3D finite-difference model using FLAC3D was developed to simulate an actual SEM project's step-by-step excavation and initial support process. A sensitivity analysis was performed using the surrogate models to determine the most influential geotechnical input parameters. The Sobol sequence sampling strategy was utilized to conduct a design of experiments. The overall and individual output accuracy of surrogate models, the robustness of training and testing, and the accuracy distribution throughout the input parameter space were evaluated and compared. The results indicate that PCK-SEQ and PCK-OPT exhibit the best performance among the four methods. The cost for a single 3D SEM evaluation model is reduced from 20 hrs to less than one second by using the PCK surrogate models.

4.2 Introduction

The sequential excavation method (SEM) is commonly employed in soft ground urban tunnel construction. Large-scale SEM in the midst of urban infrastructure is complex because allowable ground deformations are relatively small. Thus, assessing SEM-induced deformation during design and construction is critical for successful SEM implementation. The complexity of SEM construction demands the use of 3D finite element method (FEM) or finite difference

method (FDM) computational modeling (Janin et al., 2015; Möller and Vermeer, 2008; Neuner et al., 2020; Svoboda et al., 2010; Vlachopoulos and Diederichs, 2014).

Another layer of complexity is that most geotechnical parameters for computational models are not widely available or well known in practice. The uncertainties in model parameters significantly influence the prediction of SEM-induced deformations. One key feature of SEM is its design flexibility with numerous construction variables that can be varied. Therefore, probabilistic analyses are crucial to assess the effect of uncertainties in model predictions and consequently the SEM performance. For instance, sensitivity analyses are essential during the initial design stage to identify key model parameters that govern the SEM responses and test what-if scenarios. As the name implies, SEM tunneling is conducted sequentially in construction stages. It is important to update the knowledge of ground conditions learned from each construction and adapt the SEM design as construction progresses. Updating ground parameters can be done through a back-analysis procedure utilizing field measurements. A rigorous back-analysis involves optimization to minimize the difference between predicted outcomes and observed measurements. Furthermore, reliability analysis is needed for SEM to quantitatively assess the probability of failure as a measure of risk (Zheng et al., 2022a).

Probabilistic back-analyses and reliability evaluation of SEM tunneling usually require a large number of model runs. A single 3D FDM or FEM simulation modeling of SEM construction usually takes hours to days to finish. For this study, the average cost of a single 3D FDM simulation for the SEM analysis was around 20 hrs on an Intel i7-9700K CPU @ 3.60GHz and 16 GB RAM desktop computer. Employing 3D FDM modeling to conduct such analyses is time-consuming and arguably impossible as some probabilistic analyses require thousands to millions of runs. Thus, most previous probabilistic analyses of SEM tunneling used simplified or 2D numerical models that inadequately capture 3D SEM behavior (Janda et al., 2018a; Langford and Diederichs, 2013; Li et al., 2021; Lü et al., 2017b, 2017a; Wang and Fang, 2018).

This limitation motivates the development of surrogate models to reduce the model size and computationally approximate large and expensive 3D numerical models (Simpson et al., 2001). Surrogate modeling has evolved and been extensively used in many engineering fields over the past decades, aiming to approximate the relationships between the input and output of a simulation-based analysis (Keane et al., 2008). However, their application in tunneling has been minimal. Various surrogate modeling techniques are available, including response surface methods (Kim and Na, 1997), regression methods (Goh et al., 2017; Zhang and Goh, 2015), artificial neural networks (Adeli, 2001), multivariate adaptive regression splines (MARS) method (Zhang, 2019), and proper orthogonal decomposition (Buljak and Maier, 2011). Selecting proper surrogate methods depends on the problem, computational resources, required output, and engineering expertise. The best surrogate method is problem-dependent and, in many cases, not known beforehand. Surrogate modeling has been successfully applied in various industries, such as aerospace (Iuliano, 2017; Weinmeister et al., 2019), construction (Westermann and Evins, 2019), mechanical engineering (Totis and Sortino, 2020), and fluid dynamics (Margheri and Sagaut, 2016). A detailed review of surrogate methods and their applications can be found in (Bhosekar and Ierapetritou, 2018; Dey et al., 2017). However, to the best of the authors' knowledge, there has been no attempt to study the capability and applicability of surrogate modeling for predicting SEM-induced ground and structural deformations.

SEM tunneling usually involves more excavation stages, more responses of interest (number of model outputs), and more complex ground-structural interactions compared to mechanized tunneling. Construction of an SEM tunnel usually consists of multiple drifts with possible subdivisions. Each partial excavation advances sequentially with certain distances between each other. The ground and structural deformations at a monitoring section when each drift approaches and passes are of concern. Therefore the array of possible deformations induced by SEM recorded at a monitoring section is much greater than that of mechanized tunneling. The excavation geometry of SEM is more complex and higher deformation is usually expected compared to mechanized tunneling. The ground-structural interactions are therefore more complicated. The initial support deformation at a certain drift depends on both the ground-structural interactions during that drift excavation and subsequent excavations.

In recent years, studies of surrogate modeling applied in underground construction have increased (Cao et al., 2020; Qi and Zhou, 2017; Zhang et al., 2021; Zhao et al., 2019). Most previous studies on surrogate modeling of tunneling-induced deformations focus on mechanized tunnel construction. Khaledi et al. (Khaledi et al., 2014) developed a surrogate model for 3D FEM mechanized tunnel simulation based on proper orthogonal decomposition with extended radial basis functions. They use seven geotechnical inputs and nine deformation outputs in 45 excavation steps, achieving a model-average normalized root mean squared error below 5%. Zhao et al. [29] adopted a similar surrogate approach to capture TBM-induced ground surface displacements modeled by 3D FEM. The surrogate model had five geotechnical parameter inputs and four displacement outputs, achieving $R^2=0.98$ and a maximum absolute error of 0.1% compared to 3D FEM results. Miro et al. (Miro et al., 2014) used a surrogate model of a 3D FEM mechanized tunnel to conduct a global sensitivity analysis. Their surrogate model contains seven geotechnical inputs and nine displacement outputs. The results reported a validation R^2 equal to 0.99. However, other accuracy metrics, training performance, and detailed design of experiments were not reported. Cao et al. (Cao et al., 2020) proposed an artificial neural network (ANN) surrogate model for building damage prediction caused by mechanized tunneling. A hybrid recurrent neural network predicted the ground surface settlement that includes two inputs (face and grout pressures) and 18 outputs (step-wise settlements) generated from 3D FEM simulations. A testing error of 7% was obtained compared to FEM results (the number of training and testing samples are 48 and 12, respectively).

This study explored the capability and performance of a newly developed algorithm called Polynomial-Chaos-Kriging (PCK) [35] in approximating 3D numerical simulations of SEM tunneling. PCK combines two well-established surrogate modeling techniques: Polynomial Chaos Expansions (PCE) and Kriging, leveraging the benefits from each model. PCE can capture the global behavior of the numerical simulation, and the local approximation can be represented by Kriging interpolation. PCK algorithm has shown significant advantages in dealing with small experimental designs (Schobi et al., 2015) and exhibits promising performance in approximating computational simulations under various engineering settings (Pan et al., 2021; Schöbi et al., 2017; Totis and Sortino, 2020).

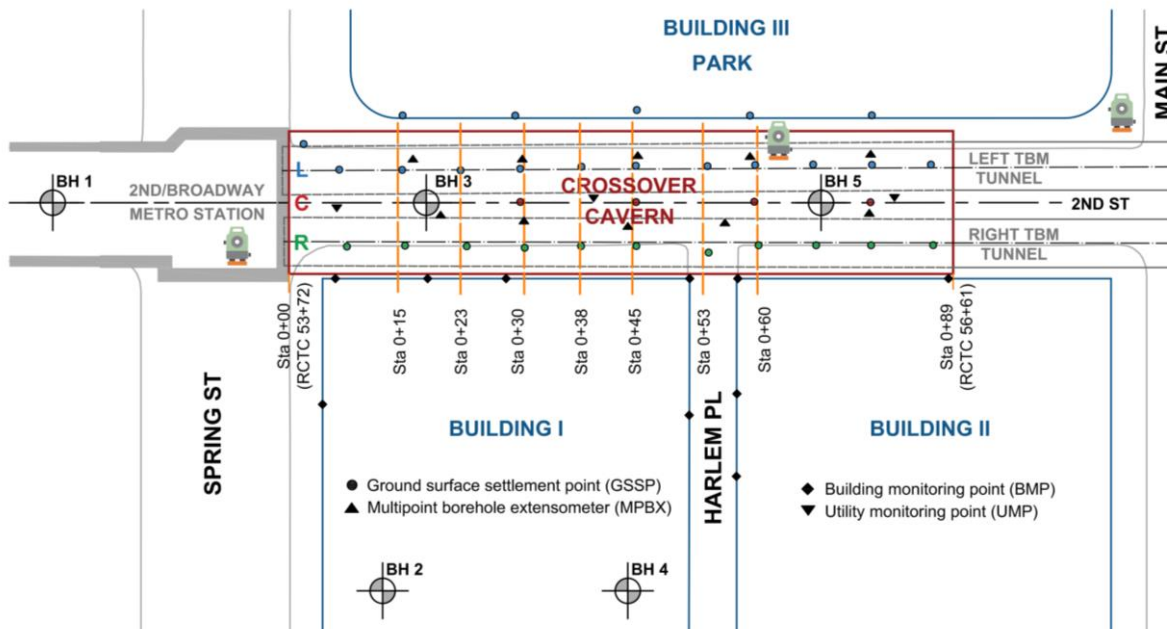
The remainder of this paper is organized as follows. The background of the project used in this study is introduced in Section 4.3. Careful development of a 3D FDM model for evaluating SEM-induced ground and structural deformations is presented in Section 4.4. The basis of surrogate methods utilized in this study is introduced in Section 4.5, followed by a

description of the procedure of SEM surrogate modeling. The sensitivity analysis conducted to determine surrogate input parameters is discussed in Section 4.6. A comparative study was performed for four different surrogate methods. The accuracy of surrogate models, the training and testing robustness, and the accuracy spectrum throughout the input space are presented in Section 4.7.

4.3 Project background

The Regional Connector Transit Corridor (RCTC) crossover cavern is located in downtown Los Angeles and is part of the 3 km light-rail line that connects the existing Gold Line to the Blue and Expo lines. The plan and profile views of the cavern are shown in Figure 4.1. The cavern was constructed underneath a busy street and a storm drain tunnel. Three buildings are close to the construction zone. The excavation size of the cavern is measured 17.7 m wide by 11 m tall and 89 m in length as shown in Figure 4.1b. Before the cavern excavation via SEM, two bored tunnels were constructed by an earth pressure balance tunnel boring machine (EPB-TBM) with an excavated diameter of approximately 6.7 m. The tunnels were lined with a 267-millimeter-thick precast concrete tunnel lining (PCTL) with double gaskets and an inner diameter of 5.74 m.

The geotechnical investigations show that the cavern excavation is within the Fernando formation overlaid with coarse-grained alluvial deposits (Qal2) and a small portion of artificial fill (Af). The Fernando formation is classified as weak clayey siltstone with unconfined compressive strength (UCS) values of 0.2 to 2.5 MPa (Ulusay, 2014). The groundwater table is approximately 7 m below the ground surface. Due to a fine-grained texture and relatively intact condition, the Fernando formation has a relatively low permeability, with hydraulic conductivity ranging from 10^{-6} to 10^{-8} cm/s. High groundwater inflow into the cavern was neither anticipated nor experienced during excavation.



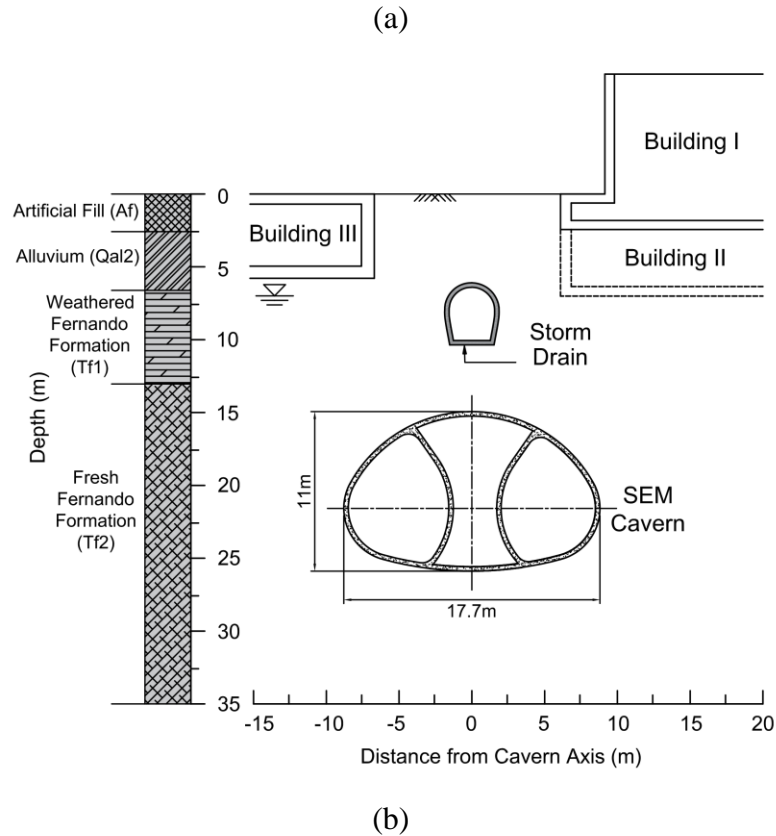


Figure 4.1 LA RCTC SEM cavern layout: (a) plan view and (b) vertical profile at Sta. 0+15 (adapted from (Zheng et al., 2021a)).

The SEM construction sequence consists of a three-drift seven-stage scheme as shown in Figure 4.2. The side drifts were divided into left and right top heading (I/LTH and III/RTH) and invert (II/LINV and IV/RINV) sequences, and the center drift consisted of top heading (V/CTH), bench (VI/CBEN), and invert (VII/CINV) sequences. The two temporary walls were demolished in a staggered pattern following the center invert placement. The initial support system consisted of 300 mm thick fiber-reinforced shotcrete, localized wire mesh, and lattice girders. The pre-existing PCTL segments were removed during the side drift excavation. The round length and excavation sequence for each drift are shown in Figure 4.2(c)(d). The lagging distance between each drift is shown in Figure 4.2(b). Refer to (Zheng et al., 2021a) for more details of the SEM construction procedure.

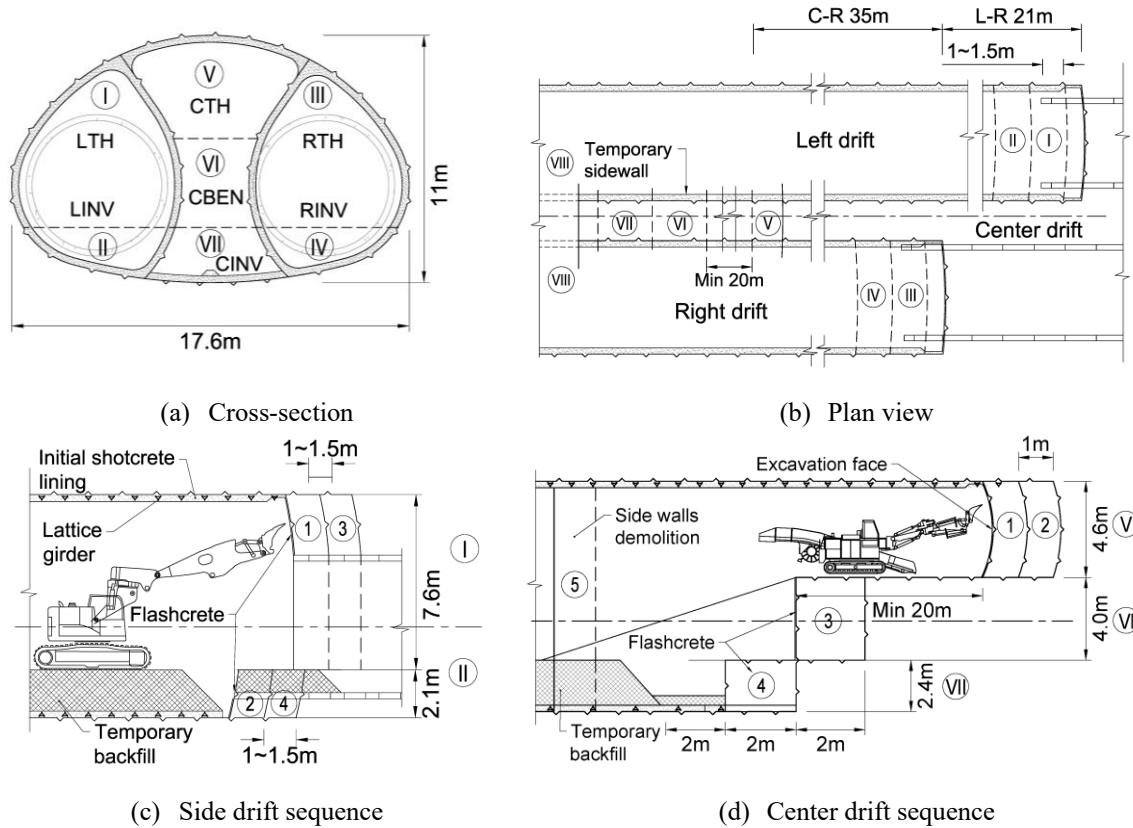


Figure 4.2 Construction sequence for the SEM cavern (adapted from (Zheng et al., 2021a)).

4.4 3D finite-difference modeling

A 3D FDM model was developed to simulate ground response during the tunnel construction process. The numerical model was established using the commercial code FLAC3D, version 7.0 (Itasca Consulting Group Inc., 2019) and its internal programming language, FISH. Figure 4.3 shows the dimensions and configuration of the model. A total number of 300,000 polyhedral-shaped elements were discretized.

Four ground layers—artificial fill (Af), alluvium (Qal2), and two layers of the Fernando formation (Tf1, Tf2)—were included in the numerical modeling. A geostatistical modeling-based approach was used to simulate the site geology (Zheng et al., 2022b). The most probable geology model was selected to represent the stratigraphy used in the 3D finite-difference model as shown in Figure 4.3. Each ground layer was considered spatially homogeneous with constitutive parameters modeled as random variables. Explicitly modeling the heterogeneity and spatial variability of the ground properties will increase the computational cost exponentially and thus was not considered here.

Undrained response was analyzed in FLAC^{3D} by employing the wet approach (Itasca Consulting Group Inc., 2019), where drained geotechnical parameters were used. The Tf1 and Tf2 layers were represented by the Hardening Soil-Small Strain (HSS) constitutive model.

Considering Af and Qal2 layers have much less influence on opening response than the Tf1 and Tf2 layers given their location well above the opening, the Af and Qal2 layers were modeled by the elastic-perfectly-plastic Mohr-Coulomb model (Zheng et al., 2021b). Key parameters used in the 3D FDM model are given in Table 4.1, where most geotechnical parameters are defined based on all available lab/field tests from the entire project alignment. One can refer to Benz (2007) for more detailed illustrations of the meaning of parameters and the HSS model itself.

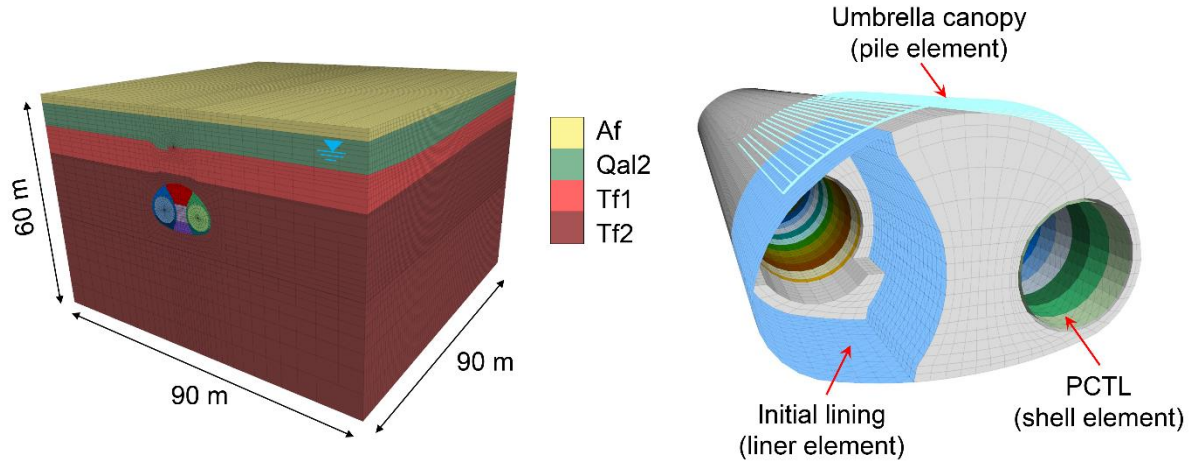


Figure 4.3 3D Finite-difference model simulation.

Table 4.1 Geotechnical properties adopted in 3D FDM model.

Parameter	Description	Af	Qal2	Tf1	Tf2
$\gamma^{(1)(3)}$ [kN/m ³]	Total unit weight	18.9	18.7	18.9	19.3
$K_0^{(2)(3)}$	Coefficient of lateral earth pressure at rest	0.50	0.50	0.60	0.65
$E^{(3)}$ [MPa]	Young's modulus	28	57	-	-
$\nu^{(3)}$	Poisson's ratio	0.35	0.35	0.4	0.4
$c'^{(3)(4)}$ [kPa]	Effective cohesion	0.0	10.3	75*	170*
$\phi'^{(3)(4)}$ [°]	Internal friction angle	28	30	25*	26*
$E_{50}^{ref(4)}$ [MPa]	Secant modulus	-	-	48*	55*
$E_{ur}^{ref(2)(5)}$ [MPa]	Unload/reload modulus	-	-	150*	183*
$m^{(4)}$	Power for stress-level dependency of stiffness	-	-	0.7*	0.9*
$p^{ref(5)}$ [kPa]	Reference pressure	-	-	100	100
$\nu_{ur}^{(5)}$	Unload/reload Poisson's ratio	-	-	0.2	0.2

$K_0^{NC(5)}$	K_0 value for normal consolidation	-	-	0.53*	0.51*
$R_f^{(5)}$	Failure ratio	-	-	0.9	0.9
$OCR^{(3)}$	Over-consolidation ratio	-	-	1.2	1.5
$E_0^{ref(6)}$ [MPa]	Small strain modulus	-	-	330*	480*
$\gamma_{0.7}^{(5)}$	Shear strain at which $G_s=0.7G_0$	-	-	2.0E-04*	2.0E-04*
$GWT^{(3)}$ [m]	Groundwater table depth		6.8*		

* Mean values of the parameters that are investigated in the sensitivity analysis

- (1) Interpreted from 166 field moisture-density tests results
- (2) Interpreted from 8 pressuremeter tests results
- (3) Referenced from the literature (Herranz et al., 2016; Yang and Huynh, 2017; Zheng et al., 2021a)
- (4) Interpreted from 11 isotropically consolidated undrained compression triaxial (CIUC) tests
- (5) Based on the literature (R. Obrzud, 2010) and engineering judgment
- (6) Interpreted from 8 shear wave tests

The SEM construction process was modeled in a step-wise manner. The actual construction sequence from stages I to VII was simulated in the model. At each stage, a one-round-length ground zone is deactivated and the “zone relax” option (Itasca Consulting Group Inc., 2019) is adopted to simulate a gradual excavation of the material. Within the same phase, the exposed portion of the PCTL ring is removed and a liner element representing the initial support is activated immediately behind the face (Figure 4.3). As the shotcrete lining was installed incrementally at the top heading, the thickness of the liner element was modified accordingly to simulate two lifts of shotcrete application (60% + 40% of the total thickness). A linear elastic material model was assigned to the lining, integrating the aging effect of shotcrete strength. A time-dependent liner stiffness was implemented by gradually increasing material characteristics. The relationship between shotcrete age and distance from excavation face is described by Eq. (4.1) and Eq. (4.2) and is visualized in Figure 4.4a.

$$t_i^{TH} = \begin{cases} t_0 = 2 \text{ hr}, & i = 1 \\ \frac{t_{i1}^{TH} + t_{i2}^{TH}}{2} = \frac{2(i-1)RL - 1}{2AR} + t_0^{TH}, & i > 1 \end{cases} \quad (4.1)$$

$$t_i^{INV} = \frac{(i-1)RL}{AR} + t_0, \quad i \geq 1 \quad (4.2)$$

where t_i^{TH} is the shotcrete age at i^{th} round behind the top heading excavation face, which is taken as an averaged value of the first and second lifts t_{i1}^{TH} and t_{i1}^{TH} . The shotcrete liner at the current construction round is assumed to develop a $t_0 = 2 \text{ hr}$ strength. RL is the round length and AR is the advance rate. The round lengths of the side drifts, center top heading, and center invert are 1.0 m or 1.5 m, 1.0 m, and 2.0 m. The advance rates of the side drifts, center top heading, and center invert are 0.04 or 0.06 m/hr, 0.17 m/hr, and 0.125 m/hr respectively.

The evolution of shotcrete compressive strength follows the recommendation from the CEB-FIP model code 2010 (*fib Model Code for Concrete Structures 2010*, 2013):

$$f_c(t) = \beta_{cc}(t) \cdot f_c \quad (4.3)$$

$$\beta_{cc}(t) = \exp \left\{ s \cdot \left[1 - \left(\frac{28}{t} \right)^{0.5} \right] \right\} \quad (4.4)$$

where $f_c(t)$ is the mean compressive strength in MPa at an age t in days, f_c is the mean compressive strength at an age of 28 days, $\beta_{cc}(t)$ is a coefficient of strength development and s is a coefficient that depends on the type of cement ($s=0.25$ for normal and rapid hardening cement). The evolution of material stiffness is described similarly to the evolution of the compressive strength with a relationship using:

$$E_c = E_{c0} \cdot \alpha_E \cdot \left(\frac{f_c}{10} \right)^{1/3} \quad (4.5)$$

$$E_c(t) = \beta_{cc}(t) \cdot E_c \quad (4.6)$$

where E_c is Young's modulus in MPa at the concrete age of 28 days, $E_{c0} = 21.5 \times 10^3$ MPa and $\alpha_E = 1.0$ for quartzite aggregates according to (*fib Model Code for Concrete Structures 2010*, 2013).

Before the commencement of the left drift excavation, a group of 18-meter-long umbrella canopy pipes was installed from the 2nd/Broadway Station shaft to increase the local stability. The umbrella canopy was modeled by pile structural elements (Figure 4.3) and consisted of straight segments with uniform bi-symmetrical cross-section between two nodes. The lining of the storm drain tunnel and the PCTL were modeled using three-node shell elements attached to the ground zones via interface links. The main properties of these structural elements are listed in Table 4.2. Building structures were modeled by applying the corresponding building surcharge at the foundation level. The storm drain tunnel was simulated by a single-step excavation followed by the installation of the lining structure. Since twin bored tunnels were constructed before the SEM excavation, a multi-stage simulation of TBM construction (Mooney et al., 2016) was also performed to consider the redistribution of ground stress and strain. Our

(a) Schematic of the data structure for the 1st lift. The grid shows time points t_i^{TH} for $i=1$ to 31 , with a time step RL . The grid is divided into three sections: 1st lift, 2nd lift, and Top heading face. The Invert face is also indicated.

(b) A 3D visualization of the elastic modulus distribution (GPa) for the 1st lift. The color scale ranges from 0 to 30 GPa, with darker colors indicating higher modulus. The distribution shows a high modulus region (dark) at the top heading face, transitioning to lower modulus regions (lighter) towards the invert face.

Table 4.2 Main properties of structural elements.

	Storm tunnel	Drain	PCTL	Cavern initial support
Elastic modulus (GPa)	21.5		31.7	0.4 to 34 (Time dependent)
Unit weight (kN/m ³)	23.5			
Poisson's ratio	0.2			

The numerical prediction of SEM-induced deformations is greatly influenced by 3D FDM model parameters. However, there is considerable uncertainty in the numerical model parameters. Given the complexity of SEM responses and the reliance of construction design on computational predictions, it is highly valuable to incorporate a back-analysis procedure during SEM construction. Furthermore, multiple SEM construction strategies (e.g., round length, shotcrete thickness, excavation sequence, support toolbox, etc.) are available to handle expected or unexpected ground conditions. Design optimization is essential and usually conducted throughout the SEM design and construction stages. These analyses require a large number (hundreds to thousands) of repeated evaluations for uncertainty quantification or optimization. However, the average cost of a single 3D FDM simulation described in Section 4.4 is around 20 hrs on an Intel i7-9700K CPU @ 3.60GHz and 16 GB RAM desktop computer. This time requirement prohibits using the 3D FDM model for directly conducting probabilistic analyses.

70

surrogate models, PCK method and its parental algorithms, PCE and Kriging are specifically of interest in this study.

4.5.1 Polynomial Chaos Expansion

Polynomial chaos expansion (PCE) approximates the computational model by a basis of orthogonal stochastic polynomials. The uncertain 3D FDM model input parameters (geotechnical and design parameters) can be represented by independent random variables $\mathbf{X} = \{X_1, \dots, X_m\}$, and the 3D FDM model output (ground and structural deformations) can also be represented by a random variable \mathbf{F} , which can be approximated by a sum of orthonormal polynomials (Blatman and Sudret, 2011; Crestaux et al., 2009):

$$\mathbf{F} \approx f_{pce}(\mathbf{X}) = \sum_{\alpha \in A} y_{\alpha} \Psi_{\alpha}(\mathbf{X}) \quad (4.7)$$

where $\Psi_{\alpha}(\mathbf{X})$ are multivariate polynomials orthonormal for the input distributions, $\alpha \in A$ are multi-indices, and y_{α} are the corresponding coefficients.

Several methods are available to calculate the coefficients y_{α} . The most commonly used method is the least-square minimization method. Eq. (4.7) can be approximated by its truncated version:

$$f_{pce}(\mathbf{X}) = \mathbf{y}^T \boldsymbol{\Psi}(\mathbf{X}) \quad (4.8)$$

where $\mathbf{y} = \{y_0, \dots, y_{p-1}\}$ is the coefficient vector and $\boldsymbol{\Psi}(\mathbf{X}) = \{\Psi_0(\mathbf{X}), \dots, \Psi_{p-1}(\mathbf{X})\}$ is the matrix containing all the orthonormal polynomials. Given a set of n samples of the experimental design $\boldsymbol{\chi} = \{\boldsymbol{\chi}_1, \dots, \boldsymbol{\chi}_n\}$ and the corresponding outputs $\mathbf{Y} = \{\mathbf{Y}_1, \dots, \mathbf{Y}_n\}$, the least-square solution calculates the coefficients as:

$$\mathbf{y} = (\boldsymbol{\Psi}(\boldsymbol{\chi})^T \boldsymbol{\Psi}(\boldsymbol{\chi}))^{-1} \boldsymbol{\Psi}(\boldsymbol{\chi})^T \mathbf{Y} \quad (4.9)$$

4.5.2 Kriging

Kriging is a statistical interpolation method that employs a Gaussian process to represent a sophisticated input and output mapping system. This method was first proposed in geostatistics by (Krige, 1951) and (Matheron, 1963). It then has been widely applied in the design and analysis of computer experiments (Sacks et al., 1989). A Kriging model in its most general form can be described as:

$$\mathbf{F} \approx f_{krig}(\mathbf{X}) = \beta^T f(\mathbf{X}) + \sigma^2 Z(\mathbf{X}) \quad (4.10)$$

where the first term $\beta^T f(\mathbf{X})$ describes the trend, which is the mean value of the Gaussian process. The second term contains the variance of the Gaussian process σ^2 and a zero mean, unit variance, stationary Gaussian process $Z(\mathbf{X})$. The local deviation at two input sample points \mathbf{x} and \mathbf{x}' is described in terms of a correlation function $R = R(|\mathbf{x} - \mathbf{x}'|; \boldsymbol{\theta})$ and an unknown hyperparameter $\boldsymbol{\theta}$ to be estimated.

Depending on the type of trend used in Eq. (4.10), three types of Kriging models are commonly used, namely simple, ordinary, and universal Kriging. The correlation function R describes the similarity between observations and new points with closer points sharing similar responses. Various correlation functions can be found in the literature (Santner et al., 2003). The estimation of hyperparameters $\boldsymbol{\theta}$ usually involves an optimization process. Both local and global optimization algorithms are available to determine the optimal correlation parameters (Schöbi et al., 2015).

4.5.3 Polynomial Chaos-Kriging

The Kriging approach efficiently interpolates local variations of computational responses based on the given experimental design points. On the other hand, PCE can approximate the global behavior of the observed model responses by a limited set of orthogonal polynomials. By linking these two methods together, the global behavior of the computational model can be captured by PCE and local approximation can be well represented by Kriging interpolation (Schöbi et al., 2015):

$$\mathbf{F} \approx f_{pck}(\mathbf{X}) = \sum_{\alpha \in A} y_{\alpha} \Psi_{\alpha}(\mathbf{X}) + \sigma^2 Z(\mathbf{X}) \quad (4.11)$$

where the parameters have the same definition in **Eqs. 7** and **10**. Hence, a more comprehensive surrogate model is achieved, and many recent research studies have demonstrated its improved accuracy (Schöbi et al., 2017). Also, the general lack of extrapolation using Kriging only is compensated by the PCE process.

The accuracy of the PCK model can be assessed by two error functions, leave-one-out error and validation error (Schöbi et al., 2015). Besides, the standard regression accuracy measure—Normalized Root Mean Squared Error (NRMSE) (Khaledi et al., 2014) is also adopted here. Those accuracy metrics are defined by:

$$\epsilon_{LoO} = \frac{\sum_{i=1}^n [f(\mathbf{X}_i) - f_{pck}^{D/i}(\mathbf{X}_i)]^2}{\sum_{i=1}^n [f(\mathbf{X}_i) - \boldsymbol{\mu}_Y]^2} \quad (4.12)$$

$$\epsilon_{val} = \frac{n_{val} - 1}{n_{val}} \left[\frac{\sum_{i=1}^{n_{val}} \left(f(\mathbf{X}_i^{val}) - f_{pck}(\mathbf{X}_i^{val}) \right)^2}{\sum_{i=1}^{n_{val}} \left(f(\mathbf{X}_i^{val}) - \boldsymbol{\mu}_{Y^{val}} \right)^2} \right] \quad (4.13)$$

$$NRMSE = \sqrt{\frac{\sum_{i=1}^n \left(f(\mathbf{X}_i) - f_{pck}(\mathbf{X}_i) \right)^2}{\sum_{i=1}^n \left(f(\mathbf{X}_i) \right)^2}} \quad (4.14)$$

where n is the number of experiment samples, $f(\mathbf{X}_i)$ is the actual response at the point \mathbf{X}_i , $f_{pck}^{D/i}(\mathbf{X}_i)$ denotes the response predicted by the PCK model constructed with all the sample points except \mathbf{X}_i . $\boldsymbol{\mu}_Y$ is the sample mean of the experimental design response. The validation error is calculated on an independent validation dataset $[\mathbf{X}^{val}, \mathbf{Y}^{val} = f(\mathbf{X}^{val})]$ with n_{val} samples. $\boldsymbol{\mu}_{Y^{val}}$ is the sample mean of the experimental response for the validation set.

Both PCE and Kriging require optimization to estimate the coefficients or hyperparameters. Given the same dataset obtained by designed computational simulations, there are several ways to construct a PCK model. In this study, two PCK approaches, namely the sequential PCK (PCK-SEQ) and the optimal PCK (PCK-OPT) (Schobi et al., 2015) are examined and compared. Figure 4.5 illustrates the procedure of constructing a PCK surrogate model using the two approaches. A series of numerical simulations first generates a dataset containing inputs and outputs pairs. The least-angle regression (LAR) algorithm for the optimal PCE model determines a sparse set of orthonormal multivariate polynomials. In PCK-SEQ approach, the PCE model is used directly as the trend for the Kriging model. The PCK-SEQ model is then obtained by calibrating Kriging hyperparameters. In PCK-OPT approach, the sparse set of P polynomials is ranked in decreasing order. The next step is to build P universal Kriging models by adding each polynomial one by one to the trend part. The coefficients of the trend, Kriging parameters, and hyperparameters are calibrated for each model. The PCK-OPT model is then selected as the one with minimal ϵ_{LOO} value.

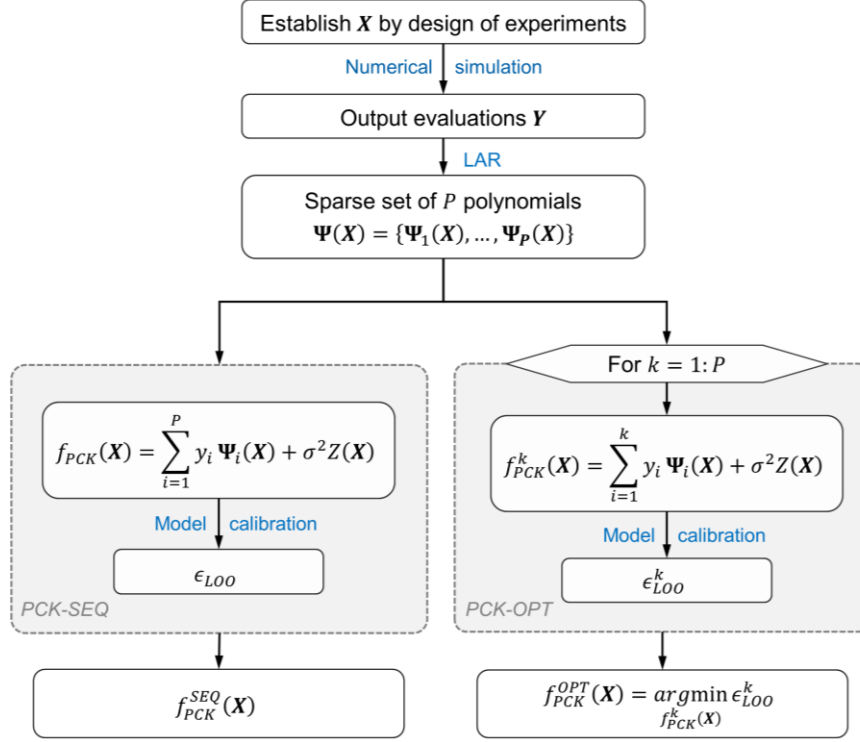


Figure 4.5 Flow chart for constructing PCK model.

4.5.4 SEM surrogate modeling

The main steps of developing a surrogate model for SEM-induced ground and structural deformations are summarized as follows:

- (1) A 3D numerical model is constructed to simulate SEM construction and evaluate the response of interest (ground and structural deformations in this case). Appropriate geological and constitutive models are assigned based on site information. The step-by-step excavation and initial support process are correctly simulated.
- (2) Governing model parameters are characterized as candidates of surrogate model inputs (e.g., geotechnical parameters, construction variables, etc.). The statistical information of considered parameters is estimated from field/lab tests and past experiences. A sensitivity analysis is performed to identify the most influential parameters \mathbf{X} as the surrogate model inputs. The deformation responses \mathbf{F} obtained from the 3D numerical simulation are defined as the surrogate model outputs. For a considered monitoring section, the output matrix is formed as $\mathbf{F} = \{\mathbf{f}_1, \mathbf{f}_2, \dots, \mathbf{f}_n\}_{s \times n}$, where s is the number of excavation rounds and n is the number of different output types.

- (3) To generate a dataset for surrogate model training, 3D numerical simulations must be carried out on selected samples (combinations) of input parameters. The practice of selecting input candidates is called sampling. Given the sample size, a design of experiments (DoE) is performed using the Sobol sequence sampling scheme to explore evenly across the parameter space.
- (4) Based on the sample pool generated in step (3), 3D numerical simulation of the entire SEM construction is called at each sample location \mathbf{X}_i to obtain corresponding model output \mathbf{F}_i . All pairs of the selected samples and their corresponding output are assembled as the dataset for surrogate model training.
- (5) The surrogate model is trained and validated using the dataset generated from the previous step. Four training algorithms, namely PCE, Kriging, PCK-SEQ, and PCK-OPT are utilized and compared in this study.

4.6 Sensitivity analysis to determine surrogate model input parameters

Among numerous FDM model input parameters, the parameters most influential on the model responses are of our most interest. Also, the number of FDM simulations needed for surrogate model training highly depends on the dimension(number) of surrogate input parameters. As the number of surrogate inputs increases, the number of FDM simulations needed might increase exponentially (Berveiller et al., 2006; Pan and Dias, 2018). Filtering out non-influential parameters is necessary for surrogate modeling efficiency. Herein a sensitivity analysis was conducted to determine the 3D FDM model parameters most influential on the SEM-induced deformation responses as the surrogate inputs.

Six 3D FDM model outputs were considered here to investigate both key ground and structural deformation responses. The outputs are the surface settlement at the left and right sides (S_L and S_R), subsurface settlement (MP) (7.6 m above cavern crown), the convergence of the left drift liner (CM_{2M3})(3 m above springline), center crown convergence (C_{CTH}), and center invert convergence (CC_{INV}) as shown in Figure 4.6. These outputs are deemed critical to SEM construction and well capture the deformation behavior at multiple levels (Zheng et al., 2021b, 2021a). In addition, each output is measured during SEM construction. The S_L and S_R are of great concern as multiple sensitive buildings are located around the cavern area. MP captures mid-level subsurface deformation and is a critical indicator of the existing storm drain deformation. In-tunnel convergences (CM_{2M3} , C_{CTH} , and CC_{INV}) evaluated the initial support performance and provide early warnings of possible local failure.

The commonly-used one-at-a-time method (Hamby, 1994) is adopted to estimate the sensitivity of the six FDM model outputs to 17 geotechnical input parameters, where the contribution of each parameter is examined independently in a local domain. The variance of the 3D FDM model responses depends not only on the mechanical nature of each parameter but also on the parameter variability. Under the same magnitude of mechanical influence, parameters with greater variability influence the model responses more than those with lower uncertainty. To consider both mechanical and variability features of 3D FDM parameters, a point estimate

method-based sensitivity analysis (Franco et al., 2019) was adopted. For each output f , the sensitivity index (SI_i) of the i^{th} parameter x_i to the output at the j^{th} excavation round f^j is formulated as:

$$SI_i^j = \frac{|f_{f_{dm}}^j(x_i^-) - f_{f_{dm}}^j(x_i^+)|}{\sum_{i=1}^n |f_{f_{dm}}^j(x_i^-) - f_{f_{dm}}^j(x_i^+)|} \quad (4.15)$$

where $f_{f_{dm}}^j(x_i^\pm)$ denotes the 3D FDM output at the j^{th} excavation round obtained by increasing or decreasing x_i by one standard deviation and fixing all the other variables. Each SI_i^j value is normalized to a 0-1 scale $SI_{i \text{ norm}}^j = \frac{SI_i^j}{\sum_{i=1}^n SI_i^j}$. The average sensitivity index for each model

output is calculated as $\overline{SI}_i = \frac{\sum_{j=1}^s SI_{i \text{ norm}}^j}{s}$, where s is the number of excavation rounds (210 for S_L , S_R and MP ; 195 for C_{M2M3} ; 100 for C_{CTH} ; 35 for C_{CINV}). In this manner, the sensitivity of deformations at every stage is taken into account and \overline{SI}_i reflects a cumulative effect. The influence of seven Tf1 and Tf2 geotechnical parameters and groundwater table elevation were investigated in this study. The statistical information of these model input parameters is summarized in Table 4.3, determined based on the same sources listed in Table 4.1. The detailed statistical interpretation of these parameters can be found in (Zheng, 2022).

Figure 4.7 presents a stacked bar plot of the sensitivity indices \overline{SI}_i of each output for all input variables. In general, Tf2 parameters are found to be more influential than Tf1 parameters in most cases as all stages of excavation are initiated within the Tf2 layer. For the surface and subsurface settlement, the cohesion of the Tf2 layer (Tf2- c') shows the most significant influence, indicating that the plastic zone initiated around the opening contributes to substantial ground deformation. The greater uncertainty of the Tf2- c' in comparison to all other input parameters (Table 4.3) also leads to a higher sensitivity in ground deformation. The magnitude of the left liner convergence 3 m above sprineline C_{M2M3} is mainly influenced by Tf2- c' and Tf2- E_{50}^{ref} values. As the subsequent excavations induce a series of unloading-reloading paths of Tf2 adjacent to the left liner, the influence of Tf2- E_{ur}^{ref} also increases for C_{M2M3} . Tf1- E_{50}^{ref} has the largest influence on C_{CTH} . This observation can be explained by the proximity of the Tf1 layer to the cavern crown. When excavating CTH, the deformation caused by the primary loading of the Tf1 above the center crown contributes significantly to C_{CTH} . S_L , S_R , and MP are less influenced by Tf1 parameters than C_{CTH} . This result is mainly because S_L , S_R , and MP contain the deformation throughout the entire excavation stages initiated within the Tf2. However, by the time C_{CTH} initiates, the excavation of the two side drifts is completed and the side initial supports are installed. The vertical movements at the center crown are therefore more influenced by the Tf1 layer in close proximity. The stiffness of Tf1 at higher strain (Tf1- E_{50}^{ref}) shows more influence on C_{CTH} than at small strain (Tf1- E_0^{ref}). The parameters Tf2- E_0^{ref} and Tf2- E_{50}^{ref} greatly influence the C_{CINV} response.

As all stiffness parameters are stress-dependent, the ground material near the cavern invert experiences a lower strain level than the upper portion ground above the cavern. The $Tf2-E_0^{ref}$ controls the degree of strain development near the cavern invert and, therefore, the magnitude of C_{CINV} as a result of CINV excavation. The influence of $Tf2-E_{ur}^{ref}$ also increases as a higher degree of the unloading process is experienced at the cavern invert. Herein, the five most influential parameters, namely $Tf2-c'$, $Tf2-E_0^{ref}$, $Tf2-E_{50}^{ref}$, GWT , $Tf1-E_{50}^{ref}$, were selected as the surrogate model inputs.

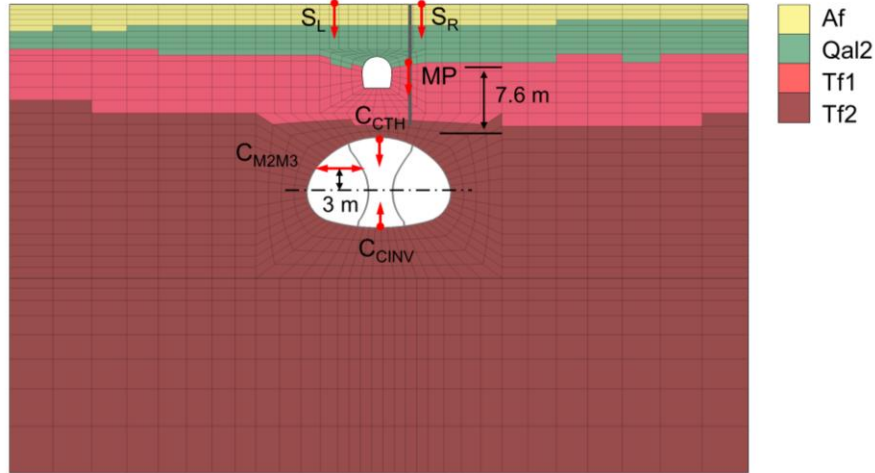


Figure 4.6 3D FDM model outputs of interest (monitoring section at Sta. 0+15).

Table 4.3 Probabilistic information of uncertain parameters.

Parameter	Mean (μ)	COV (%)
$Tf1-E_{50}^{ref}$ [MPa]	48	30
$Tf1-E_{ur}^{ref}$ [MPa]	150	50
$Tf1-c'$ [kPa]	75	40
$Tf1-\phi'$ [$^{\circ}$]	25	40
$Tf1-E_0^{ref}$ [MPa]	330	30
$Tf1-K_0^{NC}$	0.53	30
$Tf1-\gamma_{0.7}$	$2.0 \cdot 10^{-4}$	30
$Tf1-m$	0.7	20
$Tf2-E_{50}^{ref}$ [MPa]	55	50
$Tf2-E_{ur}^{ref}$ [MPa]	183	50
$Tf2-c'$ [kPa]	170	70

Tf2- ϕ' [°]	26	40
Tf2- K_0^{NC}	0.51	30
Tf2- E_0^{ref} [MPa]	480	30
Tf2- $\gamma_{0.7}$	$2.0 \cdot 10^{-4}$	30
Tf2- m	0.9	40
GWT [m]	6.8	20

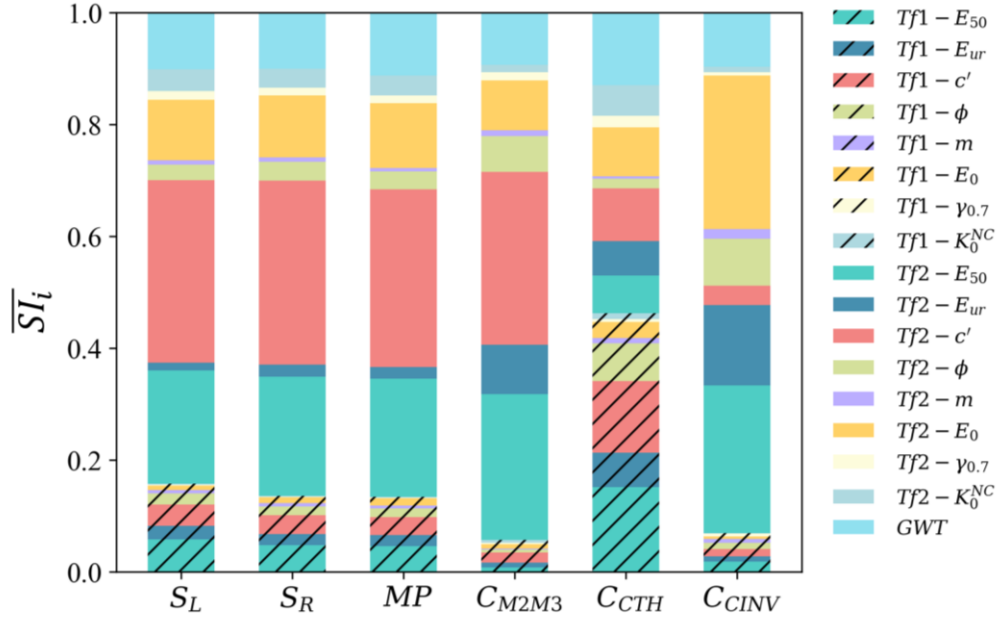


Figure 4.7 Sensitivity indices of the six model outputs w.r.t. the model input parameters.

4.7 Construction and validation of the surrogate model

Following the procedure described in Section 4.5.4, a dataset was generated from the 3D FDM simulations on selected samples (combinations) of input variables. Per the sensitivity analysis presented in the previous section, the five most influential geotechnical parameters—Tf2- c' , Tf2- E_0^{ref} , Tf2- E_{50}^{ref} , GWT, Tf1- E_{50}^{ref} — were identified and are of interest in this study. Therefore, the surrogate model inputs contain those five parameters. The statistical information of each parameter is kept the same as listed in Table 4.3 and lognormal distribution is assumed

for each parameter. Shotcrete thickness of the initial lining was also considered as an input variable and was assumed to follow a uniform distribution $t \sim U(200 \text{ mm}, 500 \text{ mm})$.

A sampling strategy is adopted to intelligently select locations that the 3D FDM simulation calls on because it is time-intensive to exhaustively explore every combination of input parameters. A design of experiments procedure was performed using the Sobol sequence sampling method (Joe and Kuo, 2003). The optimal number of experiments is problem-dependent and is usually restricted by the maximum number of simulations that can be afforded (Mack et al., 2007). This study investigates a maximum number of 500 experiments based on our affordable computational capacity. The configuration and pair-wise locations of 500 samples are visualized in Figure 4.8. The Sobol sampling ensures even coverage of samples across the statistical reach of each parameter. As shown in Figure 4.8, the samples shown in the upper triangle plots exhibit broad coverage over the range of each histogram displayed in the diagonal plots. For each input parameter set (sample point), the 3D FDM simulation of the entire SEM construction (from the start of LTH to the end of CINV) was performed to obtain the corresponding model output matrix \mathbf{F} , including the six outputs (Figure 4.6) at all excavation rounds. The assumption made is that the geometry and geotechnical parameters are spatially deterministic. This is reasonable considering the small scale of the cavern and relatively homogeneous ground behavior identified by site investigation and field observations.

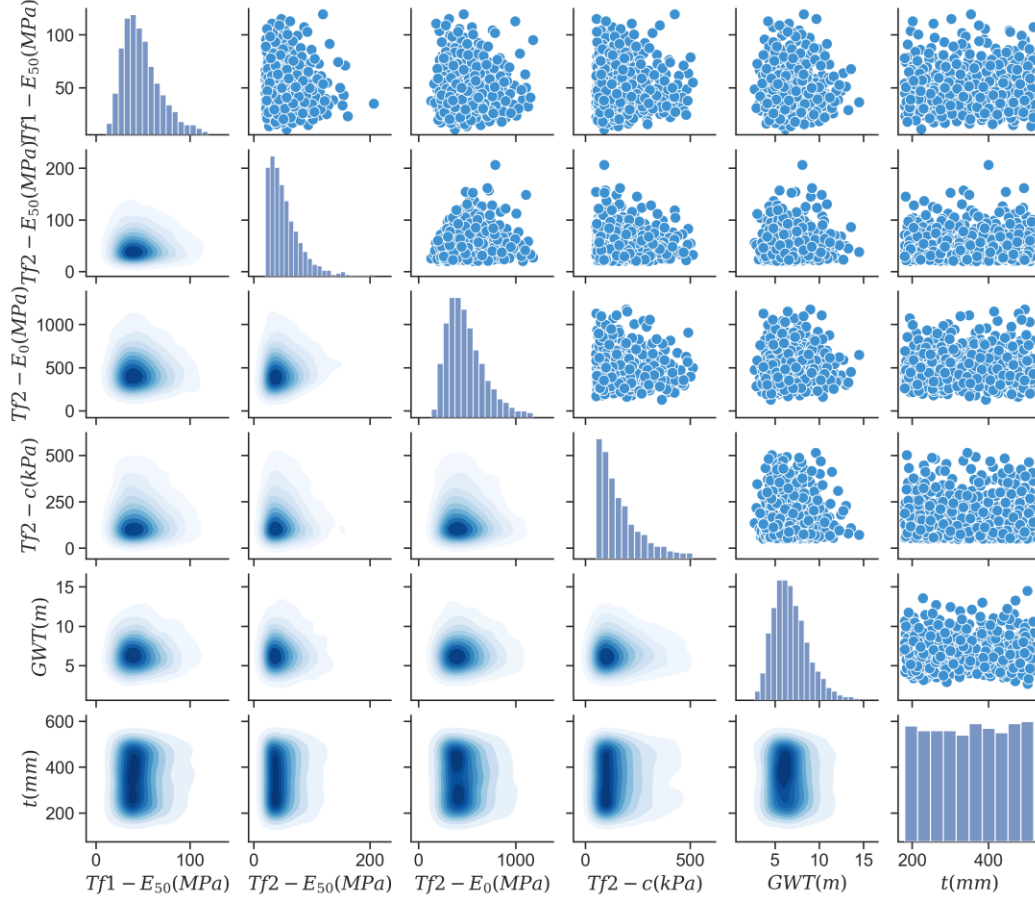


Figure 4.8 Pair plots of 500 samples DoE (The diagonal plots show univariate histograms of the data in each column; the upper diagonal plots show detailed bivariate sample scatters; the lower diagonal plots show the contours of the bivariate distribution density).

All pairs of inputs and outputs were assembled for surrogate model training. The dataset was split into training and testing subsets with 80% and 20% ratios, respectively, to avoid surrogate model overfitting. Four methods described in Sections 4.5.1 to 4.5.3 were utilized to train the surrogate model. For PCE and PCK-based methods, the family of multivariate Hermite polynomial was taken as the orthogonal basis. The optimal maximum degree of polynomials p was determined through a parametric analysis and is set to ten. A standard truncation scheme was used here to compute a finite number P of polynomial terms as $P = \frac{(M+p)!}{M!p!}$, where M is the number of variables. The LAR algorithm was applied here to obtain sparse polynomials that are

most relevant. The commonly-used ellipsoidal Matern 5-2 correlation function (Williams and Rasmussen, 2006) was utilized in all ordinary Kriging models. The covariance matrix adaptation-evolution strategy (Hansen and Ostermeier, 2001) was utilized as the optimization method for estimating the hyperparameters in the Kriging models.

It is necessary to evaluate the minimal sample size (number of 3D FDM runs) to generate a reliable surrogate model to minimize computational costs. The accuracy of the constructed surrogate models is evaluated against different sample sizes (total number of training and testing samples) from 50 to 500. The accuracy is quantified by the NRMSE Eq. (4.14) and the validation error ϵ_{val} Eq. (4.13) on the test dataset. NRMSE normalizes the root mean square error to better compare datasets with different scales. ϵ_{val} is the expectation of squared output residuals normalized by the output variance and is commonly used in the field of surrogate modeling (Schobi et al., 2015; Schöbi et al., 2017; Totis and Sortino, 2020). ϵ_{val} represents the ratio between the variation not explained by the regression versus the overall variation in experimental data. Higher ϵ_{val} indicates greater variation between surrogate model and 3D FDM results than the variation exhibited in the data itself and consequently lower predictability. Figure 4.9 shows the influence of sample size on the surrogate model-average accuracy (global NRMSE and ϵ_{val} calculated based on all six outputs). The best model-average NRMSE and ϵ_{val} values for PCE, Kriging and the two PCK models are around 13%, 7%, and 3%, respectively. Both NRMSE and ϵ_{val} decrease as the sample size increases. Except for the PCE surrogate models, the errors of all other surrogates turn to converge around 200 samples. Further increase of samples shows little improvement of the surrogate performance. Therefore, 200 samples are deemed sufficient for this numerical case when Kriging, PCK-SEQ, or PCK-OPT methods are employed. Over the whole range of sample sizes, the Kriging, PCK-SEQ, and PCK-OPT perform significantly better

than the PCE. For small sample sizes (<100), the Kriging, PCK-SEQ, and PCK-OPT show similar performance with PCK-SEQ performing slightly better. When the number of samples is larger than 200, the two PCK surrogate models exhibit better performance than the others. PCK-OPT shows an advantage over PCK-SEQ on small sample sizes. While with enough samples (≥ 200), their performances are almost the same.

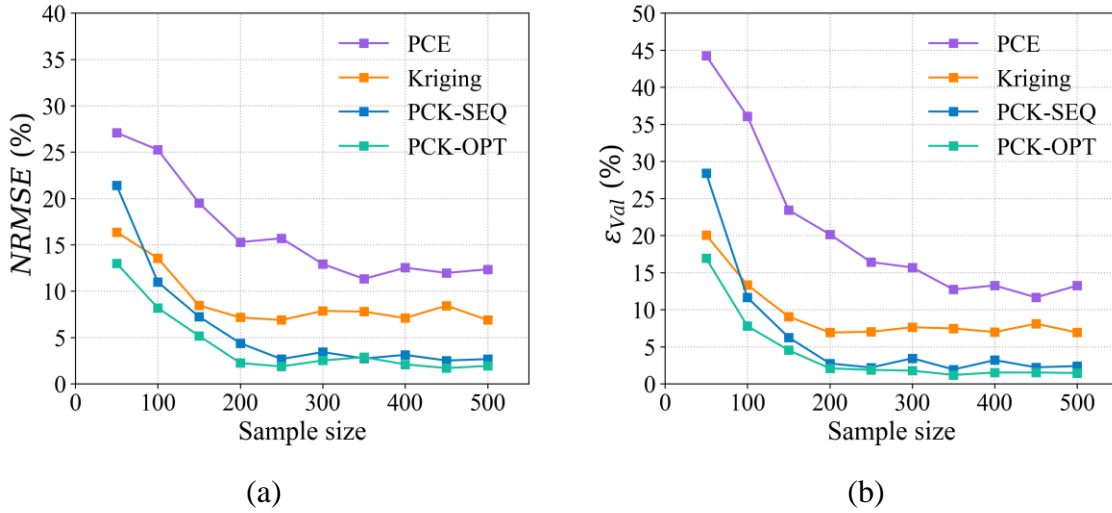


Figure 4.9 Influence of sample size (total number of samples used for 80% training and 20% testing) on the surrogate model testing performance: (a) NRMSE; (b) validation error.

Optimization-based back analysis usually requires hundreds to thousands of surrogate model evaluations (Zhao, 2018). Other applications, such as reliability analysis and reliability-based design optimization, require millions of predictions for a surrogate model to calculate small-magnitude probability of failure through Monte Carlo simulations (Lü et al., 2017a; Pan et al., 2021; Wang and Fang, 2018). Therefore, the prediction time of a surrogate model is a critical aspect contributing to the overall surrogate efficiency. Figure 4.10 shows the prediction time to compute a single SEM output matrix \mathbf{F} for each surrogate model. However, PCE exhibits the lowest prediction time around 0.05 s with the lowest accuracy. The two PCK methods need less than 1 s to compute the deformation responses. Although the Kriging model shows satisfactory

accuracy, the prediction time of the Kriging model is 6-10 times longer than that of the PCK ones. When applying the surrogate model to simulation intensive analysis, the cumulative time cost increases considerably and might become unaffordable. Therefore, two PCK models are preferred in this case.

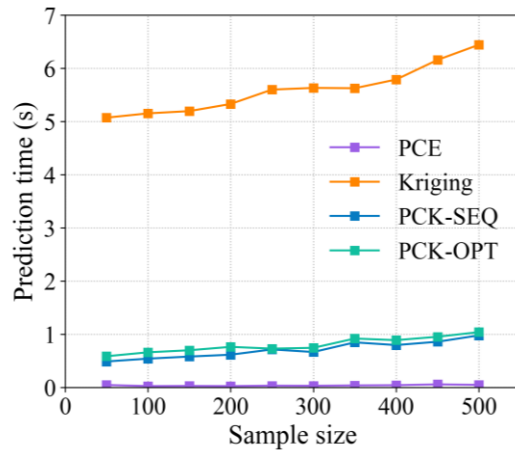
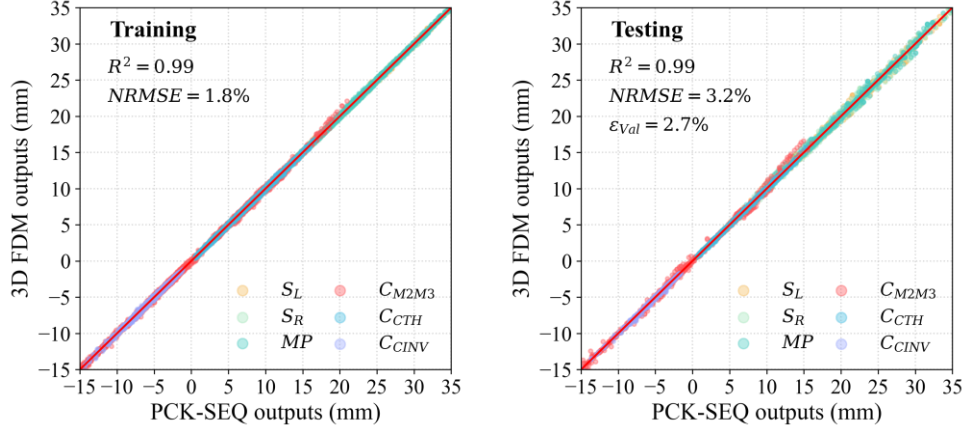
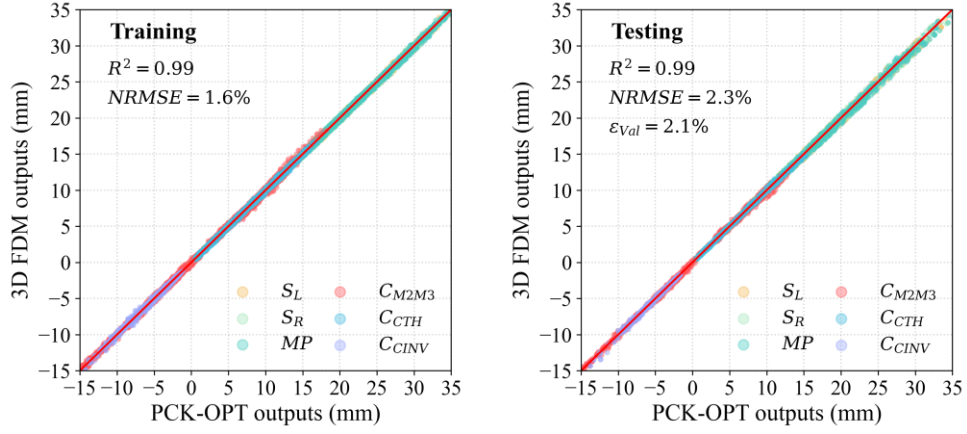


Figure 4.10 Prediction time costs of the surrogate models (time to compute a single prediction).

Figure 4.11 compares a comparison of training and testing performance for the PCK-SEQ and PCK-OPT models constructed using a 500-sample dataset. The dataset was randomly divided into training and testing subsets. The numbers of training and testing samples are 400 and 100, respectively. The detailed training and testing accuracies in terms of each model output (individual-output NMRSE and ϵ_{val} calculated based on each output) are summarized in Table 4.4. As shown in Figure 4.11, PCK-SEQ and PCK-OPT show model-average NRMSEs below 3% for the testing sets. Compared to the training datasets, the accuracies of the testing sets degrades by a factor of two. Still, the test model accuracies remain low with less than 5% for both model-average and individual-output NRMSEs. This result indicates a good generalization of the PCK models. For each model output, the NRMSE values for the PCK training and testing dataset are below 5% and the ϵ_{val} is below 3% as listed in Table 4.4.



(a) PCK-SEQ



(b) PCK-OPT

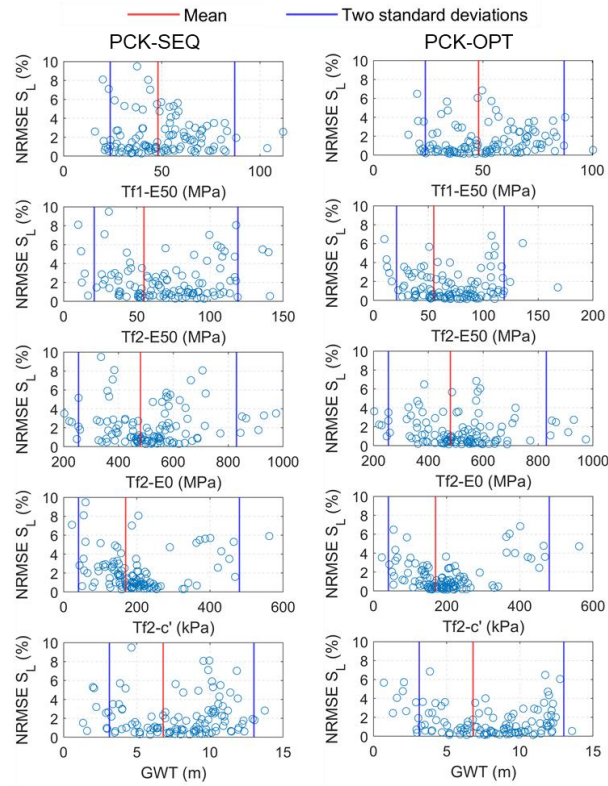
Figure 4.11 Training and testing performance comparison for the surrogate models (200-sample dataset).

Table 4.4 Surrogate model accuracy metrics for each model output (500-sample dataset with cross-validation performed).

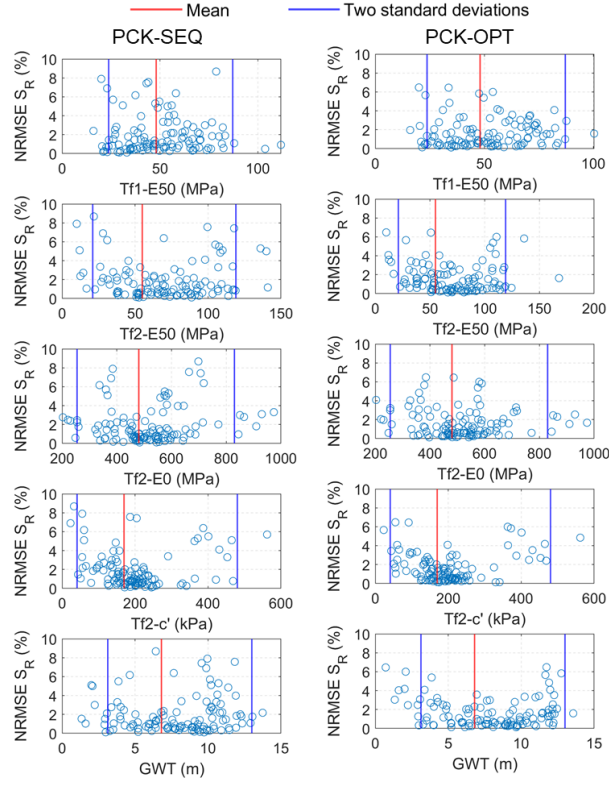
Surrogate Data model set		SL		SR		MP		CM2M3		CTH		CINV	
		NRMSE (%)	$\epsilon_{val}(\%)$	NRMSE (%)	$\epsilon_{val}(\%)$	NRMSE (%)	$\epsilon_{val}(\%)$	NRMSE (%)	$\epsilon_{val}(\%)$	NRMSE (%)	$\epsilon_{val}(\%)$	NRMSE (%)	$\epsilon_{val}(\%)$
PCK-SEQ	Train	1.7	-	1.5	-	1.5	-	3.7	-	2.3	-	2.4	-
	Test	2.6	1.5	2.5	1.5	2.3	1.3	4.7	2.7	3.1	2.4	3.7	2.5
PCK-OPT	Train	1.1	-	1.0	-	0.9	-	3.2	-	2.5	-	2.9	-
	Test	2.2	1.2	1.9	1.1	1.9	1.1	3.8	1.8	2.7	1.4	3.1	1.8

The test NRMSE values of the surrogate models constructed using the 500-sample dataset (trained on 400 and tested with 100) are plotted against each input for each model output,

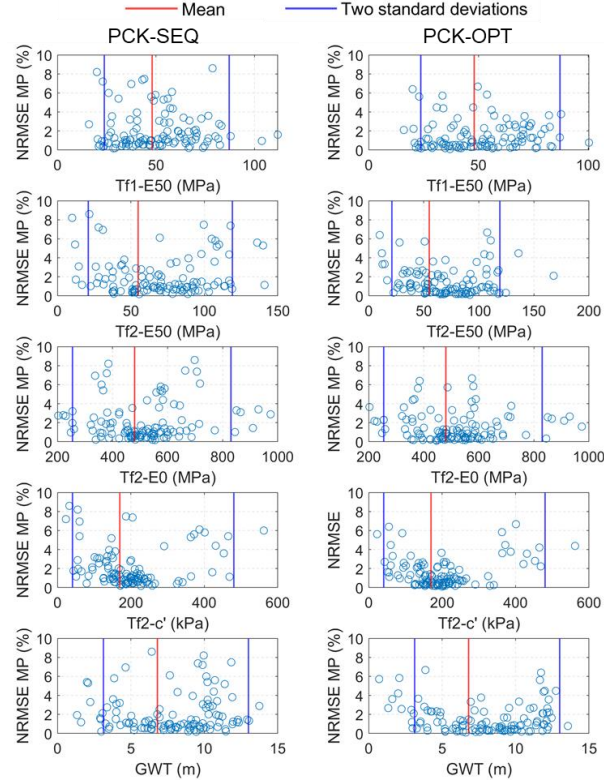
as shown in Figure 4.12, to investigate the accuracy of the surrogate models as a function of the input parameter space. Each NRMSE point captures the output deformations throughout the entire SEM construction. The number of output values is the same as the number of excavation rounds (210 for S_L , S_R and MP ; 195 for C_{M2M3} ; 100 for C_{CTH} ; 35 for C_{CINV}). The results show that no errors were greater than 10% NRMSE and 90% of the errors were less than 5% NRMSE for all the six model outputs. For those input parameters that are more influential with respect to the corresponding model output, relatively high NRMSE is observed when the input parameters are located close to the distribution margins. For instance, for output S_L , S_R , and MP , most high NRMSE values are concentrated around the margins of $Tf2-E_{50}^{ref}$ and $Tf2-c'$. This can be explained by fewer training samples deployed close to the parameter margin. Also, The more influential the parameter is, the more the surrogate model can learn from varying training sample locations and vice versa. When comparing different model outputs, the convergence outputs (C_{M2M3} , C_{CTH} , and C_{CINV}) exhibit higher NRMSE values than the ground settlement outputs (S_L , S_R , and MP) in general. One possible reason is that the magnitudes of the ground settlement variations are generally 2-5 times higher than those of the convergence outputs. Consequently, it is more difficult for the surrogate model to capture the changing pattern of the convergences. Also, the tunnel convergence responses depend more on the ground-structural interaction controlled by both ground and structural parameters. The influences of shotcrete parameters such as compressive and tensile strengths that were not considered in the surrogate model might contribute to the less accurate performance in terms of the convergence outputs.



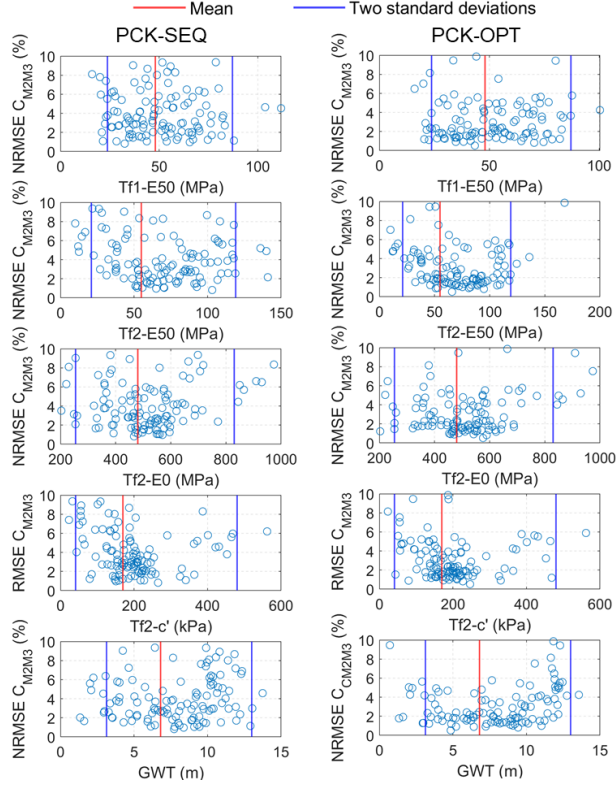
(a) S_L



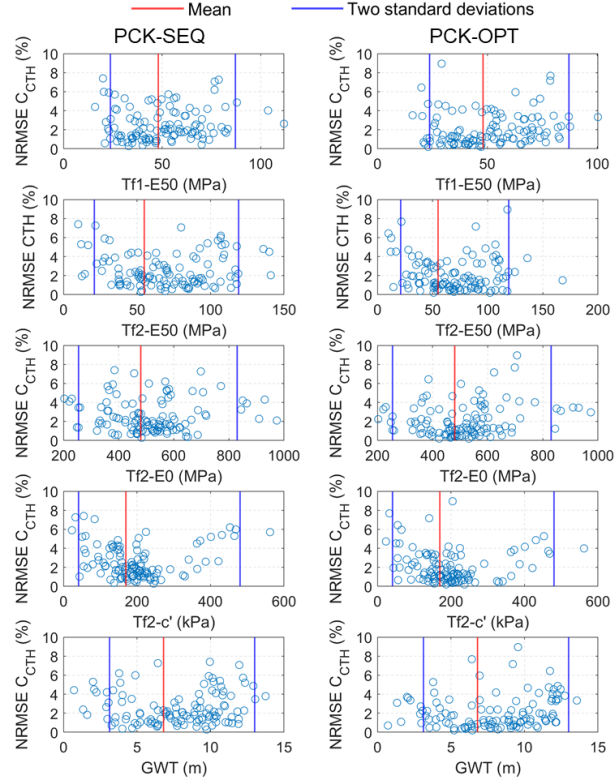
(b) S_R



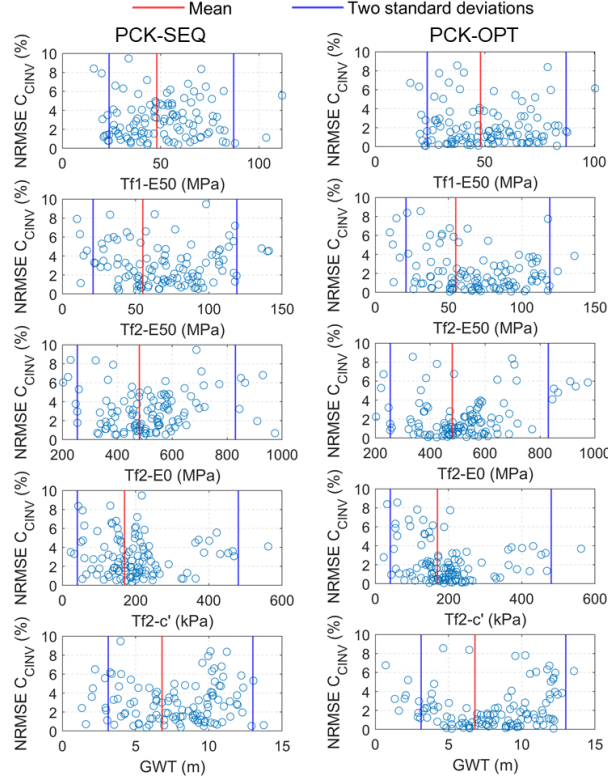
(c) MP



(d) C_{M2M3}



(e) C_{CTH}



(f) C_{CINV}

Figure 4.12 NRMSE distributions for test data throughout the surrogate input space with respect to the output: (a) S_L , (b) S_R , (c) MP , (d) C_{M2M3} , (e) C_{CTH} , and (f) C_{CINV} (tested on an independent 100-sample dataset)

4.8 Conclusions and discussion

This paper examined the capability and performance of a newly developed algorithm called Polynomial-Chaos-Kriging (PCK) in approximating 3D numerical simulations of SEM tunneling. Four surrogate modeling approaches for the prediction of SEM-induced ground and structural deformations were examined. A sensitivity analysis was conducted to determine the most influential FDM model parameters as the surrogate model inputs. A design of experiments was performed to intelligently select a limited number of input samples by employing the Sobol sampling strategy. A comparative study was performed for two PCK algorithms, PCE and Kriging methods. The main findings are summarized below.

- PCK-SEQ and PCK-OPT were demonstrated to be the best surrogate models to capture the complex 3D FDM behavior of SEM construction. The best model-average NRMSE and ϵ_{val} of the two PCK models are around 3%. The model performance converges when more than 200 samples are utilized for Kriging, PCK-SEQ, and PCK-OPT models.

- The comparison of training and testing performance of the PCK models indicates a good generalization performance. The model-average NRMSE accuracy degrades by half but the test model accuracies remain low (less than 5% for both model-average and individual-output NRMSEs).
- By investigating the surrogate accuracy as a function of the input parameter space, it is found that no errors were greater than 10% NRMSE and that 90% of the errors were less than 5% NRMSE for the six model outputs for the PCK models. Higher NRMSEs are observed in the convergence outputs than in the ground settlement outputs. This is because the variations of the ground settlement magnitudes are generally 2-5 times higher than those of the convergence magnitudes. Therefore, the changing pattern of the convergence outputs is more difficult for the surrogate model to learn. The lack of sufficient shotcrete parameters might also contribute to the lower accuracy of convergences since the ground-structural interaction controls the tunnel convergence behavior.
- The prediction time to compute a single SEM output matrix when using the PCK models is less than 1 s, compared to around 20 hrs when using the 3D FDM simulation. Although Kriging shows competitive accuracy compared to PCK-SEQ and PCK-OPT, the Kriging model's prediction time is 6-10 times slower than that of the PCK models. The cumulative time cost considerably increases when applying the Kriging model to simulation intensive analysis (e.g., probabilistic back-analysis, reliability analysis, etc.).

Surrogate modeling is a special case of supervised machine learning, i.e., training a predictive model based on the labeled training dataset generated from computational simulations. No single learning method that can outperform other methods on all datasets. PCK method systematically combines PCE and Kriging methods with PCE capturing the global behavior of the 3D FDM simulation and Kriging interpolating the local approximation. The combination of the characteristics and the advantages of both methods seems to explain the good performance of PCK in our case. The performance of PCK method on different SEM cases needs further examination. However, this study at least shows that PCK method and the proposed procedure are worth trying to use for similar datasets modeling SEM 3D FDM responses in the first place.

The distributions of the input parameters are defined based on the best knowledge of the project and experience. Additional FDM simulations are needed if the actual geotechnical parameters are updated beyond the training range during the back analysis. Surrogate models should not be trusted outside the input parameter range used during training.

Instead of using one-shot sampling in the design of experiments, adaptive sampling methods (Fuhg et al., 2021) could be integrated into the current surrogate framework to reduce further the 3D FDM simulations needed to construct an accurate surrogate model. In addition, an adaptive training process could be developed to actively add training samples in regions where the surrogate model can learn the most and in regions identified by the updated knowledge of ground conditions.

The proposed procedure does not explicitly consider the spatial variability of ground parameters, which is of our further research interest. The general desire to computationally

model with spatial variability begets the use of surrogate modeling even more due to more input variables involved and the consequent time intensity. However, the high input dimension of the surrogate model might bring new issues.

4.9 Acknowledgments

Funding from the Center of Underground at the Colorado School of Mines and by the University Transportation Center for Underground Transportation Infrastructure (UTC-UTI) at the Colorado School of Mines under Grant No. 69A3551747118 from the U.S. Department of Transportation (DOT) is gratefully acknowledged. Partial funding for this study was also provided by Skanska and Traylor Bros. We would like to offer our special thanks to Christophe Bragard and Carlos Herranz Calvo for providing the data and technical insights for this study. We would also like to express our gratitude to Traylor Bros., Skanska, Mott Macdonald, Geocomp, Sixense Soldata, and LA Metro for sharing the project data and providing the opportunity to join in this project.

CHAPTER 5

UPDATING MODEL PARAMETERS AND PREDICTIONS IN SEM TUNNELING USING A SURROGATE-BASED BAYESIAN APPROACH

*Reproduced from a draft to be submitted to Géotechnique and is presented here with
minor variations.*

5.1 Abstract

This paper presents a surrogate-based Bayesian approach for updating the ground parameters within an application of the observational method in sequential excavation method (SEM) construction. A 3D finite-difference model is used in the forward analysis to simulate SEM construction explicitly considering 3D multi-face excavation effects and ground-structure interaction. The Polynomial-Chaos-Kriging (PCK) method was employed to provide a surrogate for the 3D finite-difference model to alleviate the cost of probabilistic analysis. The uncertain geotechnical parameters are updated during SEM construction through a progressive Bayesian updating procedure. Time-series observations of multiple types of measurements are used to form the likelihood function. The posterior distributions of the uncertain parameters are derived from the affine invariant ensemble sampling (AIES) algorithm. The proposed framework is illustrated through application to data from the Regional Connector Transit Corridor (RCTC) crossover cavern project constructed in downtown Los Angeles. The uncertainties of the geotechnical parameters were substantially reduced. The posterior estimations indicate higher elastic modulus and cohesion of the Fernando formation than what was assumed before the construction. The updated predictions of the ground surface, subsurface, and structural deformations showed improvement in agreement with the field measurements through the continuous updating process.

5.2 Introduction

The sequential excavation method (SEM), also known as the New Austrian Tunneling Method (NATM) or sprayed concrete lining (SCL) method, was developed from practical experience using sprayed concrete (shotcrete) as temporary tunnel support material. Due to limited knowledge of ground conditions before construction, the SEM usually adopts a flexible and progressive design that continues into the construction phase as contractual guidelines allow. Engineers rely on the observational method (Peck, 1969) by utilizing the instrumentation data collected during construction to update the knowledge and adapt the SEM design as appropriate, aiming to achieve an overall economy without compromising safety. Physics-based computational modeling that can predict SEM-induced responses is an essential tool (Ağbay and Topal, 2020; Janin et al., 2015; Sharifzadeh et al., 2013; Svoboda et al., 2010; Yoo, 2009).

However, during SEM construction, updating a computational model that can reflect the complex SEM construction process and ground-structure interactions is too time-intensive and thus rarely applied in current practice. Developing an efficient and accurate tool to quantify uncertainties and update model predictions during SEM construction is imperative.

Keys to successful SEM application in urban areas are ground deformation control and the early installation of structural support, which requires a comprehensive understanding of small strain ground behavior. Usually, advanced constitutive models are needed to obtain more realistic deformation and stress characteristics. However, significant uncertainty and difficulty usually exist to determine advanced constitutive model parameters (Phoon and Kulhawy, 1999) (Tang et al., 1999). Given the complexity of ground response and the reliance of computational models on numerous constitutive parameters, it is valuable to incorporate a back-analysis procedure during SEM construction. Deterministic and probabilistic back analysis methodologies are available to identify or update constitutive parameters.

In deterministic back analysis, with observations available, fixed values are identified for uncertain constitutive parameters through optimization. However, fixed values back-analyzed from a deterministic approach can capture neither the uncertainty in the parameters nor the model predictions (Qi and Zhou, 2017). A single set of parameters will yield a single prediction, based on which of the decisions made to modify SEM construction are risk-taking. Also, the difficulty of non-uniqueness solution cannot be solved by deterministic back-analysis approaches but can be overcome by probabilistic back-analysis methods (Agostinetti and Malinverno, 2010; Honjo et al., 1994; Malinverno, 2002). These limitations notwithstanding, the deterministic back-analysis approaches are still prevailing in most current underground practices.

Probabilistic approaches such as Bayesian updating combine uncertainties from objective and subjective sources, and calibrate the model with new observations through Bayesian inference (Oden et al., 2010). The advantage and efficacy of Bayesian updating have been demonstrated in many geotechnical applications including slope and embankment stability, braced excavations, and tunnel construction (de Queiroz et al., 2005; Janda et al., 2018a; Jiang et al., 2018; Juang et al., 2013; Li et al., 2021; Miro et al., 2015; Qi and Zhou, 2017; Sousa and Einstein, 2012; Špačková and Straub, 2013; Wu et al., 2020; D. Zheng et al., 2018). Given the features of SEM and the associated uncertainties, the Bayesian framework is well-suited for SEM projects. Janda et al. (Janda et al., 2018a) applied Bayesian approach to update three Mohr-Coulomb parameters and the stress release factor used in the convergence-confinement method to predict SEM-induced settlements. Improved agreement and confidence level of the predictions were reported Li et al. (Li et al., 2021) adopted a Bayesian method to a full-face excavated rock tunnel, using an empirical approach to predict tunnel convergence. Based on the measured tunnel convergence, four empirical parameters were updated, and the prediction performance was improved. Previous Bayesian analyses on SEM construction adopt empirical equations or simplified 2D convergence and confinement methods as the stress-deformation prediction model. Such simplified methods are relatively abstract and imprecise, and cannot correctly model complex multi-face excavation sequences and ground interactions (Janin et al., 2015; Neuner et al., 2020; Vlachopoulos and Diederichs, 2014). As a result, the updated geotechnical parameters may not reflect the actual physical characteristics of the ground material and are therefore less valuable for future projects. However, there has not been any attempt to incorporate more

accurate three-dimensional (3D) SEM computational analysis into the Bayesian updating framework.

The complexity of SEM behavior demands the use of 3D computational modeling (Janin et al., 2015; Möller and Vermeer, 2008; Neuner et al., 2020; Svoboda et al., 2010; Vlachopoulos and Diederichs, 2014). However, Bayesian updating requires thousands of model evaluations. A single 3D FDM simulation modeling SEM construction usually takes hours to days to finish. For this study, the average cost of a single 3D FDM simulation for the SEM analysis was around 20 hrs on an Intel i7-9700K CPU @ 3.60GHz and 16 GB RAM desktop computer. Therefore, a surrogate method called Polynomial-Chaos-Kriging (PCK) (Schobi et al., 2015) was utilized to represent the 3D SEM computational model equivalently. The PCK model was demonstrated to be sophisticated enough to accurately capture 4D SEM responses and is functionally equivalent to, but more computationally efficient than 3D computational model (Zheng et al., 2022c).

Bayesian problems are commonly solved by the Markov chain Monte Carlo (MCMC) method. To the best of the authors' knowledge, all previous Bayesian approaches for underground construction adopt Gibbs (Geman and Geman, 1984), Metropolis-Hastings (Hastings, 1970; Metropolis et al., 1953), or modified Metropolis-Hastings algorithms (Haario et al., 2001) as MCMC samplers. Gibbs sampler usually shows poor performance when variables are correlated (Carlo, 2004). The Metropolis-Hastings method and its modified versions usually have $m(m + 1)/2$ tuning parameters (m is the number of uncertain parameters) that are highly sensitive to model performance. Even with heuristic searching methods, determining optimal parameters is difficult and computationally expensive (Foreman-Mackey et al., 2013). A more efficient algorithm called affine invariant ensemble sampling (AIES) method (Jonathan Goodman and Weare, 2010) was adopted in this study. The performance and advantages of AIES over other traditional MCMC samplers have been demonstrated in several studies (Allison and Dunkley, 2014; Foreman-Mackey et al., 2013; J Goodman and Weare, 2010; Huijser et al., 2015).

This paper presents a surrogate-based Bayesian framework for updating the ground parameters and providing probabilistic performance predictions for SEM tunnel construction in soft ground. A 3D finite-difference method (FDM) model was developed to simulate SEM construction and was represented by a surrogate model. Bayesian inference is then used for updating the uncertain parameters during SEM construction. At a particular excavation stage, all time-series data of ground and lining deformations available at the considered monitoring section is used during the updating. New predictions of the ground and lining deformations for the subsequent construction are made based on the updated parameters. The affine invariant ensemble sampling (AIES) algorithm (Jonathan Goodman and Weare, 2010) is adopted as the MCMC sampler in this study to improve overall efficiency. The proposed framework is demonstrated through an application to a newly constructed SEM cavern in downtown Los Angeles (Zheng et al., 2021a). The performance and the effectiveness of the proposed approach are presented in detail.

5.3 A progressive Bayesian updating framework for SEM tunneling

5.3.1 Bayesian inference for model updating

In Bayesian theory, a set of random variables represents the main uncertain input parameters (e.g., cohesion, friction angle, Young's modulus, etc.) for each soil layer of the 3D computational model, e.g., $\mathbf{X} = \{c'_i, \varphi'_i, E_i, \dots\}$. Through a computational forward model, all events of interest \mathbf{F} (e.g., estimates of deformations, stresses, probability of failure) can be expressed as a function of inputs \mathbf{X} . During construction, observations \mathbf{Y} become available, providing new information to update the values of \mathbf{X} . In Bayesian framework, this is achieved by:

$$f''(\mathbf{X}) = \frac{L(\mathbf{X}) f'(\mathbf{X})}{Z} \quad (5.1)$$

where $f'(\mathbf{X})$ is the prior probability density function (PDF) and $f''(\mathbf{X})$ is the posterior PDF. $L(\mathbf{X})$ is the likelihood function and Z ensures $f''(\mathbf{X})$ integrates to 1:

$$Z = \int_{-\infty}^{+\infty} L(\mathbf{X}) f'(\mathbf{X}) d\mathbf{X} \quad (5.2)$$

The likelihood function can be interpreted as the conditional probability of making the observation \mathbf{Y} given the assumption of \mathbf{X} . A computational forward model M is needed to estimate the responses of interest $\hat{\mathbf{y}}_i = M_i(\mathbf{X})$ and relate them to the observations. If n independent measurements \mathbf{y}_i are available, the likelihood function is proportional to the probability of observing the data under the assumption that $\mathbf{X} = \mathbf{x}$, and can be further described as

$$L(\mathbf{x}) \propto P(\mathbf{Y}|\mathbf{X} = \mathbf{x}) = \prod_{i=1}^n L_i(\mathbf{x}) = \prod_{i=1}^n f_{\varepsilon_i}(\mathbf{y}_i - \hat{\mathbf{y}}_i) \quad (5.3)$$

where ε_i denotes the discrepancy of the model prediction from the observation. Discrepancies stem from model inaccuracy and measurement error, which are considered as additive Gaussian distributions with zero mean values.

Once the prior distribution and the likelihood function are established, Bayesian updating of \mathbf{X} can be carried out using **Eq. 1**. For sequential excavation, field measurements are recorded continuously as construction progresses. The uncertain parameters \mathbf{X} can also be updated progressively. For example, at excavation stage k , cumulative field measurements \mathbf{y}_i^k are

available consisting of a $k \times n$ observation matrix. The posterior PDF of \mathbf{X} at stage k ($f_k''(\mathbf{X})$) can be estimated by the posterior estimation from stage $k - 1$ ($f_{k-1}''(\mathbf{X})$) and the likelihood function at stage k ($L_k(\mathbf{X})$):

$$f_k''(\mathbf{X}) = \frac{L_k(\mathbf{X}) f_{k-1}''(\mathbf{X})}{\int_{-\infty}^{+\infty} L_k(\mathbf{X}) f_{k-1}''(\mathbf{X}) d\mathbf{X}} \quad (5.4)$$

5.3.2 MCMC simulation using AIES

For most problems, analytically computing the integral in Eq. (5.2) is impossible. Markov chain Monte Carlo (MCMC) method is commonly used to provide an approximate inference by directly sampling from the posterior distribution (Gelman et al., 2004; Gilks et al., 1995). To overcome the difficulty in determining the optimal values of numerous tuning parameters when using traditional Metropolis-Hastings (Hastings, 1970; Metropolis et al., 1953) or modified Metropolis-Hastings methods, a more efficient MCMC sampler called the affine invariant ensemble sampling (AIES) method (Jonathan Goodman and Weare, 2010) was adopted in this study.

The AIES algorithm generates an ensemble of multiple Markov chains simultaneously. The position of each chain at each iteration t is updated sequentially according to a so-called stretch move. To update the k^{th} chain position \mathbf{X}_k , a random complementary chain \mathbf{X}_j is drawn from the remaining $k - 1$ chains with $j \neq k$, and a new position is proposed:

$$\mathbf{X}_k^{(t+1)} = \mathbf{X}_j^{(t)} + Z(\mathbf{X}_k^{(t)} - \mathbf{X}_j^{(t)}) \quad (5.5)$$

where Z is a stretching variable drawn from a distribution:

$$g(z) = \begin{cases} \frac{1}{\sqrt{z} \left(2\sqrt{a} - \frac{2}{\sqrt{a}} \right)} & \text{if } z \in \left[\frac{1}{a}, a \right], \\ 0 & \text{otherwise} \end{cases} \quad (5.6)$$

where a is an adjustable parameter, usually set to 2 which performs well in most situations (Foreman-Mackey et al., 2013). The proposed candidate $\mathbf{X}_k^{(t+1)}$ is then accepted to replace the old location $\mathbf{X}_k^{(t)}$ when:

$$\min \left\{ 1, Z^{m-1} \frac{f''(\mathbf{X}_k^{(t+1)})}{f''(\mathbf{X}_k^{(t)})} \right\} \geq \alpha_0 \quad (5.7)$$

where $\alpha_0 \in [0,1]$ is a random variate sampled from a standard uniform distribution. This process is repeated with t iterations for all chains in the ensemble. The final chains can be combined to estimate the posterior distributions.

5.3.3 Procedure of the proposed progressive Bayesian updating

The procedure of the proposed progressive Bayesian updating for SEM tunneling is summarized as follows:

- (1) A 3D computational model is built for simulating SEM construction and evaluating the responses of interest. The appropriate geology model and constitutive model are assigned. The sequential excavation and tunnel support processes are simulated properly.
- (2) Uncertain model parameters (e.g., geotechnical, constitutive, etc.) are characterized. The statistical information of each parameter is estimated from field/lab tests and past experiences. The most influential uncertain parameters \mathbf{X} are determined as the variables to be updated. Model outputs \mathbf{F} are defined to be compared with field observations. For each monitoring section, $\mathbf{F} = \{\mathbf{f}_1, \mathbf{f}_2, \dots, \mathbf{f}_n\}_{s \times n}$, where s is the number of excavation rounds and n is the number of outputs.
- (3) A surrogate model $\mathbf{F} \approx f_{pck}(\mathbf{X})$ is constructed to represent the computational model responses.
- (4) An initial prediction $f_{pck}(\mathbf{X}_0)$ is generated using the surrogate model based on the prior information of the uncertain parameters $\mathbf{X}_0 \sim f'_0(\mathbf{X})$.
- (5) Instrumentation data is harvested as SEM construction progresses. For each monitoring section, time-series measurements are compiled into an observation matrix \mathbf{Y} . For the k^{th} update, the observation matrix $\mathbf{Y}^k = \{\mathbf{y}_1^k, \mathbf{y}_2^k, \dots, \mathbf{y}_n^k\}$ contains the cumulative observations of all types of measurements up to the current stage.
- (6) Start updating. Calculate the likelihood function $L_k(\mathbf{X})$, update the posterior distributions of the parameters $f''_k(\mathbf{X})$ according to Eq. (5.4). Generate new predictions for the subsequent stages.

- (7) Iterate steps (5) and (6) with a predefined update interval Δd . The target distribution of each parameter can be obtained when the posterior solution is converged.

5.4 Application to RCTC SEM cavern project

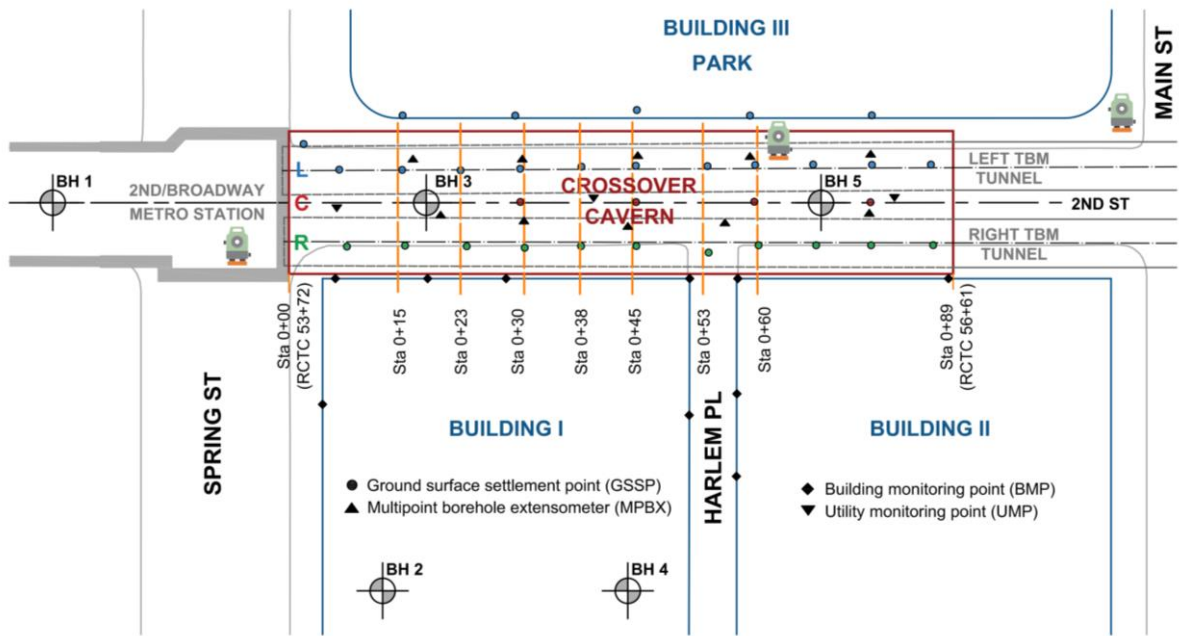
This section demonstrates the effectiveness of the proposed Bayesian updating framework by applying the approach to a real SEM tunnel project.

5.4.1 Project background

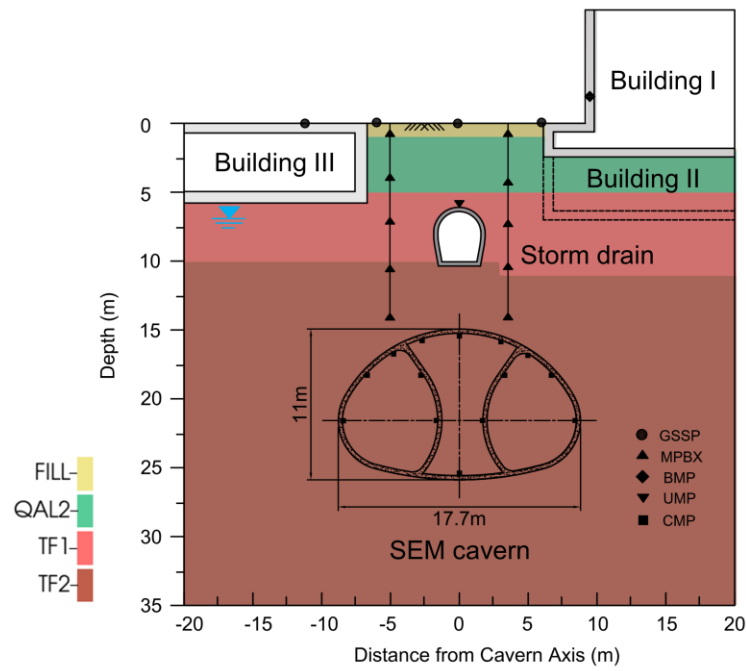
The Regional Connector Transit Corridor (RCTC) crossover cavern is located in downtown Los Angeles. The plan and profile views of the cavern are shown in Figure 5.1. The cavern was constructed underneath a busy street and a storm drain tunnel. Three buildings are close to the construction zone. The excavation size of the cavern is measured 17.7 m wide by 11 m tall and 89 m in length as shown in Figure 5.1b. Before the cavern excavation via SEM, two bored tunnels were constructed by an earth pressure balance tunnel boring machine (EPB-TBM).

The geotechnical investigations show that the cavern excavation is within the Fernando formation overlaid with coarse-grained alluvial deposits (Qal2) and a small portion of artificial fill (Af). The Fernando formation is classified as weak clayey siltstone with unconfined compressive strength (UCS) values of 0.2 to 2.5 MPa (Ulusay, 2014). The groundwater table is approximately 7 m below the ground surface. Due to a fine-grained texture and relatively intact condition, the Fernando formation has a relatively low permeability, with hydraulic conductivity ranging from 10^{-6} to 10^{-8} cm/s. High groundwater inflow into the cavern was neither anticipated nor experienced during excavation.

An extensive instrumentation system was utilized to monitor the performance of the SEM construction, including ground surface settlement points (GSSPs), multipoint borehole extensometers (MPBXs), utility monitoring points (UMPs), building monitoring points (BMPs), and in-tunnel convergence monitoring points (CMPs). The as-built locations of field instrumentations are shown in Figure 5.1. The GSSPs above the left and right drift, the MPBXs close to the center drift, and the in-tunnel CMPs are used in the back analysis procedure.



(a)



(b)

Figure 5.1 LA RCTC SEM cavern layout: (a) plan view and (b) vertical profile (adapted from (Zheng et al., 2021a)).

The SEM construction sequence consists of a three-drift seven-stage scheme as shown in Figure 5.2. The side drifts were divided into left and right top heading (I/LTH and III/RTH) and invert (II/LINV and IV/RINV) sequences, and the center drift consisted of top heading (V/CTH), bench (VI/CBEN), and invert (VII/CINV) sequences. The two temporary walls were demolished in a staggered pattern following the center invert placement. The initial support system consisted of 300 mm thick fiber-reinforced shotcrete, localized wire mesh, and lattice girders. The pre-existing PCTL segments were removed during the side drift excavation. The round length and excavation sequence for each drift are shown in Figure 5.3. The lag distance between the left and right drift is around 21 m and the center drift was excavated about 35 m behind the right drift. Refer to (Zheng et al., 2021a) for more details of the procedure applied.

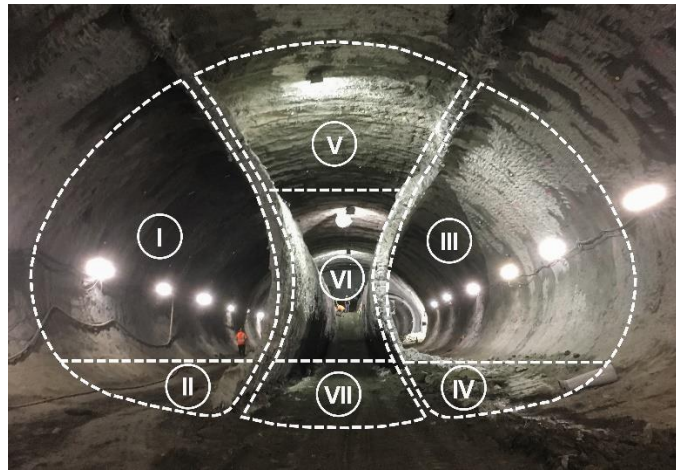


Figure 5.2 Cross-section view of the SEM construction sequence of stages: I: left top heading (LTH), II: left invert (LINV), III: right top heading (RTH), IV: right invert (RINV), V: center top heading (CTH), VI: center bench (CBEN), VII: center invert (CINV).

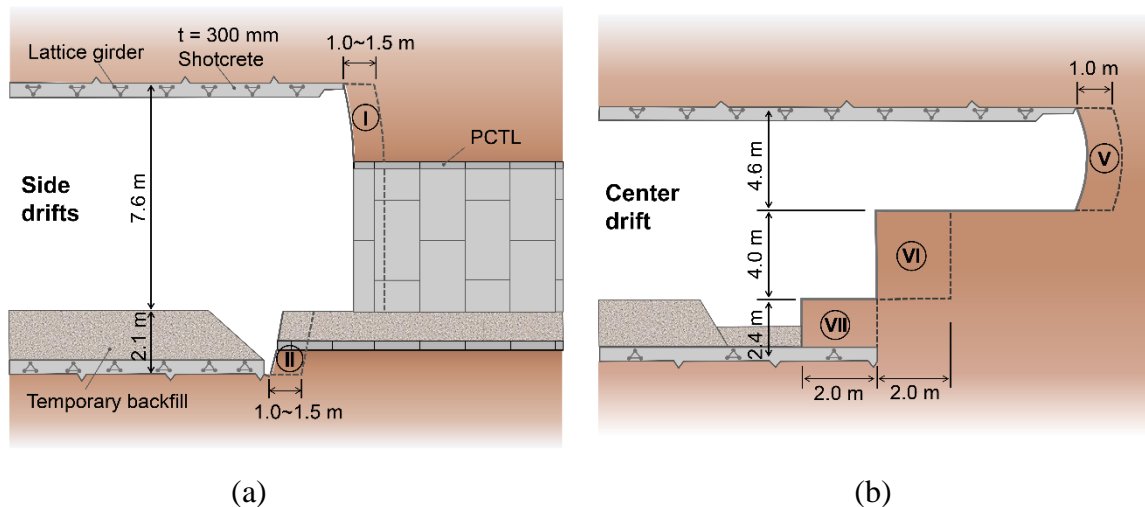


Figure 5.3 Construction sequence for each drift: (a) side drift sequence; (b) center drift sequence.

5.4.2 3D Numerical modeling

A 3D FDM model was developed to simulate the tunnel construction process using FLAC3D, version 7.0 (Itasca Consulting Group Inc., 2019). Figure 5.4 shows the dimensions and configuration of the model. A total number of 300,000 polyhedral-shaped elements were discretized.

Four ground layers—artificial fill (Af), alluvium (Qal2), and two layers of the Fernando formation (Tf1, Tf2)—were considered in the numerical modeling. A geostatistical modeling-based approach was used to simulate the site geology (Zheng, 2022). The most probable ground type was identified to generate the most probable soil condition model as shown in Figure 5.5. Each soil layer was considered spatially homogeneous in this study, with constitutive parameters modeled as random variables. Explicitly modeling the heterogeneity and spatial variability of the ground properties will increase the computational cost exponentially and thus was not considered here.

Undrained response was analyzed in FLAC^{3D} by employing the wet approach (Itasca Consulting Group Inc., 2019), where drained geotechnical parameters are used. Two different constitutive models were used to describe ground behavior. The Tf1 and Tf2 layers were represented by the Hardening Soil-Small Strain (HSS) model. Considering Af and Qal2 layers have much less influence on opening response than the Tf1 and Tf2 layers given their location well above the opening, the Af and Qal2 layers were modeled by the elastic-perfectly-plastic Mohr-Coulomb model (Zheng et al., 2021b). Key parameters used in the 3D FDM model are given in Table 5.1, where most geotechnical parameters are defined based on all available lab/field tests. One can refer to Benz (2007) for more detailed illustrations of the meaning of parameters and the HSS model itself.

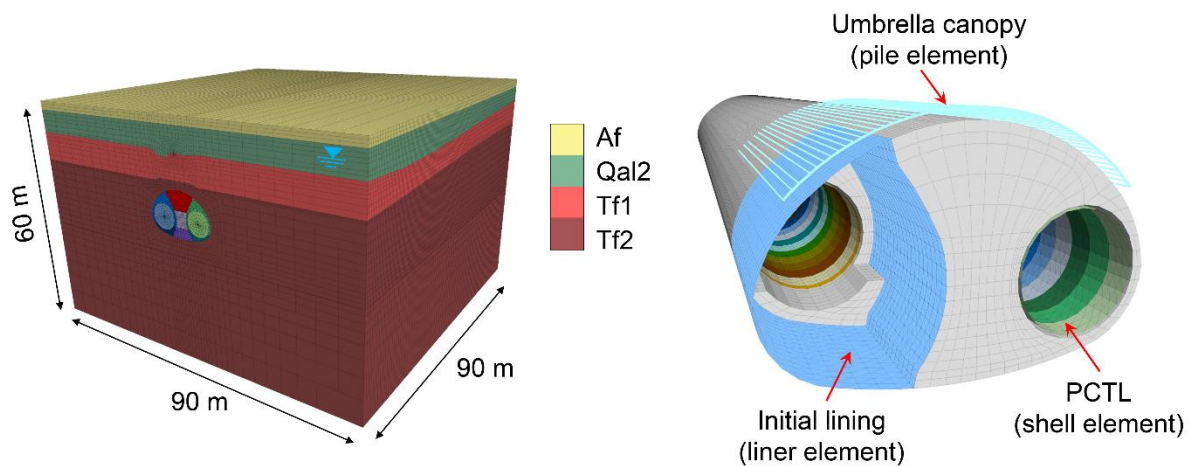


Figure 5.4 3D FDM model simulation of SEM construction.

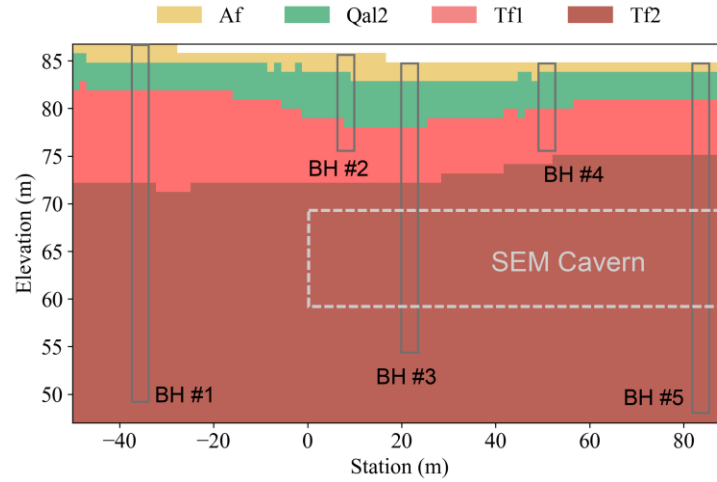


Figure 5.5 Longitudinal visualization of the most probable geology from geostatistical modeling (geology also varies into the page).

Table 5.1 Geotechnical properties adopted in the model.

Parameter	Description	Af	Qal2	Tf1	Tf2
$\gamma^{(1)(3)}$ [kN/m ³]	Total unit weight	18.9	18.7	18.9	19.3
$K_0^{(2)(3)}$	Coefficient of lateral earth pressure at rest	0.50	0.50	0.60	0.65
$E^{(3)}$ [MPa]	Young's modulus	28	57	-	-
$\nu^{(3)}$	Poisson's ratio	0.35	0.35	0.4	0.4
$c'^{(3)(4)}$ [kPa]	Effective cohesion	0.0	10.3	75	170*
$\phi'^{(3)(4)}$ [°]	Internal friction angle	28	30	25	26
$E_{50}^{ref(4)}$ [MPa]	Secant modulus	-	-	48*	55*
$E_{ur}^{ref(2)(5)}$ [MPa]	Unload/reload modulus	-	-	140	180
$m^{(4)}$	Power for stress-level dependency of stiffness	-	-	0.7	0.9
$p^{ref(5)}$ [kPa]	Reference pressure	-	-	100	100
$\nu_{ur}^{(5)}$	Unload/reload Poisson's ratio	-	-	0.2	0.2
$K_0^{NC(5)}$	K ₀ value for normal consolidation	-	-	0.53	0.51
$R_f^{(5)}$	Failure ratio	-	-	0.9	0.9
$OCR^{(3)}$	Over-consolidation ratio	-	-	1.2	1.5
$E_0^{ref(6)}$ [MPa]	Small strain modulus	-	-	330	480*

$\gamma_{0.7}^{(5)}$	Shear strain at which $G_s=0.7G_0$	-	-	2.0E-04	2.0E-04
$GWT^{(3)}$ [m]	Groundwater depth	table	6.8*		

* Mean values of the uncertain parameters to be back analyzed

- (1) Interpreted from 166 field moisture-density tests results
- (2) Interpreted from 17 pressuremeter tests results
- (3) Referenced from the literature (Herranz et al., 2016; Yang and Huynh, 2017; Zheng et al., 2021a)
- (4) Interpreted from 12 isotropically consolidated undrained compression triaxial (CIUC) tests
- (5) Based on the literature (R. Obrzud, 2010) and engineering judgment
- (6) Interpreted from 8 shear wave tests

The SEM construction process was modeled in a step-wise manner. The actual construction sequence from stages I to VII was simulated in the model. At each stage, a one-round-length ground zone is deactivated, and the “zone relax” option (Itasca Consulting Group Inc., 2019) is adopted to simulate a gradual excavation of the material. Within the same phase, the exposed portion of the PCTL ring is removed and a liner element representing the initial support is activated immediately behind the face (Figure 5.4 3D FDM model simulation of SEM construction. Figure 5.4). As the shotcrete lining was installed incrementally at the top heading, the thickness of the liner element was modified accordingly to simulate two lifts 170+130=300 mm of shotcrete application. A linear elastic material model was assigned to the lining, integrating the aging effect of shotcrete strength. A time-dependent liner stiffness was implemented by gradually increasing material characteristics following the approach described in (Zheng et al., 2022c).

A group of 18-meter-long umbrella canopy pipes was modeled by pile structural elements (Figure 5.4). The lining of the storm drain tunnel and the PCTL were modeled using three-node shell elements attached to the ground zones via interface links. The main properties of these structural elements are listed in Table 5.2.

Building structures were modeled by applying the corresponding building surcharge at the foundation level. The storm drain tunnel was simulated by a single-step excavation followed by the installation of the lining structure. Twin bored tunnels were simulated by a multi-stage excavation to implement the redistribution of ground stress and strain before the SEM construction.

Table 5.2 Main properties of structural elements.

	Storm tunnel	Drain	Precast concrete tunnel lining	Cavern initial support
Elastic modulus (GPa)	21.5		31.7	0.4 to 34 (Time dependent)

Unit weight (kN/m ³)	23.5
Poisson's ratio	0.2

Six model outputs were considered to compare with the field measurements, including the surface settlement at the left and right sides (S_L and S_R), subsurface settlement (MP) (7.6 m above cavern crown), the convergence of the left drift liner (C_{M2M3}) (3 m above the sprineline), center crown convergence (C_{CTH}), and center invert convergence (C_{CINV}) as shown in Figure 5.6. The locations of the model observation points are consistent with the field instrumentation points as shown in Figure 5.1. The ground surface and subsurface outputs are recorded from the beginning of the left drift excavation. The radial deformation at the tunnel periphery contains both non-measured apriori convergence and measured convergence. The lining convergence in the model is recorded when the actual measurement is baselined in the field to make an apples-to-apples comparison. For instance, the left liner convergence monitoring points were baselined three rounds behind the LTH face. The model output of the left liner convergence also starts to record three rounds behind the face.

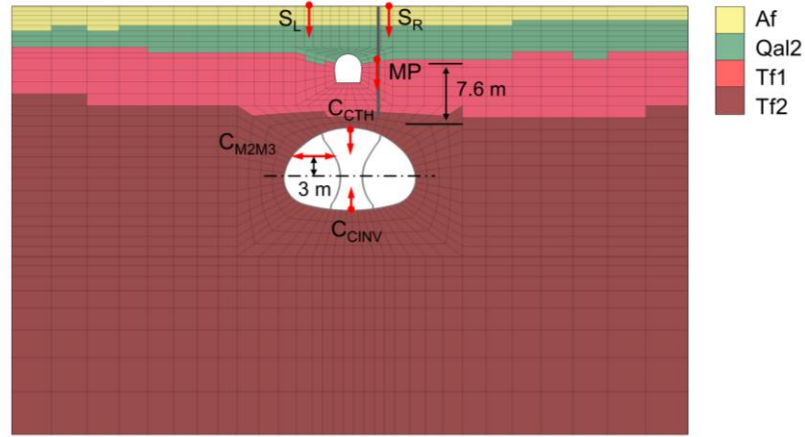


Figure 5.6 3D FDM model outputs used for back-analysis (monitoring section at Sta. 0+15).

5.4.3 Construction and validation of the surrogate model

The Bayesian framework adopted in this study requires thousands of model evaluations. Therefore, a PCK surrogate model was utilized to reduce the evaluation time for each unique input set from 20 hrs for 3D FDM to less than one second (Zheng et al., 2022c).

From the previous sensitivity analysis on the same project (Zheng et al., 2022c), the five most influential parameters on the SEM-induced deformation behavior were identified, namely $Tf2-c'$,

$Tf2-E_0^{ref}$, $Tf2-E_{50}^{ref}$, GWT , $Tf1-E_{50}^{ref}$. The surrogate model to be constructed here has these five as inputs. The statistical information of the input variables is summarized in Table 5.3, determined based on the same sources as listed in Table 5.1. The COV of each input variable used for surrogate model training is considered 30% higher than the value listed in Table 5.3 to ensure sufficient search space for the Bayesian updating process. The surrogate model outputs contain the six 3D FDM outputs (Figure 5.6) after each excavation stage.

A sample space (combinations of input parameters) was generated through a design of experiments using the Sobol sequence sampling method. Based on the previous study (Zheng et al., 2022c), 200 samples are sufficient to accurately capture the SEM responses for the PCK method. For each sample point, the 3D FDM simulation of the entire SEM construction stage was performed to obtain the corresponding model output matrix \mathbf{F} . All other parameters were assigned deterministic values as listed in Table 5.1. All pairs of inputs and outputs were assembled as the dataset for the surrogate model training. The dataset was split into training and testing subsets with sample sizes of 160 and 40, respectively, to avoid model overfitting. The PCK model was constructed using the Optimal PC-Kriging method. The detailed training process and optimization settings of the PCK model can be found in (Zheng et al., 2022c).

The accuracy of the surrogate model was measured by normalized root mean square error (NRMSE) as defined by:

$$NRMSE = \sqrt{\frac{\sum_{i=1}^n \left(f(\mathbf{X}_i) - f_{pck}(\mathbf{X}_i) \right)^2}{\sum_{i=1}^n \left(f(\mathbf{X}_i) \right)^2}} \quad (5.8)$$

where n is the number of experiment samples, $f(\mathbf{X}_i)$ is the 3D FDM response at the sample point \mathbf{X}_i , and $f_{pck}(\mathbf{X}_i)$ is the PCK model approximation. Table 5.4 summarises the test errors for

six outputs calculated per Eq. (5.8). The NRMSEs for all outputs are less than 4%. The model was further tested on an independent dataset with 100 samples to investigate the accuracy of the PCK model as a function of the input parameter space. Figure 5.7 presents the NRMSE distributions throughout the input parameter space. All NRMSE points are within 10% and most of them are below 4%, indicating a good accuracy of the PCK model throughout the given parameter ranges.

Table 5.3 Probabilistic information of uncertain parameters.

Parameter	Mean (μ)	COV (%)	Distribution
Tf1- E_{50}^{ref} [MPa]	48	30	Lognormal
Tf2- E_{50}^{ref} [MPa]	55	50	Lognormal
Tf2- c' [kPa]	170	70	Lognormal
Tf2- E_0^{ref} [MPa]	480	30	Lognormal
GWT [m]	6.8	20	Lognormal

Table 5.4 Normalized root mean square error (NRMSE) of the PCK surrogate model on testing set.

	S_L	S_R	MP	C_{M2M3}	C_{CTH}	C_{CINV}
NRMSE (%)	1.8	1.9	1.9	3.2	2.5	2.4

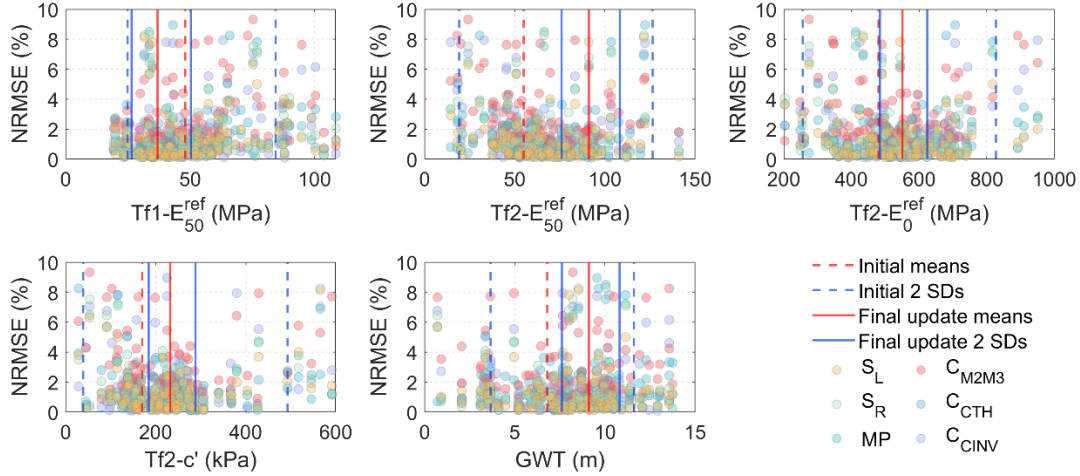


Figure 5.7 NRMSE distributions for test data throughout the input parameter space.

5.4.4 Bayesian updating ground parameters and model predictions using field measurements

Based on the sensitivity analysis results (Zheng et al., 2022c), five governing geotechnical parameters were treated as uncertain variables ($Tf2-c'$, $Tf2-E_0^{ref}$, $Tf2-E_{50}^{ref}$, GWT , $Tf1-E_{50}^{ref}$) to be updated during the SEM construction. The prior distributions of these parameters were adopted as listed in Table 4.3. The uncertain variables were considered statistically independent in this case. The Bayesian updating of the uncertain parameters starts when LTH is 5 m before arriving at the concerned monitoring section. Following the procedure described in Section 2.3, the uncertain parameters are updated progressively with the number of observations growing as the excavation progresses. Since the round length is relatively short and the change of deformation is small, the update interval Δd is set to every four excavation round for the side drifts and center top heading, and two excavation round for the center invert. Five model update phases were defined to visualize the results better, as listed in Table 5.5. These phases were chosen because they represent major excavation changes made for the concerned monitoring section. At each update stage, all measurements available at that stage are used for the analysis. The measurement used and their observed data at each major update phase are listed in Table 5.5.

Table 5.5 Major update phases and corresponding observations

Update phase	Visualization of tunnel progress	Distance between monitoring section and excavation faces	Measurements used for update	Latest observed data (mm) (Sta. 0+15 as an example)
--------------	----------------------------------	--	------------------------------	---





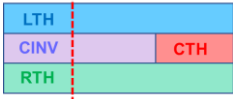
I		LTH arrival	S_L, S_R, MP	3.3, 1.6, 1.7
II		LTH beyond 10 m	S_L, S_R, MP, C_{M2M3}	4.7, 3.5, 5.1, -3.5
III		RTH beyond 10 m	S_L, S_R, MP, C_{M2M3}	8.7, 8.1, 8.1, -3.7
IV		CTH beyond 10 m	$S_L, S_R, MP, C_{M2M3}, C_{CTH}$	11.2, 11.0, 12.8, 2.5, 2.1
V		CINV beyond 60 m	$S_L, S_R, MP, C_{M2M3}, C_{CTH}, C_{CINV}$	19.3, 17.8, 19.7, 14.8, 8.9, 8.7

Figure 5.8 presents the posterior distributions of the uncertain geotechnical parameters estimated at each major update phase for Sta 0+15. The distributions are visualized by kernel density estimations to be more interpretable. Compared to the initial assumption, an obvious increase in mean value can be observed for $Tf2-E_{50}^{ref}$, $Tf2-E_0^{ref}$, and $Tf2-c'$. The mean values of $Tf2-E_{50}^{ref}$, $Tf2-E_0^{ref}$, and $Tf2-c'$ increase from prior estimates and to posterior Phase V estimates of $55 \rightarrow 90$ MPa, $480 \rightarrow 551$ MPa, and $170 \rightarrow 231$ MPa, respectively. The prior estimate of $Tf2-E_{50}^{ref}$ was based on 12 CIUC triaxial tests results interpreted from the geotechnical data report. The prior estimate of $Tf2-c'$ was based on highly variable data obtained from 12 CIUC triaxial tests and 10 direct shear tests (Zheng et al., 2021a). The updating results indicate that the actual modulus and cohesion of the Tf2 layer are underestimated initially. The updated $Tf2-E_{50}^{ref}$ drifts much more beyond the one standard deviation range estimated initially. However, as shown in Figure 5.7, the surrogate model maintain good accuracy through the initial and updated parameter ranges. As mentioned by Govindasamy et al. (Govindasamy et al., 2019), it is usually difficult to accurately predict ground deformation and stress-strain behavior by directly using HSS soil parameters obtained from the lab or in situ tests. It also has been reported by (Hsiung et al., 2018) that the HSS modulus obtained from the lab test shows lower estimations due to the disturbed state of the sample. Therefore, a proper back-analysis based on field observations to identify HSS parameters is always recommended (Miro et al., 2015; Zhao et al., 2015).

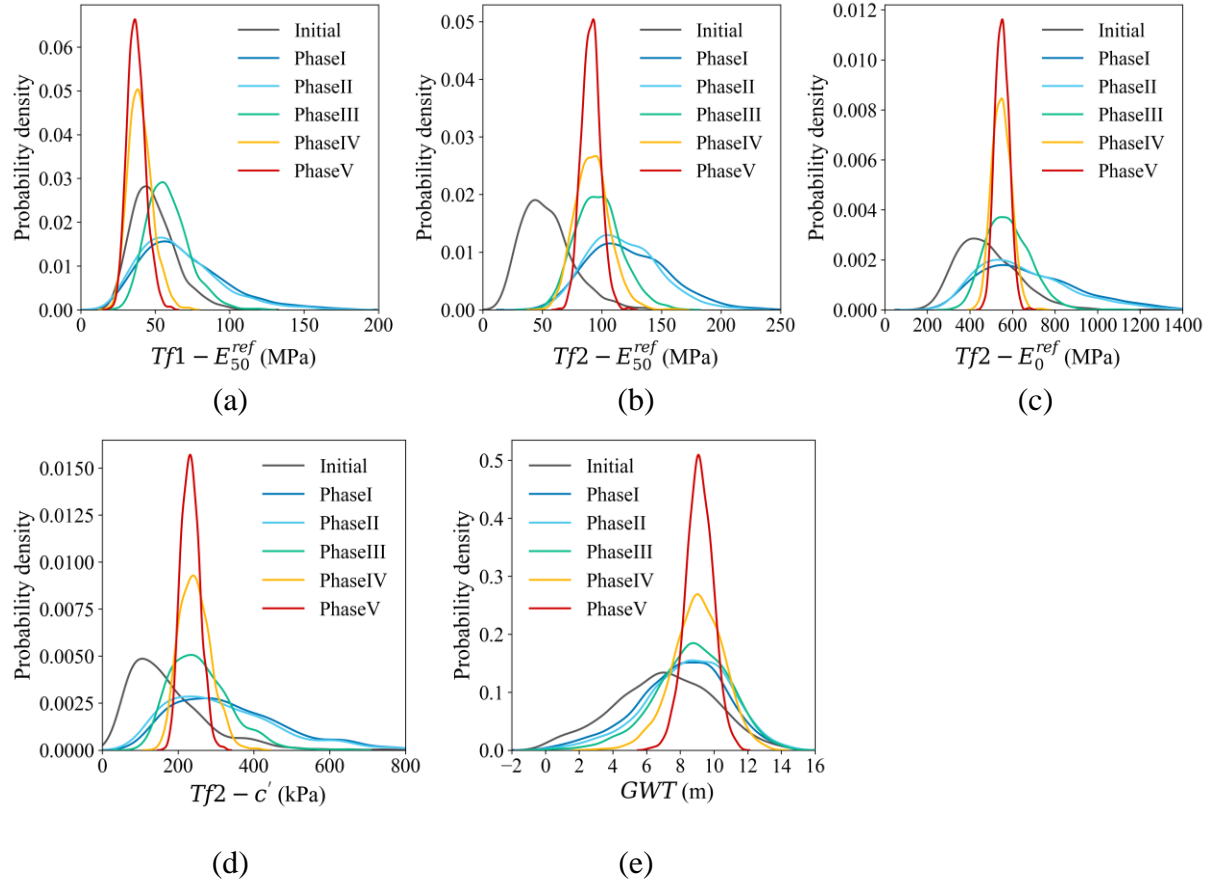


Figure 5.8 Histograms of posterior distributions for (a) $Tf1 - E_{50}^{ref}$, (b) $Tf2 - E_{50}^{ref}$, (c) $Tf2 - E_0^{ref}$, (d) $Tf2 - c'$, and (e) GWT updated at different phases (using measurements at Sta. 0+15).

The posterior PDF profiles of each parameter become narrower as observed data increases, indicating a reduction in the uncertainty of estimated parameters. The COVs of $Tf1 - E_{50}^{ref}$, $Tf2 - E_{50}^{ref}$, $Tf2 - E_0^{ref}$, $Tf2 - c'$, and GWT reduce from initial values 0.30, 0.45, 0.30, 0.65, 0.20, respectively, to Phase V posterior 0.16, 0.09, 0.06, 0.11, 0.06, respectively. These significantly reduced parameter variances translate into reduced risk simply because prediction uncertainty is far less.

Another benefit of Bayesian updating is that the prediction of the responses can also be updated with certain confidence levels. Figure 5.9 presents sets of violin plots showing the predictions of the final displacements that are generally of primary concern using the parameters updated at different phases. The predictions were generated by 1000 Monte Carlo simulations based on the distributions of the updated parameters. Without the knowledge gained from the field observations, the initial predictions overestimate all displacements associated with substantial uncertainties. As the uncertain parameters were updated progressively by Bayesian updating, gradually improved agreement between the final measured displacements and

predicted means can be observed. The uncertainty level of predicted displacement also decreases which enables higher confidence that the measurement will be within a specific range.

Figure 5.10 shows the goodness of updated displacement predictions at various phases for Sta. 0+15. The goodness factor is defined as the ratio between the mean value of the predicted deformation and the observed deformation at the corresponding stage. A value larger than 1 indicates an overestimation and vice versa. The initial predictions prior to excavation deviate much higher from the perfect match lines (goodness factor = 1.0). After Phase I excavation is completed, the observed ground surface and subsurface settlements are much smaller than the initial prediction. The ground parameters and the displacement predictions are updated using the Bayesian approach. This process is repeated stage by stage until the end. After each phase updating, the updated predictions for the following stages are gradually converged to the perfect match lines in most cases, which also indicates the estimations of the ground parameters are gradually improved.

In general, the means of the updated predictions show good agreement with the observations after the Phase III updating when all side drift excavations are completed. The Phase I and II updates underestimated the final displacements, because the measured ground and structural displacements were still of small magnitudes (below 5 mm). Consequently, higher ground modulus and strength parameters were identified through the back analysis.

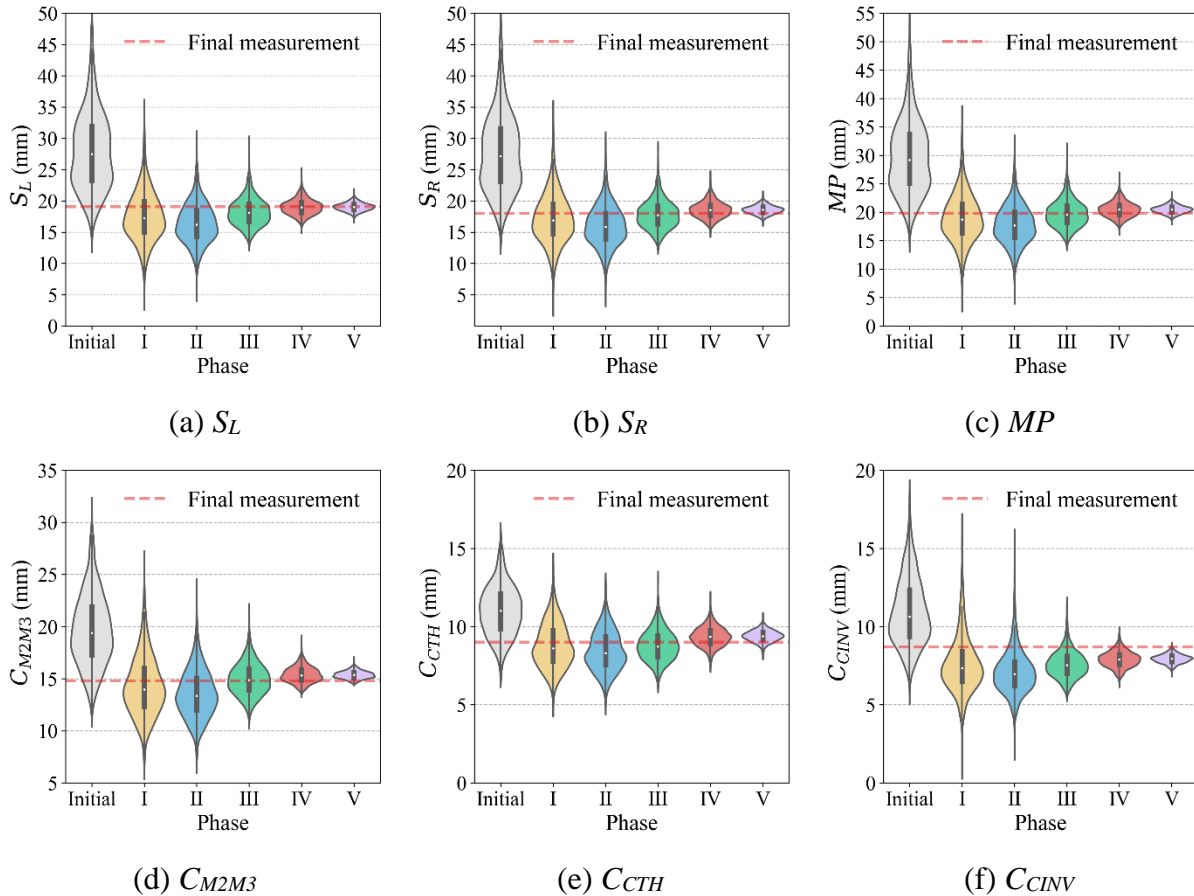


Figure 5.9 Predictions of final displacements versus the field observations at Sta. 0+15 from different update phases.

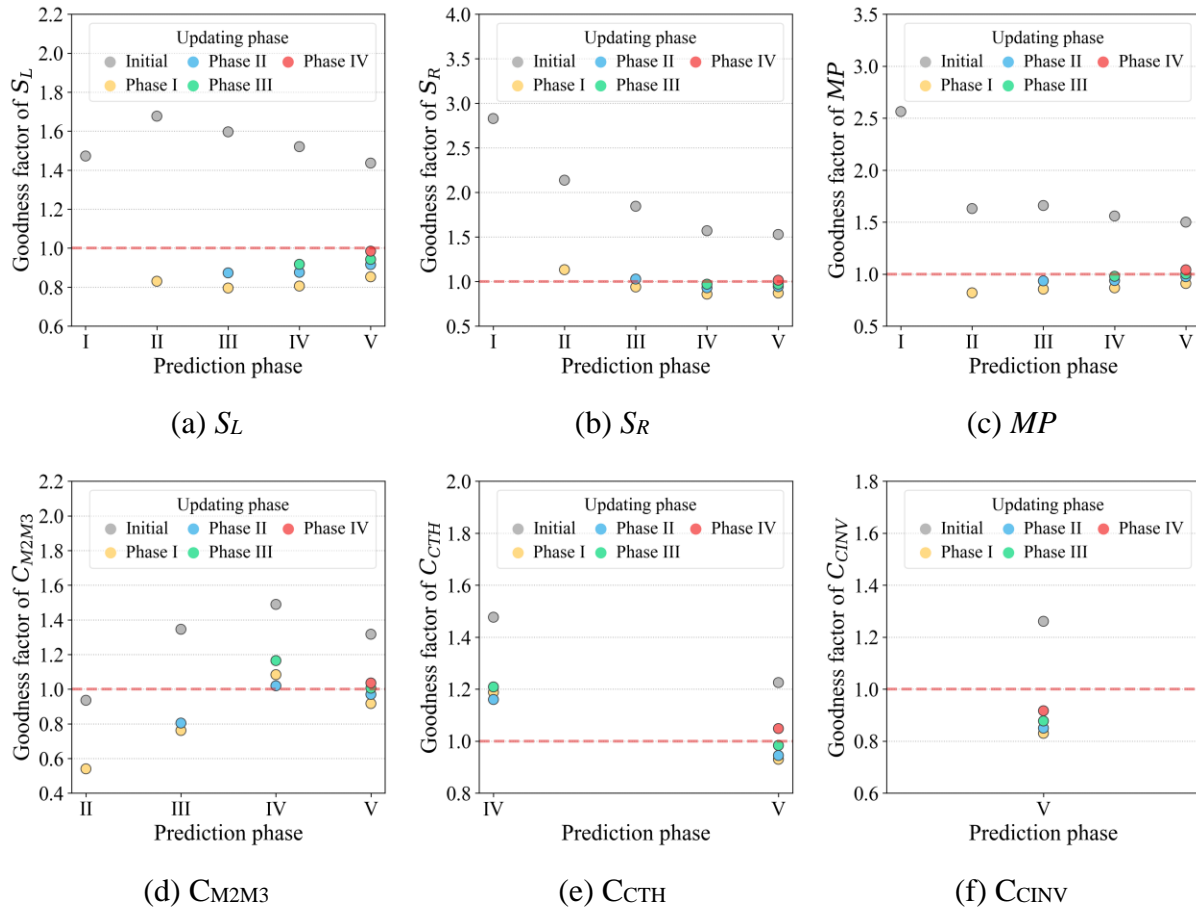
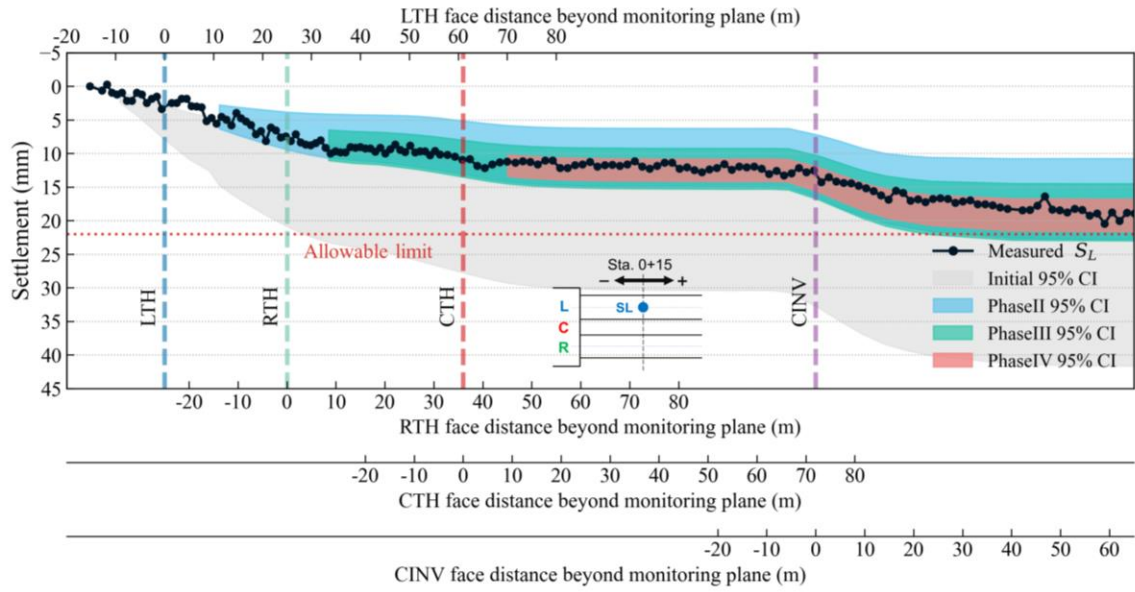
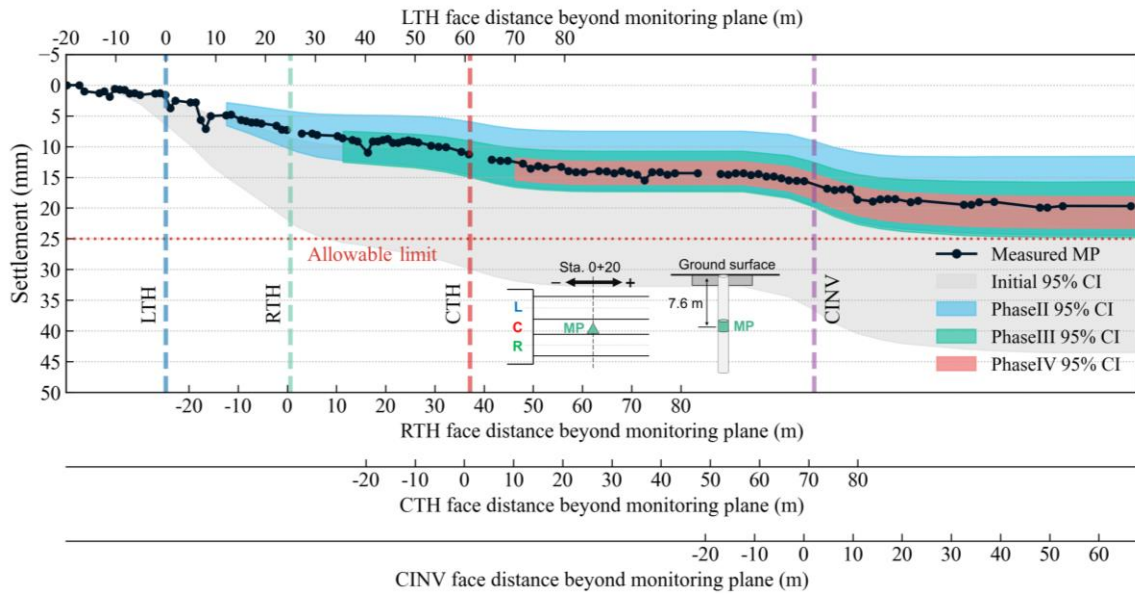


Figure 5.10 Goodness factors of the updated displacement predictions for each Phase at Sta. 0+15 (Goodness factor = mean of predictions/observed displacement).

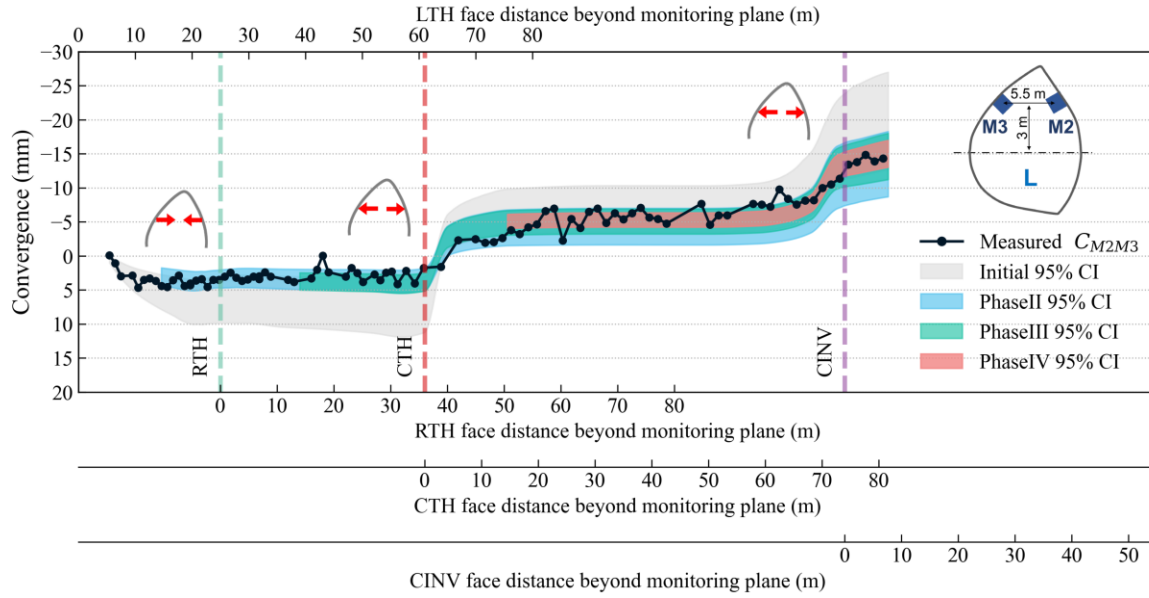
To better illustrate how the model predictions have been progressively improved through the updating, the time-series predictions at typical updating phases are compared with the field measurements as shown in Figure 5.11(a) to (e). Wider 95% confidence intervals (CI) were estimated at the initial stage as the model parameters were more uncertain. By incorporating the observations, the uncertainty in the prediction decreases as the SEM construction proceeds. The benefit of uncertainty reduction is illustrated in Figure 5.11(a) and (b). Without parameter updating, the modeling results convey a reasonably probable chance that surface settlement exceeds the allowable limit (red line). This uncertainty is cause for concern in practice and may trigger construction means and method changes. Model updating, however, clearly shows a highly improbable chance that settlement will exceed the allowable limit.



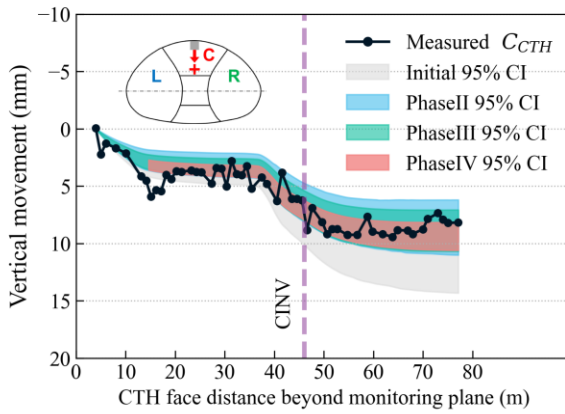
(a) S_L



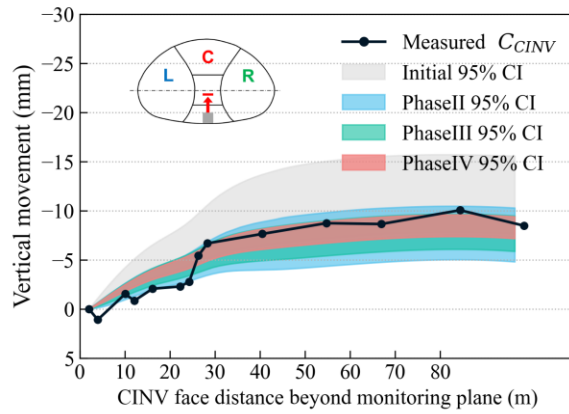
(b) MP



(c) C_{M2M3}



(d) C_{cTH}



(e) C_{cINV}

Figure 5.11 Comparison of prior and posterior predictions of time-series measurements for Sta. 0+15: (a) S_L , (b) MP , (c) C_{M2M3} , (d) C_{cTH} , and (e) C_{cINV} .

The same updating procedure was applied for all monitoring sections. To conservatively identify possible weak zones along the cavern alignment, all monitoring sections are back-analyzed independently. The statistical information of the final updated parameters for each section is shown in Table 5.6. In general, the means and variances of the updated geotechnical parameters are similar for all monitoring sections, indicating relatively homogeneous ground behavior. There is no weak zone identified along the alignment through the back-analysis.

Table 5.6 Posterior parameters after Phase V updating for all monitoring sections.

$Tf1-E_{50}^{ref}$	$Tf2-E_{50}^{ref}$	$Tf2-E_0^{ref}$	$Tf2-c'$	$GWT\ depth$
--------------------	--------------------	-----------------	----------	--------------

Monitoring section	Mean (MPa)	COV	Mean (MPa)	COV	Mean (MPa)	COV	Mean (kPa)	COV	Mean (m)	COV
Initial estimation	48	30	55	50	480	30	170	70	6.8	20
Sta. 0+15	37	16	91	9	551	6	232	11	9.1	6
Sta. 0+23	35	27	86	9	554	5	245	16	8.4	3
Sta. 0+30	45	20	94	5	511	5	248	9	7.9	4
Sta. 0+38	41	16	87	6	571	5	222	12	8.2	5
Sta. 0+45	34	16	102	7	561	3	212	13	7.2	4
Sta. 0+53	32	18	82	11	545	6	257	11	6.8	4
Sta. 0+60	47	11	90	6	576	4	248	8	6.4	5
Average	39	18	90	7	553	5	238	11	7.7	4

5.5 Conclusions

A surrogate-based Bayesian analysis framework has been introduced to assist SEM tunnel design and construction. A surrogate model was utilized to represent 3D FDM simulation of a real SEM cavern construction. The uncertain geotechnical parameters were updated through a progressive Bayesian updating procedure during SEM construction, allowing a probabilistic estimation of the parameters and corresponding responses. The following conclusions are drawn from this study:

- The Bayesian updating results indicate that the $Tf2-E_{50}^{ref}$, $Tf2-E_0^{ref}$ and $Tf2-c'$ were underestimated initially. The final updated mean values of $Tf2-E_{50}^{ref}$, $Tf2-E_0^{ref}$ and $Tf2-c'$ are 90 MPa, 553 MPa, and 238 MPa, respectively for all monitoring sections. The uncertainty of the estimated parameter is highly reduced, which translates into reduced risk simply because prediction uncertainty is far less. The variance of the predicted deformations considerably reduces when incorporating the field observations at Phase I updating. However, Phase I and II underestimate the deformations induced by the subsequent excavation, mainly because the magnitudes of measured ground and structural deformations are relatively small (<5 mm). In general, after the Phase III updating when all side drifts are excavated, the mean values of the updated predictions show satisfactory agreement with the observed measurements.
- The updated parameters for all monitoring sections considered show similar results, indicating similar ground conditions along the alignment. The average mean values of $Tf1-E_{50}^{ref}$, $Tf2-E_{50}^{ref}$, $Tf2-E_0^{ref}$, $Tf2-c'$, and GWT for all monitoring sections after the final update are 39 MPa, 90 MPa, 553 MPa, 238 kPa, and 7.7 m, respectively. The average COVs reduce from initial 0.30, 0.45, 0.30, 0.65, 0.20 to posterior 0.18, 0.07, 0.05, 0.11, 0.04, respectively.

- The proposed Bayesian framework enables progressively predicting SEM responses with certain confidence levels. Deformation tolerance (e.g., marginal safety) can be quantified accordingly based on predefined acceptable limits. This result can assist the decision-making process by continuously providing quantitative references to incorporate design modifications or optimizations during SEM construction.

5.6 Acknowledgments

Funding for this study was provided by Skanska and Traylor Bros., by the Center of Underground at the Colorado School of Mines, and by the University Transportation Center for Underground Transportation Infrastructure (UTC-UTI) at the Colorado School of Mines under Grant No. 69A3551747118 from the U.S. Department of Transportation (DOT). We would like to offer our special thanks to Christophe Bragard and Carlos Herranz Calvo for providing the data and technical insights for this study. We would also like to express our gratitude to Traylor Bros., Skanska, Mott Macdonald, Geocomp, Sixense Soldata, and LA Metro for sharing the project data and providing the opportunity to join in this project.

CHAPTER 6

RELIABILITY-BASED DESIGN OF SEM TUNNELS USING A SURROGATE MODELING APPROACH

Reproduced from a draft to be submitted to a scientific Journal

6.1 Abstract

Minimizing ground deformation and maintaining structural stability are major concerns when utilizing the sequential excavation method (SEM) for shallow urban tunnel construction. Considering ground uncertainties and various design options available, generating an economical design without compromising safety is complex and challenging for SEM designers. This paper presents a reliability-based approach to assist SEM tunnel design. A 3D finite-difference method (FDM) model was used to simulate the SEM construction. To alleviate the cost of probabilistic analysis, the Polynomial-Chaos-Kriging (PCK) method was employed to efficiently and reliably represent the 3D FDM model. The uncertainty of ground parameters—secant reference modulus E_{50}^{ref} and effective cohesion c' —was considered. The thickness (t) and 28-day compressive strength (f_c) of shotcrete, the excavation round length (RL), and three types of SEM toolbox items (face support, temporary invert, and corner reinforcement) were considered as design variables in this study. A surrogate-based reliability analysis was performed and the impacts of geotechnical parameters and design variables on the two reliability indices were quantified.

6.2 Introduction

The design principle of the sequential excavation method (SEM), also known as the New Austrian tunneling method (NATM) is to integrate the inherent strength of the surrounding ground material to stabilize the tunnel thus achieving economy and efficiency in ground support with controllable influence on the environment. However, minimizing ground deformation becomes a major concern when using SEM in urban soft ground settings. Mobilizing a high degree of ground self-support is not often possible as is commonly applied in rock tunneling or in rural areas. Generally, an early and stiff initial support is employed to reduce ground deformation. Meanwhile, the lining structure is expected to sustain higher loads. It is more complex and challenging for designers to develop reliable yet economical SEM designs in such situations.

Furthermore, various uncertainties driven by natural and human-made factors make predicting SEM-induced ground response and structural loads more challenging. To consider uncertainty, the allowable design (ASD) method using factors of safety had long dominated tunnel design practice. More recently, the limit state-based approaches such as the load and resistance factor design (LRFD) approach in North America and partial factors approach in Europe have been adopted in tunnel structure design (AASHTO, 2017; CEN, 2004). SEM

traditionally has involved temporary support (sprayed concrete, steel sets) designed via ASD and final support (cast in place) designed using limit state-based approaches. More recently, sprayed concrete liners are being adopted for final design, and the integration of initial and final lining into a composite section is being done. This then ties temporary support into the LRFD approach. However, as mentioned by many researchers, the application of LRFD or partial factors in tunnel support design is sometimes questionable and difficult to implement (Liu and Low, 2018; Phoon and Ching, 2018; Schweiger et al., 2017). Schweiger et al. (2017) mentioned that soil provides not only action but also resistance and therefore the application of partial factors is not straightforward. Phoon and Ching (2018) mentioned that applying the same rigid partial factors across different realms or different levels of parametric uncertainty may not imply the same target failure probability. Based on an example of designing support pressure for a circular tunnel, Liu and Low (2018) demonstrated that using different characteristic input values and different sets of partial factors results in inconsistent safety levels without quantification. SEM applies the principle that the ground surrounding the tunnel is integrated into the tunnel support system and shares loads with the tunnel lining (Hung et al., 2009b). Considering the correlation between loads, support resistance, and deformation, the surrounding ground and tunnel support play both roles of load and resistance and are difficult to separate. Besides, a design by LRFD provides no explicit information on the probability of failure, nor explicit guidance on how partial factors are to be modified given various types and levels of safety requirements (Kong and Phoon, 2015).

On the other hand, reliability analysis provides means of evaluating the combined effects of uncertainties and a more consistent and complete measure of risk (Sayed et al., 2010). In many cases, reliability analysis is recommended to serve as a complementary tool to LRFD based design (Phoon and Ching, 2018). LRFD can be considered as a simpler version of reliability-based design with only two variables—load and resistance. Hoek (1998) introduced a brief exposition of reliability approaches suitable for underground openings. Lü & Low (2011) conducted a reliability analysis of a horseshoe-shaped tunnel with respect to the permissible tunnel convergence criterion and compared the results calculated by FORM and SORM. Zhang and Goh (2012) proposed a quantitative probabilistic assessment by using the RMR system to determine the global factor of safety required under different ground conditions and an application in underground rock cavern design. Wang et al. (2016) utilized a radial basis function metamodel to approximate the performance function defined based on the plastic zone limit. The proposed procedure was demonstrated by an analytical example and a 2D finite element analysis case. Mollon et al. (2009a, 2009b) presented a reliability analysis of a deep circular tunnel in a homogeneous soil by integrating numerical modeling, FORM and the response surface methodology (RSM). The performance functions were defined based on the limit face pressure and the maximum ground settlement. However, all previous reliability analyses of tunnels adopted closed-forms solutions or 2D numerical models, which was demonstrated to be inadequate to accurately capture complex SEM behavior (Janin et al., 2015; Möller and Vermeer, 2008; Neuner et al., 2020; Svoboda et al., 2010; Vlachopoulos and Diederichs, 2014). Furthermore, the limit state of initial lining capacity was considered as a single limit value or an elastic limit curve in previous studies instead of a more realistic non-linear capacity curve for fiber reinforced concrete (FRC) material. Also, examining the impacts of implementing possible design modifications coupled with various ground conditions is crucial for a robust SEM design. However, various design variables (e.g., shotcrete properties, support measures) commonly

applied in SEM construction has not been explicitly considered in the aforementioned reliability analyses.

The complexity of SEM behavior demands the use of 3D computational modeling (Janin et al., 2015; Möller and Vermeer, 2008; Neuner et al., 2020; Svoboda et al., 2010; Vlachopoulos and Diederichs, 2014). However, reliability analysis usually requires millions of model evaluations to calculate small-magnitude probability of failure. A single 3D FDM simulation modeling SEM construction usually takes hours to days to finish. Therefore, a surrogate method called Polynomial-Chaos-Kriging (PCK) (Schobi et al., 2015) was utilized to equivalently represent the 3D SEM computational model. The PCK model was demonstrated to be sophisticated enough to accurately capture 4D SEM responses and is functionally equivalent to, but more computationally efficient than 3D computational model (Zheng et al., 2022c).

This paper presents a reliability-based design procedure for reliable and economical SEM design and construction. 3D finite-difference method (FDM) modeling combined with a surrogate approach was employed to simulate a typical shallow SEM construction in soft ground. The uncertainty of two soil constitutive parameters—secant reference modulus E_{50}^{ref} and effective cohesion c' —were considered. The thickness (t) and 28-day compressive strength (f_c) of the shotcrete, the excavation round length (RL), and three types of SEM toolbox items were considered as design variables. The internal forces of the initial lining and the ground surface settlement were selected as key performance indices of the SEM analysis. Several concerns of initial support design using the LRFD approach were discussed and illustrated by a design example. Full reliability analysis was conducted based on two limit state functions to provide a more consistent measure of risk, explicitly reflecting the influence of the uncertain parameters and their correlation structure. Aiming at a robust and cost-effective design, it is hoped that the insights of this study will facilitate the applications of reliability-based approaches in future SEM tunnel projects.

6.3 Deterministic model and probabilistic analysis for SEM construction

6.3.1 3D finite-difference model of SEM tunnel construction

This study was conducted on a synthetic SEM tunnel. The ground and structural responses during excavation and temporary support stages were considered. The ground-support interaction analysis of SEM tunnel excavation is realized by 3D FDM model. A commercial software FLAC3D version 7.0 (Itasca Consulting Group Inc., 2019) was used to establish the 3D FDM model and perform simulations. The geometry and mesh discretization of the reference SEM tunnel case is illustrated in Figure 6.1. The excavation size of the tunnel is assumed to be 17 m wide by 11 m tall, and 90 m in length. The excavation sequence consists of two drifts. Each drift is divided into left/right top heading (LTH/RTH) and left/right invert (LINV/RINV) sequences. The right drift is first excavated throughout the tunnel length and followed by the left drift excavation. A two-round length (RL) distance is maintained between top headings and inverts. The temporary wall in the middle is removed after the left drift excavation. The

deformations at the bottom and four side boundaries of the model are restrained in the normal direction. The top boundary representing the ground surface is free to move. Groundwater is not considered and drained analysis was used in this case. The entire model contains a total number of 170,730 polyhedral-shaped elements.

A single layer of soil was assumed in the numerical modeling. The hardening soil small-strain (HSS) model was applied to describe the soil behavior. The HSS model adopts the Mohr-Coulomb failure criterion and a double hardening plastic law. The advantage of the HSS model is its capability to consider stress-dependent soil stiffness and differentiate between load and unload stiffness, providing more realistic deformations for tunnel excavation problems (Obrzud and Truty, 2018). The assumed HSS model parameters for hard clay soil used in the 3D FDM analysis are listed in Table 6.1. One can refer to Benz (2007) for more detailed illustrations of the HSS parameters and the model itself.

The SEM construction process was modeled in a step-wise manner. At each stage, a one-round-length thick ground zone is deactivated and the “zone relax” option (Itasca Consulting Group Inc., 2019) is adopted to simulate gradual excavation of the material. Within the same phase, a liner element representing the initial support is activated behind the face. A linear elastic material model was assigned to the lining integrating the aging effect of shotcrete strength. The main parameters of the shotcrete lining are listed in Table 1. Although using an advanced nonlinear shotcrete model can consider the stress redistribution and reduce internal loads in the lining (Paternesi et al., 2017a; Schweiger et al., 2017), the nonlinear properties are usually difficult to define thus hard to implement in practice. Assuming an elastic behavior of shotcrete material might lead to an overestimation of the structural forces, the strategy of reliability analysis and optimization in this study is still valid. A time-dependent liner stiffness was implemented by gradually increasing the material characteristics. The relationship between shotcrete age and distance from the excavation face is described by:

$$T_i = \frac{i \cdot RL}{AR} \quad (6.1)$$

where T_i is the shotcrete age at i^{th} round behind the top heading/invert excavation face. RL is the round length adopted and AR is the advance rate, here $AR = 0.125 \text{ m/hr}$ is assumed.

The evolution of shotcrete compressive strength and corresponding elastic modulus is described according to the recommendation from the CEB-FIP model code 2010 (*fib Model Code for Concrete Structures 2010*, 2013):

$$f_c(T) = \beta_{cc}(T) \cdot f_c \quad (6.2)$$

$$\beta_{cc}(T) = \exp \left\{ s \cdot \left[1 - \left(\frac{28}{T} \right)^{0.5} \right] \right\} \quad (6.3)$$

$$E_c = E_{c0} \cdot \alpha_E \cdot \left(\frac{f_c}{10}\right)^{1/3} \quad (6.4)$$

$$E_c(T) = \beta_{cc}(T) \cdot E_c \quad (6.5)$$

where $f_c(T)$ is the mean compressive strength in Mpa at an age T in days, f_c is the mean compressive strength at an age of 28 days, $\beta_{cc}(T)$ is a coefficient of strength development and s is a coefficient that depends on the type of cement ($s=0.25$ for normal and rapid hardening cement). E_c is Young's modulus in MPa at the concrete age of 28 days, $E_{c0} = 21.5 \times 10^3$ MPa and $\alpha_E = 1.0$ for quartzite aggregates.

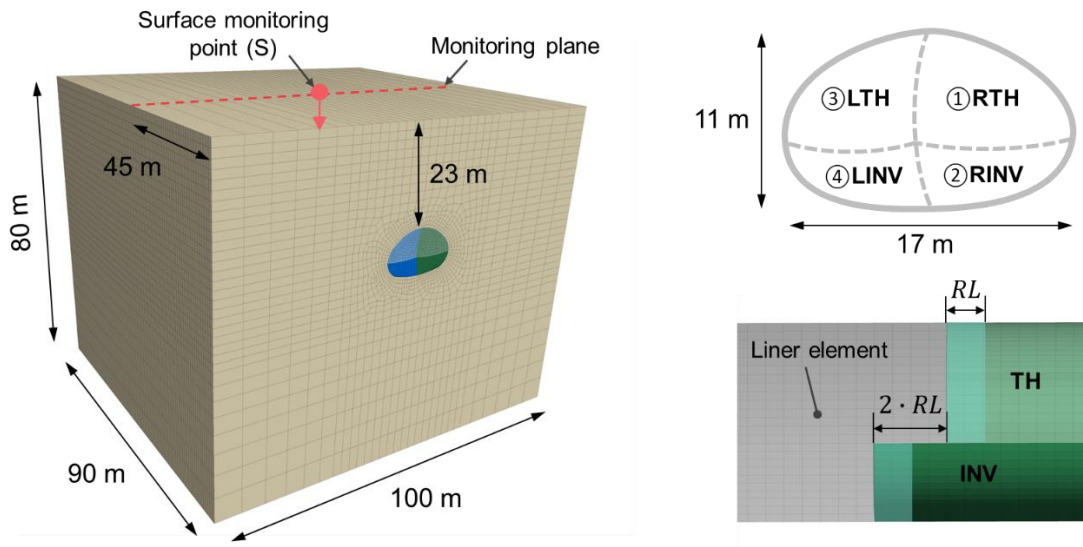


Figure 6.1 3D Finite-difference (FD) modeling.

Table 6.1 Model parameters of HSS soil and shotcrete lining.

Parameter	Description	Value
γ [kN/m ³]	Total unit weight of soil	20
E [MPa]	Young's modulus of soil	28
ν	Poisson's ratio of soil	0.35
ϕ' [°]	Internal friction angle of soil	25
c' [kPa]	Effective cohesion of soil	Variable
E_{50}^{ref} [MPa]	Secant modulus of soil	Variable

E_{ur}^{ref} [MPa]	Unload/reload modulus of soil	$3 \times E_{50}^{ref}$
m	Power for stress-level dependency of soil stiffness	0.8
p^{ref} [kPa]	Reference pressure of soil	100
ν_{ur}	Unload/reload Poisson's ratio of soil	0.2
K_0^{NC}	K_0 -value for normal consolidation of soil	0.55
R_f	Failure ratio of soil	0.9
E_0^{ref} [MPa]	Small strain stiffness of soil	$3 \times E_{ur}^{ref}$
$\gamma_{0.7}$	Shear strain at which $G_s=0.7G_0$ of soil	2×10^{-4}
E_c [GPa]	Elastic modulus of shotcrete	Time-dependent
γ_c [kN/m ³]	Unit weight of shotcrete	23.5
ν_c	Poisson's ratio of shotcrete	0.2

In addition to the standard support measure, SEM toolbox items are usually designed to provide additional support to stabilize the opening. The type and specification of the item are designed before construction. The decision whether to use or not use these items during construction mainly depends on the actual ground condition encountered. In this study, three toolbox options were considered as shown in Figure 6.2. The face support (*FS*) included 100 mm thick shotcrete at both top heading and invert faces each round to restrict ground intrusion. The temporary invert (*TI*) option equips the top heading with temporary invert support to enable ring closure for each sub-area excavation. The temporary shell is removed during subsequent excavation steps. Given the adverse loading conditions at the cavern crown, a partial reinforcement strategy is considered by integrating lattice girder (*LG*) steel sets into the installation of the initial support. The specification and location of the steel set are depicted in Figure 6.2(c). The composite support consisting of shotcrete and steel sets was modeled via the 'equivalent section' approach and the equivalent properties were calculated according to Carranza-Torres and Diederichs (2009).

The uncertainty of soil constitutive parameters and the variability of design options were both considered in this study. The soil stiffness parameter E_{50}^{ref} and cohesion c' were considered as uncertain constitutive parameters for the following analysis. Two parameters of the shotcrete, thickness t and 28-day compressive strength f_c were considered as design variables. Only one layer of shotcrete was applied after excavation. The statistical moments and ranges of these parameters were assumed and are given in Table 6.2. The selection of round length RL is usually a key challenge for soft ground SEM thus was also considered as a variable. The three toolbox

items were set to be logical (Boolean) variables with 1/0 denoting true/false of the execution status (e.g., $FS=1$ means face support is applied during construction, and vice versa.).

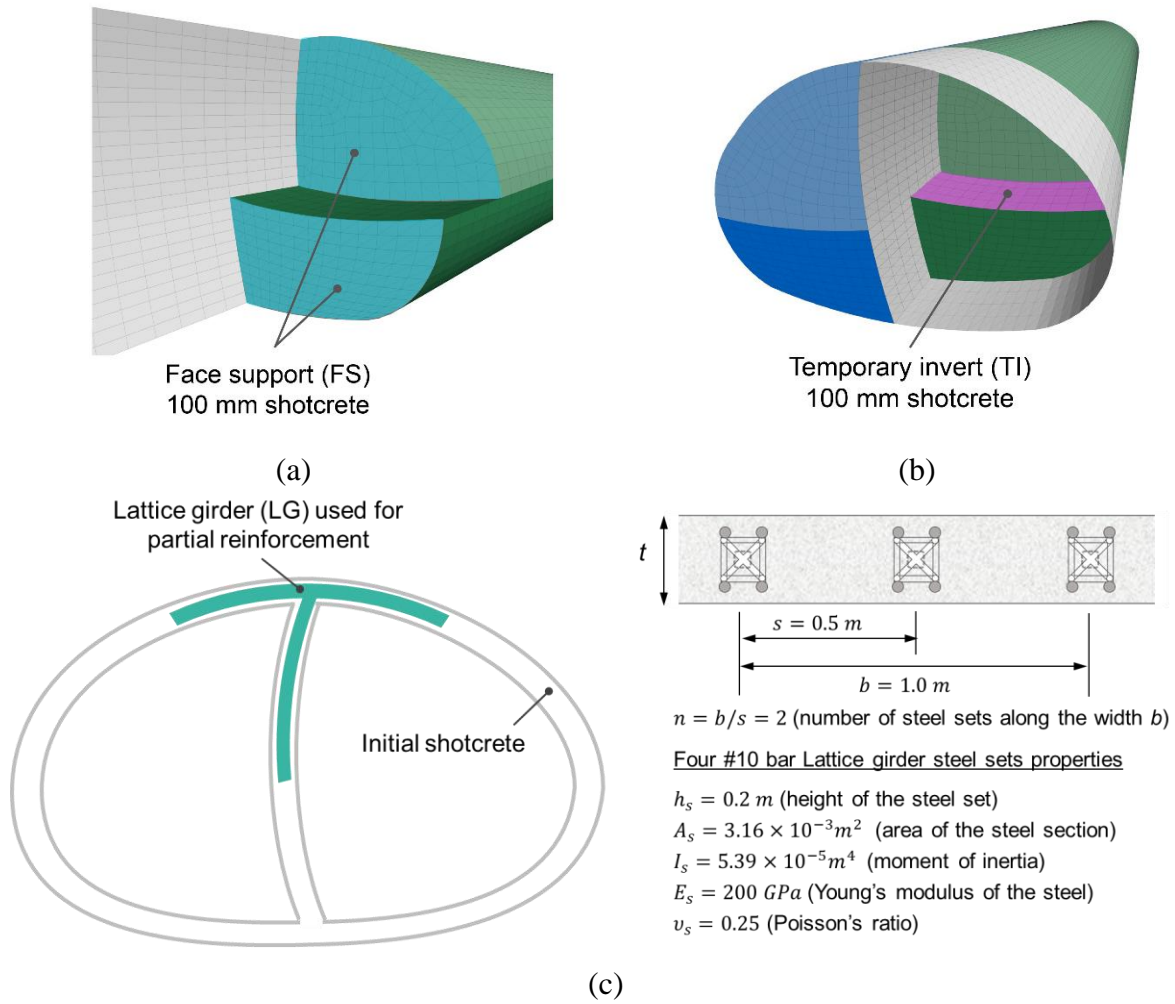


Figure 6.2. SEM design toolbox options: (a) Face support (FC), (b) Temporary invert (TI), and (c) Lattice girder (LG).

Table 6.2 Statistics of variables used in the deterministic model and probabilistic analysis.

Variable	Description	Distribution	Mean	COV	Range
E_{50}^{ref} [MPa]	Secant modulus	Lognormal	100	0.3	[20, 200]
c' [kPa]	Effective cohesion	Lognormal	100	0.3	[20, 200]

t^a [mm]	Shotcrete thickness	Uniform	300	0.4	[100, 500]
f_c [MPa]	28-day compressive strength	Lognormal	35	0.6	[20, 70]
RL [m]	Round length	Discrete		{1, 2, 3}	
FS^b	Face support	Logical		{0, 1}	
TI^b	Temporary invert	Logical		{0, 1}	
LG^b	Lattice girder reinforcement	Logical		{0, 1}	

Note:

^a Minimum t is 200 mm for the designs using LG to accommodate the installation of lattice girders.

^b Logical (Boolean) variables with 1/0 denoting true/false of the execution status. The combination between each toolbox item is not considered.

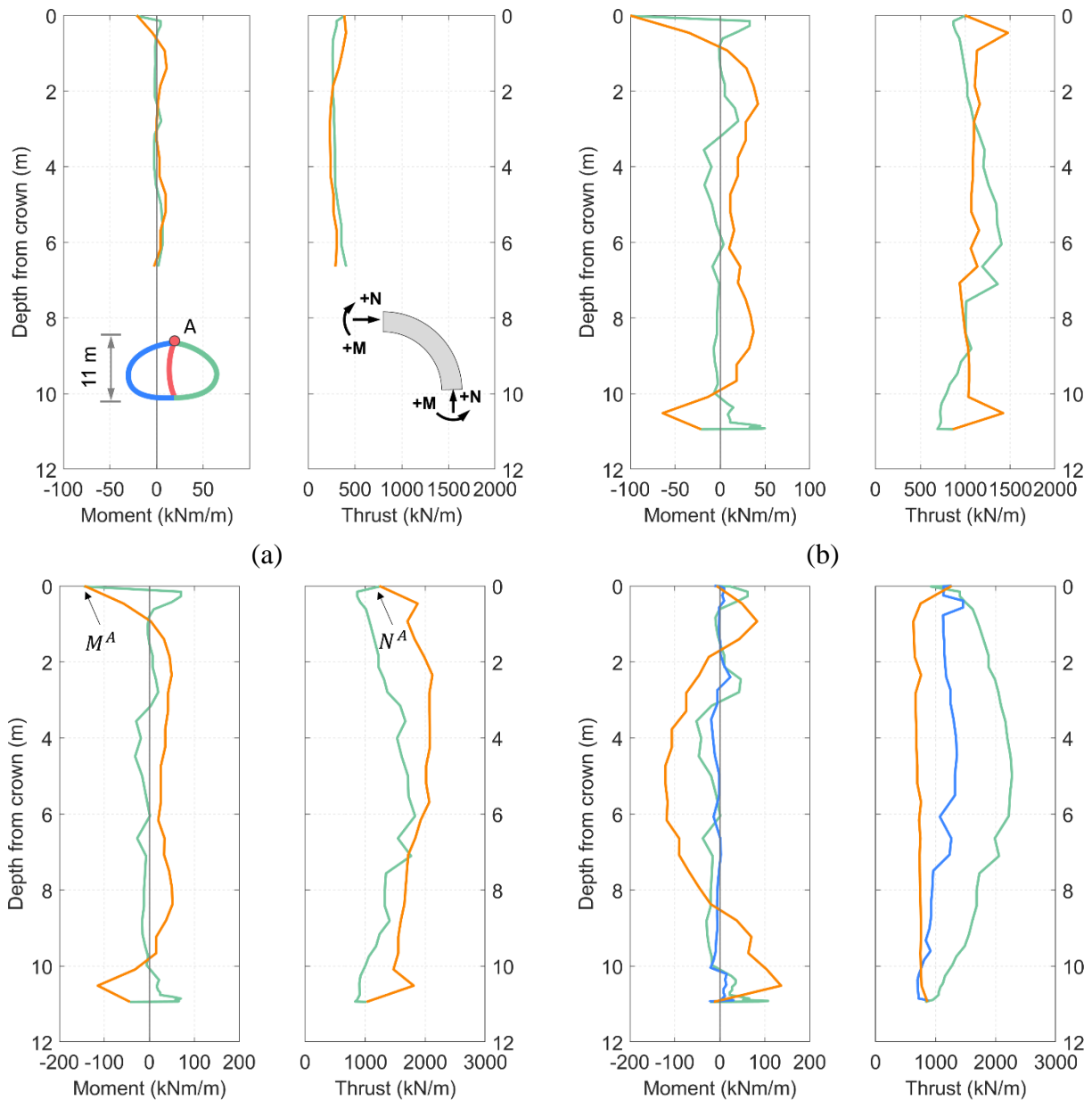
6.3.2 Key performance indicators for SEM construction

In this study, two performance indicators—liner internal forces and ground surface deformation—were considered. The liner internal forces include thrust force (N), bending moment (M), and shear force. The structural stability of an initial liner is usually evaluated by interaction diagrams (moment-thrust and shear-thrust) (Carranza-Torres and Diederichs, 2009). In this study, we only focus on the moment-thrust interaction diagram (MNID), because the initial support was mainly seen as a structural member under combined thrust force and bending moment in soft ground. The shear-thrust interaction diagram is more important in blocky rock tunnels and can be analyzed in a similar way. MNID verification is done by assessing whether the induced stresses on the liner are within allowable limits of the material strength.

Figure 6.3 shows the M and N results from a deterministic 3D FDM analysis at four SEM stages. In the deterministic analysis, the mean value of each parameter defined in Table 6.2 was used, RL was set equal to 2 m, and no toolbox items were applied. The right drift is excavated first with RTH lining installed. because of the oval shape and non-closure of the liner, the RTH liner converges and causes extension on the extrados around point A. Therefore, the moment at point A is negative as shown in Figure 6.3(a). It can be seen that as the right drift arrives and passes the monitoring plane, the bending moment and thrust force increase at both the right and temporary wall liner. The maximum moment appears at the tunnel crown because the shape of the RTH support induces a higher stress concentration around Point A. When the left drift advances close to the monitoring plane, the excavation and the installation of adjacent liners further increase the liner forces as shown in Figure 6.3(c). After the left drift is fully excavated with the liner installed, the left and right liners forming a full ring structure, which reduces the

moment born by the liners as shown in Figure 6.3(d). Meanwhile, higher thrust forces are developed within the liner section after ring closure.

For SEM construction including multiple excavation sequences as considered here, all stages and locations should theoretically be validated via MNID check because the strength of shotcrete develops with time (excavation process). However, the main purpose of this study is to demonstrate the proposed reliability framework for SEM tunnel design, instead of showing an exhaustive design procedure. Here the critical phase was selected as where the maximum moment appears. The moment and thrust at the tunnel crown (point A) obtained from when the LTH is 2 m behind the monitoring plane (M^A and N^A) were considered as the representative liner forces for the following analysis. The maximum surface settlement S_{max} at the final stage of the SEM excavation was considered as a single indicator measuring the ground deformation.



(c)

(d)

Figure 6.3. 3D FDM model results of M and N obtained from the deterministic analysis for stages at (a) RTH arrives the monitoring plane; (b) RTH is 20 m beyond the monitoring plane; (c) LTH is one round behind the monitoring plane; (d) LTH is 20 m beyond the monitoring plane (using mean values of ground parameters, $RL=2$ m, and no toolbox items).

6.3.3 Probabilistic analysis using surrogate modeling

In order to assess the reliability of SEM design under various scenarios of soil parameters and design options, it is required to conduct probabilistic analysis by repeatedly running millions of simulations. Directly using the 3D FDM model is computationally impossible. This motivates developing a surrogate model to approximate the high fidelity numerical model with relatively cheap computational cost. In this study, Polynomial-Chaos-Kriging (PCK) (Schobi et al., 2015) was employed as the surrogate modeling approach. The detailed training process and optimization settings of the PCK model can be found in (Zheng et al., 2022c).

The accuracy of the surrogate model was measured by normalized root mean square error (NRMSE) as defined by:

$$NRMSE = \sqrt{\frac{\sum_{i=1}^n (f(\mathbf{X}_i) - f_{pck}(\mathbf{X}_i))^2}{\sum_{i=1}^n (f(\mathbf{X}_i))^2}} \quad (6.6)$$

where n is the number of experiment samples, $f(\mathbf{X}_i)$ is the 3D FDM response at the sample point \mathbf{X}_i , $f_{pck}(\mathbf{X}_i)$ is the PCK model approximation.

To set up the PCK model, a total number of 250 FDM simulations with varied input parameters defined in Table 6.2 is carried out. The dataset was further split into two subsets for training and validation with ratios of 80% and 20%. The model output \mathbf{F} contains the liner internal forces M^A , N^A and the final surface settlement S_{max} . In order to select the inputs spreadings out uniformly across the available space, a design of experiments using Sobol sequences sampling method was applied. Table 3.1 presents the performance of the PCK model for both training and validation sets. The results indicate a good prediction accuracy of the PCK model for all outputs (M^A , N^A and S_{max}). Compared to the training datasets, the accuracies of the testing sets degrades by a factor of two. Still, the test model accuracies remain low with less than 3% NRMSE Eq. (6.6) for all outputs. The coefficients of determination R^2 for the training and testing sets of all outputs are around 0.99. Figure 6.4 presents the NRMSE distributions throught the input parameter space. All NRMSE points are within 5%, indicating a good accuracy of the PCK model throughout the given parameter ranges. The average computational cost for a surrogate simulation using the PCK model takes about 0.07 s, compared to 4 hrs when using the 3D FDM model on an Intel i7-9700K CPU @ 3.60GHz and 16 GB RAM desktop computer.

Table 6.3 Accuracies of the PCK model in training and testing.

Accuracy	Data set	M^A	N^A	S_{max}
R2	Training	0.99	0.99	0.99
	Testing	0.99	0.99	0.99
NRMSE (%)	Training	1.7	1.0	0.8
	Testing	2.5	1.8	1.4

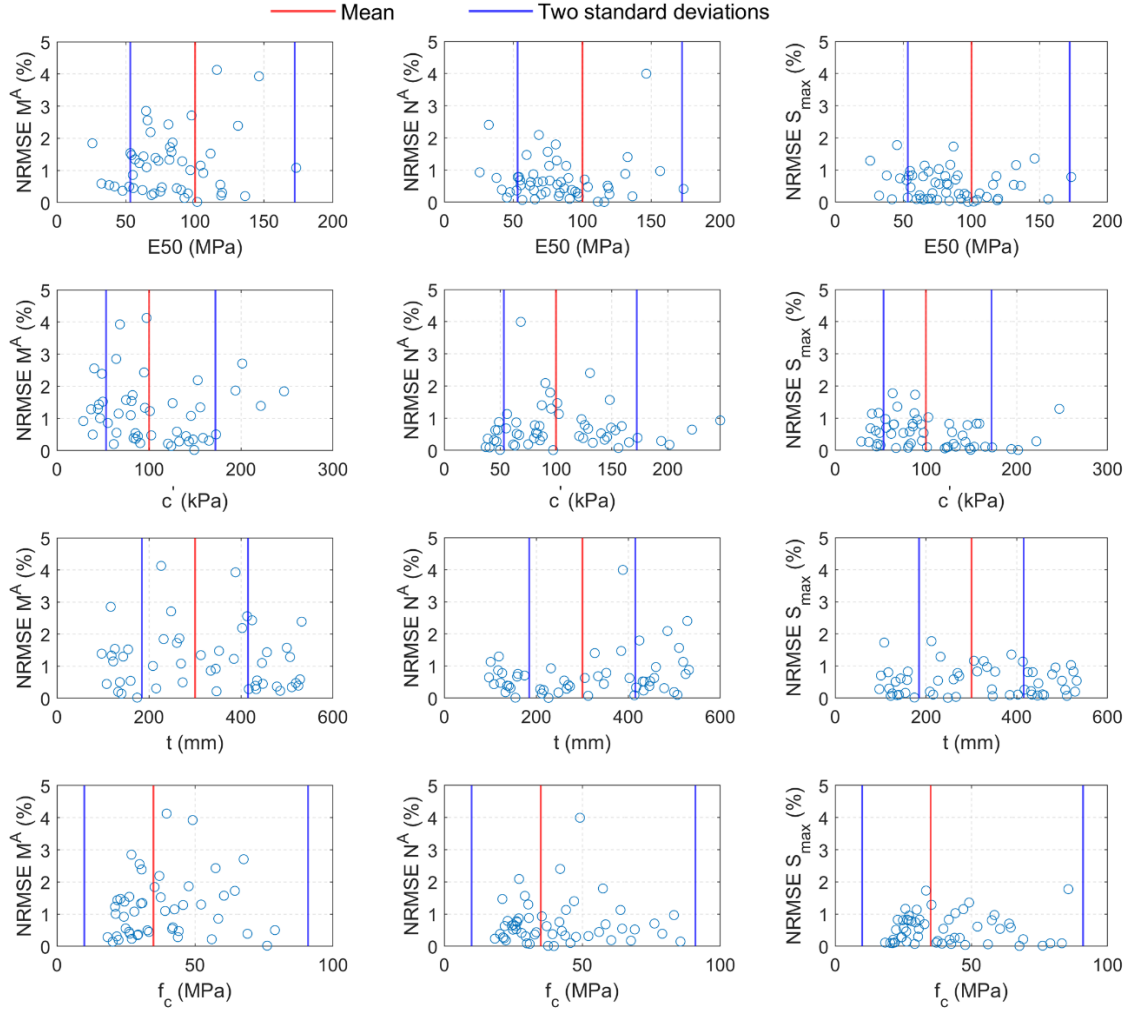


Figure 6.4 NRMSE distributions for test data throughout the surrogate input space with respect to the output M^A , N^A , and S_{max} .

6.4 Initial support design concerns using LRFD

As part of tunnel internal structures, the initial support shall be designed in accordance with the LRFD framework. According to LRFD practice in North America (AASHTO, 2017), for a specified limit state, tunnel lining design should satisfy:

$$Q_u = \sum \eta_i \gamma_i Q_i \leq \phi R_n = R_r \quad (6.7)$$

where γ_i is the load factor applied to force effects Q_i to account for load uncertainty. ϕ represents the resistance factor applied to nominal resistance R_n to account for material property and resistance analysis uncertainty. R_n is usually defined by nominal capacity using mean values of initial support strength and designed support thickness. and Q_u and R_r are the factored load and resistance. η_i is the load modifier relating to ductility, redundancy, and operational classification, $\sum \eta_i = 1$ is assumed in this analysis. Q_i represents the internal structural forces induced by ground and water loads and any type of loads the lining experiences during SEM construction. R_n is the structural capacity to resist those internal forces.

MNID is used to verify Eq. (6.7) by checking if the combination of induced moment and thrust exceeds the allowable limit of the liner capacity. The failure envelope defined by concrete design standards separates the acceptable load combinations and those that exceed elastic limits. A nonlinear capacity curve developed for fiber reinforced concrete (FRC) material was adopted as MNID in this study. Since no specific recommendation for the resistance factor of shotcrete MNID is available, the resistance factor ϕ is selected as 0.7 according to *ACI-544-7R-16 (Report on Design and Construction of Fiber-Reinforced Precast Concrete Tunnel Segments, 2016)* as shown in Figure 6.5.

The first difficulty when implementing LRFD in deterministic tunnel lining design is how to appropriately assign load and resistance factors. The determination of load effects for tunnel linings should take into account ground-structure interaction. Thus, the moment (M) and thrust forces (N) of tunnel lining are usually obtained through numerical analysis. The effects of earth loads, water loads and surcharge loads on thrust and moment are not separable. The internal forces in the lining will reflect the combined effect of all acting loads and will not be specific to any one load effect. The recommended factors of horizontal and vertical earth load are 1.35 and the recommended factor of water pressure is 1.25 according to LRFD design guidelines (AASHTO, 2017). The common practice in the current design is applying a conservative overall load factor ($\gamma_i = 1.35$ for Strength I condition) to the unfactored internal force results obtained from numerical analysis. The factored loads are then compared to the predefined concrete design capacity ($\phi R_n = \phi M, \phi N_n$) to determine any need for redesign or conventional reinforcement. This procedure is also consistent with the DA2* approach recommended by Eurocode 7 which is widely employed in European countries (CEN, 2004; Paternes et al., 2017a). However, the uncertainties of ground and liner parameters are implicitly considered in a fixed load factor that is subjectively selected. Using the same load factor for different levels of parameter uncertainty does not suggest the same reliability of the liner system.

A second issue that comes with the initial lining LRFD design is selecting characteristic values of ground properties. In LRFD design, a single set of characteristic values of ground properties is defined for numerical analysis. The common tendency is to use mean values or conservatively use 5th/20th percentile values according to the statistical information of ground parameters (Gong et al., 2016). However, the LRFD design method does not prescribe the probability of failure corresponding to the characteristic values used. Also, since characteristic ground properties influence liner thrust and moment, applying a rigid load factor γ to different characteristic ground properties does not imply the same target failure probability, and the level of conservative cannot be quantified. Figure 6.5 presents the results of factored MNID choosing different characteristic ground parameters under the design using $t=300$ mm, $f_c=35$ MPa, and without any toolbox item applied. Q_u^A and R_r^A stand for the factored loads (M^A , N^A) and the factored liner capacity at the corresponding stage, respectively. Choosing the 5th percentile of ground parameters with a 1.35 load factor applied might be far from the ground truth and lead to an over-conservative design.

300 Monte Carlo simulations (MCS) were performed by randomly selecting E_{50}^{ref} and c' from the distributions described in Table 6.2. The probabilistic result indicates that the Q_u^A calculated by the set of mean ground parameters is different from the most probable Q_u^A that is interpreted from the MCS as shown in Figure 6.5. Care should be taken when using mean ground properties to represent the most probable behavior as the difference might be substantial for a highly nonlinear system.

Furthermore, for a certain design attempt, if the section of the liner does not satisfy the safety requirement, the thickness or strength of the shotcrete can be increased, or local reinforcement can be applied. Figure 6.6 shows the results of four design attempts by varying the shotcrete thickness t . This brings another concern. To reach a safe design, increasing liner thickness/stiffness will increase liner capacity. While on the other hand, due to ground-structure interaction, thicker/stiffer structures restrain deformations around the opening and tend to attract higher loads. With amplified effects from the load and resistance factors, a converged solution for a valid LRFD design is not always guaranteed and the safety margin cannot be quantified considering the uncertainties of ground and liner properties. Applying design principles commonly valid in structural engineering may make SEM tunnels more expensive.

The conflicts or concerns described above stem from the fact that the loads and resistances are interdependent for ground-tunnel interaction problems (Langford and Diederichs, 2013; Paternesi et al., 2017a). In the context of SEM construction, tunnel lining and its surrounding ground are combined as an integrated support system, representing both sources of load and resistance at the same time.

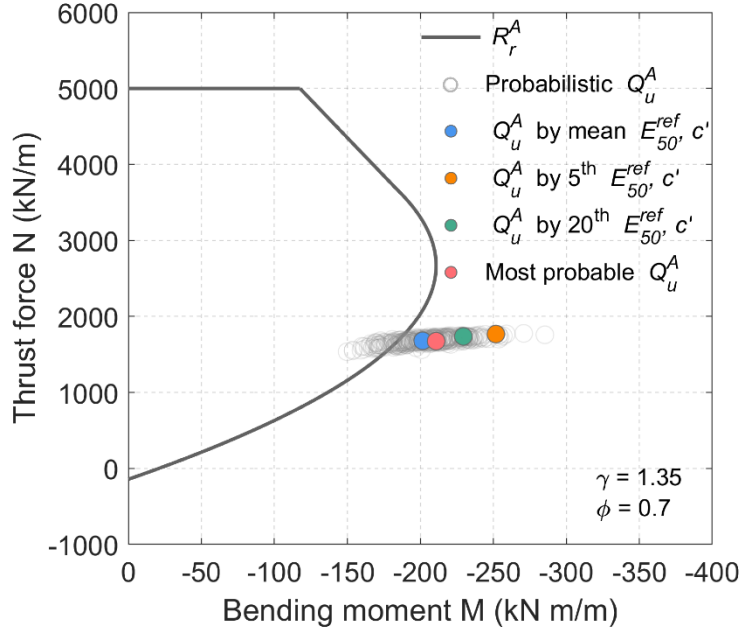


Figure 6.5. Factored MNID for various sets of characteristic ground properties and probabilistic Q_u^A from 300 MCS (for the design using $t=300$ mm, $f_c=35$ MPa, without any toolbox item applied).

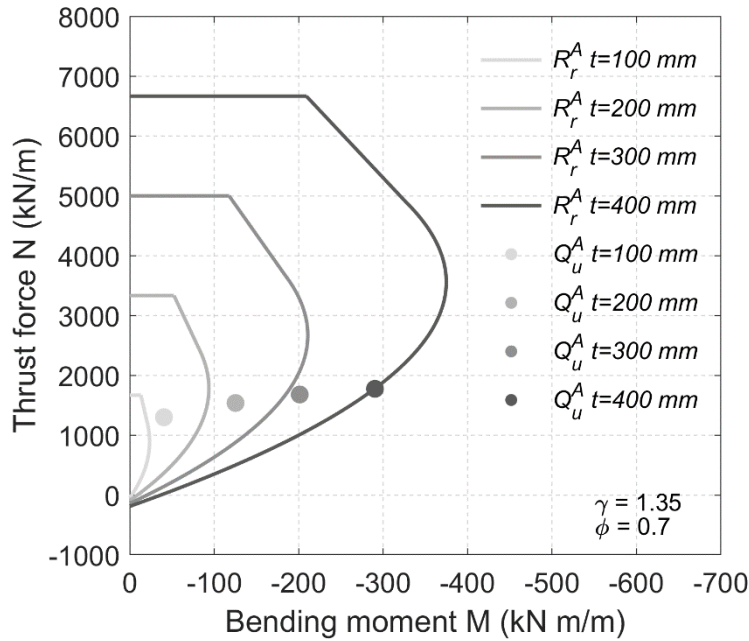


Figure 6.6. Factored MNIDs for various designs of shotcrete thickness (for the design using mean soil properties, $f_c=35$ MPa, without any toolbox item applied).

6.5 Reliability analysis of SEM-induced ground deformation and lining forces

Reliability analysis can consider the combined effects of uncertainties explicitly and provide a more consistent measure of risk. The same probability of failure calculated by reliability analysis implies the same safety margin and is invariant to uncertainty levels and design variations. Various failure modes or limit states can be considered to evaluate the system risk. For these reasons, reliability analysis is a robust complement to the current LRFD design for SEM tunnels.

Reliability analysis is defined as the quantitative assessment of the probability of failure for different limit state functions. A limit state is defined as a state beyond which a system no longer satisfies certain performance criteria (Phoon and Ching, 2018). Two limit state functions were defined in this study based on the key performances of SEM construction:

$$g_1(\mathbf{x}, \mathbf{d}) = \begin{cases} 1 & \text{if } Q_n^A(\mathbf{x}, \mathbf{d}) \in D_s \\ 0 & \text{if } Q_n^A(\mathbf{x}, \mathbf{d}) \in D_f \end{cases} \quad (6.8)$$

$$g_2(\mathbf{x}, \mathbf{d}) = S_{limit} - S_{max}(\mathbf{x}, \mathbf{d}) \quad (6.9)$$

where \mathbf{x} is a vector of random ground parameters, \mathbf{d} is a vector of design variables. Limit state function g_1 corresponds to the strength limit state and g_2 corresponds to the service limit state as defined by (AASHTO, 2017). Limit state g_1 is represented by an indicator function characterizing the structural stability of the initial lining. As illustrated in Figure 6.8, if the calculated nominal (unfactored) load Q_n^A plots outside the nominal (unfactored) capacity envelope R_n^A , the limit state function g_1 equals zero. For the designs using corner reinforcement, forces were first calculated for the composite section with given input parameters, and then the distributed forces of the shotcrete section were used to compare to the shotcrete capacity. The second limit state function g_2 is defined as the difference between the allowable surface settlement S_{limit} and the calculated maximum surface settlement S_{max} . An allowable 15 mm surface settlement S_{limit} is assumed in this study. In practice, this limit can be the tolerance value required by the owner. The probability of failure P_f and reliability index β of each limit state are defined as:

$$P_{fi} = P(g_i(\mathbf{x}, \mathbf{d}) \leq 0) \quad (6.10)$$

$$\beta_i = \Phi^{-1}(1 - P_{fi}) \quad (6.11)$$

where Φ^{-1} is the inverse of the standard normal cumulative distribution function. For a certain design \mathbf{d} , MCS was used to evaluate the P_{fi} and β_i by repeatedly running the surrogate model

using different sets of input parameters \mathbf{x} . The estimation of Eq. (6.10) can be obtained by calculating the fraction of samples that fall into the failure domain $\frac{N_{fail}}{N}$.

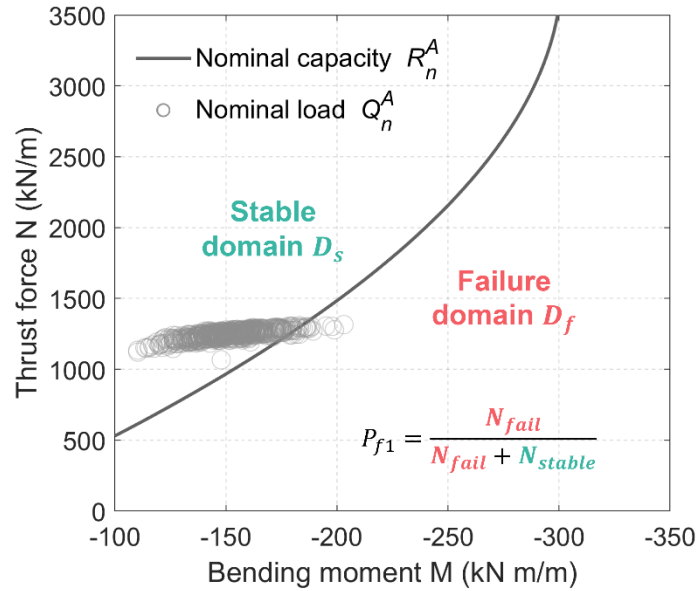


Figure 6.7. Illustration of the limit state function g_1 using 500 MCS by varying ground parameters with constant $t=300$ mm and $f_c=35$ MPa.

Table 6.4 summaries the calculated reliability results of a base design example using various E_{50}^{ref} , c' , t , and f_c through MCS. Considering the quality of shotcrete construction, t , and f_c were also assigned as random variables for the reliability analysis. Lognormal distributions were assumed for t and f_c with mean values of 300 mm and 35 MPa, respectively. The COV of t was conservatively assumed to be 0.4 according to Bjureland et al. (2019) and the COV of f_c was assumed to be 0.25 according to Badr (2016). Figure 6.8 shows the convergence of the MCS for each limit state g_1 and g_2 using the base design. It can be observed that about 1×10^5 simulations are needed to reach stable failure probabilities for both g_1 and g_2 limit states.

Table 6.4 Reliability results of the base design with various E_{50}^{ref} and c' using $t=300$ mm and $f_c=35$ MPa.

RL	FS	TI	CR	P_{f1}	β_1	P_{f2}	β_2
2.0 m	0	0	0	0.21	0.78	0.02	1.96

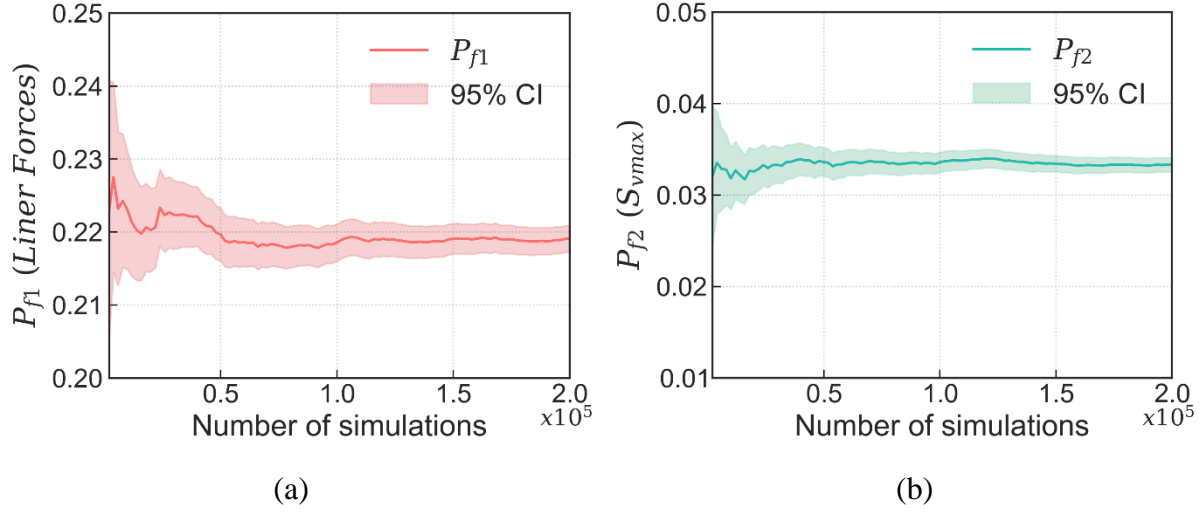
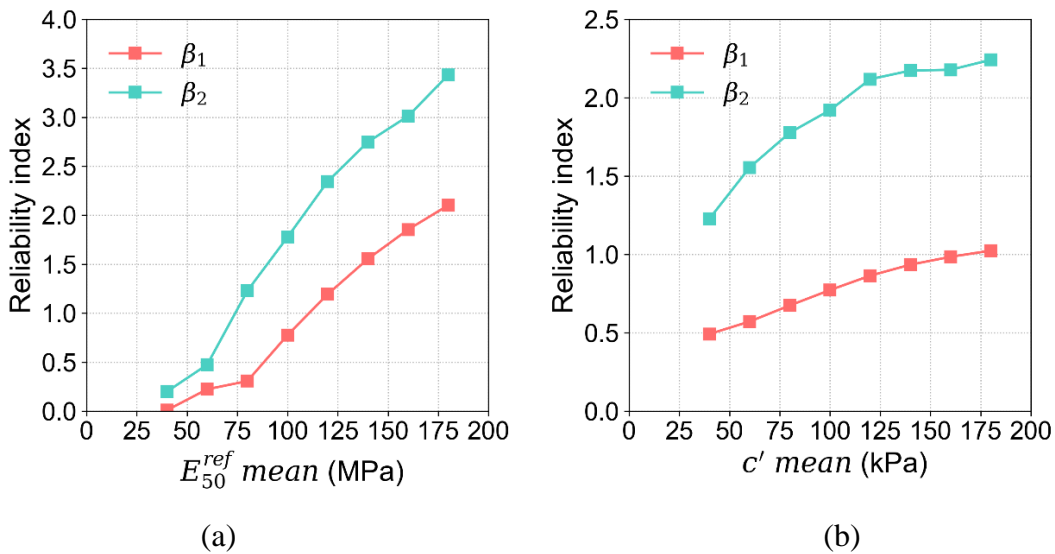


Figure 6.8. Convergence of MCS for (a) limit state g_1 and (b) limit state g_2 for the base design.

To quantify the influence of ground properties on the reliability results, varied mean and COV values of E_{50}^{ref} and c' were evaluated for each limit state. Figure 6.9 shows the reliability results for the base design using various mean and COV values of E_{50}^{ref} and c' . Both reliability indices increase with the increase of E_{50}^{ref} and c' means and decrease with the increase of COVs, indicating higher ground stiffness and strength properties increase the liner stability and reduce the ground deformation. The liner internal forces and deformations are attributed to the ground stress and strain redistribution induced by SEM tunneling. The magnitude and distribution of the liner forces are mainly influenced by ground-liner interaction. Given the condition of $K_0=0.55$, excavation induces different levels of stress reduction developing at the tunnel crown, invert, and springline. Smaller E_{50}^{ref} or c' causes larger uneven deformations around the opening, increasing the bending moment withstood by the liner, thus reducing the structural reliability. E_{50}^{ref} shows a higher sensitivity to both reliability indices.



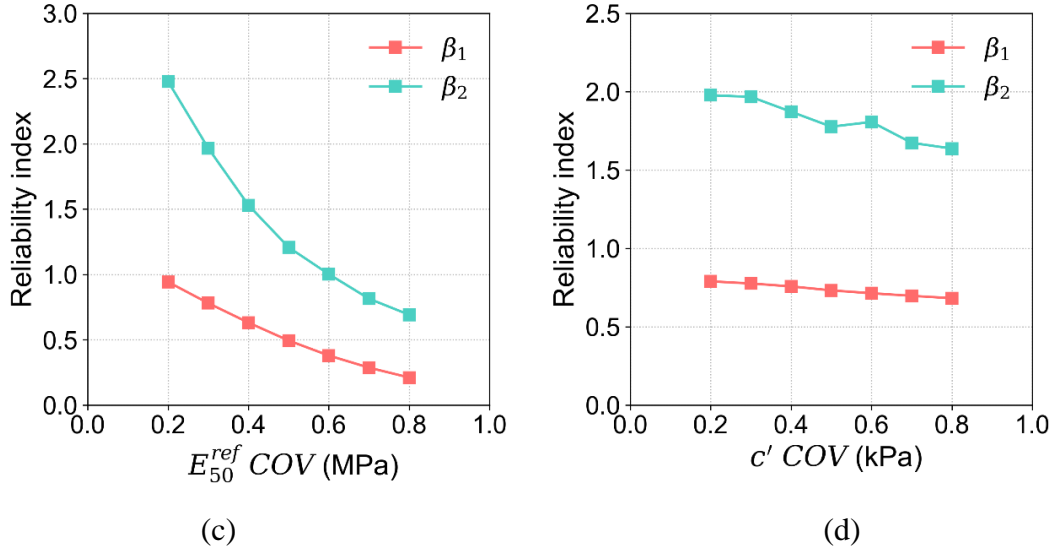


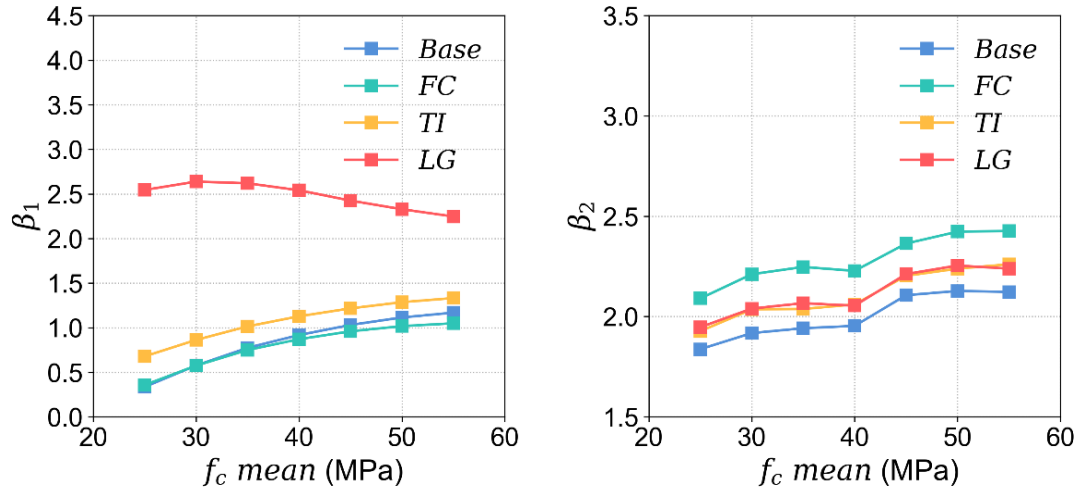
Figure 6.9. Influence of (a) E_{50}^{ref} mean, (b) c' mean, (c) E_{50}^{ref} COV, and (d) c' COV on the reliability indices (other parameters are the same as the base design).

From a design perspective, the selection of shotcrete strength and thickness has a crucial influence on the failure probability and depends on whether a certain reliability level is achieved. As shown in Figure 6.10(a) and (b), when mean values of f_c and t increase, the reliability of liner forces increases. It indicates that when applying thicker/stronger shotcrete, the advantage of increasing the liner capacity outweighs the disadvantage of attracting higher loads in this case. Using 28-day compressive strength higher than 40 MPa exhibits a degraded contribution to increasing the liner reliability. Increasing the shotcrete thickness t was found to be an efficient way to increase both β_1 and β_2 . Extremely low liner reliability was observed when using a shotcrete thickness of less than 200 mm. As shown in Figure 6.10(c), increasing the RL induces higher tunnel convergence and ground deformation, which is unfavorable for deformation control. However, higher ground relaxation reduces the loads shared by the liner. Therefore, with the increase of RL , β_1 increases and β_2 decreases.

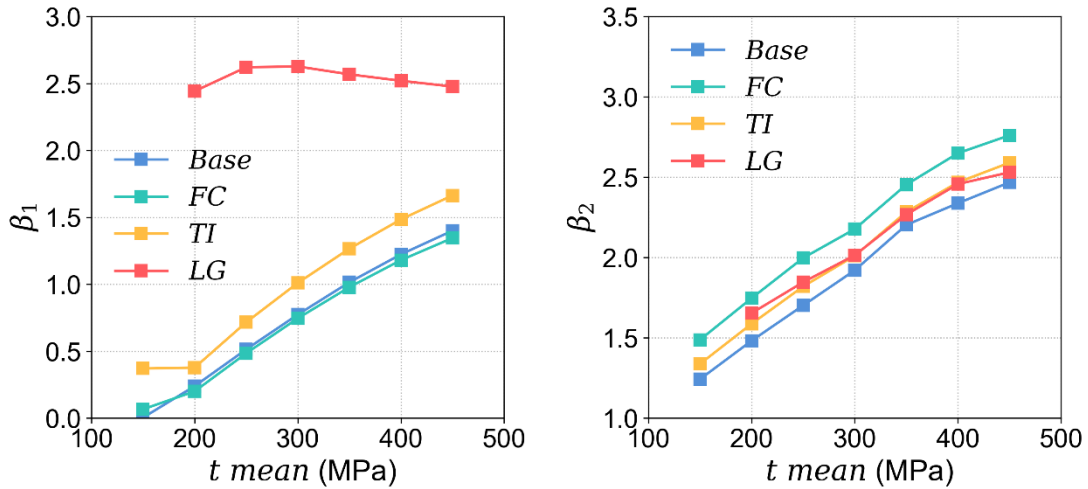
Applying different SEM toolbox items also influences the reliability results. All toolbox item designs show similar trends as the base design for β_1 except for LG . Using LG provides a constant high level of β_1 (~ 2.5) against different f_c , t , and RL . In this case, increasing the shotcrete thickness or strength is not an economical choice for the liner stability when using LG . Incorporating TI into the initial lining construction enables an early ring closure, reducing the ground deformation. In addition, the early formation of a full-ring structure increases the liner thrust force, which is favorable for structural stability as the normal stress increases and the tension zone reduces within the lining cross-section. Therefore, a moderate increase of β_1 is also observed for TI designs. For the settlement reliability β_2 , all toolbox item designs exhibit similar trends and perform better than the base design. Applying FC is the best option to increase β_2 .

Given a target reliability reference, these charts can assist designers to select appropriate design methods with a quantitative measure of safety margin. The target reliability for a

geotechnical system is usually in the range of 2.0 to 4.0 (Phoon and Ching, 2018; Zhang et al., 2012). The selection of target reliability index is problem-dependent, depending on experiences on similar projects, the significance of the structure, and the consequences of failure (Lü et al., 2017a). Recommendations in related codes can also be referenced (CEN, 2007; Diamantidis, 2001; ISO2394, 2015).



(a)



(b)

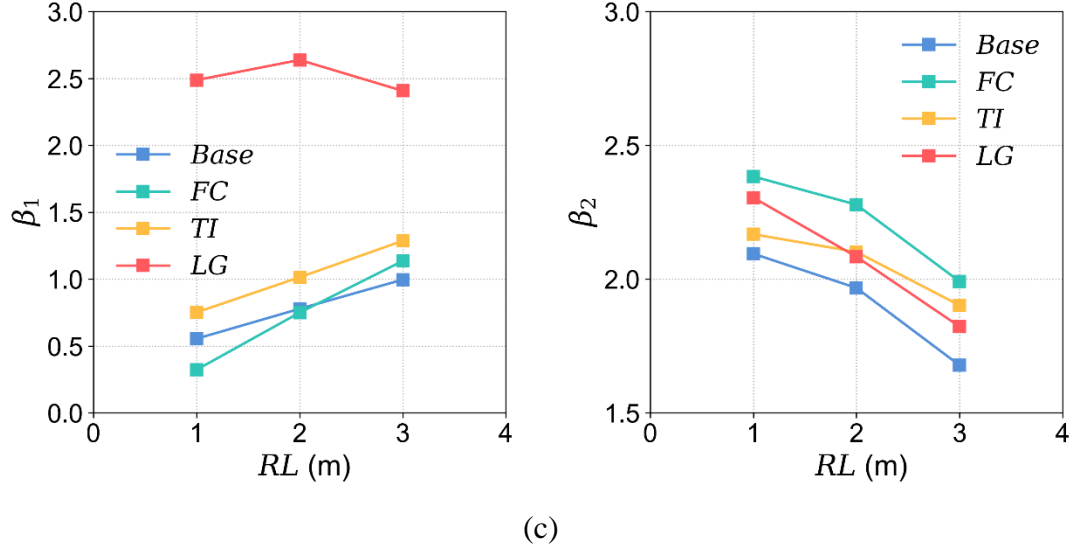


Figure 6.10. Influence of (a) f_c and (b) t on the reliability indices (using Design 2 and ground parameter variabilities defined in Table 1).

In the LRFD design for initial support, the uncertainties of ground and structure parameters are implicitly considered by fixed load and resistance factors, which cannot reflect the influence of various parameter uncertainty levels. Selecting a set of deterministic characteristic values of ground and structural parameters using the LRFD method does not quantify the safety margin of the initial support design. The reliability analysis, however, explicitly considers the uncertainty of each parameter and provides a quantitative measure of risk. In addition, both liner and settlement reliabilities are considered at the same time in the reliability analysis.

6.6 Conclusions

This paper presents a reliability-based procedure for SEM tunnel design. The 3D FDM model was used to simulate ground-structure interaction and the 3D effects induced by SEM construction. A PCK surrogate model was used to approximate the 3D FDM model to perform the probabilistic analysis. The uncertainty of ground parameters and the variability of design options were both considered in the analysis. Full reliability analysis was performed based on two limit states—the lining structural stability and the ground surface settlement. The probability of failure and reliability index were calculated by MCS. With various ground parameters and designated combinations of design variables, the reliability levels were evaluated and compared. The main conclusions from this study are summarized below:

- For the given design example, the results indicate that both two reliability indices increase with means of E_{50}^{ref} and c' and decrease with COVs of E_{50}^{ref} and c' . Compared to c' , E_{50}^{ref} is more influential to both liner and settlement reliability indices

- The reliability of liner forces β_1 increases as the means of shotcrete f_c or t increases. Increasing t is an efficient way to increase both β_1 and β_2 . Reducing the excavation RL increases β_2 and decreases β_1 in general. Applying LG is the most efficient way to achieve a high level of β_1 . Using FC is the best option to increase β_2 . Applying any SEM toolbox item increases β_2 compared to the base design.
- The influence of various parameter uncertainty levels cannot be considered by the LRFD method for SEM initial lining design. Considering the correlation between liner forces, liner resistance, and ground deformation, the reliability analysis provides a quantitative measure of risk in terms of liner stability and ground deformation, providing a complementary tool for the current LRFD design when detailed knowledge of parameter uncertainty is available.

6.7 Acknowledgments

Partial funding for this study was provided by Skanska and Traylor Bros., by the Center of Underground at the Colorado School of Mines, and by the University Transportation Center for Underground Transportation Infrastructure (UTC-UTI) at the Colorado School of Mines under Grant No. 69A3551747118 from the U.S. Department of Transportation (DOT). The opinions expressed in this paper are those of the authors and not of the DOT.

CHAPTER 7

CONCLUSIONS AND RECOMMENDATIONS FOR FUTURE RESEARCH

7.1 Conclusions

The research completed and presented in this thesis demonstrates how the proposed methodologies can aid current SEM design and construction by employing a surrogate model accurately and efficiently capturing 4D SEM responses, incorporating uncertainties in geotechnical parameters, and updating the knowledge of risk and design performance along with the construction progress. The primary conclusions drawn from this thesis are summarized in the following paragraphs.

The successful practice of the RCTC SEM cavern construction indicates a relatively homogeneous behavior of the Fernando formation and the ground surface settlement can be limited to 20 mm. When adopting SEM for urban shallow tunnel construction, the ground deformation pattern is influenced by surrounding infrastructure. Relatively uniform vertical subsurface movements were identified during the side drifts excavation that mainly results from the shallow cover depth, the ovate excavation shape, and the bracing effect from subsurface structures. When SEM is combined with a mechanized tunneling approach where a routine removal of TBM segments is needed, it is recommended to start with dislodging the key segment, followed by removing the remainder of segments one at a time in a reverse ring building sequence by shearing the circumferential joint plastic dowels. The compatibility of SEM round length and PCTL width will influence the overall SEM performance and needs to be considered. Extensive instrumentation is the key to urban SEM construction. Monitoring alone and simple visualizations are not sufficient. Real-time (or near real-time) analysis with high-quality and functional analyses during SEM construction is recommended as urban environments are highly sensitive to deformations and timely feedback and understanding of ground and structural behavior is crucial.

The capability and performance of four surrogate methods in approximating 3D FDM simulation of SEM tunneling were examined. PCK-SEQ and PCK-OPT surrogates were demonstrated to be the best surrogate models to capture the complex 3D FDM behavior of SEM construction. The best model-average NRMSE and ϵ_{val} of the two PCK models are around 3%. The PCK surrogate models also show good generalization between the training and the testing datasets. When examining the surrogate accuracy throughout the input parameter space, it is found that no errors were greater than 10% NRMSE and that 90% of the errors were less than 5% NRMSE for the six model outputs for the PCK models. Relatively higher NRMSEs are observed in the convergence outputs than those in the ground settlement outputs. This is mainly because the variations of the ground settlement magnitudes are generally 2-5 times higher than those of the convergence magnitudes. Therefore, the changing pattern of the convergence outputs is more difficult for the surrogate model to learn. The computation time for a single SEM prediction using a unique set of input parameters reduces from 20 hrs for the 3D FEM to less than one second for the PCK surrogates.

A surrogate-based Bayesian analysis was developed for updating the ground parameters and ground and structural deformations during the RCTC SEM construction. The results from Bayesian analysis indicate that mean values of $Tf2-E_{50}^{ref}$, $Tf2-E_0^{ref}$, and $Tf2-c'$ increase from prior estimates and to posterior Phase V estimates of $55 \rightarrow 90$ MPa, $480 \rightarrow 553$ MPa, and $170 \rightarrow 238$ MPa, respectively. The uncertainty of the estimated parameter is highly reduced which translates into reduced risk because prediction uncertainty is gradually reduced. The variance of the predicted deformations reduces considerably when incorporating the field observations during the left drift excavation. However, the initial updating phases underestimate the deformations induced by the subsequent excavation, mainly because the magnitudes of measured ground and structural deformations are relatively small. In general, when incorporating the observations after all side drifts are excavated, the mean values of the updated predictions for the subsequent excavations show satisfactory agreement with the observed measurements. The proposed Bayesian approach progressively quantifies the uncertainty associated with the predicted SEM-induced deformations. Given allowable deformation limits, the margin of safety can be evaluated, providing a quantitative assessment of risk, based on which possible design modifications or optimizations can be implemented promptly.

Through an illustrative example, several concerns raised by using the LRFD method for SEM initial support design were discussed. A surrogate-based reliability approach was developed to quantify uncertainties and provide a consistent measure of risk. Two limit state functions—the initial lining capacity and ground surface settlement—were considered and the reliability level of each limit state was evaluated for the given SEM case. The results from the reliability analysis indicate that both two reliability indices increase with an increase in ground E_{50}^{ref} or c' means and decrease in COVs. The lining structural reliability β_1 increases as the f_c or t of the shotcrete increases. Reducing RL or applying additional SEM toolbox items can both increase the reliability of ground settlement β_2 . LG is demonstrated to be the most efficient way to increase the lining structural reliability β_1 . Optimal SEM design options can be searched based on target reliability references.

7.2 Recommendations for future research

In terms of characterizing the initial lining behavior when using SEM in shallow soft ground tunnels, due to the lack of lining stress instrumentation in the RCTC project, the development of the lining stresses has not been studied in this work. It would be of great value to monitor the stresses developed in initial support during SEM construction for future projects. This could also provide another type of observation to be compared to 3D FDM model responses, improving the computational realization of actual ground-structural interactions.

Surrogate modeling is a special case of supervised machine learning, i.e., training a predictive model based on the labeled training dataset generated from computational simulations. Depending on the structure of data and complexity of the input-output relationship, no single learning method can outperform other methods on all datasets. The performance of the PCK surrogate model needs to be further examined on different SEM datasets (e.g., different geometries, excavation sequences, cover depths, constitutive models) and possibly with different input/output configurations.

Instead of using one-shot sampling in the design of experiments, adaptive sampling methods (Fuhg et al., 2021) could be integrated into the current surrogate framework to further reduce the 3D FDM simulations needed to construct an accurate surrogate model. An adaptive training process could be developed to actively add training samples in regions where the surrogate model can learn the most and in regions identified by the updated knowledge of ground conditions.

Incorporating the spatial variability of ground parameters into the current 3D FDM model by using geostatistical methods or random field methods is of our great research interest. The general desire to computationally model with spatial variability begets the use of surrogate modeling even more due to more input variables involved and the consequent time intensity. However, the high input dimension created by the variability in both space and magnitude of parameters would bring a major concern for the surrogate model training and the following probabilistic back-analysis procedure.

As design optimization is another critical concern for SEM tunneling, more design variables (e.g., round length, trailing distance, shotcrete strength, various pre-support measures) could be incorporated into the current probabilistic framework. Then a surrogate model can be trained based on different combinations of design variables, coupled with various ground conditions, creating a more versatile model that can be used for quantitative design optimization during SEM construction.

Searching for the optimal design option/options using the reliability analysis can be further leveraged by incorporating reliability-based optimization design (RBDO) approaches. RBDO formulates design optimizations subjected to reliability constraints that can be estimated by probabilistic approaches (Aoues and Chateauneuf, 2010; Enevoldsen and Sørensen, 1994; Tu et al., 1999). Incorporating RBDO into the observational method would further assist progressive design during SEM construction.

REFERENCES

- AASHTO, 2017. LRFD Road Tunnel Design and Construction Guide Specifications.
- Abaqus, D., 2011. ABAQUS/Standard Analysis User's Manual.
- ACI-544-7R-16 Report on Design and Construction of Fiber- Reinforced Precast Concrete Tunnel Segments, 2016.
- Adeli, H., 2001. Neural networks in civil engineering: 1989--2000. *Comput. Civ. Infrastruct. Eng.* 16, 126–142.
- Ağbay, E., Topal, T., 2020. Evaluation of twin tunnel-induced surface ground deformation by empirical and numerical analyses (NATM part of Eurasia tunnel, Turkey). *Comput. Geotech.* <https://doi.org/10.1016/j.compgeo.2019.103367>
- Agostinetti, N.P., Malinverno, A., 2010. Receiver function inversion by trans-dimensional Monte Carlo sampling. *Geophys. J. Int.* 181, 858–872. <https://doi.org/10.1111/j.1365-246X.2010.04530.x>
- Allen, T.M., 2012. AASHTO geotechnical design specification development in the USA. *Mod. Geotech. Des. Codes Pract.* 243–260.
- Allison, R., Dunkley, J., 2014. Comparison of sampling techniques for bayesian parameter estimation. *Mon. Not. R. Astron. Soc.* 437, 3918–3928. <https://doi.org/10.1093/mnras/stt2190>
- Antony, J., 2014. Design of experiments for engineers and scientists. Elsevier.
- Aoues, Y., Chateaufneuf, A., 2010. Benchmark study of numerical methods for reliability-based design optimization. *Struct. Multidiscip. Optim.* 41, 277–294. <https://doi.org/10.1007/s00158-009-0412-2>
- Au, S.-K., Beck, J.L., 2001. Estimation of small failure probabilities in high dimensions by subset simulation. *Probabilistic Eng. Mech.* 16, 263–277.
- Badr, A., 2016. Statistical Analysis of the Variability in Shotcrete Strength. *Glob. J. Res. Eng. E Civ. Struct. Eng.* 16, 12–23.
- Baecher, G.B., Christian, J.T., 2005. Reliability and statistics in geotechnical engineering. John Wiley & Sons.
- Benz, T., 2007. Small-strain stiffness of soils and its numerical consequences, University of Stuttgart.
- Berg, J.P. van der, Clayton, C.R.I., Powell, D.B., 2003. Displacements ahead of an advancing NATM tunnel in the London clay. *Géotechnique* 53, 767–784.
- Berveiller, M., Sudret, B., Lemaire, M., 2006. Stochastic finite element: A non intrusive approach by regression. *Eur. J. Comput. Mech.* 15, 81–92. <https://doi.org/10.3166/remn.15.81-92>
- Bhosekar, A., Ierapetritou, M., 2018. Advances in surrogate based modeling, feasibility analysis, and optimization: A review. *Comput. Chem. Eng.* 108, 250–267. <https://doi.org/10.1016/j.compchemeng.2017.09.017>
- Bjureland, W., Johansson, F., Sjölander, A., Spross, J., Larsson, S., 2019. Probability distributions of shotcrete parameters for reliability-based analyses of rock tunnel support. *Tunn. Undergr. Sp. Technol.* 87, 15–26. <https://doi.org/10.1016/j.tust.2019.02.002>
- Blatman, G., Sudret, B., 2011. Adaptive sparse polynomial chaos expansion based on least angle regression. *J. Comput. Phys.* 230, 2345–2367. <https://doi.org/10.1016/j.jcp.2010.12.021>
- Bobet, A., 2001. Analytical solutions for shallow tunnels in saturated ground. *J. Eng. Mech.* 127,

- 1258–1266.
- Box, G.E.P., 1951. Wilson. KB [1951] On the Experimental Attainment of Optimum Conditions. *J. R. Stat. Soc. Ser. B* 13, 1–45.
- Brinkgreve, R.B.J., Engin, E., Swolfs, W.M., 2013. Plaxis 3D 2013 user manual. Delft, the Netherlands.
- Brodback, C., Penrice, D., Coibion, J., Frederick, C., 2018. Downtown Bellevue Tunnel—Analysis and Design of SEM Optimization, in: *Proceedings of the North American Tunneling Conference 2018*.
- Brooks, S.P., Gelman, A., 1998. General methods for monitoring convergence of iterative simulations. *J. Comput. Graph. Stat.* 7, 434–455.
- Broomhead, D.S., Lowe, D., 1988. Radial basis functions, multi-variable functional interpolation and adaptive networks.
- Buljak, V., Maier, G., 2011. Proper orthogonal decomposition and radial basis functions in material characterization based on instrumented indentation. *Eng. Struct.* 33, 492–501.
- Cai, G.Q., Elishakoff, I., 1994. Refined second-order reliability analysis. *Struct. Saf.* 14, 267–276.
- Cao, B.T., Obel, M., Freitag, S., Mark, P., Meschke, G., 2020. Artificial neural network surrogate modelling for real-time predictions and control of building damage during mechanised tunnelling. *Adv. Eng. Softw.* 149, 102869. <https://doi.org/10.1016/j.advengsoft.2020.102869>
- Cao, W., Jiang, Y., Sakaguchi, O., Li, N., Han, W., 2021. Predication of Displacement of Tunnel Rock Mass Based on the Back-Analysis Method-BP Neural Network. *Geotech. Geol. Eng.* 0. <https://doi.org/10.1007/s10706-021-01874-0>
- Carlo, C.M., 2004. Markov chain monte carlo and gibbs sampling. *Lect. notes EEB* 581, 540.
- Carranza-Torres, C., Diederichs, M., 2009. Mechanical analysis of circular liners with particular reference to composite supports. For example, liners consisting of shotcrete and steel sets. *Tunn. Undergr. Sp. Technol.* 24, 506–532.
- Carranza-Torres, C., Fairhurst, C., 2000. Application of the convergence-confinement method of tunnel design to rock masses that satisfy the Hoek-Brown failure criterion. *Tunn. Undergr. Sp. Technol.* 15, 187–213.
- Carranza-Torres, C., Rysdahl, B., Kasim, M., 2013. On the elastic analysis of a circular lined tunnel considering the delayed installation of the support. *Int. J. Rock Mech. Min. Sci.* 61, 57–85. <https://doi.org/10.1016/j.ijrmms.2013.01.010>
- ÇELİK, S., 2017. Comparison of Mohr-Coulomb and Hardening Soil Models ' Numerical Estimation of Ground Surface Settlement Caused by Tunneling Tünel Kazısından Dolayı Zemin Yüzeyindeki Oturmaların Mohr- Coulomb ve Pekleşen Zemin Modelleriyle Nümerik Tahminlerinin Karşılaşt 7, 95–102.
- CEN, 2007. Eurocode - Basis of structural design (EN 1990).
- CEN, 2004. Eurocode 7: Geotechnical Design--Part 1: General Rules. *Eur. Comm. Stand.* Brussels.
- Chakeri, H., Ünver, B., 2014. A new equation for estimating the maximum surface settlement above tunnels excavated in soft ground. *Environ. Earth Sci.* 71, 3195–3210. <https://doi.org/10.1007/s12665-013-2707-2>
- Chou, W.I., Bobet, A., 2002. Predictions of ground deformations in shallow tunnels in clay. *Tunn. Undergr. Sp. Technol.* 17, 3–19. [https://doi.org/10.1016/S0886-7798\(01\)00068-2](https://doi.org/10.1016/S0886-7798(01)00068-2)
- Clarke, B.G., Menard, 1997. *Pressuremeter Testing in Ground Investigation. Part II -*

- Interpretation. *Proc. Inst. Civ. Eng. Eng.* 125, 42–52.
- Crestaux, T., Le Maître, O., Martinez, J.-M., 2009. Polynomial chaos expansion for sensitivity analysis. *Reliab. Eng. & Syst. Saf.* 94, 1161–1172.
- de Farias, M.M., Moraes, Á.H., de Assis, A.P., 2004. Displacement control in tunnels excavated by the NATM: 3-D numerical simulations. *Tunn. Undergr. Sp. Technol.* 19, 283–293. <https://doi.org/10.1016/j.tust.2003.11.006>
- de Queiroz, P.I.B., del Roure, R.N., Negro Jr, A., 2005. Bayesian updating of tunnel performance for K0 estimate of Santiago gravel, in: *Geotechnical Aspects of Underground Construction in Soft Ground: Proceedings of the 5th International Symposium TC28*. Amsterdam, the Netherlands, 15-17 June 2005. p. 211.
- Deane, A.P., Bassett, R.H., 2007. the Heathrow Express Trial Tunnel. *Proc. Inst. Civ. Eng. - Geotech. Eng.* 113, 144–156. <https://doi.org/10.1680/igeng.1995.27810>
- Dey, S., Mukhopadhyay, T., Adhikari, S., 2017. Metamodel based high-fidelity stochastic analysis of composite laminates: A concise review with critical comparative assessment. *Compos. Struct.* 171, 227–250. <https://doi.org/10.1016/j.compstruct.2017.01.061>
- Diamantidis, D., 2001. Report 32: Probabilistic Assessment of Existing Structures-A publication for the Joint Committee on Structural Safety (JCSS). RILEM publications.
- Dindarloo, S.R., Siامي-irdemoosa, E., 2015. Maximum surface settlement based classification of shallow tunnels in soft ground. *Tunn. Undergr. Sp. Technol. Inc. Trenchless Technol. Res.* 49, 320–327. <https://doi.org/10.1016/j.tust.2015.04.021>
- Ditlevsen, O., 1981. Uncertainty modeling with applications to multidimensional civil engineering systems. McGraw-Hill International Book Company.
- Duncan, J.M., 2000. Factors of safety and reliability in geotechnical engineering. *J. Geotech. geoenvironmental Eng.* 126, 307–316.
- Einstein, H.H., Schwartz, C.W., 1979. Simplified analysis for tunnel supports. *J. Geotech. Eng. Div.* 105, 499–518.
- Enevoldsen, I., Sørensen, J.D., 1994. Reliability-based optimization in structural engineering. *Struct. Saf.* 15, 169–196.
- Epel, T., Mooney, M.A., Gutierrez, M., 2021. The influence of face and shield annulus pressure on tunnel liner load development. *Tunn. Undergr. Sp. Technol.* 117, 104096. <https://doi.org/10.1016/j.tust.2021.104096>
- Ercelebi, S.G., Copur, H., Oca, I., 2011. Surface settlement predictions for Istanbul Metro tunnels excavated by EPB-TBM. *Environ. Earth Sci.* 62, 357–365. <https://doi.org/10.1007/s12665-010-0530-6>
- Fang, Q., Zhang, D., Wong, L.N.Y., 2012. Shallow tunnelling method (STM) for subway station construction in soft ground. *Tunn. Undergr. Sp. Technol.* 29, 10–30. <https://doi.org/10.1016/j.tust.2011.12.007>
- Fargnoli, V., Boldini, D., Amorosi, A., 2013. TBM tunnelling-induced settlements in coarse-grained soils : The case of the new Milan underground line 5. *Tunn. Undergr. Sp. Technol. Inc. Trenchless Technol. Res.* 38, 336–347. <https://doi.org/10.1016/j.tust.2013.07.015>
- Fenton, G.A., Naghibi, F., Dundas, D., Bathurst, R.J., Griffiths, D.V., 2015. Reliability-based geotechnical design in 2014 Canadian highway bridge design code. *Can. Geotech. J.* 53, 236–251.
- fib Model Code for Concrete Structures 2010, 2013. . International Federation for Structural Concrete (fib), Lausanne.
- Fiessler, B., Neumann, H.-J., Rackwitz, R., 1979. Quadratic limit states in structural reliability. *J.*

- Eng. Mech. Div. 105, 661–676.
- Foreman-Mackey, D., Hogg, D.W., Lang, D., Goodman, J., 2013. emcee : The MCMC Hammer . Publ. Astron. Soc. Pacific 125, 306–312. <https://doi.org/10.1086/670067>
- Forrester, A.I.J., Keane, A.J., 2009. Recent advances in surrogate-based optimization. Prog. Aersp. Sci. 45, 50–79. <https://doi.org/10.1016/j.paerosci.2008.11.001>
- Franco, V.H., Gitirana, G. de F.N., de Assis, A.P., 2019. Probabilistic assessment of tunneling-induced building damage. Comput. Geotech. 113, 103097. <https://doi.org/10.1016/j.compgeo.2019.103097>
- Fuhg, J.N., Fau, A., Nackenhorst, U., 2021. State-of-the-Art and Comparative Review of Adaptive Sampling Methods for Kriging, Archives of Computational Methods in Engineering. Springer Netherlands. <https://doi.org/10.1007/s11831-020-09474-6>
- Garud, S.S., Karimi, I.A., Kraft, M., 2017. Design of computer experiments: A review. Comput. Chem. Eng. 106, 71–95. <https://doi.org/10.1016/j.compchemeng.2017.05.010>
- Gelman, A., Carlin, J.B., Stern, H.S., Rubin, D.B., 2004. Bayesian Data Analysis Chapman \& Hall. CRC Texts Stat. Sci.
- Geman, S., Geman, D., 1984. Stochastic relaxation, Gibbs distributions, and the Bayesian restoration of images. IEEE Trans. Pattern Anal. Mach. Intell. 721–741.
- Gilks, W.R., Richardson, S., Spiegelhalter, D., 1995. Markov chain Monte Carlo in practice. CRC press.
- Gioda, G., Maier, G., 1980. Direct search solution of an inverse problem in elastoplasticity: identification of cohesion, friction angle and in situ stress by pressure tunnel tests. Int. J. Numer. Methods Eng. 15, 1823–1848.
- Glynn, P.W., Iglehart, D.L., 1989. Importance sampling for stochastic simulations. Manage. Sci. 35, 1367–1392.
- Goh, A.T.C., Zhang, F., Zhang, W., Zhang, Y., Liu, H., 2017. A simple estimation model for 3D braced excavation wall deflection. Comput. Geotech. 83, 106–113. <https://doi.org/10.1016/j.compgeo.2016.10.022>
- Gong, W., Juang, C.H., Khoshnevisan, S., Phoon, K.K., 2016. R-LRFD: Load and resistance factor design considering robustness. Comput. Geotech. 74, 74–87. <https://doi.org/10.1016/j.compgeo.2015.12.017>
- Goodman, Jonathan, Weare, J., 2010. Ensemble samplers with affine invariance. Commun. Appl. Math. Comput. Sci. 5, 65–80.
- Goodman, J, Weare, J., 2010. Ensemble Samplers With Affine. Commun. Appl. Math. Comput. Sci. 5, 65–80.
- Govindasamy, D., Ismail, M.A.M., Zaki, M.F.M., Abidin, M.H.Z., 2019. Calibration of stiffness parameters for hardening soil model in residual soil from Kenny hill formation. Bull. Geol. Soc. Malaysia 2019, 131–137. <https://doi.org/10.7186/bgsm67201915>
- GRAGNANO, C.G., FARGNOLI, V., AMOROSI, A., BOLDINI, D., 2015. 3D numerical modelling of soil–structure interaction during EPB tunnelling. Géotechnique 65, 23–37. <https://doi.org/10.1680/geot.14.P.091>
- Griffiths, D. V, Fenton, G.A., 2008. Risk assessment in geotechnical engineering. Hoboken, New Jersey: John Wiley & Sons, Inc.
- Haario, H., Saksman, E., Tamminen, J., 2001. An adaptive Metropolis algorithm. Bernoulli 223–242.
- Hamby, D.M., 1994. A review of techniques for parameter sensitivity analysis of environmental models. Environ. Monit. Assess. 32, 135–154.

- Hammer, A.L., Thewes, M., Galler, R., 2020. Time-dependent material behaviour of shotcrete – New empirical model for the strength development and basic experimental investigations. *Tunn. Undergr. Sp. Technol.* <https://doi.org/10.1016/j.tust.2019.103238>
- Hamrouni, A., Dias, D., Sbartai, B., 2017. Reliability analysis of shallow tunnels using the response surface methodology. *Undergr. Sp.* 2, 246–258. <https://doi.org/10.1016/j.undsp.2017.11.003>
- Hansen, N., Ostermeier, A., 2001. Completely derandomized self-adaptation in evolution strategies. *Evol. Comput.* 9, 159–195.
- Hasofer, A.M., Lind, N.C., 1974. An exact and invariant first order reliability format. *J. Eng. Mech. Div.* 100, 111–121.
- Hastings, W.K., 1970. Monte Carlo sampling methods using Markov chains and their applications.
- Hecht-Nielsen, R., 1992. Theory of the backpropagation neural network, in: *Neural Networks for Perception*. Elsevier, pp. 65–93.
- Herranz, C., Bragard, C., Hee, I., Cerulli, D., 2019. SEM Cavern Construction in Downtown LA, in: *Rapid Excavation & Tunneling Conference Proceedings*. pp. 1037–1050.
- Herranz, C., Penrice, D., 2018. Mining under downtown Los Angeles. *Ita-aitecs* 27, 4–14. <https://doi.org/10.7868/s1811806218020103>
- Herranz, C., Penrice, D., Lianides, J., Horvath, Z., 2016. SEM crossover cavern in downtown L.A. *Geotech. Struct. Eng. Congr.* 2043–2053.
- Hoek, E., 1998. *Rock Engineering--The application of Modern Techniques to Underground Design*. Notes from a short course by Dr Evert Hoek, Kochen & Cella, Brazil (also available from <http://www.rocsience.com>).
- Hohenbichler, M., Rackwitz, R., 1988. Improvement of second-order reliability estimates by importance sampling. *J. Eng. Mech.* 114, 2195–2199.
- Honjo, Y., Wen-Tsung, L., Guha, S., 1994. Inverse analysis of an embankment on soft clay by extended Bayesian method. *Int. J. Numer. Anal. Methods Geomech.* 18, 709–734. <https://doi.org/10.1002/nag.1610181004>
- Hsiung, B.B., Yang, K., Aila, W., Ge, L., 2018. Evaluation of the wall deflections of a deep excavation in Central Jakarta using three-dimensional modeling. *Tunn. Undergr. Sp. Technol.* 72, 84–96. <https://doi.org/10.1016/j.tust.2017.11.013>
- Huijser, D., Goodman, J., Brewer, B.J., 2015. Properties of the Affine Invariant Ensemble Sampler in high dimensions 1–18.
- Hung, C.J., Monsees, J.E., Munfah, N., Wisniewski, J., 2009a. Technical Manual for Design and Construction of Road Tunnels - Civil Elements 1–702.
- Hung, C.J., Monsees, J.E., Munfah, N., Wisniewski, J., 2009b. Technical Manual for Design and Construction of Road Tunnels--civil Elements. US Department of Transport Federal Highway Administration.
- Ieronymaki, E.S., Asce, A.M., Whittle, A.J., Asce, M., Sureda, D.S., 2017. Interpretation of Free-Field Ground Movements Caused by Mechanized Tunnel Construction 143, 1–13. [https://doi.org/10.1061/\(ASCE\)GT.1943-5606.0001632](https://doi.org/10.1061/(ASCE)GT.1943-5606.0001632)
- Irshad, M., Heflin, L.H., 1988. Soft-ground NATM tunnel designs for the Washington, DC Metro. *Tunn. Undergr. Sp. Technol.* 3, 385–392.
- ISO2394, 2015. General principles on reliability for structures. Switzerland.
- Itasca Consulting Group, I., 2016. 3DEC 3-Dimensional Distinct Element Code.
- Itasca Consulting Group, I., 2014. UDEC version 6.0: theory and background. Minneapolis,

- Minnesota.
- Itasca Consulting Group Inc., 2019. FLAC3D — Fast Lagrangian analysis of continua in three-dimensions, ver. 7.0.
- Iuliano, E., 2017. Global optimization of benchmark aerodynamic cases using physics-based surrogate models. *Aerosp. Sci. Technol.* <https://doi.org/10.1016/j.ast.2017.04.013>
- Janda, T., Šejnoha, M., Šejnoha, J., 2018a. Applying Bayesian approach to predict deformations during tunnel construction. *Int. J. Numer. Anal. Methods Geomech.* 42, 1765–1784. <https://doi.org/10.1002/nag.2810>
- Janda, T., Šejnoha, M., Šejnoha, J., 2018b. Applying Bayesian approach to predict deformations during tunnel construction. *Int. J. Numer. Anal. Methods Geomech.* 42, 1765–1784. <https://doi.org/10.1002/nag.2810>
- Janin, J.P., Dias, D., Emeriault, F., Kastner, R., Le Bissonnais, H., Guilloux, A., 2015. Numerical back-analysis of the southern Toulon tunnel measurements: A comparison of 3D and 2D approaches. *Eng. Geol.* 195, 42–52. <https://doi.org/10.1016/j.enggeo.2015.04.028>
- Jiang, S.H., Papaioannou, I., Straub, D., 2018. Bayesian updating of slope reliability in spatially variable soils with in-situ measurements. *Eng. Geol.* 239, 310–320. <https://doi.org/10.1016/j.enggeo.2018.03.021>
- Jin, D., Yuan, D., Li, X., Zheng, H., 2018. Analysis of the settlement of an existing tunnel induced by shield tunneling underneath. *Tunn. Undergr. Sp. Technol.* 81, 209–220. <https://doi.org/10.1016/j.tust.2018.06.035>
- Joe, S., Kuo, F.Y., 2003. Remark on algorithm 659: Implementing Sobol’s quasirandom sequence generator. *ACM Trans. Math. Softw.* 29, 49–57.
- Juang, C.H., Asce, F., Luo, Z., Asce, A.M., Atamturktur, S., Asce, M., Huang, H., 2013. Bayesian updating of soil parameters for braced excavations using field observations. *J. Geotech. geoenvironmental Eng.* 139, 395–406. [https://doi.org/10.1061/\(ASCE\)GT.1943-5606.0000782](https://doi.org/10.1061/(ASCE)GT.1943-5606.0000782)
- Karakus, M., Fowell, R.J., 2005. Back analysis for tunnelling induced ground movements and stress redistribution. *Tunn. Undergr. Sp. Technol.* 20, 514–524. <https://doi.org/10.1016/j.tust.2005.02.007>
- Karakus, M., Fowell, R.J., 2004. An insight into the new Austrian tunnelling method (NATM), in: *Proceedings of the VIIth Regional Rock Mechanics Symposium. Cumhuriyet Üniversitesi Maden Mühendisliği Bölümü : Türk Ulusal Kaya Mekaniği Derneği, Sivas, Turkey.*
- Keane, A., Forrester, A., Sobester, A., 2008. *Engineering design via surrogate modelling: a practical guide.* American Institute of Aeronautics and Astronautics, Inc.
- Khaledi, K., Miro, S., König, M., Schanz, T., 2014. Robust and reliable metamodels for mechanized tunnel simulations. *Comput. Geotech.* 61, 1–12. <https://doi.org/10.1016/j.compgeo.2014.04.005>
- Khamesi, H., Torabi, S.R., Mirzaei-Nasirabad, H., Ghadiri, Z., 2015. Improving the Performance of Intelligent Back Analysis for Tunneling Using Optimized Fuzzy Systems: Case Study of the Karaj Subway Line 2 in Iran. *J. Comput. Civ. Eng.* 29, 05014010. [https://doi.org/10.1061/\(ASCE\)CP.1943-5487.0000421](https://doi.org/10.1061/(ASCE)CP.1943-5487.0000421)
- Kim, S.-H., Na, S.-W., 1997. Response surface method using vector projected sampling points. *Struct. Saf.* 19, 3–19.
- Kitchah, F., Benmebarek, S., 2016. Finite difference analysis of an advance core pre-reinforcement system for Toulon’s south tube. *J. Rock Mech. Geotech. Eng.* 8, 703–713.

- <https://doi.org/10.1016/j.jrmge.2016.05.006>
- Kong, B., Phoon, K., 2015. Reliability-based design and its complementary role to Eurocode 7 design approach. *Comput. Geotech.* 65, 30–44.
- Kovari, K., 1994. Erroneous concepts behind the new Austrian tunnelling method. *Tunnels Tunn.* 26, 38–42.
- Krige, D.G., 1951. A statistical approach to some basic mine valuation problems on the Witwatersrand. *J. South. African Inst. Min. Metall.* 52, 119–139.
- Lackner, R., Mang, H.A., 2003. Cracking in shotcrete tunnel shells. *Eng. Fract. Mech.* 70, 1047–1068.
- Lamar, D., 1970. Geology of the Elysian Park-Repetto Hills Area, Los Angeles County, California. California. Division of Mines and Geology, San Francisco.
- Langford, J.C., Diederichs, M.S., 2014. Reliable Support Design for Excavations in Brittle Rock Using a Global Response Surface Method. *Rock Mech. Rock Eng.* 48, 669–689. <https://doi.org/10.1007/s00603-014-0567-z>
- Langford, J.C., Diederichs, M.S., 2013. Reliability based approach to tunnel lining design using a modified point estimate method. *Int. J. Rock Mech. Min. Sci.* 60, 263–276. <https://doi.org/10.1016/j.ijrmms.2012.12.034>
- Li, P., Zhao, Y., Zhou, X., 2016. Displacement characteristics of high-speed railway tunnel construction in loess ground by using multi-step excavation method. *Tunn. Undergr. Sp. Technol.* 51, 41–55. <https://doi.org/10.1016/j.tust.2015.10.009>
- Li, Z., Gong, W., Li, T., Juang, C.H., Chen, J., Wang, L., 2021. Probabilistic back analysis for improved reliability of geotechnical predictions considering parameters uncertainty, model bias, and observation error. *Tunn. Undergr. Sp. Technol.* 115, 104051. <https://doi.org/10.1016/j.tust.2021.104051>
- Liu, H., Low, B.K., 2018. Reliability-based design of tunnelling problems and insights for Eurocode 7. *Comput. Geotech.* 97, 42–51. <https://doi.org/10.1016/j.compgeo.2017.12.005>
- Loganathan, N., 2011. An Innovative Method For Assessing Tunnelling-Induced Risks To Adjacent Structures. PB2009 William Barclay Parsons Fellowsh. Monogr. 25 118.
- Low, B.K., Tang, W.H., 2007. Efficient Spreadsheet Algorithm for First-Order Reliability Method. *J. Eng. Mech.* 133, 1378–1387. [https://doi.org/10.1061/\(asce\)0733-9399\(2007\)133:12\(1378\)](https://doi.org/10.1061/(asce)0733-9399(2007)133:12(1378))
- Low, B.K., Tang, W.H., 2004. Reliability analysis using object-oriented constrained optimization. *Struct. Saf.* 26, 69–89. [https://doi.org/10.1016/S0167-4730\(03\)00023-7](https://doi.org/10.1016/S0167-4730(03)00023-7)
- Lü, Q., Low, B.K., 2011. Probabilistic analysis of underground rock excavations using response surface method and SORM. *Comput. Geotech.* 38, 1008–1021. <https://doi.org/10.1016/j.compgeo.2011.07.003>
- Lü, Q., Xiao, Z.P., Ji, J., Zheng, J., 2017a. Reliability based design optimization for a rock tunnel support system with multiple failure modes using response surface method. *Tunn. Undergr. Sp. Technol.* 70, 1–10. <https://doi.org/10.1016/j.tust.2017.06.017>
- Lü, Q., Xiao, Z.P., Ji, J., Zheng, J., Shang, Y.Q., 2017b. Moving least squares method for reliability assessment of rock tunnel excavation considering ground-support interaction. *Comput. Geotech.* 84, 88–100. <https://doi.org/10.1016/j.compgeo.2016.11.019>
- Lunardi, P., 2008a. Design and Construction of Tunnels, Design and Construction of Tunnels: Analysis of Controlled Deformation in Rocks and Soils (ADECO-RS). <https://doi.org/10.1007/978-3-540-73875-6>
- Lunardi, P., 2008b. Design and construction of tunnels: Analysis of Controlled Deformations in

- Rock and Soils (ADECO-RS). Springer Science & Business Media.
- Macht, J., 2002. Hybrid analysis of shotcrete tunnel linings: assessment and online monitoring of the level of loading. na.
- Mack, Y., Goel, T., Shyy, W., Haftka, R., 2007. Surrogate model-based optimization framework: a case study in aerospace design. *Evol. Comput. Dyn. uncertain Environ.* 323–342.
- Mair, R.J., 2008. Tunnelling and geotechnics: new horizons. *Géotechnique* 58, 695–736.
- Mair, R.J., Taylor, R.N., Bracegirdle, A., 1993. Subsurface settlement profiles above tunnels in clays. *Geotechnique* 43, 315–320.
- Mair, R.J., Wood, D.M., 2013. Pressuremeter testing: methods and interpretation. Elsevier.
- Malinverno, A., 2002. Parsimonious Bayesian Markov chain Monte Carlo inversion in a nonlinear geophysical problem. *Geophys. J. Int.* 151, 675–688.
<https://doi.org/10.1046/j.1365-246X.2002.01847.x>
- Margheri, L., Sagaut, P., 2016. A hybrid anchored-ANOVA – POD/Kriging method for uncertainty quantification in unsteady high-fidelity CFD simulations. *J. Comput. Phys.*
<https://doi.org/10.1016/j.jcp.2016.07.036>
- Mašin, D., 2009. 3D Modeling of an NATM Tunnel in High K0 Clay Using Two Different Constitutive Models. *J. Geotech. Geoenvironmental Eng.* 135, 1326–1335.
[https://doi.org/10.1061/\(ASCE\)GT.1943-5606.0000017](https://doi.org/10.1061/(ASCE)GT.1943-5606.0000017)
- Matheron, G., 1963. Principles of geostatistics. *Econ. Geol.* 58, 1246–1266.
- Meschke, G., Kropik, C., Mang, H.A., 1996. Numerical analyses of tunnel linings by means of a viscoplastic material model for shotcrete. *Int. J. Numer. Methods Eng.* 39, 3145–3162.
- Metropolis, N., Rosenbluth, A.W., Rosenbluth, M.N., Teller, A.H., Teller, E., 1953. Equation of state calculations by fast computing machines. *J. Chem. Phys.* 21, 1087–1092.
- Miranda, T., Dias, D., Eclaircy-Caudron, S., Gomes Correia, A., Costa, L., 2011. Back analysis of geomechanical parameters by optimisation of a 3D model of an underground structure. *Tunn. Undergr. Sp. Technol.* 26, 659–673. <https://doi.org/10.1016/j.tust.2011.05.010>
- Miro, S., Hartmann, D., Schanz, T., 2014. Global sensitivity analysis for subsoil parameter estimation in mechanized tunneling. *Comput. Geotech.* 56, 80–88.
<https://doi.org/10.1016/j.compgeo.2013.11.003>
- Miro, S., König, M., Hartmann, D., Schanz, T., 2015. A probabilistic analysis of subsoil parameters uncertainty impacts on tunnel-induced ground movements with a back-analysis study. *Comput. Geotech.* 68, 38–53. <https://doi.org/10.1016/j.compgeo.2015.03.012>
- Möller, S.C., Vermeer, P.A., 2008. On numerical simulation of tunnel installation. *Tunn. Undergr. Sp. Technol.* 23, 461–475.
- Mollon, G., Dias, D., Soubra, A.H., 2011. Probabilistic analysis of pressurized tunnels against face stability using collocation-based stochastic response surface method. *J. Geotech. Geoenvironmental Eng.* 137, 385–397. [https://doi.org/10.1061/\(ASCE\)GT.1943-5606.0000443](https://doi.org/10.1061/(ASCE)GT.1943-5606.0000443)
- Mollon, G., Dias, D., Soubra, A.H., 2009a. Probabilistic analysis of circular tunnels in homogeneous soil using response surface methodology. *J. Geotech. Geoenvironmental Eng.* 135, 1314–1325. [https://doi.org/10.1061/\(ASCE\)GT.1943-5606.0000060](https://doi.org/10.1061/(ASCE)GT.1943-5606.0000060)
- Mollon, G., Dias, D., Soubra, A.H., 2009b. Probabilistic analysis and design of circular tunnels against face stability. *Int. J. Geomech.* 9, 237–249. [https://doi.org/10.1061/\(ASCE\)1532-3641\(2009\)9:6\(237\)](https://doi.org/10.1061/(ASCE)1532-3641(2009)9:6(237))
- Mooney, M.A., Grasmick, J., Kenneally, B., Fang, Y., 2016. The role of slurry TBM parameters on ground deformation: Field results and computational modelling. *Tunn. Undergr. Sp.*

- Technol. 57, 257–264.
- Moritz, B., Brandtner, M., 2008. Advanced Observation Techniques for Sophisticated Shallow Tunnel Projects – Experience Gained Using Innovative Monitoring Methods at the Lainzer Tunnel LT31. *Geomech. und Tunnelbau Geomech. und Tunnelbau* 1, 466–476.
<https://doi.org/10.1002/geot.200800051>
- Mottahedi, A., Sereshki, F., Ataei, M., 2018. Overbreak prediction in underground excavations using hybrid ANFIS-PSO model. *Tunn. Undergr. Sp. Technol.* 80, 1–9.
<https://doi.org/10.1016/j.tust.2018.05.023>
- Munfah, N., Gall, V., Matthei, S., 2016. Recent trends in conventional tunneling (SEM/NATM) in the US. *ITA-AITES World Tunn. Congr. 2016, WTC 2016* 1, 505–514.
- Negro, A., Queiroz, B.I.P., 1999. Prediction and performance of soft ground tunnels. *Geotech. Asp. Undergr. Constr. Soft Ground*. Balkema, Tokyo, Japan 409–418.
- Neuner, M., Cordes, T., Drexel, M., Hofstetter, G., 2017a. Time-dependent material properties of shotcrete: Experimental and numerical study. *Materials (Basel)*. 10, 1–17.
<https://doi.org/10.3390/ma10091067>
- Neuner, M., Gamnitzer, P., Hofstetter, G., 2017b. An extended damage plasticity model for shotcrete: Formulation and comparison with other shotcrete models. *Materials (Basel)*. 10, 82.
- Neuner, M., Schreter, M., Gamnitzer, P., Hofstetter, G., 2020. On discrepancies between time-dependent nonlinear 3D and 2D finite element simulations of deep tunnel advance: A numerical study on the Brenner Base Tunnel. *Comput. Geotech.*
<https://doi.org/10.1016/j.compgeo.2019.103355>
- New, B.M., Bowers, K.H., 1984. Ground movement model validation at the Heathrow Express trail tunnel.
- Ng, C.W., Lee, K.M., Tang, D.K., 2004. Three-dimensional numerical investigations of new Austrian tunnelling method (NATM) twin tunnel interactions. *Can. Geotech. J.* 41, 523–539. <https://doi.org/10.1139/t04-008>
- Ninić, J., Meschke, G., 2015. Model update and real-time steering of tunnel boring machines using simulation-based meta models. *Tunn. Undergr. Sp. Technol.* 45, 138–152.
<https://doi.org/10.1016/j.tust.2014.09.013>
- O'Reilly, M.P., New, B.M., 1982. Settlements above tunnels in the United Kingdom-their magnitude and prediction.
- Obrzud, R., 2010. The hardening soil model: A practical guidebook. Zace Services.
- Obrzud, R.F., 2010. On the use of the Hardening Soil Small Strain model in geotechnical practice. *Numer. Geotech. Struct.* 16.
- Obrzud, R.F., Truty, A., 2018. the hardening soil model - a practical guidebook z soil 05.
- Oden, J.T., Moser, R., Ghattas, O., 2010. Computer predictions with quantified uncertainty, part II. *SIAM News* 43, 1–4.
- Oliver, M.A., Webster, R., 1990. Kriging: a method of interpolation for geographical information systems. *Int. J. Geogr. Inf. Syst.* 4, 313–332.
- Pan, Q., Dias, D., 2018. Probabilistic analysis of a rock tunnel face using polynomial chaos expansion method. *Int. J. Geomech.* 18. [https://doi.org/10.1061/\(ASCE\)GM.1943-5622.0001116](https://doi.org/10.1061/(ASCE)GM.1943-5622.0001116)
- Pan, Q.J., Zhang, R.F., Ye, X.Y., Li, Z.W., 2021. An efficient method combining polynomial-chaos kriging and adaptive radial-based importance sampling for reliability analysis. *Comput. Geotech.* 140, 104434. <https://doi.org/10.1016/j.compgeo.2021.104434>

- Panet, M., Guenot, A., 1982. Analysis of convergence behind the face of a tunnel, in: *Proceeding of the International Symposium Tunnelling, (IST82)*. The Institution of Mining and Metallurgy, London, pp. 197–204.
- Park, K.H., 2005. Analytical solution for tunnelling-induced ground movement in clays. *Tunn. Undergr. Sp. Technol.* 20, 249–261. <https://doi.org/10.1016/j.tust.2004.08.009>
- Paternes, A., Schweiger, H.F., Ruggeri, P., Fruzzetti, V.M.E., Scarpelli, G., 2017a. Comparisons of Eurocodes design approaches for numerical analysis of shallow tunnels. *Tunn. Undergr. Sp. Technol.* <https://doi.org/10.1016/j.tust.2016.12.003>
- Paternes, A., Schweiger, H.F., Scarpelli, G., 2017b. Parameter Calibration and Numerical Analysis of Twin Shallow Tunnels. *Rock Mech. Rock Eng.* 50, 1243–1262. <https://doi.org/10.1007/s00603-016-1152-4>
- Peck, R.B., 1969. Advantages and limitations of the observational method in applied soil mechanics. *Geotechnique* 19, 171–187. <https://doi.org/10.1680/geot.1969.19.2.171>
- Peila, D., Marchino, C., Todaro, C., Luciani, A., 2017. Comparison of the Results of Analytical and Numerical Models of Pre-Reinforcement in Shallow Tunnels. *Arch. Civ. Eng.* 63, 135–147. <https://doi.org/10.1515/ace-2017-0045>
- Phelps, D.J., Gildner, J., Tattersall, C., Laubbichler, J., McAllister, D., 2005. Design and risk management strategy for the Sound Transit Beacon Hill Station and tunnels. 2005 RETC Proc.
- Phoon, K.-K., Kulhawy, F.H., 1999. Characterization of geotechnical variability. *Can. Geotech. J.* 36, 612–624.
- Phoon, K.-K., Kulhawy, F.H., Grigoriu, M.D., 2003. Development of a reliability-based design framework for transmission line structure foundations. *J. Geotech. Geoenvironmental Eng.* 129, 798–806.
- Phoon, K., Ching, J., 2018. *Risk and Reliability in Geotechnical Engineering*, Risk and Reliability in Geotechnical Engineering. CRC Press. <https://doi.org/10.1201/b17970>
- Pinto, F., Zymnis, D.M., Asce, S.M., Whittle, A.J., Asce, M., 2014. Ground Movements due to Shallow Tunnels in Soft Ground . II : Analytical Interpretation and Prediction 04013041, 1–11. [https://doi.org/10.1061/\(ASCE\)GT.1943-5606.0000947](https://doi.org/10.1061/(ASCE)GT.1943-5606.0000947)
- Prieto, A., Prieto, B., Ortigosa, E.M., Ros, E., Pelayo, F., Ortega, J., Rojas, I., 2016. Neural networks: An overview of early research, current frameworks and new challenges. *Neurocomputing* 214, 242–268. <https://doi.org/10.1016/j.neucom.2016.06.014>
- Qi, C., Fourie, A., 2018. A real-time back-analysis technique to infer rheological parameters from field monitoring. *Rock Mech. Rock Eng.* 0, 0. <https://doi.org/10.1007/s00603-018-1513-2>
- Qi, X., Zhou, W., 2017. An efficient probabilistic back-analysis method for braced excavations using wall deflection data at multiple points. *Comput. Geotech.* 85, 186–198. <https://doi.org/10.1016/j.compgeo.2016.12.032>
- Razavi, S., Tolson, B.A., Burn, D.H., 2012. Review of surrogate modeling in water resources. *Water Resour. Res.* 48. <https://doi.org/10.1029/2011WR011527>
- Regional Connector Transit Corridor project - final geotechnical data report, 2012.
- Rocscience, 2008. Phase2 v7.0 finite element analysis for excavations and slopes. Toronto.
- Romero, V., 2002. NATM/SHOTCRETE FOCUS-NATM in soft ground--A contradiction in terms? Views on NATM and its application to soft-ground tunnelling dispelling some misconceptions about this sometimes controversial. *World Tunn.* 15, 338–344.
- Sabatini, P.J., Bachus, R.C., Mayne, P.W., Schneider, J.A., Zettler, T.E., others, 2002.

- Geotechnical Engineering Circular No. 5 Evaluation of Soil and Rock Properties.
- Sacks, J., Welch, W.J., Mitchell, T.J., Wynn, H.P., 1989. Design and analysis of computer experiments. *Stat. Sci.* 4, 409–423.
- Sagaseta, C., 1987. Analysis of undrained soil deformation due to ground loss. *Geotechnique* 37, 301–320.
- Sandstrom, G.E., 1963. *History of Tunnelling*. Barrie & Rockcliff, London.
- Santner, T.J., Williams, Brian J, Notz, W.I., Williams, Brian J, 2003. *The design and analysis of computer experiments*. Springer.
- Sayed, S., Dodagoudar, G.R., Rajagopal, K., 2010. Finite element reliability analysis of reinforced retaining walls. *Geomech. Geoenviron. An Int. J.* 5, 187–197.
- Schädlich, B., Schweiger, H.F., 2014. A new constitutive model for shotcrete. *Numer. methods Geotech. Eng.* 1, 103–108.
- Schanz, T., Vermeer, a, Bonnier, P., 1999. The hardening soil model: formulation and verification. *Beyond 2000 Comput. Geotech. 10 years PLAXIS Int. Proc. Int. Symp. beyond 2000 Comput. Geotech. Amsterdam Netherlands 1820 March 1999* 281.
- Schmidhuber, J., 2015. Deep Learning in neural networks: An overview. *Neural Networks* 61, 85–117. <https://doi.org/10.1016/j.neunet.2014.09.003>
- Schöbi, R., Sudret, B., Marelli, S., 2017. Rare event estimation using Polynomial-Chaos Kriging. *ASCE-ASME J. Risk Uncertain. Eng. Syst. Part A Civ. Eng.* 3, 1–12. <https://doi.org/10.1061/ajrua6.0000870>
- Schobi, R., Sudret, B., Wiart, J., 2015. Polynomial-chaos-based Kriging. *Int. J. Uncertain. Quantif.* 5.
- Schweiger, H.F., Paternesi, A., Tschuchnigg, F., 2017. Eurocode 7-based design of SCL tunnels by means of numerical analyses. *Géotechnique* 67, 837–844. <https://doi.org/10.1680/tue.63778.177>
- Scott, B., Kim, B.J., Salgado, R., 2003. Assessment of current load factors for use in geotechnical load and resistance factor design. *J. Geotech. Geoenvironmental Eng.* 129, 287–295. [https://doi.org/10.1061/\(ASCE\)1090-0241\(2003\)129:4\(287\)](https://doi.org/10.1061/(ASCE)1090-0241(2003)129:4(287))
- Sharifzadeh, M., Kolivand, F., Ghorbani, M., Yasrobi, S., 2013. Design of sequential excavation method for large span urban tunnels in soft ground - Niayesh tunnel. *Tunn. Undergr. Sp. Technol.* 35, 178–188.
- Simpson, T.W., Poplinski, J.D., Koch, P.N., Allen, J.K., 2001. Metamodels for computer-based engineering design: survey and recommendations. *Eng. Comput.* 17, 129–150.
- Smola, A.J., Schölkopf, B., 2004. A tutorial on support vector regression. *Stat. Comput.* 14, 199–222.
- Soga, K., Bolton, M.D., Au, S.K.A., Komiya, K., Hamelin, J.P., Van Cotthem, A., Buchet, G., Michel, J.P., 1999. Development of compensation grouting modelling and control system. *Geotech. Asp. Undergr. Constr. soft Gr.* 3, 425–430.
- Son, M., Cording, E., 2005. Estimation of Building Damage Due to Excavation-Induced Ground Movements 131, 162–177. [https://doi.org/10.1061/\(ASCE\)1090-0241\(2005\)131](https://doi.org/10.1061/(ASCE)1090-0241(2005)131)
- Sousa, R.L., Einstein, H.H., 2012. Risk analysis during tunnel construction using Bayesian Networks: Porto Metro case study. *Tunn. Undergr. Sp. Technol.* 27, 86–100.
- Špačková, O., Straub, D., 2013. Dynamic Bayesian network for probabilistic modeling of tunnel excavation processes. *Comput. Civ. Infrastruct. Eng.* 28, 1–21. <https://doi.org/10.1111/j.1467-8667.2012.00759.x>
- Spyridis, P., Fortsakis, P., Schwind, T., 2018. *Geotechnical Engineering and Innovative Support*

- System for Shallow Urban Subway Caverns in Rock, in Confined Built Environment. *Geotech. Geol. Eng.* 36, 2967–2983.
- Ssenyonga, A., 2018. An Investigation of Surface Settlement and Volume Loss Associated with SCL Tunnelling at Stepney Green, in: *Crossrail Project: Infrastructure Design and Construction*. ICE Publishing, pp. 1–38.
- Su, J., 2013. Design of sprayed concrete lining in soft ground - A Crossrail perspective. *Undergr. - W. to Futur. Proc. World Tunn. Congr. WTC 2013* 593–600.
<https://doi.org/10.1201/b14769-83>
- Svoboda, T., Mašín, D., Boháč, J., 2010. Class A predictions of a NATM tunnel in stiff clay. *Comput. Geotech.* 37, 817–825. <https://doi.org/10.1016/j.compgeo.2010.07.003>
- Tang, W.H., Stark, T.D., Angulo, M., 1999. Reliability in back analysis of slope failures. *Soils Found.* 39, 73–80.
- Thomas, A., 2019. *Sprayed concrete lined tunnels*, CRC Press, Taylor & Francis Group. CRC Press.
- Tonon, F., 2010. Sequential excavation, NATM and ADECO: What they have in common and how they differ. *Tunn. Undergr. Sp. Technol.* 25, 245–265.
- Totis, G., Sortino, M., 2020. Polynomial Chaos-Kriging approaches for an efficient probabilistic chatter prediction in milling. *Int. J. Mach. Tools Manuf.* 157, 103610.
<https://doi.org/10.1016/j.ijmachtools.2020.103610>
- Tu, J., Choi, K.K., Park, Y.H., 1999. A new study on reliability-based design optimization.
- Tvedt, L., 1990. Distribution of quadratic forms in normal space—application to structural reliability. *J. Eng. Mech.* 116, 1183–1197.
- Tvedt, L., 1983. Two second-order approximations to the failure probability. *Verit. Rep. RDIV/20-004083*.
- Ulusay, R., 2014. *The ISRM suggested methods for rock characterization, testing and monitoring: 2007-2014*. Springer, Switzerland.
- Vapnik, V., 2013. *The nature of statistical learning theory*. Springer science & business media.
- Vardakos, S., Gutierrez, M., Xia, C., 2016. Back-Analysis of Tunnel Response from Field Monitoring Using Simulated Annealing. *Rock Mech. Rock Eng.* 49, 4833–4852.
<https://doi.org/10.1007/s00603-016-1074-1>
- Vardakos, S., Gutierrez, M., Xia, C., 2012. Parameter identification in numerical modeling of tunneling using the Differential Evolution Genetic Algorithm (DEGA). *Tunn. Undergr. Sp. Technol.* 28, 109–123. <https://doi.org/10.1016/j.tust.2011.10.003>
- Vermeer, P.A., 1978. A double hardening model for sand. *Geotechnique* 28, 413–433.
- Verruijt, A., 2021. A complex variable solution for a non-circular tunnel in an elastic half-plane. *Int. J. Numer. Anal. Methods Geomech.* 45, 1833–1853. <https://doi.org/10.1002/nag.3244>
- Verruijt, A., Booker, J.R., 1996. Surface settlements due to deformation of a tunnel in an elastic half plane. *Geotechnique* 46, 753–756. <https://doi.org/10.1680/geot.1996.46.4.753>
- Verruijt, A., Strack, O.E., 2008. Buoyancy of tunnels in soft soils. *Geotechnique* 58, 513–515.
<https://doi.org/10.1680/geot.2008.58.6.513>
- Vlachopoulos, N., Diederichs, M.S., 2014. Appropriate uses and practical limitations of 2D numerical analysis of tunnels and tunnel support response. *Geotech. Geol. Eng.* 32, 469–488. <https://doi.org/10.1007/s10706-014-9727-x>
- Vlachopoulos, N., Diederichs, M.S., 2009. Improved longitudinal displacement profiles for convergence confinement analysis of deep tunnels. *Rock Mech. Rock Eng.* 42, 131–146.
<https://doi.org/10.1007/s00603-009-0176-4>

- Von Rabcewicz, L., 1964. The new austrian tunnelling method. *Water Power* 65.
- Vorster, T.E., Klar, A., Soga, K., Mair, R.J., 2005. Estimating the effects of tunneling on existing pipelines. *J. Geotech. Geoenvironmental Eng.* 131, 1399–1410.
- Wang, L.-Z., Li, L.-L., Lv, X.-J., 2009. Complex Variable Solutions for Tunneling-Induced Ground Movement. *Int. J. Geomech.* 9, 63–72. [https://doi.org/10.1061/\(asce\)1532-3641\(2009\)9:2\(63\)](https://doi.org/10.1061/(asce)1532-3641(2009)9:2(63))
- Wang, M., 2006. Outline of tunnel construction by means of method of undercutting with shallow overburden. *Tunn. Constr.* 5.
- Wang, Q., Fang, H., 2018. Reliability analysis of tunnels using an adaptive RBF and a first-order reliability method. *Comput. Geotech.* 98, 144–152. <https://doi.org/10.1016/j.compgeo.2018.02.011>
- Wang, Q., Fang, H., Shen, L., 2016. Reliability analysis of tunnels using a metamodeling technique based on augmented radial basis functions. *Tunn. Undergr. Sp. Technol.* 56, 45–53. <https://doi.org/10.1016/j.tust.2016.02.007>
- Weinmeister, J., Gao, X., Roy, S., 2019. Analysis of a polynomial chaos-kriging metamodel for uncertainty quantification in aerodynamics. *AIAA J.* 57, 2280–2296. <https://doi.org/10.2514/1.J057527>
- Wendland, H., 2006. Computational Aspects of Radial Basis Function Approximation, *Studies in Computational Mathematics*. Elsevier Masson SAS. [https://doi.org/10.1016/S1570-579X\(06\)80010-8](https://doi.org/10.1016/S1570-579X(06)80010-8)
- Westermann, P., Evins, R., 2019. Surrogate modelling for sustainable building design – A review. *Energy Build.* 198, 170–186. <https://doi.org/10.1016/j.enbuild.2019.05.057>
- Williams, C.K., Rasmussen, C.E., 2006. Gaussian processes for machine learning. MIT press Cambridge, MA.
- Wood, A.M.M., 1975. The circular tunnel in elastic ground. *Geotechnique* 25, 115–127.
- Wu, R., Fujita, Y., Soga, K., 2020. Integrating domain knowledge with deep learning models : An interpretable AI system for automatic work progress identification of NATM tunnels. *Tunn. Undergr. Sp. Technol.* 105, 103558. <https://doi.org/10.1016/j.tust.2020.103558>
- Xiu, D., Karniadakis, G.E., 2002. The Wiener--Askey polynomial chaos for stochastic differential equations. *SIAM J. Sci. Comput.* 24, 619–644.
- Yang, H., Huynh, K., 2017. Characteristics of the weak rock at regional connector project in los angeles. 51st US Rock Mech. / Geomech. Symp. 2017 3, 1508–1512.
- Yang, J.S., Liu, B.C., Wang, M.C., 2004. Modeling of tunneling-induced ground surface movements using stochastic medium theory. *Tunn. Undergr. Sp. Technol.* 19, 113–123. <https://doi.org/10.1016/j.tust.2003.07.002>
- Yang, X.L., Wang, J.M., 2011. Ground movement prediction for tunnels using simplified procedure. *Tunn. Undergr. Sp. Technol.* 26, 462–471. <https://doi.org/10.1016/j.tust.2011.01.002>
- Yeo, C.H., Lee, F.H., Tan, S.C., Hasegawa, O., Suzuki, H., Shinji, M., 2009. Three dimensional numerical modelling of a NATM tunnel. *Japanese Comm. Rock Mech.* 5, 33–38.
- Yoo, C., 2009. Performance of multi-faced tunnelling - A 3D numerical investigation. *Tunn. Undergr. Sp. Technol.* 24, 562–573. <https://doi.org/10.1016/j.tust.2009.02.005>
- Youn, B.D., Choi, K.K., 2004. A new response surface methodology for reliability-based design optimization. *Comput. Struct.* 82, 241–256. <https://doi.org/10.1016/j.compstruc.2003.09.002>
- Zeng, B., Huang, D., 2016. Soil deformation induced by Double-O-Tube shield tunneling with

- rolling based on stochastic medium theory. *Tunn. Undergr. Sp. Technol.* 60, 165–177.
<https://doi.org/10.1016/j.tust.2016.09.001>
- Zhang, J., Zhang, L.M., Tang, W.H., 2012. Reliability-based optimization of geotechnical systems. *J. Geotech. Geoenvironmental Eng.* 137, 1211–1221.
[https://doi.org/10.1061/\(ASCE\)GT.1943-5606.0000551](https://doi.org/10.1061/(ASCE)GT.1943-5606.0000551)
- Zhang, T., Baroth, J., Dias, D., 2021. Probabilistic basal heave stability analyses of supported circular shafts in non-homogeneous clayey soils. *Comput. Geotech.* 140, 104457.
<https://doi.org/10.1016/j.compgeo.2021.104457>
- Zhang, W., 2019. MARS applications in geotechnical engineering systems: Multi-dimension with big data, *MARS Applications in Geotechnical Engineering Systems: Multi-Dimension with Big Data*.
- Zhang, W., Goh, A.T.C., 2012. Reliability assessment on ultimate and serviceability limit states and determination of critical factor of safety for underground rock caverns. *Tunn. Undergr. Sp. Technol.* 32, 221–230.
- Zhang, W.G., Goh, A.T.C., 2015. Regression models for estimating ultimate and serviceability limit states of underground rock caverns. *Eng. Geol.* 188, 68–76.
<https://doi.org/10.1016/j.enggeo.2015.01.021>
- Zhang, Y., Su, G., Liu, B., Li, T., 2020. A novel displacement back analysis method considering the displacement loss for underground rock mass engineering. *Tunn. Undergr. Sp. Technol.* 95, 103141. <https://doi.org/10.1016/j.tust.2019.103141>
- Zhang, Z., Pan, Y., Zhang, M., Lv, X., Jiang, K., Li, S., 2020. Complex variable analytical prediction for ground deformation and lining responses due to shield tunneling considering groundwater level variation in clays. *Comput. Geotech.* 120, 103443.
<https://doi.org/10.1016/j.compgeo.2020.103443>
- Zhao, C., 2018. A Contribution to Modeling of Mechanized Tunnel Excavation Heft 65.
- Zhao, C., Hölter, R., König, M., Alimardani Lavasan, A., 2019. A hybrid model for estimation of ground movements due to mechanized tunnel excavation. *Comput. Civ. Infrastruct. Eng.*
<https://doi.org/10.1111/mice.12438>
- Zhao, C., Lavasan, A.A., Barciaga, T., Zarev, V., Datcheva, M., Schanz, T., 2015. Model validation and calibration via back analysis for mechanized tunnel simulations - The Western Scheldt tunnel case. *Comput. Geotech.* 69, 601–614.
<https://doi.org/10.1016/j.compgeo.2015.07.003>
- Zhao, Y.-G., Ono, T., 1999. New approximations for SORM: Part 1. *J. Eng. Mech.* 125, 79–85.
- Zheng, D., Huang, J., Li, D.Q., Kelly, R., Sloan, S.W., 2018. Embankment prediction using testing data and monitored behaviour: A Bayesian updating approach. *Comput. Geotech.* 93, 150–162. <https://doi.org/10.1016/j.compgeo.2017.05.003>
- Zheng, G., Yang, X., Zhou, H., Du, Y., Sun, J., Yu, X., 2018. A simplified prediction method for evaluating tunnel displacement induced by laterally adjacent excavations. *Comput. Geotech.* 95, 119–128. <https://doi.org/10.1016/j.compgeo.2017.10.006>
- Zheng, H., 2022. Applying probabilistic approach for reliable SEM tunnel design and construction. Colorado School of Mines.
- Zheng, H., Bragard, C., Calvo, C.H., Mooney, M., Gutierrez, M., 2021a. Observed performance and analysis of SEM cavern construction in downtown Los Angeles. *J. Geotech. Geoenvironmental Eng.* 147, 05021011. [https://doi.org/10.1061/\(ASCE\)GT.1943-5606.0002639](https://doi.org/10.1061/(ASCE)GT.1943-5606.0002639)
- Zheng, H., Mooney, M., Gutierrez, M., 2022a. Reliability-Based Design of SEM Tunneling in

- Urban Settings, in: Proceedings of the Geo-Congress 2022. Charlotte, North Carolina.
- Zheng, H., Mooney, M., Gutierrez, M., 2022b. A Surrogate-Based Bayesian Approach to update ground parameters and model predictions in SEM Tunnelling (in review).
- Zheng, H., Mooney, M., Gutierrez, M., 2022c. Surrogate model representation of sequential excavation method 3D finite-difference method ground deformation (in review).
- Zheng, H., Mooney, M., Gutierrez, M., Bragard, C., 2021b. SEM deformation prediction and observation by 3D numerical analysis, in: Geotechnical Aspects of Underground Construction in Soft Ground. CRC Press, pp. 459–466.

APPENDIX A

BUILDING DEFORMATION ASSESSMENT

Figure A.1 presents the measurements on the Building I and Building II structure adjacent to the RCTC cavern excavation. These two historic buildings are more than 100 years old and the structural systems are primarily composed of reinforced concrete frames and walls. All the BMPs were measured by the same AMTSs that monitored GSSPs and shared the same recording and processing procedure. The BMPs settlements show similar trends with larger settlements developing in the facets parallel and close to the excavation, except B8 showing lower settlement due to the boundary effect at the end of the excavation. The maximum building settlement was approximately 15 mm. At a distance larger than 25 m from the cavern centerline (B1, B5, B6), building settlements were reduced to less than 2 mm. The magnitudes and characteristics of building deformations depend on ground-structure interaction. Figure A.2 shows a comparison of measured building settlement with the greenfield settlement obtained from fitted profiles in Figure 3.10. The settlements of the Building I (B1 to B4) are closer to the identity line, compared with those of the Building II (B5 to B8), which indicates a more flexible behavior of the Building I structure due to either low stiffness or existing cracking. To continuously monitor and estimate the damage of these critical buildings, the methodology proposed by Son and Cording (2005) was integrated into the analysis. Since only a few points of the building were monitored, the angular distortion and lateral strain were evaluated based on the deformations at points A and B as shown in Figure A.3. The deformations and tilting at point B were obtained from field BMP and tiltmeter measurements, while the horizontal (A_x) and vertical deformations (A_z) at point A were conservatively assumed to be equal to the greenfield deformation (A_{xg} , A_{zg}). The procedure was applied to four cross-sections (B2, B3, B4, and B7), and corresponding lateral strain and angular distortion were calculated for each excavation stage. Results are shown in Figure A.4 and Figure A.5, which indicate all cases were restricted to the “negligible” or “very slight damage” categories.

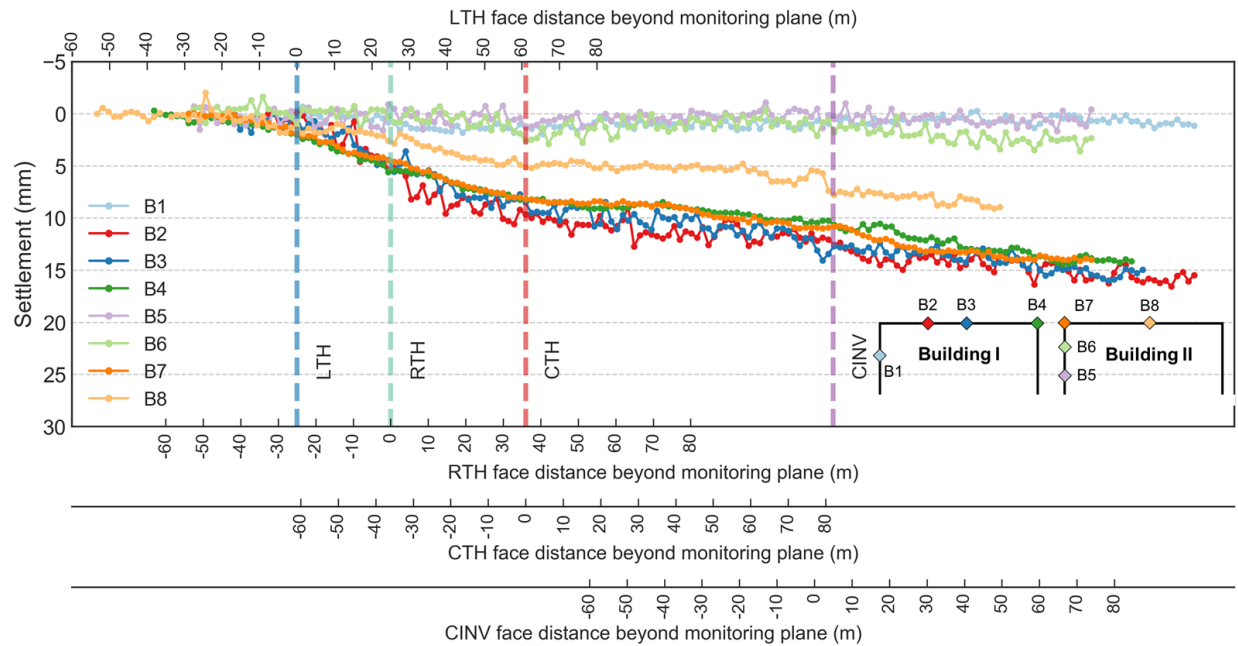


Figure A.1 Measured building settlement.

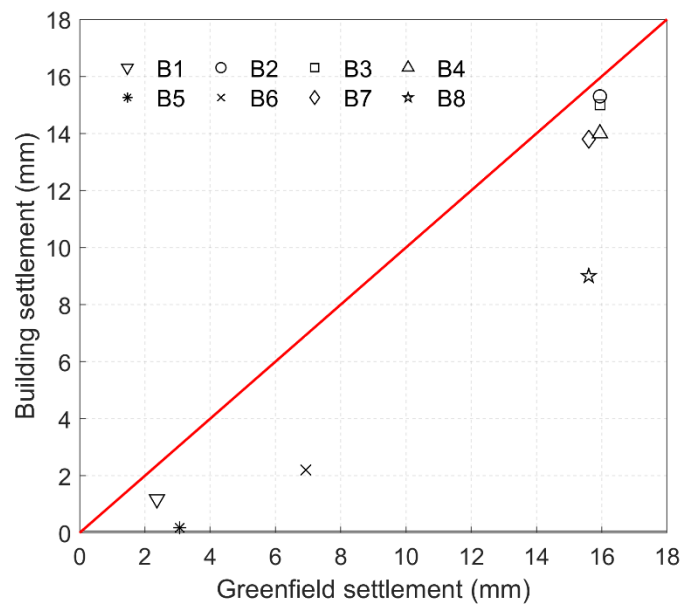


Figure A.2 Comparison of building settlement and greenfield settlement (fitted).

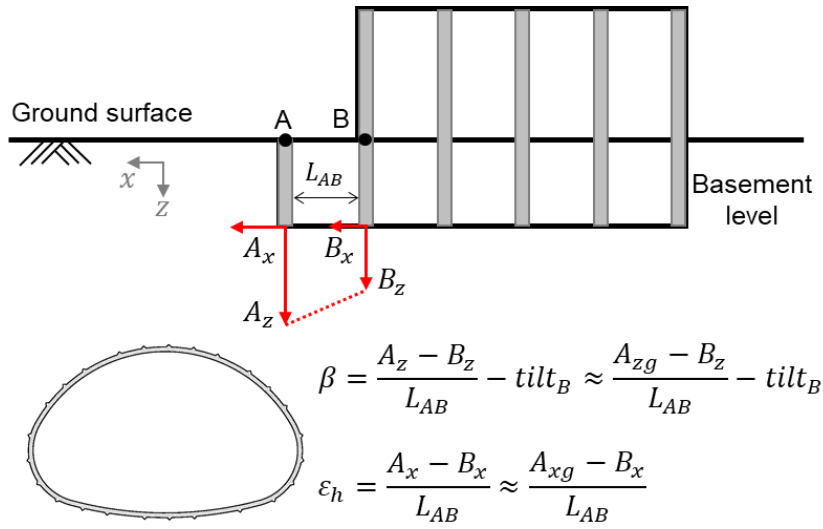


Figure A.3 Evaluation of angular distortion and lateral strain.

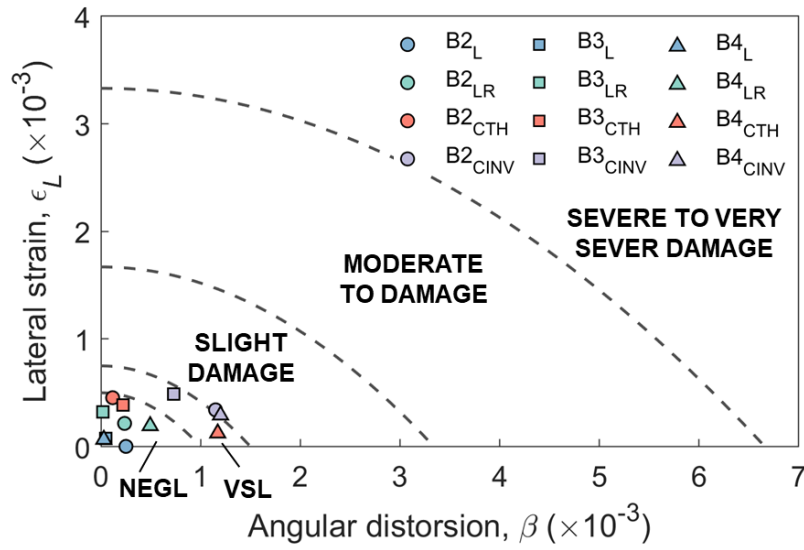


Figure A.4 Damage category assessment of Building I.

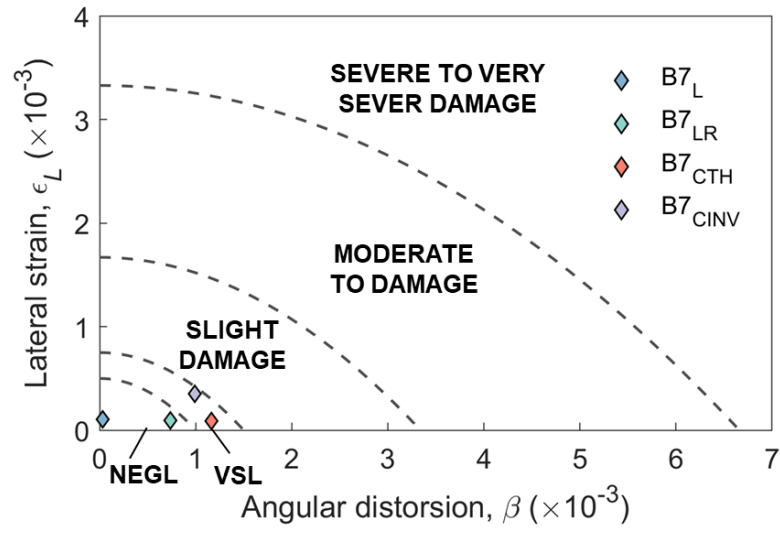


Figure A.5 Damage category assessment of Building II.

APPENDIX B

HARDENING SOIL SMALL STRAIN MODEL KEY PARAMETERS INTERPRETATION

This section summarises the interpretation of hardening soil small strain (HSS) model key parameters that are used in the uncertainty analysis presented in Chapter 4 and Chapter 5.

The HSS parameter calibration was carried out by exploiting all available laboratory and in situ tests along the entire tunnel alignment from the RCTC project (*Regional Connector Transit Corridor project - final geotechnical data report*, 2012). The calibration procedure mainly follows the recommended sequence and methods described in (Obrzud and Truty, 2018). The calibration procedure and statistical interpretation of selected parameters are presented as follows.

First, the effective cohesion and friction were determined based on 12 CIUC triaxial tests and 10 direct shear tests (Figure B.1). The mean values of effective cohesion for Tf1 and Tf2 are 75 kPa and 170 kPa, respectively. The values of Tf2 cohesion increase with depth for the CIUC tests. However, considering the high variation (even at the same depth) of the CIUC data and relatively constant values with depths shown in the direct shear tests, an assumption was made to treat the mean cohesion values as constant for Tf1 and Tf2. The COVs of effective cohesion for Tf1 and Tf2 are 33% and 62% and were considered as 40% and 70%, respectively for the uncertainty analysis.

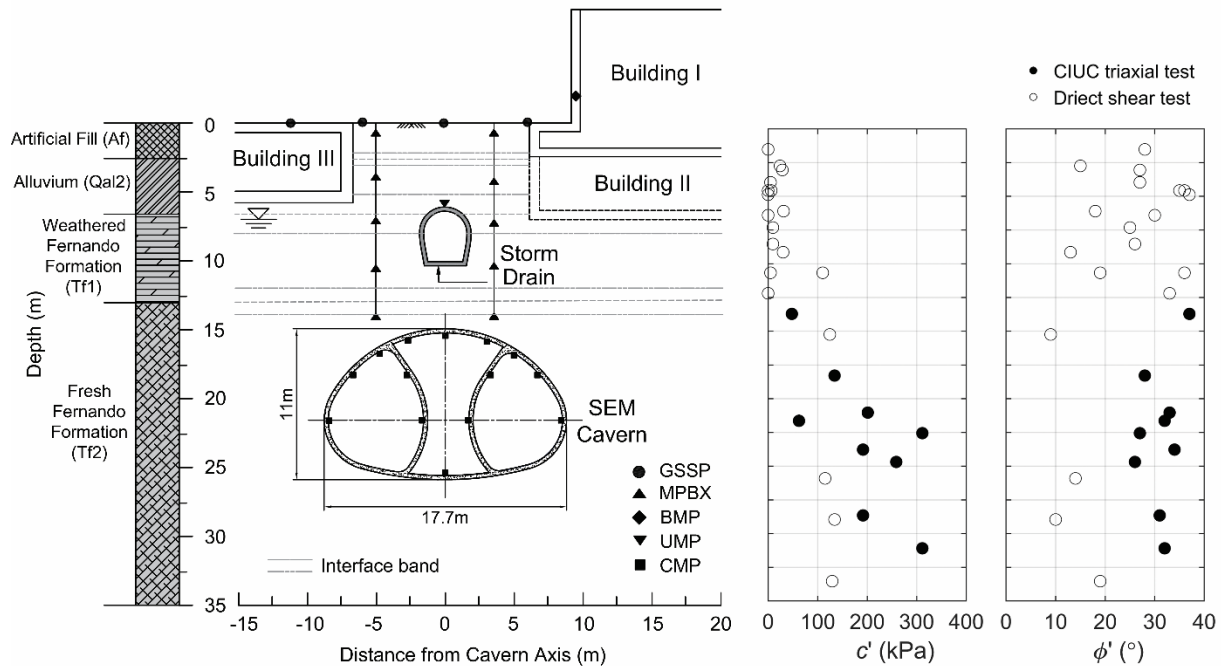


Figure B.1 Cross-section view of the RCTC cavern and the cohesion c' , friction angle ϕ' interpreted from direct shear tests and consolidated isotropic undrained compression (CIUC) triaxial tests.

The ground stiffness parameters were estimated using both triaxial and pressuremeter tests. The secant modulus E_{50}^{ref} is assumed equal to the oedometric modulus E_{oed}^{ref} . The unloading-reloading modulus E_{ur}^{ref} defines the slope of the unloading-reloading curve. The secant modulus E_{50}^{ref} and the power for stress-level dependency m were estimated from a set of triaxial compression tests with various cell stresses. Figure B.2 plots the secant modulus at 50% of failure deviatoric stress against the corresponding normalized minor effective stresses obtained from 12 CIUC tests. A linear regression line was fitted for each set of test results. Pairs of E_{50}^{ref} and m values were obtained based on the intercepts and slopes of the regression lines. The means of E_{50}^{ref} for Tf1 and Tf2 are 47.8 MPa and 54.8 MPa, respectively. The COVs of E_{50}^{ref} for Tf1 and Tf2 are 22% and 39% and were considered as 30% and 50%, respectively in the uncertainty analysis.

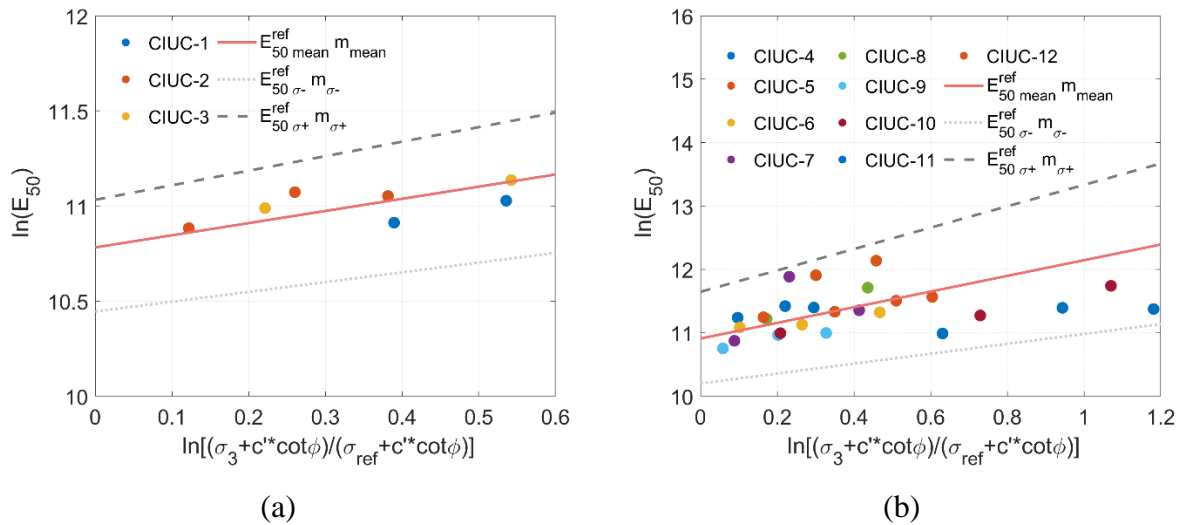


Figure B.2 Determination of E_{50}^{ref} and stress-level dependencies of (a) Tf1 and (b) Tf2.

Since the available triaxial tests did not involve unloading-reloading stress paths, E_{ur}^{ref} cannot be directly estimated from the lab tests. Instead, E_{ur}^{ref} was estimated from the pressuremeter tests results with unloading-reloading cycles as shown in Figure B.3. The mean values for Tf1 and Tf2 are 150 MPa and 183 MPa, respectively. Since the data is quite sparse, COVs of the E_{ur}^{ref} were conservatively assumed equal to 50%.

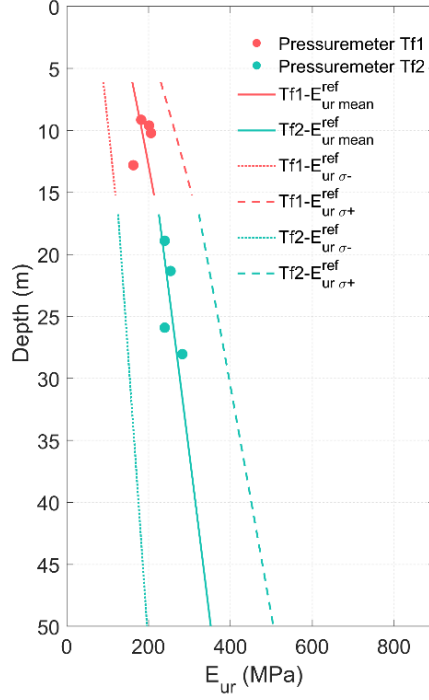
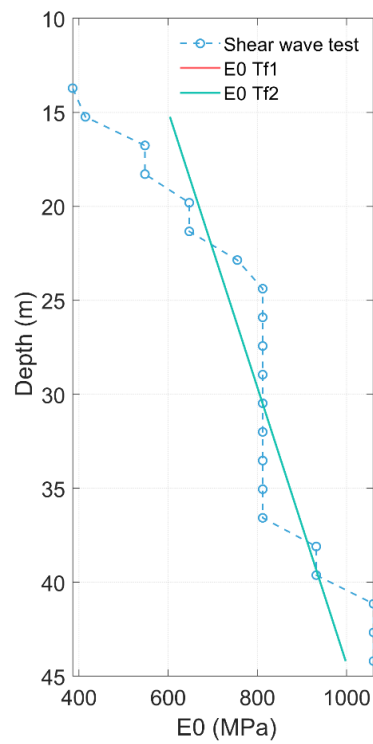
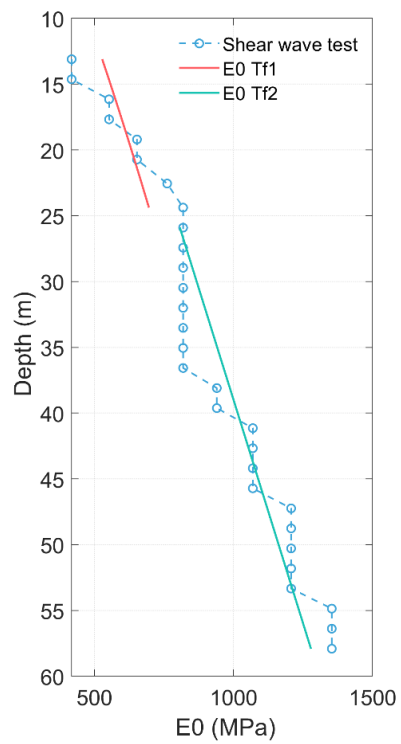
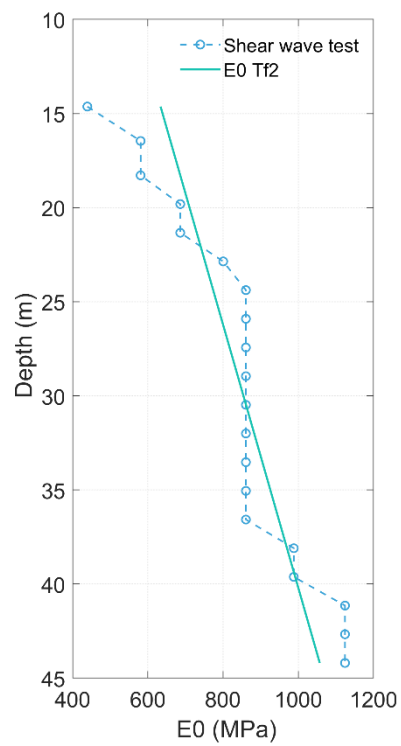
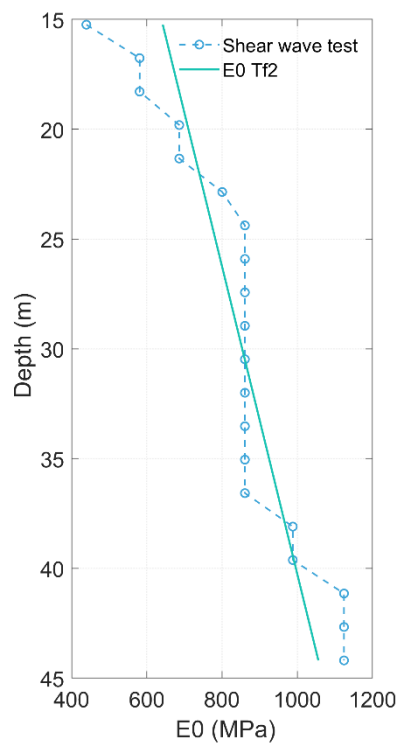


Figure B.3 Determination of E_{ur}^{ref} from pressuremeter tests.

The calibration of the HSS model also contains two additional parameters characterizing the small strain behavior, namely the initial modulus at the reference pressure E_0^{ref} and the characteristic shear strain level at which the secant shear modulus reduces to 70% of the initial shear modulus $\gamma_{0.7}$, respectively. The small strain parameter E_0^{ref} was directly derived from the field shear wave tests (Figure B.4). The means of E_0^{ref} for Tf1 and Tf2 are 331 MPa and 480 MPa, respectively. The COVs of E_0^{ref} for Tf1 and Tf2 are 21% and 24% and were both considered as 30% in the uncertainty analysis. The mean value of $\gamma_{0.7}$ is assumed to be 2×10^{-4} and COV is conservatively assumed as 30% for both Tf1 and Tf2 according to Obrzud and Truty (2018).



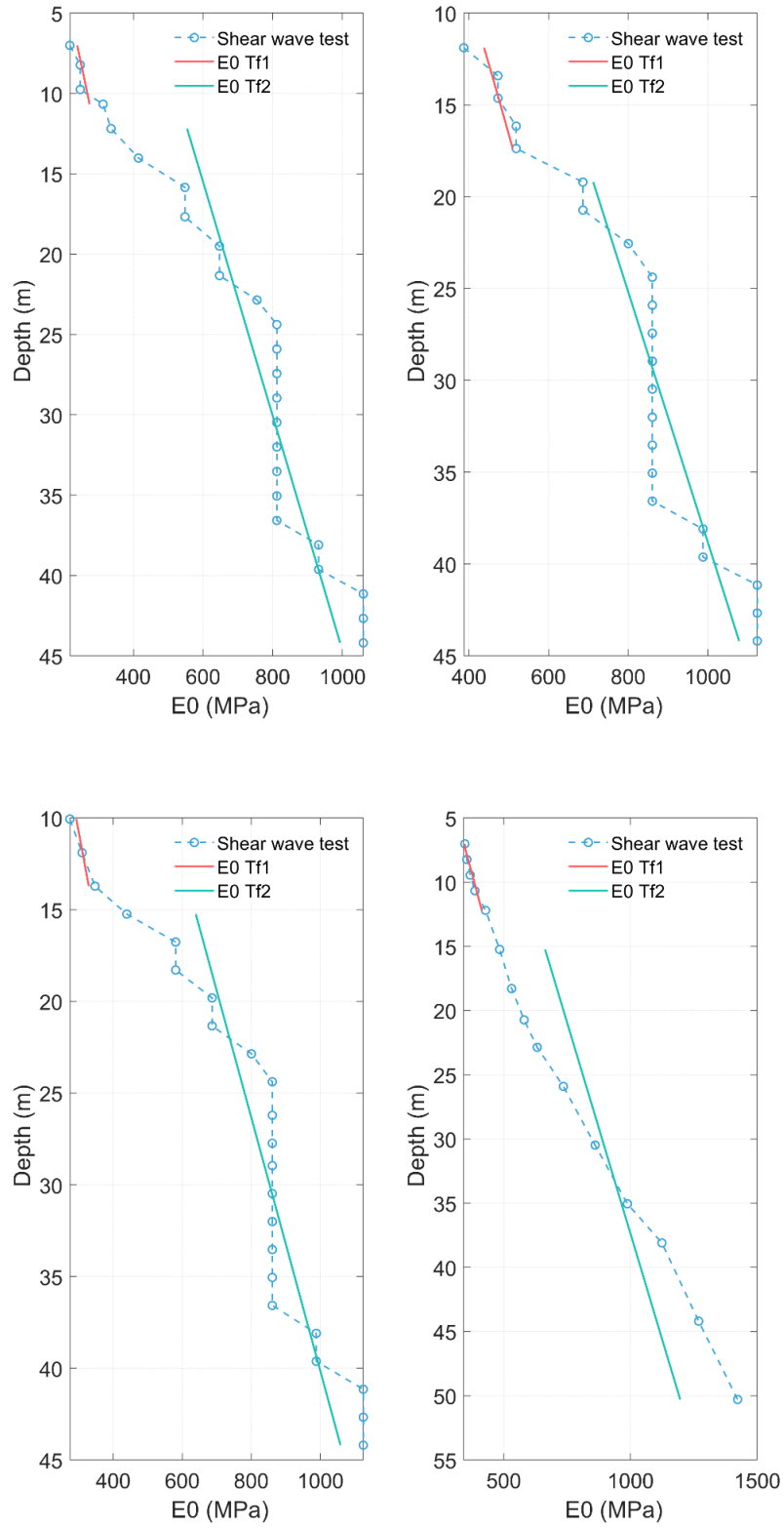


Figure B.4 Determination of E_0^{ref} for Tf1 and Tf2 from geophysical shear wave tests.

APPENDIX C

PERFORMANCE OF THE AIES MARKOV CHAIN MONTE CARLO SIMULATION

This section presents the efficacy of the proposed AIES MCMC sampler used in Chapter 5 for an efficient Bayesian updating.

For an efficiently working MCMC simulation, proper properties of the AIES algorithm need to be selected. It has been demonstrated that setting the single scalar tuning parameter $\alpha=2$ shows good performance in most situations (Foreman-Mackey et al., 2013). The number of walkers (parallel Markov chains) was set to 100 here. To ensure the convergence of MCMC simulations, the number of steps needed for all walkers was examined. The Gelman-Rubin approach (Brooks and Gelman, 1998) was used to quantitatively assess the MCMC convergence. By running a set of parallel MCMC chains initiated at different seed points, the multivariate potential scale reduction factor (MPSRF) proposed by (Brooks and Gelman, 1998) can be calculated. Good MCMC convergence is diagnosed when MPSRF is close to 1 (general goal is <1.1). In this case, the convergence criterion of $\text{MPSRF} < 1.1$ can be achieved when the number of MCMC steps is greater than 3000 for all update stages. Therefore, the length of each MCMC chain was set equal to 3000 steps. As an example, Figure C.1 shows the convergence of the MPSRF for the first updating stage. The MPSRF value reaches below 1.1 after 3000 steps and plateaus out. Another indicator to assess MCMC convergence is the acceptance rate which shows how many proposed sample points were accepted. Either too low (close to 0) or too high (close to 1) acceptance rate indicates a badly performed algorithm. A rule of thumb is that a good acceptance rate should be between 0.2 and 0.5 (Foreman-Mackey et al., 2013). For our case, the acceptance rates for all MCMC simulations are between 0.26 and 0.34. To prevent some initial samples from polluting the estimation, the first 1500 sample points generated in the Markov chain were discarded as burn-in samples. Figure C.2 presents the trace plots of the MCMC simulations for the five uncertain geotechnical parameters. The results show that all the chains move dynamically, not flattening out or getting stuck in one direction. The relatively good mixing of the MCMC chains indicates efficient sampling of all the parameters.

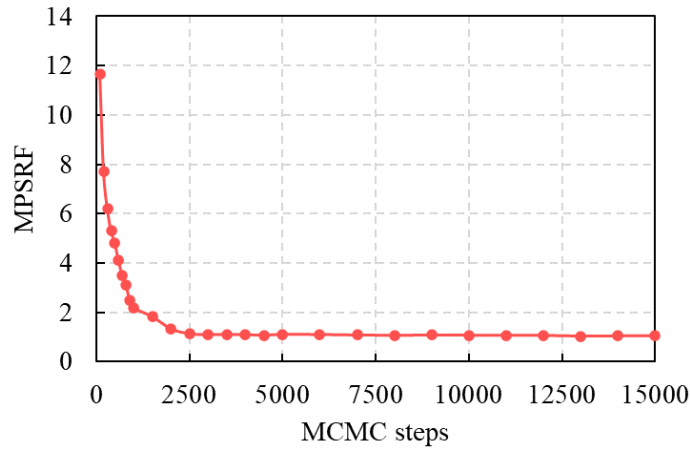


Figure C.1 Convergence of the MPSRF for the first updating.

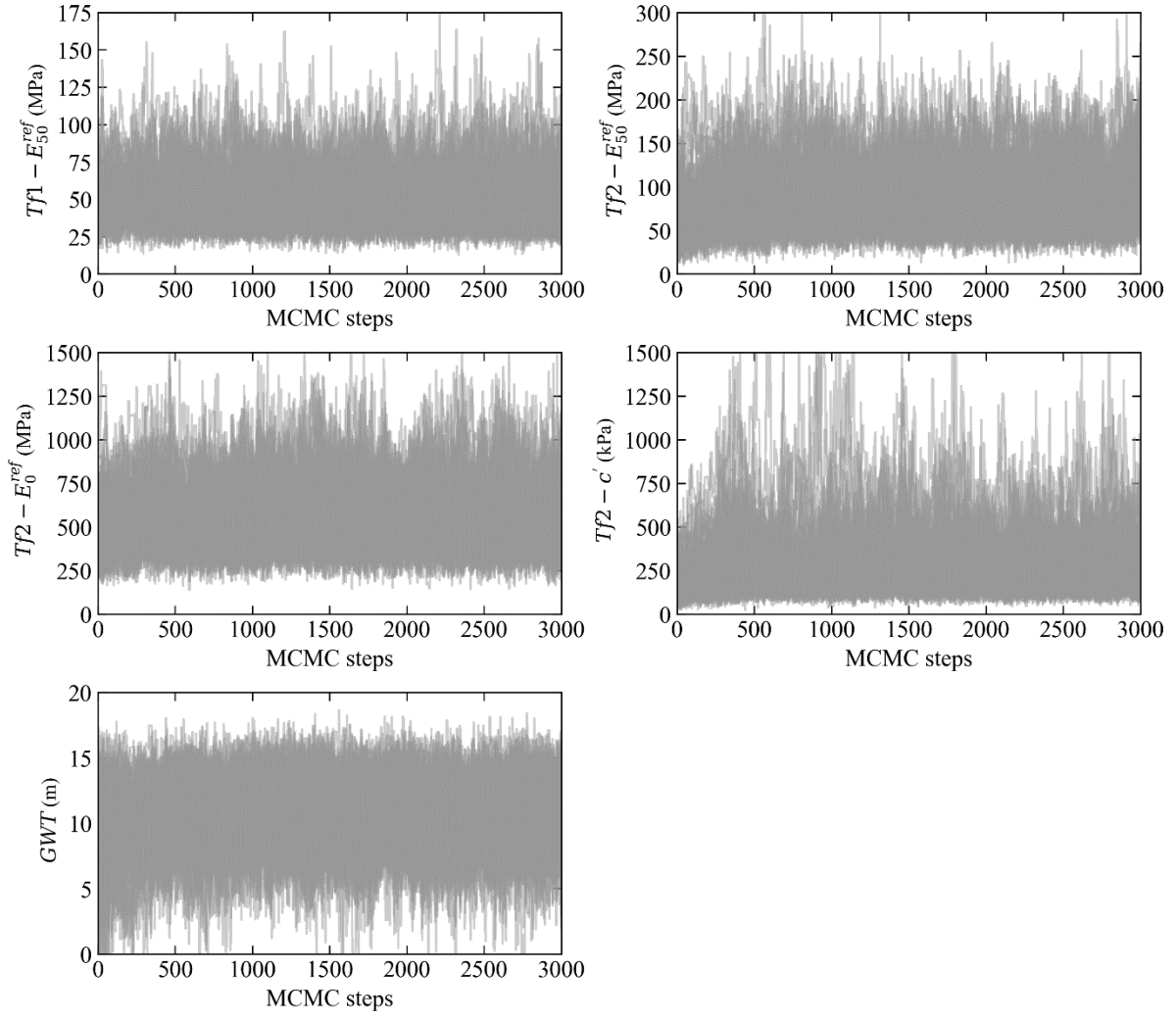


Figure C.2 Trace plots of MCMC simulations for all chains during the first updating.

APPENDIX D

TECHNOLOGY TRANSFER ACTIVITIES

1 Accomplishments

1.1 What was done? What was learned?

- A comprehensive case study of the Regional Connector Transit Corridor (RCTC) cavern construction is conducted. The performance of the three-drift seven-stage urban SEM was assessed, and complex ground and structural behaviors were evaluated at every excavation step by analyzing the field observations.
- A three-dimensional (3D) finite-difference method (FDM) model is developed to simulate the SEM construction process and surrogate models are developed to accurately and efficiently capture the complex 3D FDM deformation responses induced by SEM tunneling.
- A surrogate-based Bayesian approach is developed to update uncertain ground parameters and deformation predictions during the RCTC SEM construction.
- A reliability approach is developed to evaluate ground and structural stabilities induced by SEM construction under the uncertainty of ground conditions and the variability of design measures.

1.2 How have the results been disseminated?

- The results were presented at the 2021 Rapid Excavation and Tunneling Conference, Las Vegas, Nevada, June 12, 2021.
- One journal paper has been published in a journal
- A second paper was submitted and reviewed in a journal
- A third journal paper is completed and is to be submitted to a journal
- The results were presented at UTC-UTI workshops

2 Participants and Collaborating Organizations

Traylor Bros.
Skanska

3 Outputs

Journal publications

Zheng, H., Bragard, C., Calvo, C. H., Mooney, M., & Gutierrez, M. (2021). *Observed Performance and Analysis of SEM Cavern Construction in Downtown Los Angeles*. *Journal of Geotechnical and Geoenvironmental Engineering*, 147(11), 05021011.

Conference presentations and proceedings

Zheng, H., Mooney, M., Gutierrez, M., & Bragard, C. (2021). *SEM deformation prediction and observation by 3D numerical analysis*. In *Geotechnical Aspects of Underground Construction in Soft Ground* (pp. 459-466). CRC Press.

Zheng, H., Mooney, M., Gutierrez, M., & Bragard, C. (2021). *Application of Surrogate Modeling for SEM Tunneling Simulation*. In *Rapid Excavation and Tunneling Conference 2021* (pp. 1042-1054).

Zheng, H., Mooney, M., & Gutierrez, M. *Reliability-Based Design of SEM Tunneling in Urban Settings*. In *Geo-Congress 2022* (pp. 486-495).

4 Outcomes

- The case study of the Regional Connector SEM cavern construction characterized the ground and structural responses at spatial and temporal scales. A real-time analysis tool developed during the construction assisted tunnel engineers in promptly understanding the ground and structure behavior, facilitating the decision-making process and enabling an adaptive SEM design.
- The developed surrogate model can accurately and efficiently capture 3D numerical responses of SEM construction, providing a powerful tool for uncertainty quantification, reliability analysis, and other probabilistic analyses.
- The proposed Bayesian updating quantifies uncertainties and updates model predictions during SEM construction, improving the knowledge of ground conditions and informing the risk along with the entire construction.
- The reliability approach quantifies the risks of exceeding ground and structure limit states given uncertain ground conditions and various SEM design options, providing an alternative tool to the conventional LRFD method for the initial support design.

5 Impacts

The analyses conducted in this report provide efficient and accurate probabilistic approaches to help designers and contractors make well-grounded decisions based on updated knowledge of risk along the SEM design and construction process, relieving technical and financial risks taken by SEM projects.

APPENDIX E

FIELD MEASUREMENTS OF RCTC SEM CAVERN

Table E.1 Ground surface measurements subsection 1 of the RCTC SEM cavern

Time	GSSP-361D (in)	GSSP-362 (in)	GSSP-359 (in)	GSSP-360 (in)	GSSP-353 (in)	GSSP-354 (in)
2018-05-30 00:00:00	0.03	-0.048	-0.024	0.012	0.084	-0.06
2018-05-31 00:00:00	-0.03	-0.06	-0.048	-0.024	0.012	-0.084
2018-06-01 00:00:00	0.138	-0.06	0	-0.012	0.072	-0.084
2018-06-04 00:00:00	0.09	-0.06	-0.036	-0.012	0.036	-0.096
2018-06-05 00:00:00	0.09	0	0.012	0.048	0.084	-0.048
2018-06-06 00:00:00	0.09	-0.012	0.024	0.036	0.096	-0.06
2018-06-08 00:00:00	0.174	-0.024	0.048	0.024	0.096	-0.048
2018-06-11 00:00:00	0.186	-0.048	0.012	0.012	0.06	-0.072
2018-06-12 00:00:00	0.21	0	0.06	0.036	0.108	-0.06
2018-06-13 00:00:00	0.138	-0.024	0.06	0.024	0.108	-0.072
2018-06-14 00:00:00	0.198	-0.024	0.06	0.036	0.108	-0.06
2018-06-15 00:00:00	0.198	0	0.012	0.036	0.072	-0.06
2018-06-18 00:00:00	0.174	-0.012	0.024	0.024	0.072	-0.096
2018-06-19 00:00:00	0.198	0.012	0.072	0.048	0.132	-0.048
2018-06-20 00:00:00	0.174	0.024	0.048	0.06	0.096	-0.06
2018-06-21 00:00:00	0.222	0	0.036	0.048	0.084	-0.06
2018-06-22 00:00:00	0.114	0.024	0.108	0.072	0.132	-0.048
2018-06-24 00:00:00		0.0526	0.0943	0.0879	0.114094	-0.03685
2018-06-25 00:00:00	0.246	0.037	0.0615	0.1037	0.117969	-0.02813
2018-06-26 00:00:00	0.222	0.048	0.072	0.084	0.105564	-0.027
2018-06-27 00:00:00	0.21	0.0308	0.0561	0.06	0.121123	-0.06
2018-06-28 00:00:00		0.0592	0.072	0.0978	0.151496	
2018-06-29 00:00:00		0.0808	0.1022	0.103	0.143622	-0.00174
2018-06-30 00:00:00		0.0815	0.0989	0.1214	0.06357	-0.00371
2018-07-01 00:00:00		0.05	0.0707	0.1162	0.100315	
2018-07-02 00:00:00		0.0598	0.0956	0.1057	0.135748	
2018-07-03 00:00:00	0.2193	0.0985	0.1009	0.1017	0.123281	
2018-07-04 00:00:00	0.2016	0.0624	0.1081	0.1303	0.127874	
2018-07-05 00:00:00	0.2311	0.0624	0.1461	0.1057	0.210551	
2018-07-06 00:00:00	0.2377	0.0742	0.1783	0.1076	0.18168	
2018-07-07 00:00:00	0.26	0.1576	0.1586	0.1431	0.239423	
2018-07-08 00:00:00	0.2758	0.1235	0.1816	0.1509	0.232205	
2018-07-09 00:00:00	0.2895	0.1044	0.1862	0.149	0.225643	

2018-07-10 00:00:00	0.2981	0.1136	0.1776	0.1549	0.226955	-0.09918
2018-07-11 00:00:00	0.3086	0.0933	0.1678	0.1654	0.190866	0.049769
2018-07-12 00:00:00	0.2882	0.0985	0.177	0.1654	0.165932	0.056331
2018-07-13 00:00:00	0.2797	0.1018	0.1521	0.1686	0.173806	0.016961
2018-07-14 00:00:00	0.3099	0.1248	0.2045	0.1686	0.184304	0.037302
2018-07-15 00:00:00	0.3204	0.1477	0.1934	0.1805	0.196772	0.03599
2018-07-16 00:00:00	0.2941	0.1648	0.1711	0.1942	0.186929	0.048457
2018-07-17 00:00:00	0.3197	0.151	0.1521	0.1805	0.196116	0.071423
2018-07-18 00:00:00	0.3158	0.1359	0.1402	0.1896	0.214488	0.050425
2018-07-19 00:00:00	0.3059	0.1819	0.1914	0.2257	0.240079	0.060924
2018-07-20 00:00:00	0.3191	0.1733	0.1816	0.2343	0.222362	0.07536
2018-07-21 00:00:00	0.342	0.1628	0.2216	0.227	0.23811	0.093076
2018-07-22 00:00:00	0.3328	0.197	0.2249	0.227	0.253858	0.098326
2018-07-23 00:00:00	0.3263	0.1996	0.2137	0.2257	0.255171	0.097013
2018-07-24 00:00:00	0.3538	0.2127	0.2557	0.2612	0.244672	0.107512
2018-07-25 00:00:00	0.3742	0.2508	0.2689	0.2405	0.248609	0.121291
2018-07-26 00:00:00	0.3591	0.2553	0.2465	0.273	0.244672	0.130478
2018-07-27 00:00:00	0.3269	0.2081	0.217	0.2743	0.257795	0.146226
2018-07-28 00:00:00	0.3571	0.197	0.2406	0.2769	0.292572	0.149507
2018-07-29 00:00:00	0.3735	0.2344	0.2452	0.2782	0.291916	0.141633
2018-07-30 00:00:00	0.3702	0.2442	0.2584	0.2782	0.289291	0.148194
2018-07-31 00:00:00	0.3899	0.2567	0.2826	0.2756	0.306352	0.159349
2018-08-01 00:00:00	0.3729	0.2462	0.2925	0.2992	0.312913	0.173785
2018-08-02 00:00:00	0.3617	0.2429	0.2767	0.3012	0.318163	0.179034
2018-08-03 00:00:00	0.3755	0.2462	0.2597	0.2966	0.317507	0.177722
2018-08-04 00:00:00	0.4057	0.2626	0.28	0.3045	0.309633	0.187564
2018-08-05 00:00:00	0.3926	0.258	0.301	0.3163	0.340473	0.196095
2018-08-06 00:00:00	0.3912	0.258	0.3115	0.3189	0.326693	0.196751
2018-08-07 00:00:00	0.4162	0.2796	0.3187	0.3202	0.321444	0.194782
2018-08-08 00:00:00	0.3991	0.2868	0.3095	0.3301	0.320788	0.207906
2018-08-09 00:00:00	0.3912	0.2678	0.3095	0.3392	0.316194	0.240714
2018-08-10 00:00:00	0.4109	0.2914	0.3154	0.3399	0.340473	0.237433
2018-08-11 00:00:00	0.3834	0.296	0.3168	0.3399	0.318163	0.236121
2018-08-12 00:00:00	0.4201	0.2928	0.3168	0.3399	0.297165	0.236777
2018-08-13 00:00:00	0.4385	0.2901	0.3633	0.3392	0.34769	0.239402
2018-08-14 00:00:00	0.4516	0.2973	0.3345	0.3327	0.341129	0.229559
2018-08-15 00:00:00	0.4667	0.2934	0.3633	0.3589	0.37	0.231528
2018-08-16 00:00:00	0.4674	0.2882	0.366	0.3478	0.375906	0.239402
2018-08-17 00:00:00	0.4293	0.298	0.3712	0.3517	0.377218	0.432315
2018-08-18 00:00:00	0.4188	0.317	0.3509	0.3606	0.377218	0.259087
2018-08-19 00:00:00	0.4398	0.3026	0.3653	0.3576	0.405433	0.262368

2018-08-20 00:00:00	0.4444	0.3092	0.3364	0.3635	0.397559	0.265648
2018-08-21 00:00:00	0.426	0.2895	0.3384	0.3478	0.410026	0.261711
2018-08-22 00:00:00	0.4529	0.3236	0.3338	0.357	0.447428	0.261055
2018-08-23 00:00:00	0.4431	0.3203	0.3338	0.3616	0.406089	0.264992
2018-08-24 00:00:00	0.4306	0.3144	0.406	0.3635	0.445459	0.282053
2018-08-25 00:00:00	0.449	0.3328	0.3876	0.3727	0.43168	0.284021
2018-08-26 00:00:00	0.4477	0.3393	0.385	0.3714	0.432336	0.282709
2018-08-27 00:00:00	0.4634	0.3203	0.366	0.3688	0.413963	0.293208
2018-08-28 00:00:00	0.4011	0.3256	0.3397	0.3734	0.416588	0.302394
2018-08-29 00:00:00	0.3939	0.338	0.3371	0.3819	0.450053	0.305019
2018-08-30 00:00:00	0.4477	0.3584	0.3456	0.3747	0.377218	0.33389
2018-08-31 00:00:00	0.428	0.3197	0.3358	0.3767	0.468425	0.321421
2018-09-01 00:00:00	0.4523	0.3249	0.3423	0.3753	0.455302	0.302394
2018-09-02 00:00:00	0.4805	0.3485	0.345	0.3812	0.443491	0.303706
2018-09-03 00:00:00	0.4569	0.3308	0.3496	0.3753	0.442179	0.297801
2018-09-04 00:00:00	0.4779	0.3124	0.3568	0.3773	0.407402	0.295176
2018-09-05 00:00:00	0.5185	0.3479	0.3601	0.397	0.442179	0.302394
2018-09-06 00:00:00	0.445	0.3092	0.3174	0.3812	0.42315	0.314205
2018-09-07 00:00:00	0.4385	0.321	0.324	0.3819	0.405433	0.315517
2018-09-08 00:00:00	0.428	0.3249	0.3246	0.3839	0.419213	0.319454
2018-09-09 00:00:00	0.4483	0.3407	0.3338	0.3878	0.446772	0.335858
2018-09-10 00:00:00	0.451	0.3577	0.3561	0.3858	0.458583	0.341764
2018-09-11 00:00:00	0.4444	0.3616	0.3568	0.3871	0.43168	0.337827
2018-09-12 00:00:00	0.4588	0.3636	0.3377	0.4042	0.423806	0.33389
2018-09-13 00:00:00	0.4614	0.3308	0.3548	0.3976	0.437585	0.337827
2018-09-14 00:00:00	0.4483	0.338	0.3712	0.399	0.471706	0.337818
2018-09-15 00:00:00	0.4542	0.3551	0.3568	0.395	0.468425	0.337171
2018-09-16 00:00:00	0.4844	0.3518	0.3542	0.399	0.44874	0.331921
2018-09-17 00:00:00	0.4943	0.3498	0.3528	0.3931	0.440866	0.329953
2018-09-18 00:00:00	0.489	0.3426	0.3824	0.4016	0.457271	0.329953
2018-09-19 00:00:00	0.4614	0.3466	0.3725	0.4016	0.446772	0.327328
2018-09-20 00:00:00	0.4345	0.3407	0.3574	0.4095	0.421181	0.329953
2018-09-21 00:00:00	0.4496	0.4102	0.3791	0.4108	0.513701	0.33389
2018-09-22 00:00:00	0.5074	0.3649	0.4519	0.4134	0.511732	0.344389
2018-09-23 00:00:00	0.4628	0.3446	0.4303	0.4108	0.455958	0.348982
2018-09-24 00:00:00	0.491	0.3984	0.3751	0.416	0.457271	0.354887
2018-09-25 00:00:00	0.529	0.3971	0.3837	0.4246	0.454646	0.353575
2018-09-26 00:00:00	0.5363	0.4102	0.3922	0.42	0.437585	0.347013
2018-09-27 00:00:00	0.491	0.3826	0.3909	0.4246	0.442179	0.348326
2018-09-28 00:00:00	0.5126	0.4082	0.4014	0.4291	0.459239	0.353575
2018-09-29 00:00:00	0.5185	0.4384	0.3948	0.4423	0.489423	0.362105

2018-09-30 00:00:00	0.5015	0.4404	0.408	0.4383	0.473019	0.357512
2018-10-01 00:00:00	0.531	0.4056	0.4132	0.4396	0.476956	0.364074
2018-10-02 00:00:00	0.5225	0.4069	0.4303	0.4475	0.470394	0.39032
2018-10-03 00:00:00	0.5428	0.4161	0.4368	0.456	0.472362	0.4041
2018-10-04 00:00:00	0.5441	0.4135	0.4591	0.4587	0.511076	0.403444
2018-10-05 00:00:00	0.5402	0.4115	0.4513	0.456	0.47105	0.417223
2018-10-06 00:00:00	0.531	0.4141	0.4217	0.458	0.481549	0.390977
2018-10-07 00:00:00	0.5284	0.4102	0.4381	0.4593	0.494016	0.366698
2018-10-08 00:00:00	0.5192	0.384	0.4224	0.4626	0.465801	0.3562
2018-10-09 00:00:00	0.5198	0.4181	0.4257	0.4685	0.494016	0.379822
2018-10-10 00:00:00	0.5015	0.4102	0.4165	0.4593	0.455958	0.382446
2018-10-11 00:00:00	0.4916	0.384	0.4066	0.4672	0.440866	0.383759
2018-10-12 00:00:00	0.5198	0.4128	0.4185	0.4672	0.48483	0.328641
2018-10-13 00:00:00	0.5048	0.4181	0.4329	0.4784	0.483517	0.360137
2018-10-14 00:00:00	0.5002	0.4102	0.3994	0.4738	0.473019	0.393601
2018-10-15 00:00:00	0.5067	0.4023	0.4224	0.4764	0.464488	0.390977
2018-10-16 00:00:00	0.5192	0.4089	0.4257	0.4738	0.469082	0.396882
2018-10-17 00:00:00	0.5264	0.3945	0.4224	0.4895	0.463832	0.389008
2018-10-18 00:00:00	0.4923	0.3872	0.408	0.4902	0.492047	0.392945
2018-10-19 00:00:00	0.5264	0.4043	0.4539	0.4974	0.508452	0.404756
2018-10-20 00:00:00	0.5369	0.4312	0.4624	0.4961	0.522887	0.408037
2018-10-21 00:00:00	0.5389	0.4273	0.4322	0.5	0.550446	0.416567
2018-10-22 00:00:00	0.5277	0.4004	0.448	0.4928	0.51895	0.423768
2018-10-23 00:00:00	0.5395	0.3918	0.4434	0.5039	0.499253	0.4264
2018-10-24 00:00:00	0.5185	0.4214	0.4276	0.5144	0.51042	0.437565
2018-10-25 00:00:00	0.5251	0.4036	0.4329	0.5276	0.521575	0.446751
2018-10-26 00:00:00	0.5192	0.4351	0.4394	0.6004	0.526839	0.448067
2018-10-27 00:00:00	0.5061	0.4023	0.4263	0.5164	0.5209	0.445467
2018-10-28 00:00:00	0.5238	0.4154	0.4329	0.5131	0.5255	0.439567
2018-10-29 00:00:00	0.5317	0.422	0.4329	0.5105	0.513685	0.429706
2018-10-30 00:00:00	0.5238	0.4004	0.444	0.5092	0.507139	0.442814
2018-10-31 00:00:00	0.5225	0.4102	0.4388	0.5171	0.494672	0.447407
2018-11-01 00:00:00	0.5303	0.3905	0.4237	0.5144	0.5242	0.431659
2018-11-02 00:00:00	0.5139	0.4227	0.4447	0.4974	0.520263	0.434284
2018-11-03 00:00:00	0.5185	0.4128	0.4506	0.5177	0.530761	0.442814
2018-11-04 00:00:00	0.5251	0.4122	0.4526	0.5158	0.527481	0.448719
2018-11-05 00:00:00	0.5172	0.4023	0.4513	0.5289	0.494672	0.448063
2018-11-06 00:00:00	0.5185	0.3866	0.4828	0.5263	0.512389	0.455937
2018-11-07 00:00:00	0.5238	0.4141	0.4355	0.5322	0.530761	0.459874
2018-11-08 00:00:00	0.5238	0.3899	0.4198	0.5066	0.543229	0.440189
2018-11-09 00:00:00	0.533	0.4063	0.4342	0.5092	0.525512	0.434284

2018-11-10 00:00:00	0.5356	0.4168	0.4578	0.5105	0.537323	0.441502
2018-11-11 00:00:00	0.5264	0.4056	0.4605	0.5013	0.502546	0.425097
2018-11-12 00:00:00	0.5408	0.4391	0.4631	0.502	0.525512	0.444126
2018-11-13 00:00:00	0.5264	0.447	0.486	0.5105	0.542572	0.467748
2018-11-14 00:00:00	0.5363	0.4371	0.4519	0.5112	0.545197	0.440189
2018-11-15 00:00:00	0.531	0.4161	0.4788	0.5381	0.533386	0.446751
2018-11-16 00:00:00	0.5422	0.4174	0.4414	0.5407	0.526824	0.448719
2018-11-17 00:00:00	0.5428	0.4181	0.4401	0.5079	0.549134	0.453313
2018-11-18 00:00:00	0.5507	0.3931	0.4532	0.5079	0.550446	0.459218
2018-11-19 00:00:00	0.5408	0.4141	0.4486	0.4994	0.561601	0.446751
2018-11-20 00:00:00	0.5428	0.405	0.4486	0.4961	0.556352	0.441502
2018-11-21 00:00:00	0.5395	0.3945	0.4375	0.5053	0.537323	0.450688
2018-11-22 00:00:00	0.5461	0.4207	0.4526	0.5033	0.538635	0.453313
2018-11-23 00:00:00	0.5238	0.4076	0.4467	0.5066	0.547822	0.462499
2018-11-24 00:00:00	0.5468	0.3853	0.4427	0.5066	0.537979	0.482184
2018-11-25 00:00:00	0.5599	0.4095	0.4644	0.5013	0.539292	
2018-11-26 00:00:00	0.5592	0.4141	0.4723	0.5026	0.568163	0.465124
2018-11-27 00:00:00	0.6084	0.443	0.4788	0.5118	0.589817	0.453313
2018-11-28 00:00:00	0.5704	0.4496	0.4834	0.5171	0.573412	0.466436
2018-11-29 00:00:00	0.5802	0.4686	0.4972	0.5197	0.568819	0.488746
2018-11-30 00:00:00	0.6025	0.464	0.4828	0.5177	0.545854	0.446742
2018-12-01 00:00:00	0.5894	0.4732	0.4729	0.5243	0.553727	0.452656
2018-12-02 00:00:00	0.5763	0.4502	0.4775	0.5318	0.531418	0.460859
2018-12-03 00:00:00	0.5927	0.483	0.4591	0.5387	0.55832	0.455937
2018-12-04 00:00:00	0.5979	0.4903	0.4755		0.533386	0.450032
2018-12-05 00:00:00	0.596	0.5099	0.5005	0.5486	0.598347	0.476935
2018-12-06 00:00:00	0.6242	0.4903	0.5517	0.5164	0.605565	0.463811
2018-12-07 00:00:00	0.6314	0.4889	0.5123	0.5512	0.55504	0.483496
2018-12-08 00:00:00	0.6393	0.5165	0.5274	0.5643	0.572756	0.48809
2018-12-09 00:00:00	0.6511	0.5073	0.5339	0.5761	0.598347	0.502525
2018-12-10 00:00:00	0.6412	0.5204	0.5425	0.5788	0.597691	0.505806
2018-12-11 00:00:00	0.6426	0.5099	0.5412	0.582	0.612126	0.505806
2018-12-12 00:00:00	0.6511	0.5401	0.5444	0.5768	0.597691	0.535662
2018-12-13 00:00:00	0.6668	0.5395	0.5694	0.6037	0.623937	0.534677
2018-12-14 00:00:00	0.6616	0.5257	0.591	0.647	0.630499	0.5583
2018-12-15 00:00:00	0.6767	0.5559	0.6094	0.6043	0.661339	0.550426
2018-12-16 00:00:00	0.678	0.5552	0.593	0.6129	0.652809	0.541239
2018-12-17 00:00:00	0.7088	0.5592	0.6028	0.6201	0.660027	0.547801
2018-12-18 00:00:00	0.7029	0.5546	0.6258	0.6398	0.645591	0.556987
2018-12-19 00:00:00	0.7134	0.5657	0.6311	0.6293	0.683649	0.550426
2018-12-20 00:00:00	0.6878	0.5874	0.593	0.6358	0.65084	0.558956

2018-12-21 00:00:00	0.7062	0.5631	0.6127	0.6332	0.65937	0.565517
2018-12-22 00:00:00	0.7036	0.5493	0.6074	0.6378	0.639029	0.550426
2018-12-23 00:00:00	0.7029	0.5677	0.616	0.6352	0.653465	
2018-12-24 00:00:00	0.701	0.569	0.6206	0.6391	0.665276	0.58389
2018-12-25 00:00:00	0.7279	0.5605	0.6219	0.6391	0.672494	0.572079
2018-12-26 00:00:00	0.7246	0.5729	0.6402	0.646	0.68168	0.560924
2018-12-27 00:00:00	0.7213	0.5677	0.6488	0.6483	0.68168	0.577328
2018-12-28 00:00:00	0.7095	0.5565	0.6409	0.6181	0.65609	0.548457
2018-12-29 00:00:00	0.7101	0.5532	0.6192	0.6194	0.644935	0.554363
2018-12-30 00:00:00	0.699	0.5611	0.6101	0.6299	0.644278	0.559612
2018-12-31 00:00:00	0.7095	0.567	0.6179	0.646	0.654121	0.586515
2019-01-01 00:00:00	0.7055	0.5828	0.6337	0.6417	0.633124	0.572735
2019-01-02 00:00:00	0.6977	0.5546	0.6278	0.6365	0.654777	0.565517
2019-01-03 00:00:00	0.7101	0.5729	0.6396	0.6371	0.661995	0.551082
2019-01-04 00:00:00	0.7206	0.5729	0.6402	0.6437	0.65609	0.570111
2019-01-05 00:00:00	0.7193	0.5631	0.6448	0.6457	0.665932	0.586515
2019-01-06 00:00:00	0.716	0.5592	0.654	0.6404	0.669213	0.576672
2019-01-07 00:00:00	0.7252	0.5834	0.654	0.6371	0.676431	0.575032
2019-01-08 00:00:00	0.7338	0.569	0.6507	0.6627	0.660683	0.583234
2019-01-09 00:00:00	0.7548	0.5769	0.654	0.6588	0.662651	0.593733
2019-01-10 00:00:00	0.7548	0.5828	0.6652	0.647	0.675775	0.586515
2019-01-11 00:00:00	0.7482	0.5828	0.6639	0.647	0.685617	0.572079
2019-01-12 00:00:00	0.7626	0.5802	0.6527	0.6549	0.694803	0.578641
2019-01-13 00:00:00	0.7653	0.571	0.6619	0.6404	0.672494	0.574704
2019-01-14 00:00:00	0.7626	0.5834	0.6744	0.649	0.677743	0.591764
2019-01-15 00:00:00	0.7705	0.5815	0.6881	0.6411	0.686929	0.574048
2019-01-16 00:00:00	0.7534	0.5618	0.6133	0.6739	0.665276	0.532709
2019-01-17 00:00:00	0.7856	0.5519		0.7067	0.652809	
2019-01-18 00:00:00	0.7777	0.6031	0.6993	0.6647	0.682992	0.615386
2019-01-19 00:00:00	0.7692	0.5874	0.677	0.6614	0.667244	0.585859
2019-01-20 00:00:00	0.7797	0.5716	0.6822	0.6627	0.701365	0.589139
2019-01-21 00:00:00	0.7869	0.6064	0.6895	0.6647	0.701365	0.59242
2019-01-22 00:00:00	0.7712	0.5782	0.6796	0.6667	0.685617	0.585859
2019-01-23 00:00:00	0.7698	0.733	0.6081	0.6706	0.744672	0.596685
2019-01-24 00:00:00	0.7738	0.5933	0.7059	0.6706	0.69546	0.619323
2019-01-25 00:00:00	0.7849	0.5966	0.6888	0.6746	0.685617	0.59767
2019-01-26 00:00:00	0.7915	0.5939	0.6901	0.6791	0.697428	0.610793
2019-01-27 00:00:00	0.7902	0.6097	0.7072	0.6844	0.707927	0.61473
2019-01-28 00:00:00	0.7712	0.5952	0.7026	0.6706	0.701365	0.616042
2019-01-29 00:00:00	0.7508	0.5939	0.6914	0.6326	0.681024	0.61473
2019-01-30 00:00:00	0.7856	0.6057	0.7183	0.6818	0.710552	0.63704

2019-01-31 00:00:00	0.8138	0.6569	0.7354	0.6851	0.70399	0.636384
2019-02-01 00:00:00	0.7954	0.6044	0.7137	0.6759	0.702677	0.619979
2019-02-02 00:00:00	0.7863	0.5985	0.6875	0.6614	0.721706	0.615386
2019-02-03 00:00:00	0.7935	0.5992	0.7295	0.666	0.703334	0.604887
2019-02-04 00:00:00	0.8073	0.6116	0.7544	0.6798	0.723019	0.604231
2019-02-05 00:00:00	0.7731	0.5736	0.7216	0.7165	0.717113	0.582578
2019-02-06 00:00:00	0.7738	0.5802	0.759	0.6509	0.717113	0.598326
2019-02-07 00:00:00	0.8112	0.609	0.7255	0.6811	0.740735	0.635727
2019-02-08 00:00:00	0.7994	0.6097	0.7282	0.6667	0.722363	0.619979
2019-02-09 00:00:00	0.7915	0.59	0.7177	0.6759	0.730237	0.627853
2019-02-10 00:00:00	0.8033	0.6057	0.7295	0.6831	0.742048	0.640321
2019-02-11 00:00:00	0.825	0.6241	0.7479	0.712	0.761076	0.63704
2019-02-12 00:00:00	0.741	0.6228	0.8781	0.6824	0.763701	0.63179
2019-02-13 00:00:00	0.8013	0.6136	0.7426	0.6791	0.751234	0.646226
2019-02-14 00:00:00	0.8223	0.6326	0.6829	0.6706	0.759108	0.677066
2019-02-15 00:00:00	0.8118	0.6261	0.7433	0.6864	0.731549	0.644914
2019-02-16 00:00:00	0.8302	0.6136	0.7544	0.6785	0.768294	0.663943
2019-02-17 00:00:00	0.8204	0.6267	0.7715	0.6805	0.763045	0.6541
2019-02-18 00:00:00	0.8112	0.6208	0.7853	0.6791	0.745328	0.640977
2019-02-19 00:00:00	0.8079	0.5966	0.7597	0.6844	0.65937	0.647538
2019-02-20 00:00:00	0.7771	0.6208	0.7229	0.6982	0.755171	0.640977
2019-02-21 00:00:00	0.7915	0.6208	0.7275	0.6903	0.756483	0.652788
2019-02-22 00:00:00	0.781	0.6156	0.7459	0.6903	0.739423	0.647538
2019-02-23 00:00:00	0.7817	0.6071	0.7485	0.6942	0.750578	0.656725
2019-02-24 00:00:00	0.8013	0.6294	0.7649	0.6772	0.770919	0.652788
2019-02-25 00:00:00	0.8125	0.6241	0.7754	0.6732	0.769607	0.67641
2019-02-26 00:00:00	0.8335	0.6346	0.7662	0.7257	0.761733	0.678378
2019-02-27 00:00:00	0.8237	0.6169	0.7833	0.7152	0.764357	0.672473
2019-02-28 00:00:00	0.8374	0.632	0.7859	0.7001	0.779449	0.672473
2019-03-01 00:00:00	0.8387	0.6451	0.7682	0.708	0.774856	0.702657
2019-03-02 00:00:00	0.8591	0.6379	0.7689	0.7375	0.769607	0.685596
2019-03-03 00:00:00	0.8335	0.6202	0.7485	0.7218	0.761733	0.682972
2019-03-04 00:00:00	0.8263	0.6431	0.7734	0.7159	0.781418	0.695439
2019-03-05 00:00:00	0.8269	0.6294	0.778	0.7395	0.76895	0.702
2019-03-06 00:00:00	0.8151	0.6254	0.7538	0.6982	0.771575	0.690189
2019-03-07 00:00:00	0.9949	0.609	0.7164	0.7625	0.784699	0.689533
2019-03-08 00:00:00	0.8361	0.6326	0.7728	0.7179	0.793885	0.647538
2019-03-09 00:00:00	0.8256	0.6267	0.7833	0.7126	0.780105	0.658037
2019-03-10 00:00:00	0.8361	0.6372	0.7629	0.6929	0.76567	0.672473
2019-03-11 00:00:00	0.8394	0.6399	0.7833	0.7257	0.778793	0.680347
2019-03-12 00:00:00	0.823	0.651	0.7905	0.7218	0.789948	0.690846

2019-03-13 00:00:00	0.8256	0.6792	0.7951	0.7041	0.794541	0.689533
2019-03-14 00:00:00	0.8755	0.672	0.8069	0.7402	0.80504	0.690846
2019-03-15 00:00:00	0.8637	0.6589	0.8108	0.7375	0.801759	0.69872
2019-03-16 00:00:00	0.8466	0.6655	0.8069	0.7415	0.7742	0.709218
2019-03-17 00:00:00	0.8433	0.6635	0.8305	0.7441	0.764357	0.711187
2019-03-18 00:00:00	0.8348	0.6648	0.8364	0.7441	0.769607	0.720373
2019-03-19 00:00:00	0.8335	0.6609	0.8207	0.7454	0.78273	0.722342
2019-03-20 00:00:00	0.8374	0.6858	0.7997	0.6982	0.812914	0.713155
2019-03-21 00:00:00	0.8342	0.676	0.7938		0.781418	0.691174
2019-03-22 00:00:00	0.8473	0.6714	0.8227	0.7139	0.797822	0.684284
2019-03-23 00:00:00	0.8486	0.6897	0.8253	0.7326	0.820788	0.692814
2019-03-24 00:00:00	0.8512	0.6845	0.8305	0.7369	0.820788	0.710531
2019-03-25 00:00:00	0.8407	0.6996	0.82	0.7494	0.815538	0.706594
2019-03-26 00:00:00	0.8427		0.8056	0.7448	0.819475	0.709218
2019-03-27 00:00:00	0.8532		0.8161	0.769	0.811601	0.709218
2019-03-28 00:00:00	0.823		0.7918	0.7507	0.801103	0.710859
2019-03-29 00:00:00	0.8125		0.7846	0.7395	0.81357	0.708562
2019-03-30 00:00:00	0.8348		0.7925	0.7375	0.812914	0.701344
2019-03-31 00:00:00	0.8151	0.6258	0.7833	0.7454	0.79651	0.706594

Table E.2 Ground surface measurements subsection 2 of the RCTC SEM cavern

Time	GSSP-350 (in)	GSSP-351D (in)	GSSP-352 (in)	GSSP-344D (in)	GSSP-345 (in)	GSSP-341 (in)
2018-05-30 00:00:00	0.024	0.084	-0.012	-0.072	-0.12	0.144
2018-05-31 00:00:00	-0.024	0.036	0.012	-0.12	-0.156	0.096
2018-06-01 00:00:00	-6.8E-13	0.072	-0.048	-0.072	-0.144	0.156
2018-06-04 00:00:00	-0.024	0.036	-0.048	-0.024	-0.168	0.096
2018-06-05 00:00:00	0.036	0.096	0.012	-0.06	-0.096	0.168
2018-06-06 00:00:00	0.036	0.096	0	-0.048	-0.12	0.168
2018-06-08 00:00:00	0.036	0.108	-0.012	-0.036	-0.108	0.168
2018-06-11 00:00:00	0.012	0.072	-0.036	-0.072	-0.144	0.132
2018-06-12 00:00:00	0.06	0.12	-0.012	-0.024	-0.108	0.192
2018-06-13 00:00:00	0.048	0.12	-0.024	-0.036	-0.12	0.192
2018-06-14 00:00:00	0.024	0.096	-0.024	-0.036	-0.12	0.156
2018-06-15 00:00:00	-6.8E-13	0.072	-0.012	-0.084	-0.132	0.132
2018-06-18 00:00:00	0.012	0.072	-0.036	-0.072	-0.156	0.132
2018-06-19 00:00:00	0.036	0.108	-0.012	-0.036	-0.12	0.18
2018-06-20 00:00:00	0.024	0.096	-0.012	-0.06	-0.132	0.144
2018-06-21 00:00:00	0.036	0.096	-0.048	-0.048	-0.132	0.156
2018-06-22 00:00:00	0.072	0.132	-0.012	-0.012	-0.12	0.204
2018-06-24 00:00:00	0.032719	0.072378	-3.5E-14	-0.09412	-0.11738	0.129375

2018-06-25 00:00:00	0.047874	0.109186	0.018499	-0.00732	-0.10413	0.145312
2018-06-26 00:00:00	0.047155	0.063848	-0.02165	-0.05475	-0.11475	0.137906
2018-06-27 00:00:00	0.007596	0.085312	0.041055	-0.03913	-0.168	0.130562
2018-06-28 00:00:00	0.004504	0.081564	0.017717	-0.03507	-0.11344	0.147748
2018-06-29 00:00:00	0.005816	0.082877	0.020997	-0.08559	-0.11475	0.135937
2018-06-30 00:00:00	0.011722	0.036945	0.023622	-0.0974	-0.13378	0.155622
2018-07-01 00:00:00	0.033375	0.023821	0.036089	-0.06328	-0.12459	0.138562
2018-07-02 00:00:00	0.077995	0.055318	0.047244	-0.04688	-0.12787	0.148404
2018-07-03 00:00:00	0.038625	0.081564	0.057743	-0.039	-0.07866	0.146436
2018-07-04 00:00:00	0.039281	0.15768	0.001969	-0.07575	-0.08457	0.142499
2018-07-05 00:00:00	0.064871	0.126184	0.047244	-0.07247	-0.09835	0.154966
2018-07-06 00:00:00	0.064871	0.107811	0.05643	-0.08953	-0.13575	0.132
2018-07-07 00:00:00	0.074058	0.124871	0.062992	0.037113	-0.09047	0.152997
2018-07-08 00:00:00	0.060278	0.140619	0.060367	0.023333	-0.08325	0.178588
2018-07-09 00:00:00	0.061591	0.147837	0.051181	-0.09215	-0.08194	0.158903
2018-07-10 00:00:00	0.051748	0.160304	0.018373	-0.0285	-0.099	0.152341
2018-07-11 00:00:00	0.016315	0.15243	0.047244	0.037769	-0.07472	0.147748
2018-07-12 00:00:00	0.029438	0.165554	0.019685	0.002992	-0.07407	0.145123
2018-07-13 00:00:00	0.127864	0.157024	-1.1E-13	0.050892	-0.04651	0.160215
2018-07-14 00:00:00	0.104242	0.155055	0.066929	0.012179	-0.06948	0.153654
2018-07-15 00:00:00	0.097024	0.155711	0.065617	0.006929	-0.08457	0.158247
2018-07-16 00:00:00	0.043874	0.164898	0.066929	-0.10462	-0.07801	0.154966
2018-07-17 00:00:00	0.052404	0.172116	0.047244	-0.03507	-0.07079	0.167433
2018-07-18 00:00:00	0.079307	0.145869	0.074803	-0.03507	-0.04126	0.160215
2018-07-19 00:00:00	0.11474	0.163585	0.07874	-0.04031	-0.06685	0.160215
2018-07-20 00:00:00	0.091774	0.195738	0.07185	-0.02457	-0.07669	0.184493
2018-07-21 00:00:00	0.163953	0.212798	0.068898	0.01021	-0.08325	0.187118
2018-07-22 00:00:00	0.144268	0.204924	0.08727	0.019396	-0.07735	0.194336
2018-07-23 00:00:00	0.131144	0.206892	0.091207	-0.00948	-0.07013	0.180556
2018-07-24 00:00:00	0.12327	0.215423	0.106299	-0.01538		0.185806
2018-07-25 00:00:00	0.153454	0.197706	0.116798	-0.00029	-0.04782	0.196304
2018-07-26 00:00:00	0.188231	0.206236	0.120735	0.013491	-0.04585	0.184493
2018-07-27 00:00:00	0.177732	0.196394	0.129921	0.002992	-0.04192	0.20221
2018-07-28 00:00:00	0.143612	0.185895	0.133858	0.044987	-0.03076	0.205491
2018-07-29 00:00:00	0.167234	0.209517	0.150919	0.047612	-0.03076	0.209428
2018-07-30 00:00:00	0.179045	0.229202	0.145669	0.054173	-0.04651	0.213365
2018-07-31 00:00:00	0.183638	0.246263	0.142389	0.085669	-0.05504	0.219927
2018-08-01 00:00:00	0.182982	0.23642	0.163386	0.084357	-0.02026	0.219927
2018-08-02 00:00:00	0.15936	0.229202	0.161417	0.02727	-0.0137	0.225176
2018-08-03 00:00:00	0.15936	0.203612	0.167323	0.033832	-0.00911	0.225832
2018-08-04 00:00:00	0.194793	0.245606	0.174541	0.06336	-0.00386	0.358378

2018-08-05 00:00:00	0.22432	0.262011	0.178478	0.092231	-0.0032	0.264546
2018-08-06 00:00:00	0.213165	0.269228	0.178478	0.103386	0.007297	0.231738
2018-08-07 00:00:00	0.207916	0.256105	0.187664	0.101417	0.012874	0.236987
2018-08-08 00:00:00	0.182982	0.268572	0.192913	0.105354	0.026326	0.247486
2018-08-09 00:00:00	0.203323	0.277102	0.211286	0.104042	0.039449	0.253391
2018-08-10 00:00:00	0.239412	0.273165	0.223753	0.182782	0.044042	0.263234
2018-08-11 00:00:00	0.171827	0.281696	0.217848	0.148662	0.045354	0.27242
2018-08-12 00:00:00	0.223664	0.275134	0.21916	0.151286	0.03748	0.269795
2018-08-13 00:00:00	0.26369	0.292194	0.212599	0.176877	0.03748	0.277013
2018-08-14 00:00:00	0.232851	0.304662	0.225066	0.141444	0.055853	0.278982
2018-08-15 00:00:00	0.242037	0.317785	0.248688	0.18147	0.045354	0.284231
2018-08-16 00:00:00	0.218415	0.313192	0.187992	0.145381	0.049291	0.296042
2018-08-17 00:00:00	0.214478	0.2981	0.217192	0.157848	0.06832	0.309165
2018-08-18 00:00:00	0.284032	0.307286	0.253281	0.168347	0.116877	0.320976
2018-08-19 00:00:00	0.276158	0.300068	0.248032	0.161785	0.094567	0.32032
2018-08-20 00:00:00	0.290593	0.307286	0.25853	0.170971	0.067664	0.326882
2018-08-21 00:00:00	0.297155	0.303349	0.257218	0.158504	0.075538	0.318352
2018-08-22 00:00:00	0.312903	0.302037	0.271654	0.179501	0.09916	0.332788
2018-08-23 00:00:00	0.305029	0.286289	0.257218	0.168347	0.071601	0.339349
2018-08-24 00:00:00	0.293218	0.298756	0.274278	0.185407	0.083412	0.339349
2018-08-25 00:00:00	0.301748	0.301381	0.288714	0.203124	0.103753	0.35116
2018-08-26 00:00:00	0.276158	0.339438	0.291339	0.172284	0.096536	0.35116
2018-08-27 00:00:00	0.291906	0.329596	0.301181	0.210341	0.122782	0.347223
2018-08-28 00:00:00	0.282063	0.344032	0.310368	0.172284	0.135249	0.360347
2018-08-29 00:00:00	0.318152	0.311223	0.330709	0.195906	0.120158	0.364284
2018-08-30 00:00:00	0.270908	0.338126	0.322835	0.191969	0.134593	0.362971
2018-08-31 00:00:00	0.327339	0.349281	0.329397	0.145381	0.14378	0.376095
2018-09-01 00:00:00	0.329963	0.344032	0.324803	0.199843	0.147717	0.378719
2018-09-02 00:00:00	0.317496	0.330252	0.321522	0.231339	0.141155	0.377407
2018-09-03 00:00:00	0.305029	0.353218	0.322835	0.188032	0.142467	0.374782
2018-09-04 00:00:00	0.31684	0.319097	0.283465	0.194593	0.142467	0.372158
2018-09-05 00:00:00	0.340462	0.326971	0.336614	0.178845	0.177244	0.377407
2018-09-06 00:00:00	0.313559	0.340095	0.324147	0.179501	0.18315	0.381344
2018-09-07 00:00:00	0.329963	0.344032	0.346457	0.216247	0.163465	0.381344
2018-09-08 00:00:00	0.308966	0.344032	0.346457	0.197218	0.168714	0.396436
2018-09-09 00:00:00	0.310935	0.363061	0.354331	0.212966	0.176588	0.402998
2018-09-10 00:00:00	0.31684	0.368966	0.351706	0.232651	0.184462	0.414152
2018-09-11 00:00:00	0.316184	0.39062	0.360893	0.228058	0.17462	0.415465
2018-09-12 00:00:00	0.36999	0.403087	0.354331	0.257585		0.414152
2018-09-13 00:00:00	0.343743	0.365685	0.374016	0.263491	0.185118	0.410872
2018-09-14 00:00:00	0.336525	0.391932	0.375328	0.266772	0.206772	0.425963

2018-09-15 00:00:00	0.337837	0.395869	0.379265	0.247087	0.214646	0.432525
2018-09-16 00:00:00	0.335869	0.394557	0.376641	0.240525	0.21399	0.431213
2018-09-17 00:00:00	0.350305	0.397837	0.379265	0.215591	0.210709	0.431213
2018-09-18 00:00:00	0.361459	0.383402	0.374672	0.230026	0.214646	0.428588
2018-09-19 00:00:00	0.352273	0.398494	0.390748	0.248399	0.212021	0.419402
2018-09-20 00:00:00	0.345711	0.38537	0.395013	0.2379	0.218583	0.419402
2018-09-21 00:00:00	0.386394	0.358467	0.388452	0.257914	0.227113	0.4194
2018-09-22 00:00:00	0.334557	0.402431	0.381234	0.252992	0.23105	
2018-09-23 00:00:00	0.363428	0.41621	0.384515	0.264803	0.235643	
2018-09-24 00:00:00	0.342431	0.400462	0.387795	0.249055	0.241549	0.4194
2018-09-25 00:00:00	0.358835	0.38537	0.388452	0.201811	0.236956	0.428588
2018-09-26 00:00:00	0.387706	0.382089	0.383202	0.218872	0.233019	0.432525
2018-09-27 00:00:00	0.344399	0.39915	0.374016	0.261522	0.230394	0.420714
2018-09-28 00:00:00	0.370646	0.424084	0.37336	0.257585	0.246142	0.440399
2018-09-29 00:00:00	0.361459	0.434583	0.404856	0.302861	0.263202	0.463365
2018-09-30 00:00:00	0.366709	0.412929	0.400263	0.262835	0.257953	0.464677
2018-10-01 00:00:00	0.371958	0.451643	0.392389	0.294331	0.267795	0.490268
2018-10-02 00:00:00	0.365397	0.454924	0.423885	0.281864	0.297323	0.495517
2018-10-03 00:00:00	0.362772	0.441801	0.419948	0.281208	0.290761	0.484362
2018-10-04 00:00:00	0.375239	0.456893	0.454068	0.262179	0.276965	0.494205
2018-10-05 00:00:00	0.373271	0.430646	0.417323	0.262835	0.254672	0.465334
2018-10-06 00:00:00	0.389675	0.46083	0.408793	0.259554	0.263202	0.459428
2018-10-07 00:00:00	0.389019	0.437864	0.402231	0.296299	0.265171	0.463365
2018-10-08 00:00:00	0.402142	0.437864	0.4042	0.243806	0.262546	0.466646
2018-10-09 00:00:00	0.413953	0.46083	0.41273	0.329764	0.263202	0.478457
2018-10-10 00:00:00	0.381145	0.447706	0.414698	0.287769	0.267139	0.468614
2018-10-11 00:00:00	0.400173	0.450331	0.410761	0.253648	0.268452	0.469271
2018-10-12 00:00:00	0.401486	0.446394	0.413386	0.256929	0.280919	0.468614
2018-10-13 00:00:00	0.411328	0.483139	0.425853	0.249711	0.271732	0.502079
2018-10-14 00:00:00	0.391643	0.454268	0.424541	0.232651	0.27567	0.49158
2018-10-15 00:00:00	0.385082	0.443769	0.423229	0.302205	0.281575	0.48305
2018-10-16 00:00:00	0.415921	0.472641	0.422572	0.325171	0.279607	0.475832
2018-10-17 00:00:00	0.392299	0.451643	0.442257	0.304173	0.30126	0.485019
2018-10-18 00:00:00	0.342431	0.463454	0.44357	0.262179	0.30126	0.49158
2018-10-19 00:00:00	0.39558	0.481827	0.46063	0.279239	0.311103	0.518483
2018-10-20 00:00:00	0.421171	0.51726	0.472441	0.292362	0.31504	0.526357
2018-10-21 00:00:00	0.408047	0.512667	0.464567	0.324515	0.317008	0.523076
2018-10-22 00:00:00	0.394924	0.495607	0.46063	0.304173	0.314383	0.524389
2018-10-23 00:00:00	0.415265	0.467391	0.452756	0.307454	0.313071	0.546698
2018-10-24 00:00:00	0.434294	0.465423	0.46588	0.323202	0.328819	0.525701
2018-10-25 00:00:00	0.455948	0.461486	0.484908	0.323858	0.343255	0.545386

2018-10-26 00:00:00	0.461187	0.507418	0.480305	0.347471	0.336698	0.528325
2018-10-27 00:00:00	0.4402	0.484467	0.485567	0.3455	0.342633	0.534233
2018-10-28 00:00:00	0.442833	0.484467	0.4856	0.3324	0.338	0.525733
2018-10-29 00:00:00	0.436271	0.500196	0.48558	0.35207	0.33932	0.521776
2018-10-30 00:00:00	0.432982	0.49495	0.484252	0.327795	0.34063	0.52767
2018-10-31 00:00:00	0.444137	0.510698	0.484252	0.342896	0.348504	0.527013
2018-11-01 00:00:00	0.439544	0.491013	0.490158	0.312704	0.363596	0.528326
2018-11-02 00:00:00	0.442824	0.470016	0.509843	0.291706	0.365565	0.534887
2018-11-03 00:00:00	0.449386	0.505449	0.510499	0.277927	0.366221	0.544074
2018-11-04 00:00:00	0.432982	0.50873	0.513124	0.36126	0.373439	0.553916
2018-11-05 00:00:00	0.441512	0.508074	0.515748	0.354042	0.370814	0.541449
2018-11-06 00:00:00	0.421827	0.468704	0.519685	0.348793	0.378688	0.541449
2018-11-07 00:00:00	0.445449	0.496263	0.517717	0.359948	0.380656	0.548011
2018-11-08 00:00:00	0.401486	0.515948	0.541995	0.388163	0.375407	0.57032
2018-11-09 00:00:00	0.446761	0.501512	0.507874	0.357323	0.374095	0.569008
2018-11-10 00:00:00	0.44873	0.5002	0.527559	0.403255	0.410184	
2018-11-11 00:00:00	0.43495	0.504793	0.538058	0.367822	0.382625	
2018-11-12 00:00:00	0.461197	0.550068	0.532809	0.359292	0.393124	
2018-11-13 00:00:00	0.465134	0.561223	0.53937	0.381601	0.412809	0.587709
2018-11-14 00:00:00	0.463822	0.541538	0.555118	0.427533	0.407559	0.574257
2018-11-15 00:00:00	0.493349	0.568441	0.54462	0.403911	0.41937	0.566383
2018-11-16 00:00:00	0.470383	0.516604	0.549213	0.363885	0.431181	0.554572
2018-11-17 00:00:00	0.447418	0.509386	0.536746	0.395381	0.421995	0.585412
2018-11-18 00:00:00	0.444793	0.516604	0.534121	0.416378	0.417402	0.59263
2018-11-19 00:00:00	0.446761	0.532352	0.531496	0.419659	0.413465	0.603129
2018-11-20 00:00:00	0.456604	0.534977	0.535433	0.392756	0.420027	0.589349
2018-11-21 00:00:00	0.454635	0.527759	0.536746	0.353386	0.408872	0.597223
2018-11-22 00:00:00	0.480882	0.532352	0.538058	0.375696	0.418058	0.622158
2018-11-23 00:00:00	0.436263	0.543507	0.53937	0.369134	0.423307	0.624126
2018-11-24 00:00:00	0.449386	0.544819	0.543307	0.372415	0.425932	0.618877
2018-11-25 00:00:00	0.472352	0.555318		0.355355	0.423307	0.59263
2018-11-26 00:00:00	0.495318	0.579596	0.545276	0.382257	0.42462	0.588693
2018-11-27 00:00:00	0.473008	0.56188	0.545276	0.451155	0.431181	0.600504
2018-11-28 00:00:00	0.468415	0.577628	0.548557	0.429502	0.421995	0.599192
2018-11-29 00:00:00	0.441512	0.590751	0.552494	0.404567	0.440368	0.612315
2018-11-30 00:00:00	0.461853	0.594032	0.532153	0.379633	0.418058	0.605754
2018-12-01 00:00:00	0.475633	0.57894	0.533465	0.356667	0.411496	0.620845
2018-12-02 00:00:00	0.473664	0.550068	0.557087	0.389475	0.411496	0.605754
2018-12-03 00:00:00	0.446105	0.569754	0.54462	0.366509	0.410512	0.59788
2018-12-04 00:00:00	0.467103	0.573034	0.557087	0.371759	0.440368	0.600504
2018-12-05 00:00:00	0.50188	0.598625	0.562992	0.398662	0.431181	0.593286

2018-12-06 00:00:00	0.467103	0.547444	0.507218	0.350761	0.360315	0.624782
2018-12-07 00:00:00	0.492037	0.584189	0.524935	0.371103	0.42462	0.599192
2018-12-08 00:00:00	0.492037	0.612404	0.562992	0.388819	0.428557	0.620189
2018-12-09 00:00:00	0.500567	0.619622	0.57546	0.387507	0.440368	0.615596
2018-12-10 00:00:00	0.501223	0.607811	0.582021	0.410473	0.443649	0.613628
2018-12-11 00:00:00	0.492693	0.602562	0.586614	0.398005	0.416418	0.627407
2018-12-12 00:00:00	0.492693	0.611748	0.603675	0.380945	0.437091	0.628063
2018-12-13 00:00:00	0.483507	0.645213	0.62336	0.42294	0.452835	0.628063
2018-12-14 00:00:00	0.535344	0.622247		0.426877	0.479738	0.651685
2018-12-15 00:00:00	0.536	0.634058	0.616142	0.44853	0.458084	0.633313
2018-12-16 00:00:00	0.552404	0.653743	0.618111	0.433439	0.46399	0.634625
2018-12-17 00:00:00	0.565528	0.638651	0.624672	0.457061	0.471208	0.64053
2018-12-18 00:00:00	0.577339	0.642588	0.614174	0.415722	0.470552	0.651029
2018-12-19 00:00:00	0.555685	0.654399	0.610893	0.450499	0.471864	0.655622
2018-12-20 00:00:00	0.547811	0.641932	0.632546	0.412441	0.483675	0.663496
2018-12-21 00:00:00	0.571433	0.662929	0.624672	0.485276	0.500079	0.667433
2018-12-22 00:00:00	0.571433	0.66621	0.615486	0.438032	0.496142	0.666777
2018-12-23 00:00:00	0.556341	0.661617		0.423596		0.675964
2018-12-24 00:00:00	0.556341	0.650462	0.610237	0.443281	0.454803	0.657591
2018-12-25 00:00:00	0.543874	0.678677	0.622704	0.462966	0.478426	0.660872
2018-12-26 00:00:00	0.559622	0.67146	0.620079	0.464278	0.4863	0.647748
2018-12-27 00:00:00	0.570777	0.672772	0.647638	0.419659	0.485643	0.651685
2018-12-28 00:00:00	0.574714	0.665554	0.655512	0.432126	0.494174	0.635281
2018-12-29 00:00:00	0.535344	0.64062	0.629922	0.424252	0.496142	0.642499
2018-12-30 00:00:00	0.559622	0.647181	0.62336	0.426221	0.509265	0.643811
2018-12-31 00:00:00	0.536	0.658992	0.64567	0.443281	0.524357	0.754048
2019-01-01 00:00:00	0.532719	0.678021	0.628609	0.43147	0.499423	0.89578
2019-01-02 00:00:00	0.560935	0.644557	0.639108	0.424252	0.504016	0.886594
2019-01-03 00:00:00	0.566184	0.65768	0.627297	0.423596	0.516483	0.881344
2019-01-04 00:00:00	0.566184	0.665554	0.635171	0.453124	0.494174	0.687118
2019-01-05 00:00:00	0.559622	0.649806	0.635171	0.439344	0.504672	0.689743
2019-01-06 00:00:00	0.556341	0.659649	0.629265	0.424252	0.496798	0.688431
2019-01-07 00:00:00	0.586525	0.672772	0.633859	0.437376	0.500079	0.704835
2019-01-08 00:00:00	0.564872	0.670803	0.656825	0.46231	0.508609	0.704179
2019-01-09 00:00:00	0.579964	0.678677	0.629922	0.452467	0.501391	0.687118
2019-01-10 00:00:00	0.568809	0.691801	0.64042	0.413097	0.521733	0.689743
2019-01-11 00:00:00	0.579307	0.684583	0.653544	0.456404	0.517796	0.691712
2019-01-12 00:00:00	0.581276	0.703612	0.649607	0.469528	0.502048	0.706147
2019-01-13 00:00:00	0.566184	0.67474	0.645013	0.449187	0.507297	0.701554
2019-01-14 00:00:00	0.572746	0.687864	0.652231	0.478714	0.509922	0.69368
2019-01-15 00:00:00	0.587838	0.7023	0.603019	0.51874	0.508609	0.64578

2019-01-16 00:00:00	0.570777	0.691145	0.649607	0.51874	0.511234	0.681869
2019-01-17 00:00:00	0.568809	0.717391	0.651575	0.475433	0.572914	0.719927
2019-01-18 00:00:00	0.572746	0.706237	0.675853	0.487901	0.525013	0.70746
2019-01-19 00:00:00	0.590462	0.700331	0.664042	0.465591	0.525013	0.713365
2019-01-20 00:00:00	0.606866	0.689176	0.663386	0.487244	0.528294	0.714677
2019-01-21 00:00:00	0.610803	0.709517	0.669948	0.489869	0.533544	0.703523
2019-01-22 00:00:00	0.562247	0.662929	0.670604	0.494462	0.530263	0.702866
2019-01-23 00:00:00	0.452011	0.667851	0.665355	0.306798	0.521733	0.728457
2019-01-24 00:00:00	0.600961	0.707549	0.694882	0.491838	0.539449	0.758641
2019-01-25 00:00:00	0.583901	0.684583	0.692914	0.443937	0.550604	0.74158
2019-01-26 00:00:00	0.59768	0.695738	0.692914	0.451811	0.554541	0.883313
2019-01-27 00:00:00	0.553061	0.680646	0.691601	0.426221	0.555853	0.788168
2019-01-28 00:00:00	0.572746	0.687208	0.702756	0.446562	0.557166	0.754048
2019-01-29 00:00:00	0.587181	0.714111	0.67979	0.470184	0.544042	0.763234
2019-01-30 00:00:00	0.59768	0.718048	0.691601	0.480683	0.55126	0.759297
2019-01-31 00:00:00	0.598992	0.739045	0.705381	0.476746	0.555197	0.760609
2019-02-01 00:00:00	0.594399	0.713454	0.672573	0.50168	0.536825	0.801292
2019-02-02 00:00:00	0.633769	0.734452	0.698819	0.459685	0.447914	0.803916
2019-02-03 00:00:00	0.610803	0.699019	0.708662	0.504961	0.513859	0.72452
2019-02-04 00:00:00	0.618677	0.732483	0.744095	0.514803	0.529607	0.742237
2019-02-05 00:00:00	0.608835	0.721985	0.704725	0.453124	0.578819	0.760609
2019-02-06 00:00:00	0.654111	0.729859	0.704725	0.455092	0.635906	0.74158
2019-02-07 00:00:00	0.666578	0.7502	0.717691	0.525302	0.595223	0.754704
2019-02-08 00:00:00	0.648205	0.740357	0.702756	0.516116	0.596536	0.788168
2019-02-09 00:00:00	0.6423	0.735764	0.71916	0.526614	0.605066	0.794074
2019-02-10 00:00:00	0.657391	0.777103	0.736877	0.544331	0.610315	0.799979
2019-02-11 00:00:00	0.661985	0.792195	0.742126	0.544987	0.602441	0.802604
2019-02-12 00:00:00	0.595055	0.569754	0.748032	0.434095	0.614252	0.794074
2019-02-13 00:00:00	0.673139	0.777759	0.759843	0.581076	0.633281	0.824914
2019-02-14 00:00:00	0.654767	0.81516	0.71916	0.499712	0.622783	0.85641
2019-02-15 00:00:00	0.682982	0.786289	0.748688	0.545643	0.62672	0.838037
2019-02-16 00:00:00	0.675108	0.78957	0.755906	0.579764	0.651654	0.829507
2019-02-17 00:00:00	0.684294	0.794163	0.746063	0.602074	0.637218	0.843943
2019-02-18 00:00:00	0.688231	0.812536	0.727035	0.648662	0.632625	0.834756
2019-02-19 00:00:00	0.653454	0.833533	0.765748	0.611916	0.656247	0.806541
2019-02-20 00:00:00	0.646237	0.779071	0.762468	0.54105	0.607035	0.830163
2019-02-21 00:00:00	0.667234	0.787601	0.733596	0.5942	0.618846	0.8341
2019-02-22 00:00:00	0.65936	0.773166	0.75	0.555486	0.635906	0.821633
2019-02-23 00:00:00	0.660016	0.788914	0.761155	0.558111	0.649685	0.8341
2019-02-24 00:00:00	0.701355	0.823035	0.770342	0.558767	0.664121	0.85116
2019-02-25 00:00:00	0.689544	0.817785	0.781496	0.604042	0.664449	0.862315

2019-02-26 00:00:00	0.71251	0.817129	0.784777	0.569922	0.670683	1.008641
2019-02-27 00:00:00	0.709229	0.825003	0.804462	0.591575	0.672651	0.925964
2019-02-28 00:00:00	0.673796	0.815817	0.783465	0.609292	0.656903	0.914809
2019-03-01 00:00:00	0.688231	0.838126	0.789371	0.605355	0.672323	0.918746
2019-03-02 00:00:00	0.735475	0.857811	0.764436	0.587638	0.679869	0.916777
2019-03-03 00:00:00	0.690856	0.855843	0.772966	0.597481	0.675276	0.948273
2019-03-04 00:00:00	0.702011	0.82894	0.780184	0.612573	0.683806	0.925308
2019-03-05 00:00:00	0.703979	0.841407	0.796588	0.61126	0.673308	1.025045
2019-03-06 00:00:00	0.709885	0.844032	0.765092	0.5942	0.668058	0.968615
2019-03-07 00:00:00	0.685607	0.829596		0.586982	0.664121	0.887906
2019-03-08 00:00:00	0.686263	0.845344	0.791339	0.621103	0.654279	0.907591
2019-03-09 00:00:00	0.683638	0.846	0.782809	0.643412	0.663465	0.885937
2019-03-10 00:00:00	0.689544	0.832221	0.78609	0.621103	0.670683	0.897748
2019-03-11 00:00:00	0.682982	0.829596	0.797245	0.586982	0.665433	0.888562
2019-03-12 00:00:00	0.702011	0.846657	0.812336	0.592231	0.676588	0.889218
2019-03-13 00:00:00	0.718415	0.836158	0.805775	0.565985	0.689712	0.891843
2019-03-14 00:00:00	0.703979	0.85978	0.801838	0.630289	0.698242	0.901685
2019-03-15 00:00:00	0.728914	0.853218	0.81693	0.667035	0.706772	0.915465
2019-03-16 00:00:00	0.709229	0.85978	0.827428	0.634226	0.706772	0.924651
2019-03-17 00:00:00	0.69873	0.874216	0.82546	0.65588	0.714646	0.920714
2019-03-18 00:00:00	0.700699	0.860436	0.837271	0.646693	0.740237	0.932197
2019-03-19 00:00:00	0.726289	0.84272	0.840552	0.615853	0.744174	
2019-03-20 00:00:00	0.736788	0.847969	0.812336	0.634226	0.741221	
2019-03-21 00:00:00	0.711197	0.83747	0.802494	0.617822	0.727769	
2019-03-22 00:00:00	0.726289	0.832221	0.808399	0.575171	0.684462	
2019-03-23 00:00:00	0.739412	0.846	0.817586	0.583701	0.700867	
2019-03-24 00:00:00	0.737444	0.851906	0.835958	0.651286	0.707428	
2019-03-25 00:00:00	0.739412	0.826972	0.843832	0.626352	0.70546	
2019-03-26 00:00:00	0.740725	0.840751	0.828084	0.620447	0.703491	
2019-03-27 00:00:00	0.724977	0.851906	0.832678	0.626352	0.711365	0.920058
2019-03-28 00:00:00	0.740725	0.824347	0.84252	0.609292	0.714646	0.93515
2019-03-29 00:00:00	0.722352	0.842063	0.84252	0.596168	0.712678	0.927276
2019-03-30 00:00:00	0.713822	0.848625	0.816273	0.605355	0.709397	0.914153
2019-03-31 00:00:00	0.705948	0.826972	0.82021	0.632914	0.719239	0.946961

Table E.3 Ground surface measurements subsection 3 of the RCTC SEM cavern

Time	GSSP-342 (in)	GSSP-343 (in)	GSSP-332 (in)	GSSP-333 (in)	GSSP-329D (in)	GSSP-330 (in)
2018-05-30 00:00:00	0.264	0	-0.084	-0.06	-0.08	-0.012
2018-05-31 00:00:00	0.192	-0.048	-0.132	-0.084	-0.132	-0.036

2018-06-01 00:00:00	0.252	-0.012	-0.096	-0.06	-0.06	-0.012
2018-06-04 00:00:00	0.204	0	-0.12	-0.084	-0.12	-0.06
2018-06-05 00:00:00	0.252	0.036	-0.072	-0.012	-0.084	-0.012
2018-06-06 00:00:00	0.264	0.024	-0.072	-0.036	-0.048	-0.012
2018-06-08 00:00:00	0.276	0.036	-0.06	-0.024	-0.06	0.048
2018-06-11 00:00:00	0.24	0.012	-0.084	-0.06	-0.084	0.012
2018-06-12 00:00:00	0.288	0.048	-0.048	-0.024	-0.048	0.036
2018-06-13 00:00:00	0.288	0	-0.048	-0.036	-0.036	0.036
2018-06-14 00:00:00	0.252	-0.012	-0.06	-0.048	-0.036	0.036
2018-06-15 00:00:00	0.252	-0.024	-0.096	-0.06	-0.084	-0.048
2018-06-18 00:00:00	0.228	-0.012	-0.084	-0.072	-0.06	0
2018-06-19 00:00:00	0.276	-0.012	-0.048	-0.012	-0.048	0.048
2018-06-20 00:00:00	0.24	-0.024	-0.096	-0.06	-0.072	-0.012
2018-06-21 00:00:00	0.24	0.012	-0.096	-0.048	-0.072	-0.072
2018-06-22 00:00:00	0.288	0	-0.048	0	-0.072	-0.012
2018-06-24 00:00:00	0.255937	-0.01791	-0.10997	-0.03009	-0.09206	-0.07069
2018-06-25 00:00:00	0.254625	-0.021	-0.09338	-0.02269	-0.09731	-0.03875
2018-06-26 00:00:00	0.261186	-0.0435	-0.11325	-0.03206	-0.09075	-0.06938
2018-06-27 00:00:00	0.243874	-0.02138	-0.116	-0.05134	-0.10131	-0.05338
2018-06-28 00:00:00	0.265123	0.008997	-0.10669	-0.03338	-0.09403	-0.06675
2018-06-29 00:00:00	0.26906	-0.02053	-0.108	-0.03928	-0.08681	-0.05953
2018-06-30 00:00:00	0.276278	-0.02906	-0.08635	-0.015	-0.0691	-0.0556
2018-07-01 00:00:00	0.272997	-0.01856	-0.11522	-0.01894	-0.04285	-0.05756
2018-07-02 00:00:00	0.266436	-0.02053	-0.10997	-0.03338	-0.07041	-0.05428
2018-07-03 00:00:00	0.27431	-0.07827	-0.10669	-0.0255	-0.075	-0.05625
2018-07-04 00:00:00	0.275622	-0.0622	-0.0975	-0.03141	-0.07763	-0.05625
2018-07-05 00:00:00	0.287433	0.00178	-0.08503	-0.03469	-0.07369	-0.05363
2018-07-06 00:00:00	0.286121	-0.00019	-0.08438	-0.02681	-0.06516	-0.03591
2018-07-07 00:00:00	0.287433	-0.00413	-0.08044	-0.00844	-0.06254	-0.01885
2018-07-08 00:00:00	0.295307	-0.0015	-0.07519	0.005995	-0.0645	-0.0077
2018-07-09 00:00:00	0.297932	-0.00019	-0.06732	-0.00057	-0.05269	-0.0077
2018-07-10 00:00:00	0.304493	-0.0435	-0.06863	-0.00188	-0.05335	-0.01294
2018-07-11 00:00:00	0.307118	-0.0435	-0.06272	-0.00254	-0.04482	-0.01229
2018-07-12 00:00:00	0.30515	-0.01298	-0.0765	-0.01172	-0.07107	-0.02082
2018-07-13 00:00:00	0.311711	0.009654	-0.08307	-0.01303	-0.06254	-0.02082
2018-07-14 00:00:00	0.299244	-0.00806	-0.08503	-0.01763	-0.08616	-0.03001
2018-07-15 00:00:00	0.303181	0.013591	-0.08372	-0.01631	-0.08944	-0.02804
2018-07-16 00:00:00	0.304493	-0.01987	-0.08831	-0.01566	-0.06647	-0.03001
2018-07-17 00:00:00	0.305806	-0.00609	-0.087	-0.0091	-0.07238	-0.02738
2018-07-18 00:00:00	0.30843	0.003748	-0.08831	-0.00975	-0.06844	-0.03001
2018-07-19 00:00:00	0.318929		-0.087	-0.01172	-0.08485	-0.02869

2018-07-20 00:00:00	0.312367	-0.012	-0.08635	-0.02747	-0.08419	-0.02672
2018-07-21 00:00:00	0.324179	0.003748	-0.07847	-0.01763	-0.07303	-0.02082
2018-07-22 00:00:00	0.326803	0.003092	-0.08831	-0.01369	-0.07238	-0.02607
2018-07-23 00:00:00	0.325491	0.00178	-0.08307	-0.01041	-0.0855	-0.0241
2018-07-24 00:00:00	0.340583	0.003748	-0.07191	-0.00319	-0.06975	-0.01688
2018-07-25 00:00:00	0.347801	0.040493	-0.06601	0.005339	-0.05794	-0.01098
2018-07-26 00:00:00	0.351738	0.030651	-0.06994	0.007307	-0.06975	-0.01294
2018-07-27 00:00:00	0.355675	0.024745	-0.06207	0.005995	-0.07303	-0.01426
2018-07-28 00:00:00	0.355675	0.033932	-0.06929	0.004682	-0.06647	-0.01557
2018-07-29 00:00:00	0.363549	0.035244	-0.06207	0.0119	-0.06582	-0.00901
2018-07-30 00:00:00	0.371423	0.033276	-0.05813	0.004026	-0.05925	-0.00638
2018-07-31 00:00:00	0.377984	0.031307	-0.05419	0.0119	-0.05794	-0.00507
2018-08-01 00:00:00	0.387827	0.050992	-0.05026	0.021743	-0.04744	0.001491
2018-08-02 00:00:00	0.384546	0.050992	-0.05551	0.022399	-0.05925	0.001491
2018-08-03 00:00:00	0.393076	0.047055	-0.05682	0.02568	-0.05663	0.005428
2018-08-04 00:00:00	0.393732	0.054929	-0.04107	0.021743	-0.06122	0.00674
2018-08-05 00:00:00	0.402263	0.056242	-0.03188	0.019118	-0.06254	0.010677
2018-08-06 00:00:00	0.399638	0.062147	-0.03451	0.019774	-0.06582	0.00674
2018-08-07 00:00:00	0.398982	0.07199	-0.02795	0.032242	-0.05269	0.009365
2018-08-08 00:00:00	0.410793	0.068053	-0.03385	0.033554	-0.04941	0.01199
2018-08-09 00:00:00	0.413417	0.086425	-0.02401	0.040116	-0.04744	0.017239
2018-08-10 00:00:00	0.418667	0.081832	-0.0122	0.052583	-0.04416	0.022488
2018-08-11 00:00:00	0.421291	0.081176	-0.01089	0.045365	-0.04876	0.019864
2018-08-12 00:00:00	0.439664	0.090362	-0.02729	0.036835	-0.04613	0.015927
2018-08-13 00:00:00	0.432446	0.091347	-0.03188	0.032898	-0.05007	0.014614
2018-08-14 00:00:00	0.427197	0.099549	-0.03057	0.035522	-0.0481	0.017239
2018-08-15 00:00:00	0.436383	0.110047	-0.02532	0.045365	-0.04482	0.02052
2018-08-16 00:00:00	0.451475	0.108735	-0.01942	0.062425	-0.04482	0.025113
2018-08-17 00:00:00	0.461974	0.120546	-0.00367	0.068987	-0.04482	0.028394
2018-08-18 00:00:00	0.465911	0.117921	-0.00236	0.068331	-0.03432	0.031675
2018-08-19 00:00:00	0.467879	0.123171	0.007486	0.066362	-0.03235	0.033643
2018-08-20 00:00:00	0.467223	0.124483	0.011423	0.074892	-0.02579	0.036268
2018-08-21 00:00:00	0.469192	0.12842	0.01011	0.080798	-0.02382	0.040861
2018-08-22 00:00:00	0.478378	0.125795	0.008798	0.089984	-0.00873	0.044798
2018-08-23 00:00:00	0.478378	0.125795	0.014703	0.092609	-0.00414	0.04611
2018-08-24 00:00:00	0.482315	0.148761	0.031764	0.09064	-0.02054	0.048735
2018-08-25 00:00:00	0.490845	0.157948	0.037669	0.107045	0.001113	0.056609
2018-08-26 00:00:00	0.488221	0.163197	0.040294	0.109013	-0.01201	0.057921
2018-08-27 00:00:00	0.487564	0.164509	0.041606	0.112294	0.001113	0.055953
2018-08-28 00:00:00	0.492158	0.169759	0.041606	0.116231	-0.00282	0.055297
2018-08-29 00:00:00	0.500032	0.182226	0.041606	0.107045	-0.00282	0.059234

2018-08-30 00:00:00	0.503969	0.194037	0.055386	0.110982	0.003081	0.069732
2018-08-31 00:00:00	0.505937	0.1967	0.066541	0.116231	0.014236	0.074982
2018-09-01 00:00:00	0.517092	0.188788	0.069822	0.116887	0.036546	0.0822
2018-09-02 00:00:00	0.517092	0.190756	0.067197	0.11295	0.021126	0.081543
2018-09-03 00:00:00	0.51053	0.194693	0.061291	0.124105	0.015549	0.081543
2018-09-04 00:00:00	0.516436	0.184851	0.062604	0.120168	0.045732	0.084168
2018-09-05 00:00:00	0.524966	0.178945	0.074415	0.129354	0.053606	0.088105
2018-09-06 00:00:00	0.517092	0.199286	0.083601	0.133291	0.050326	0.086793
2018-09-07 00:00:00	0.521685	0.209785	0.08557	0.134604	0.026703	0.09073
2018-09-08 00:00:00	0.53284	0.216347	0.095412	0.141822	0.050982	0.105165
2018-09-09 00:00:00	0.540714	0.225533	0.103286	0.145102	0.06148	0.113696
2018-09-10 00:00:00	0.547276	0.228158	0.106567	0.153633	0.064105	0.116976
2018-09-11 00:00:00	0.552525	0.220284	0.108536	0.160194	0.065417	0.124851
2018-09-12 00:00:00	0.557118	0.254404	0.11641	0.175942	0.062793	0.132725
2018-09-13 00:00:00	0.557118	0.259654	0.124284	0.170693	0.081165	0.143879
2018-09-14 00:00:00	0.560399	0.261615	0.129533	0.18841	0.085759	0.145848
2018-09-15 00:00:00	0.563024	0.268184	0.128221	0.197596	0.089696	0.14716
2018-09-16 00:00:00	0.561711	0.271465	0.129533	0.204814	0.081165	0.145848
2018-09-17 00:00:00	0.5499	0.270809	0.129533	0.193659	0.079197	0.144536
2018-09-18 00:00:00	0.554494	0.263591	0.129533	0.190378	0.084446	0.144536
2018-09-19 00:00:00	0.5499	0.263591	0.132814	0.183816	0.087727	0.143879
2018-09-20 00:00:00	0.561055	0.283276	0.146593	0.195627	0.101507	0.151097
2018-09-21 00:00:00	0.565648	0.283276	0.15053	0.209407	0.100851	0.158971
2018-09-22 00:00:00	0.570898	0.285244	0.157092	0.211375	0.119879	0.162908
2018-09-23 00:00:00	0.576147	0.294431	0.159717	0.20547	0.11463	0.16947
2018-09-24 00:00:00	0.573522	0.29115	0.168903	0.202189	0.115286	0.166845
2018-09-25 00:00:00	0.57221	0.269496	0.158404	0.204814	0.11463	0.168158
2018-09-26 00:00:00	0.573522	0.284588	0.161029	0.208751	0.125129	0.166189
2018-09-27 00:00:00	0.578772	0.287213	0.182026	0.22253	0.126441	0.174719
2018-09-28 00:00:00	0.592551	0.302305	0.175465	0.233029	0.122504	0.187843
2018-09-29 00:00:00	0.602394	0.323302	0.180714	0.248121	0.092976	0.202278
2018-09-30 00:00:00	0.593208	0.317397	0.180714	0.244184	0.144158	0.200966
2018-10-01 00:00:00	0.610268	0.33052	0.191213	0.249433	0.163186	0.210152
2018-10-02 00:00:00	0.626016	0.342331	0.19515	0.262557	0.169092	0.2259
2018-10-03 00:00:00	0.627328	0.342331	0.19515	0.265837	0.171717	0.228525
2018-10-04 00:00:00	0.612893	0.337071	0.19515	0.26715	0.163186	0.224588
2018-10-05 00:00:00	0.614205	0.306898	0.191213	0.267806	0.16253	0.22262
2018-10-06 00:00:00	0.622079	0.325927	0.19515	0.271743	0.167124	0.227869
2018-10-07 00:00:00	0.622079	0.337082	0.19515	0.273711	0.165155	0.224588
2018-10-08 00:00:00	0.615517	0.337082	0.192525	0.2619	0.157281	0.227213
2018-10-09 00:00:00	0.626016	0.343643	0.200399	0.263213	0.163843	0.235087

2018-10-10 00:00:00	0.620767	0.341019	0.203024	0.264525	0.16778	0.237711
2018-10-11 00:00:00	0.618142	0.331832	0.209585	0.267806	0.175654	0.241648
2018-10-12 00:00:00	0.624704	0.327895	0.214179	0.271743	0.178278	0.249522
2018-10-13 00:00:00	0.645701	0.342987	0.225334	0.285522	0.171717	0.259365
2018-10-14 00:00:00	0.65095	0.346924	0.225334	0.276336	0.17631	0.265271
2018-10-15 00:00:00	0.65095	0.352173	0.225334	0.275024	0.191402	0.266583
2018-10-16 00:00:00	0.645701	0.351517	0.231239	0.273711	0.190746	0.271832
2018-10-17 00:00:00	0.648326	0.346268	0.237801	0.278961	0.197307	0.279706
2018-10-18 00:00:00	0.6562	0.376452	0.246987	0.292084	0.207806	0.288893
2018-10-19 00:00:00	0.670635	0.374483	0.25683	0.307832	0.216336	0.300704
2018-10-20 00:00:00	0.68179	0.405323	0.253549	0.319643	0.216992	0.311202
2018-10-21 00:00:00	0.679822	0.413197	0.258142	0.32358	0.213711	0.311858
2018-10-22 00:00:00	0.657512	0.38695	0.248956	0.315706	0.208462	0.304641
2018-10-23 00:00:00	0.679822	0.377764	0.260767	0.324893	0.216336	0.312515
2018-10-24 00:00:00	0.671292	0.3922	0.25683	0.327517	0.231428	0.311202
2018-10-25 00:00:00	0.683759	0.396137	0.264704	0.334079	0.231428	0.31842
2018-10-26 00:00:00	0.687036	0.406006	0.264705	0.343284	0.257038	0.326946
2018-10-27 00:00:00	0.695567	0.406633	0.2726	0.3498	0.247833	0.3361
2018-10-28 00:00:00	0.6864	0.402033	0.2739	0.3459	0.243867	0.3335
2018-10-29 00:00:00	0.685081	0.404672	0.275193	0.349818	0.247826	0.333508
2018-10-30 00:00:00	0.691633	0.409916	0.276515	0.352452	0.254394	0.337449
2018-10-31 00:00:00	0.694257	0.406635	0.281764	0.351139	0.254394	0.345323
2018-11-01 00:00:00	0.694257	0.405323	0.285701	0.355076	0.261612	0.353197
2018-11-02 00:00:00	0.699507	0.420415	0.288326	0.36295	0.262268	0.362383
2018-11-03 00:00:00	0.720504	0.421727	0.293575	0.370824	0.264893	0.370257
2018-11-04 00:00:00	0.727066	0.43157	0.297512	0.378698	0.267517	0.375507
2018-11-05 00:00:00	0.713943	0.43157	0.294887	0.373449	0.269486	0.372882
2018-11-06 00:00:00	0.709349	0.430914	0.293575	0.372793	0.276704	0.368945
2018-11-07 00:00:00	0.715255	0.443381	0.299481	0.380011	0.278016	0.372882
2018-11-08 00:00:00	0.720504	0.430257	0.300137	0.378042	0.276704	0.374194
2018-11-09 00:00:00	0.758562	0.425008	0.318509	0.399696	0.304263	0.391255
2018-11-10 00:00:00	0.750688	0.440756	0.314572	0.404289	0.305575	0.389943
2018-11-11 00:00:00	0.736252	0.438131	0.314572	0.38526	0.292452	0.380756
2018-11-12 00:00:00	0.740189	0.444693	0.314572	0.395103	0.293108	0.383381
2018-11-13 00:00:00	0.736252	0.465691	0.321134	0.416756	0.296389	0.437187
2018-11-14 00:00:00	0.744126	0.478814	0.317853	0.406257	0.29442	0.386005
2018-11-15 00:00:00	0.746751	0.467659	0.319822	0.40232	0.297701	0.38863
2018-11-16 00:00:00	0.753313	0.47947	0.327696	0.406914	0.305575	0.392567
2018-11-17 00:00:00	0.756593	0.483407	0.33557	0.418068	0.315418	0.392567
2018-11-18 00:00:00	0.75725	0.47094	0.336882	0.421349	0.310168	0.395848
2018-11-19 00:00:00	0.759874	0.495874	0.336882	0.437754	0.309512	0.397817

2018-11-20 00:00:00	0.756593	0.480782	0.334914	0.426599	0.307544	0.396504
2018-11-21 00:00:00	0.762499	0.476189	0.336882	0.422005	0.310168	0.396504
2018-11-22 00:00:00	0.771029	0.484063	0.346068	0.436441	0.312137	0.407659
2018-11-23 00:00:00	0.783496	0.484063	0.348693	0.425943	0.306887	0.408315
2018-11-24 00:00:00	0.783496	0.489969	0.348693	0.42988	0.310168	0.416189
2018-11-25 00:00:00	0.781528		0.340819	0.418725		0.412252
2018-11-26 00:00:00	0.780216	0.489313	0.340819	0.420693	0.312793	0.420126
2018-11-27 00:00:00	0.783496	0.50178	0.347381	0.427255	0.314105	0.428
2018-11-28 00:00:00	0.786121	0.497843	0.348693	0.42463	0.317386	0.421439
2018-11-29 00:00:00	0.784153	0.456504	0.351318	0.426599	0.312793	0.426688
2018-11-30 00:00:00	0.782184	0.467659	0.342131	0.412819	0.295732	0.418158
2018-12-01 00:00:00	0.777591	0.478814	0.342131	0.408882	0.300326	0.418814
2018-12-02 00:00:00	0.771685	0.486688	0.338194	0.410194	0.292452	0.420126
2018-12-03 00:00:00	0.769061	0.478158	0.338194	0.414788	0.323292	0.422095
2018-12-04 00:00:00	0.780216	0.482095	0.340163	0.420693	0.334446	0.426688
2018-12-05 00:00:00	0.785465	0.489969	0.344756	0.42463	0.307544	0.429313
2018-12-06 00:00:00	0.776278	0.488	0.350005	0.408882	0.300326	0.417502
2018-12-07 00:00:00	0.771685	0.476189	0.344756	0.40757	0.298357	0.418814
2018-12-08 00:00:00	0.783496	0.490625	0.35263	0.417412	0.308856	0.422751
2018-12-09 00:00:00	0.786121	0.494562	0.355255	0.42463	0.315418	0.429313
2018-12-10 00:00:00	0.780872	0.495218	0.353943	0.42463	0.316074	0.430625
2018-12-11 00:00:00	0.782184	0.499811	0.35263	0.42463	0.318698	0.430625
2018-12-12 00:00:00	0.79137	0.500467	0.356567	0.42463	0.310168	0.43325
2018-12-13 00:00:00	0.795307	0.53262	0.360504	0.42988	0.320011	0.438499
2018-12-14 00:00:00	0.81368	0.545743	0.369691	0.443003	0.341008	0.45031
2018-12-15 00:00:00	0.803181	0.514247	0.363129	0.435129	0.322635	0.439155
2018-12-16 00:00:00	0.803838	0.51031	0.361817	0.43841	0.336415	0.439811
2018-12-17 00:00:00	0.799244	0.515559	0.363129	0.431192	0.326572	0.435874
2018-12-18 00:00:00	0.804494	0.512935	0.369034	0.428567	0.321979	0.432593
2018-12-19 00:00:00	0.807118	0.511622	0.37494	0.440378	0.327229	0.438499
2018-12-20 00:00:00	0.818929	0.52737	0.384126	0.454814	0.331822	0.45031
2018-12-21 00:00:00	0.820898	0.528683	0.382814	0.458751	0.341008	0.453591
2018-12-22 00:00:00	0.819586	0.558866	0.378877	0.466625	0.337727	0.45031
2018-12-23 00:00:00	0.809087		0.380189	0.464	0.337071	0.449654
2018-12-24 00:00:00	0.809087	0.526386	0.384126	0.466625	0.337071	0.452935
2018-12-25 00:00:00	0.816961	0.526058	0.388063	0.463344	0.340352	0.455559
2018-12-26 00:00:00	0.804494	0.530651	0.386751	0.453502	0.335759	0.452278
2018-12-27 00:00:00	0.809743	0.530651	0.384126	0.461376	0.340352	0.458184
2018-12-28 00:00:00	0.798588	0.547712	0.376252	0.464	0.343633	0.457528
2018-12-29 00:00:00	0.813024	0.54115	0.376252	0.467937	0.339696	0.458184
2018-12-30 00:00:00	0.820242	0.539181	0.382814	0.475811	0.344945	0.458184

2018-12-31 00:00:00	0.84452	0.562803	0.403811	0.492216	0.366599	0.479181
2019-01-01 00:00:00	0.83074	0.550336		0.481061	0.350851	0.47262
2019-01-02 00:00:00	0.812368	0.547712	0.419559	0.475811	0.348882	0.464746
2019-01-03 00:00:00	0.813024	0.555586		0.476467	0.351507	0.468683
2019-01-04 00:00:00	0.83074	0.556242		0.497465	0.359381	0.479181
2019-01-05 00:00:00	0.843864	0.554929		0.496809	0.362662	0.484431
2019-01-06 00:00:00	0.845832	0.546399	0.498956	0.487622	0.362662	0.488368
2019-01-07 00:00:00	0.856331	0.572646	0.465491	0.494184	0.376441	0.502803
2019-01-08 00:00:00	0.851738	0.560179	0.418247	0.498121	0.383659	0.499523
2019-01-09 00:00:00	0.845832	0.568709	0.380189	0.499433	0.383003	0.508053
2019-01-10 00:00:00	0.838614	0.568053	0.392	0.505995	0.390221	0.515927
2019-01-11 00:00:00	0.838614	0.569365	0.391344	0.505995	0.389565	0.51199
2019-01-12 00:00:00	0.851738	0.570677	0.392	0.509932	0.388908	0.516583
2019-01-13 00:00:00	0.854363	0.575927	0.402499	0.515838	0.390877	0.513302
2019-01-14 00:00:00	0.856331	0.571334	0.410373	0.523055	0.401376	0.517895
2019-01-15 00:00:00	0.837958	0.565428	0.40053	0.491559	0.377097	0.513958
2019-01-16 00:00:00	0.858956	0.568709	0.397906	0.505339	0.384315	0.521176
2019-01-17 00:00:00	0.900294	0.574614	0.43137	0.515838	0.404656	0.536924
2019-01-18 00:00:00	0.868798	0.570021	0.411685	0.515181	0.404	0.530363
2019-01-19 00:00:00	0.856987	0.576583	0.415622	0.516494	0.402032	0.530363
2019-01-20 00:00:00	0.855675	0.575927	0.42284	0.520431	0.401376	0.539549
2019-01-21 00:00:00	0.860924	0.573302	0.423496	0.521743	0.406625	0.539549
2019-01-22 00:00:00	0.850426	0.591019	0.410373	0.523055	0.394814	0.535612
2019-01-23 00:00:00	0.876672	0.577239	0.423496	0.52568	0.420733	0.547423
2019-01-24 00:00:00	0.881922	0.595612	0.426777	0.534866	0.419092	0.555297
2019-01-25 00:00:00	0.897013	0.606111	0.433995	0.541428	0.433528	0.563171
2019-01-26 00:00:00	0.889796	0.604142	0.438588	0.546677	0.435496	0.563171
2019-01-27 00:00:00	0.899638	0.60283	0.447775	0.559801	0.435496	0.587449
2019-01-28 00:00:00	0.896357	0.596924	0.437932	0.553239	0.431559	0.56842
2019-01-29 00:00:00	0.89767	0.598237	0.419559	0.544053	0.423685	0.561859
2019-01-30 00:00:00	0.905544	0.606111	0.428746	0.549958	0.438121	0.565796
2019-01-31 00:00:00	0.910137	0.606111	0.437276	0.551271	0.436809	0.56842
2019-02-01 00:00:00	0.889139	0.607423	0.428746	0.537491	0.423685	0.556609
2019-02-02 00:00:00	0.893733	0.588394	0.43137	0.537491	0.423029	0.557265
2019-02-03 00:00:00	0.895701	0.584457	0.447775	0.540116	0.410562	0.549391
2019-02-04 00:00:00	0.895701	0.591675	0.446462	0.54799	0.423685	0.550048
2019-02-05 00:00:00	0.89767	0.62842	0.443181	0.54274	0.404656	0.557265
2019-02-06 00:00:00	0.891108	0.636294	0.441213	0.532898	0.414499	0.55136
2019-02-07 00:00:00	0.901607	0.645998	0.439901	0.555208	0.415811	0.563171
2019-02-08 00:00:00	0.915386	0.640231	0.448431	0.570956	0.417124	0.565796
2019-02-09 00:00:00	0.922604	0.659916	0.458929	0.580142	0.430247	0.581544

2019-02-10 00:00:00	0.927853	0.657948	0.473365	0.588672	0.421061	0.586793
2019-02-11 00:00:00	0.929166	0.63367	0.486489	0.593922	0.41253	0.588105
2019-02-12 00:00:00	0.933103	0.665166	0.483208	0.59589	0.449276	0.581544
2019-02-13 00:00:00	0.963286	0.680914	0.496987	0.610982	0.474866	0.605166
2019-02-14 00:00:00	0.982972	0.678289	0.4983	0.614919	0.507675	0.605166
2019-02-15 00:00:00	0.97116	0.662541	0.514704	0.62673	0.526048	0.627475
2019-02-16 00:00:00	0.980347	0.691412	0.517328	0.630011	0.514893	0.636662
2019-02-17 00:00:00	0.973785	0.696662	0.509454	0.62673	0.507019	0.617633
2019-02-18 00:00:00	0.963943	0.71241	0.512079	0.624762	0.484053	0.609103
2019-02-19 00:00:00	0.981003	0.72947	0.519953	0.637229	0.5103	0.624851
2019-02-20 00:00:00	0.988221	0.711098	0.519953	0.64379	0.524079	0.640599
2019-02-21 00:00:00	0.975098	0.705192	0.525202	0.63526	0.522767	0.653722
2019-02-22 00:00:00	0.97116	0.727502	0.520609	0.633948	0.510956	0.644536
2019-02-23 00:00:00	0.985596	0.724221	0.530452	0.649696	0.536546	0.659628
2019-02-24 00:00:00	0.992158	0.720284	0.53767	0.658226	0.539171	0.667502
2019-02-25 00:00:00	1.010531	0.70716	0.548168	0.667412	0.548357	0.677344
2019-02-26 00:00:00	1.012499	0.725533	0.556042	0.671349	0.540483	0.679969
2019-02-27 00:00:00	1.023654	0.733407	0.564573	0.672662	0.533922	0.682594
2019-02-28 00:00:00	1.043995	0.771465	0.586882	0.684473	0.562793	0.69178
2019-03-01 00:00:00	1.023654	0.759654	0.597381	0.693003	0.567386	0.701622
2019-03-02 00:00:00	1.03284	0.767528	0.588851	0.694315	0.568042	0.70884
2019-03-03 00:00:00	1.03809	0.755061	0.589507	0.687098	0.568699	0.700966
2019-03-04 00:00:00	1.021029	0.742594	0.591475	0.685129	0.5582	0.693092
2019-03-05 00:00:00	1.028247	0.744562	0.71746	0.686441	0.556231	0.697029
2019-03-06 00:00:00	1.040714	0.75178	0.610504	0.694315	0.578541	0.698342
2019-03-07 00:00:00	1.039402	0.767528	0.554074	0.691035	0.583134	0.698342
2019-03-08 00:00:00	1.03284	0.749155	0.584914	0.680536	0.581166	0.693092
2019-03-09 00:00:00	1.030872	0.739313	0.569822	0.679223	0.573948	0.690468
2019-03-10 00:00:00	1.030216	0.740625	0.567197	0.679223	0.560168	0.695717
2019-03-11 00:00:00	1.037433	0.726846	0.579008	0.685785	0.56673	0.700966
2019-03-12 00:00:00	1.051869	0.72947	0.578352	0.696284	0.569355	0.706216
2019-03-13 00:00:00	1.053838	0.733407	0.581633	0.691691	0.562137	0.710153
2019-03-14 00:00:00	1.063024	0.765559	0.604599	0.706783	0.586415	0.716714
2019-03-15 00:00:00	1.067617	0.785901	0.5941	0.715969	0.589696	0.732462
2019-03-16 00:00:00	1.074835	0.786557	0.584914	0.730405	0.600851	0.771832
2019-03-17 00:00:00	1.081397	0.793775	0.592132	0.738279	0.611349	0.778394
2019-03-18 00:00:00	1.093208	0.795087	0.601318	0.731061	0.615286	0.749523
2019-03-19 00:00:00	1.100426	0.785245	0.604599	0.731061	0.612662	0.733119
2019-03-20 00:00:00	1.083365	0.785245	0.60263	0.733029	0.608069	0.727213
2019-03-21 00:00:00	1.082053	0.788525	0.61641	0.733029	0.611349	0.725901
2019-03-22 00:00:00	1.048588	0.745874	0.596725	0.706783	0.591008	0.721964

2019-03-23 00:00:00	1.059087	0.759654	0.600006	0.709407	0.589696	0.725901
2019-03-24 00:00:00	1.075491	0.780323	0.603943	0.717937	0.600851	0.727869
2019-03-25 00:00:00	1.075491	0.778683	0.605911	0.719906	0.6061	0.728525
2019-03-26 00:00:00	1.086646	0.780651	0.615098	0.724499	0.602163	0.728525
2019-03-27 00:00:00	1.088615	0.799024	0.612473	0.722531	0.598882	0.726557
2019-03-28 00:00:00	1.097801	0.814116	0.619691	0.733029	0.606756	0.733775
2019-03-29 00:00:00	1.089271	0.795743	0.615098	0.729748	0.608725	0.730494
2019-03-30 00:00:00	1.082709	0.783932	0.607223	0.724499	0.604788	0.724588
2019-03-31 00:00:00	1.103706	0.787869	0.615098	0.733685	0.610693	0.735087